



**Geoscience BC**

# SUMMARY OF ACTIVITIES **2018:** **Energy and Water**

**GEOSCIENCE BC  
SUMMARY OF ACTIVITIES 2018:  
ENERGY AND WATER**

© 2019 by Geoscience BC.

All rights reserved. Electronic edition published 2019.

This publication is also available, free of charge, as colour digital files in Adobe Acrobat® PDF format from the Geoscience BC website: <http://www.geosciencebc.com/s/SummaryofActivities.asp>.

Every reasonable effort is made to ensure the accuracy of the information contained in this report, but Geoscience BC does not assume any liability for errors that may occur. Source references are included in the report and the user should verify critical information.

When using information from this publication in other publications or presentations, due acknowledgment should be given to Geoscience BC. The recommended reference is included on the title page of each paper. The complete volume should be referenced as follows:

Geoscience BC (2019): Geoscience BC Summary of Activities 2018: Energy and Water; Geoscience BC, Report 2019-2, 132 p.

Summary of Activities: Energy (Geoscience BC)  
Annual publication

ISSN 2562-2757 (Print)  
ISSN 2562-2765 (Online)

Geoscience BC  
1101–750 West Pender Street  
Vancouver, British Columbia V6C 2T7  
Canada

## Foreword

Geoscience BC is pleased to once again present results from our ongoing projects in our annual *Summary of Activities* publication. Following on from last year, we are publishing the papers in two separate volumes: *Minerals and Mining*, and this volume, *Energy and Water* (previously published as *Summary of Activities: Energy*). Both volumes are available in print and online via [www.geosciencebc.com](http://www.geosciencebc.com).

### Summary of Activities 2018: Energy and Water

This volume, *Summary of Activities 2018: Energy and Water*, contains 13 papers from Geoscience BC–funded projects or 2018 scholarship winners that are within Geoscience BC’s strategic focus areas of energy (including oil & gas and geothermal) and water. The papers are divided into five sections, based on Geoscience BC’s strategic objectives of

- 1) Identifying New Natural Resource Opportunities;
- 2) Advancing Science and Innovative Geoscience Technologies;
- 3) Facilitating Responsible Natural Resource Development;
- 4) Enabling Clean Energy; and
- 5) Understanding Water.

In the first section, *Identifying New Natural Resource Opportunities*, Wilson and Bustin, and Silva and Bustin describe their ongoing research into the quantification of the gas- and liquids-in-place, and flow characteristics in northeastern British Columbia (BC), a Geoscience BC–funded project that is nearing completion. In addition, scholarship recipient Kunert (et al.) discusses spatial and temporal trends during deposition of the Gordondale member and Poker Chip Shale. In the *Advancing Science and Innovative Geoscience Technologies* section, Chalmers et al. introduce a new Geoscience BC–supported project that aims to reduce the uncertainty of producing H<sub>2</sub>S from the Montney reservoir.

The three papers in the *Facilitating Responsible Natural Resource Development* section are focused on hydraulic fracturing in northeastern BC. Babaie Mahani and Kao discuss the determination of accurate local magnitude for induced earthquakes, and Bustin et al. give an update on the ongoing collection of ground-motion data from induced seismicity. Scholarship recipient Onwuemeka (et al.) discusses upcoming research aimed at increasing our understanding of earthquake processes and helping adequately assess seismic hazards to better inform the public and assist both regulators and industry operators in developing policies to reduce risk and improve hazard assessment.

In the *Enabling Clean Energy* section, Whiticar et al. present an update on testing a drone-mounted open-path laser spectrometer to measure greenhouse-gas emissions; Evans highlights ongoing development of a natural gas atlas for BC; and scholarship recipient Warwick (et al.) discusses the development of a volcanic-hazard map for Mount Meager.

Finally, in the *Understanding Water* section, Cahill, Ladd et al. discuss ongoing technical and community-engagement work focused on better understanding the impacts of fugitive gas on groundwater. Cahill, Beckie et al. introduce a new Geoscience BC–supported project characterizing methane in groundwater in the Peace region. Haynes et al. present their final report on understanding changes in permafrost in northeastern BC.

### Geoscience BC Energy and Water Publications 2018

In addition to the two *Summary of Activities* volumes, Geoscience BC releases interim and final products from our projects as Geoscience BC reports. The following seven Energy and Water reports were published in 2018, with an eighth report to be released in early 2019:

- Ten technical papers in the *Geoscience BC Summary of Activities 2017: Energy and Water* volume (Geoscience BC Report 2018-04)
- **Processing and Inversion of SkyTEM Data Leading to a Hydrogeological Interpretation of the Peace River North Western Area**, by Aarhus Geophysics Aps and GEUS–Department of Groundwater and Quaternary Geology Mapping (Geoscience BC Report 2018-06)

- **Peace Area Project – Comparison of Resistivity, Gamma and Geological Logs with Airborne EM Inversions**, by M. Best and V. Levson (Geoscience BC Report 2018-08)
- **Geoscience BC Peace Project: Final Report**, by S.E. Morgan and D.M. Allen (Geoscience BC Report 2018-13)
- **Mapping the Susceptibility to Amplification of Seismic Ground Motions in the Montney Play Area of Northeast British Columbia**, by P.A. Monahan, V.M. Levson, B.J. Hayes, K. Dorey, Y. Mykula, R. Brenner, J. Clarke, B. Galambos, C. Candy, C. Krumbiegel and E. Calderwood (Geoscience BC Report 2018-16) – *scheduled for release early January 2019*
- **Techno-Economic Assessment of Geothermal Energy Resources in the Sedimentary Basin in Northeastern British Columbia**, by K. Palmer-Wilson, W. Walsh, J. Banks and P. Wild (Geoscience BC Report 2018-18)
- **Clarke Lake Gas Field Reservoir Characterization**, by E. Renaud, J. Banks, N.B. Harris and J. Weissenberger (Geoscience BC Report 2018-19)
- **Identification and Evaluation of New Resource Oil Plays in Northeast British Columbia’s Portion of the Western Canadian Sedimentary Basin**, by Petrel Robertson Consulting Ltd. (Geoscience BC Report 2018-20)

All releases of Geoscience BC reports and data are published on our website and are announced through our website and e-mail updates. Most final reports and data can also be viewed through our Earth Science Viewer at <http://www.geosciencebc.com/s/WebMaps.asp>.

### Acknowledgments

Geoscience BC would like to thank all authors and reviewers of the *Summary of Activities* for their contributions to this volume. RnD Technical is also acknowledged for their work in editing and assembling both volumes. As well, Geoscience BC would like to acknowledge the Province of British Columbia and our project-funding partners for their ongoing support of public geoscience, and express our appreciation for the leaders and volunteers in British Columbia’s mineral exploration, mining and energy sectors who support our organization through their guidance, use and recognition of the information that we collect and distribute.

Christa Pellett  
Project Co-ordinator  
Geoscience BC  
[www.geosciencebc.com](http://www.geosciencebc.com)

## Contents

### Identifying New Natural Resource Opportunities

- T.K. Wilson and R.M. Bustin:** Basin modelling and thermal history of the Horn River and Liard basins, Cordova Embayment, and adjacent parts of the Western Canada Sedimentary Basin . . . . . 1
- P.L. Silva and R.M. Bustin:** Variability and controls on the matrix permeability of the Doig Formation in northeastern British Columbia. . . . . 21
- A. Kunert, B. Kendall, T.F. Moslow, G. Nyberg, B. Pederson and C. Smith:** Preliminary characterization of Early Jurassic source rocks and ocean-redox conditions based on trace-metal and organic geochemistry of the Gordondale and Poker Chip Shale members, Fernie Formation, northeastern British Columbia. . . . . 29

### Advancing Science and Innovative Geoscience Technologies

- G.R.L. Chalmers, R.M. Bustin and A.A. Bustin:** Stratigraphic and lateral distribution of hydrogen sulphide within the Triassic Montney Formation, northern regional play area, northeastern British Columbia and northwestern Alberta . . . . . 43

### Facilitating Responsible Natural Resource Development

- A. Babaie Mahani and H. Kao:** Local magnitude scale for earthquakes in the Western Canada Sedimentary Basin, northeastern British Columbia and northwestern Alberta. . . . . 47
- A.M.M. Bustin, E.O. Munson, D.J. Jones and G.R.L. Chalmers:** Ground-motion data from seismicity induced in the southern Montney Formation, northeastern British Columbia . . . . . 55

- J. Onwuemeka, R.M. Harrington, Y. Liu and H. Kao:** Source properties of earthquakes around hydraulic-fracturing sites near Dawson Creek, northeastern British Columbia . . . . . 63

### Enabling Clean Energy

- M.J. Whiticar, L.E. Christensen, C.J. Salas and P. Reece:** GHGMap: detection of fugitive methane leaks from natural gas pipelines, British Columbia and Alberta . . . . . 67
- C. Evans:** Molecular composition and isotope mapping of natural gas in the British Columbia Natural Gas Atlas . . . . . 77
- R.K. Warwick, G. Williams-Jones, J. Witter and M.C. Kelman:** Comprehensive volcanic-hazard map for Mount Meager volcano, southwestern British Columbia. . . . . 85

### Understanding Water

- A.G. Cahill, B. Ladd, J. Chao, J. Soares, T. Cary, N. Finke, C. Manning, C. Chopra, I. Hawthorne, O.N. Forde, K.U. Mayer, A. Black, S. Crowe, B. Mayer, R. Lauer, C. van Geloven, L. Welch and R.D. Beckie:** Implementation and operation of a multidisciplinary field investigation involving a subsurface controlled natural gas release, northeastern British Columbia. . . . . 95
- A.G. Cahill, R.D. Beckie, M. Goetz, A. Allen, B. Ladd, L. Welch, D. Kirste, B. Mayer, C. van Geloven:** Characterizing dissolved methane in groundwater in the Peace region, northeastern British Columbia, using a regional, dedicated, groundwater monitoring well network . . . . . 105
- K.M. Haynes, O.A. Carpino, R.F. Connon, É. Devoie and W.L. Quinton:** Thaw-induced land-cover change in the southern margin of discontinuous permafrost, northeastern British Columbia and southwestern Northwest Territories. . . . . 123



# Basin Modelling and Thermal History of the Horn River and Liard Basins, Cordova Embayment, and Adjacent Parts of the Western Canada Sedimentary Basin

T.K. Wilson, The University of British Columbia, Vancouver, BC, tessakwils@gmail.com

R.M. Bustin, The University of British Columbia, Vancouver, BC

Wilson, T.K. and Bustin, R.M. (2019): Basin modelling and thermal history of the Horn River and Liard basins, Cordova Embayment, and adjacent parts of the Western Canada Sedimentary Basin; *in* Geoscience BC Summary of Activities 2018: Energy and Water, Geoscience BC, Report 2019-1, p. 1–20.

## Introduction

In sedimentary basins, it is important to gain an understanding of basin evolution. Basin modelling through numerical simulations is a powerful tool in quantifying the burial and thermal history of a basin and hydrocarbon generation, migration and entrapment. Basin modelling requires the integration and knowledge of numerous variables, including regional geology, lithology, stratigraphy, tectonic history and heat flow. The northeastern British Columbia (northeastern BC) portion of the Western Canada Sedimentary Basin (WCSB) is relatively understudied and underexplored compared to most other areas in the basin. Hence, basin modelling can provide significant insights and constraints on the basin history and contribute to predicting the economic potential of this important area.

Previous work in the study area on the Devonian stratigraphy of the Horn River Basin (HRB) and adjacent areas has focused on reservoir properties and resource potential (Stasiuk and Fowler, 2004; Ross, 2007; Ross and Bustin, 2008, 2009a, 2009b; Ferri et al., 2011, 2015; Chalmers et al., 2012; Fiess et al., 2013; Harris and Dong, 2013; Balogun, 2014; Dong et al., 2014; Ferri and Griffiths, 2014; Dong, 2016). There have been few studies that have contributed to understanding the basin evolution and burial history. The few studies that include a basin-modelling component have focused on the Liard Basin and Interior Plains (Morrow et al., 1993; Potter, 1998), on the Peace River arch area (Kalkreuth and McMechan, 1988; Dubey et al., 2017) or farther to the east near the oil-sands deposits (Higley et al., 2009; Berbesi et al., 2012). All of these studies provide important information and methodologies, and lay the groundwork on which the present modelling study is based. Most notably, the Morrow et al. (1993) study of the Liard Basin (mainly within the Northwest Territories) provides key data and insights.

The objective of this study is to use basin modelling to understand the basin evolution and determine the role of various geological properties in the burial and thermal history and subsequent present-day petroleum systems of northeastern BC. One-dimensional (1-D) modelling and sensitivity analysis were performed at 24 well locations throughout the study area, leveraged by publicly available data and a multitude of prior research on the regional geology, lithology and stratigraphy.

## Regional Geology and Stratigraphy

### Overview and Study Area

This study focuses on the Horn River Basin and the Cordova Embayment in northeastern BC, northwestern Alberta and adjacent areas, as well as a portion of the Liard Basin (Figure 1). This roughly encompasses an area extending from 59 to 60°N and from 118 to 124°W. This large area contains a thick succession of Phanerozoic sedimentary rocks, including the extensive Devonian-age, organic-rich source rocks that are the focus of this research. The main

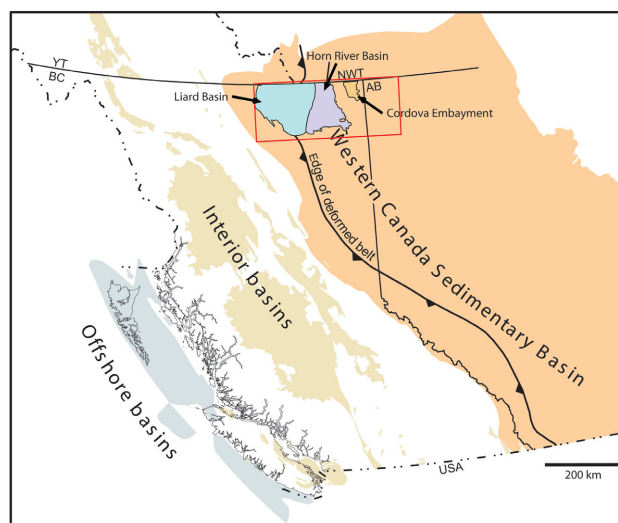


**Figure 1.** The study area in the geographic context of western Canada (modified from Ferri et al., 2015). The study area is outlined in red and encompasses the Liard Basin (blue), the Horn River Basin (purple) and the Cordova Embayment (orange), as well as western Alberta.

*This publication is also available, free of charge, as colour digital files in Adobe Acrobat® PDF format from the Geoscience BC website: <http://www.geosciencebc.com/s/SummaryofActivities.asp>.*

structural feature of the study area is the Bovie fault complex, which separates the Horn River Basin from the Liard Basin.

## Tectonic History

The evolution of the WCSB can be divided into two main tectonic phases: a late Proterozoic to Jurassic continental-margin setting and a compressional Jurassic to Eocene fore-land basin. During the Paleozoic, northeastern BC experienced extensive subsidence, block faulting and volcanism (Price, 1994). The study area likely experienced extension behind an east-dipping subduction zone, coeval with the compression of the Devonian-age Antler orogeny occurring to the south. Such extension is thought to have led to the block faulting that formed the Peace River Embayment, Fort St. John graben and Prophet Trough during the Devonian and Mississippian. These salient features affected the Late Paleozoic deposition and clastic provenance (Wright et al., 1994). The first stage of Bovie fault motion occurred during the Late Carboniferous and is interpreted by Maclean and Morrow (2004) to have been a crustal-scale convergent fault. This movement caused the subsequent erosion of the Mattson and Fantasque formations east of the fault within the HRB.

Beginning in the Jurassic, terrane accretion along the western edge of North America formed the Cordilleran fold-and-thrust belt. The tectonic regime during this time can be broadly split into a Jurassic to mid-Cretaceous collision and terrane accretion, and a Late Cretaceous to Paleocene right-lateral transpression phase (Price, 1994). Significant shortening and thickening of the Phanerozoic strata occurred; however, the amount of shortening varies across the margin, with the largest values estimated to be in the south and decreasing toward the north. The decrease in shortening in northeastern BC, relative to southern British Columbia and Alberta, is fundamentally connected to the change in plate motion from compressional in the south to more oblique convergence in the north (Wright et al., 1994). There is a change in structural style in the north due to changes in lithology: the overall lower competency of the area, due to thick shale successions, led to a fold-dominated structural style, rather than thrust-dominated (Wright et al., 1994). The Bovie fault was reactivated during the Laramide orogeny as a shallow décollement (Maclean and Morrow 2004). The tectonic style changed in the early Eocene, and the transpressional regime became transtensional. As a result, subsidence was replaced by uplift and subsequent erosion (Price, 1994).

## Stratigraphy

The Phanerozoic stratigraphic succession in northeastern BC is several kilometres thick, varying from approximately 2 km near Alberta to more than 4 km within the Liard Basin, with the majority of the thickness associated with Devonian

and Mississippian formations (Figure 2). These periods are characterized by a series of stacked carbonate and mudrock packages related to multiple sea-level changes and continued subsidence. West of the main carbonate platform and the Presqu'île barrier reef that formed during the early Givetian, the carbonate transitions into shale of the Horn River, Muskwa and Besa River formations. On the cratonic platform, a mixed siliciclastic-carbonate system persisted throughout the upper Devonian (CBM Solutions, 2005). A major transgression and inundation of the entire platform led to the deposition of the Muskwa Formation (Switzer et al., 1994). The Devonian shale units are siliceous in nature due to the accumulation of pelagic radiolarians in a deep-basinal depositional environment (Ross and Bustin, 2008). The Muskwa Formation is overlain by the Fort Simpson Formation and several carbonate formations. The Exshaw Formation and equivalents are present throughout North America and represent another major marine transgression. Above the Exshaw Formation are the siliciclastic and lime-mudstone of the Banff Formation, overlain by the Rundle Group (Kent, 1994). In the Liard Basin, the Besa River Formation was still exposed during deposition of the Rundle Group. During the Late Mississippian, however, the Liard Basin became a dominantly deltaic and coastal-plain environment, resulting in deposition of the Mattson Formation, which is only observed in the Liard area but likely coeval with the Kiskatinaw Formation within the Peace River Embayment (Richards, 1989; Richards et al., 1994). The rock record in the study area becomes sparse from the Permian until the mid-Cretaceous. This is due to a significant drop in sea level during the Late Permian, leading to a period of erosion and the beginning of compressional deformation during the Jurassic, which eroded earlier deposits as the deformation front moved east (Wright et al., 1994). The Cretaceous strata are the deltaic, fluvial and marine deposits of the Fort St. John Group (Stott, 1982). Accumulation of Upper Cretaceous sedimentary rocks is rarely present; the sedimentary section is capped by relatively thick Quaternary overburden.

## Materials and Methodology

This study focuses on reconstructing the basin through a series of 1-D basin models across the study area (Figure 3). The models were built using Schlumberger's PetroMod<sup>®</sup> 2015 software suite. In order for the models to be fully representative of the basin, all of the inputs need to be defined according to the best available knowledge and data. Important modelling inputs include lithology for the entire stratigraphic column, source-rock properties, boundary conditions (heat flow, surface-water interface temperature and paleo-water depths), erosion and hiatus events, and any thermal-maturity calibration data available (mainly vitrinite reflectance). Some inputs, such as heat flow, are particularly difficult to constrain; therefore, sensitivity analysis was performed on each model to address these uncertain-

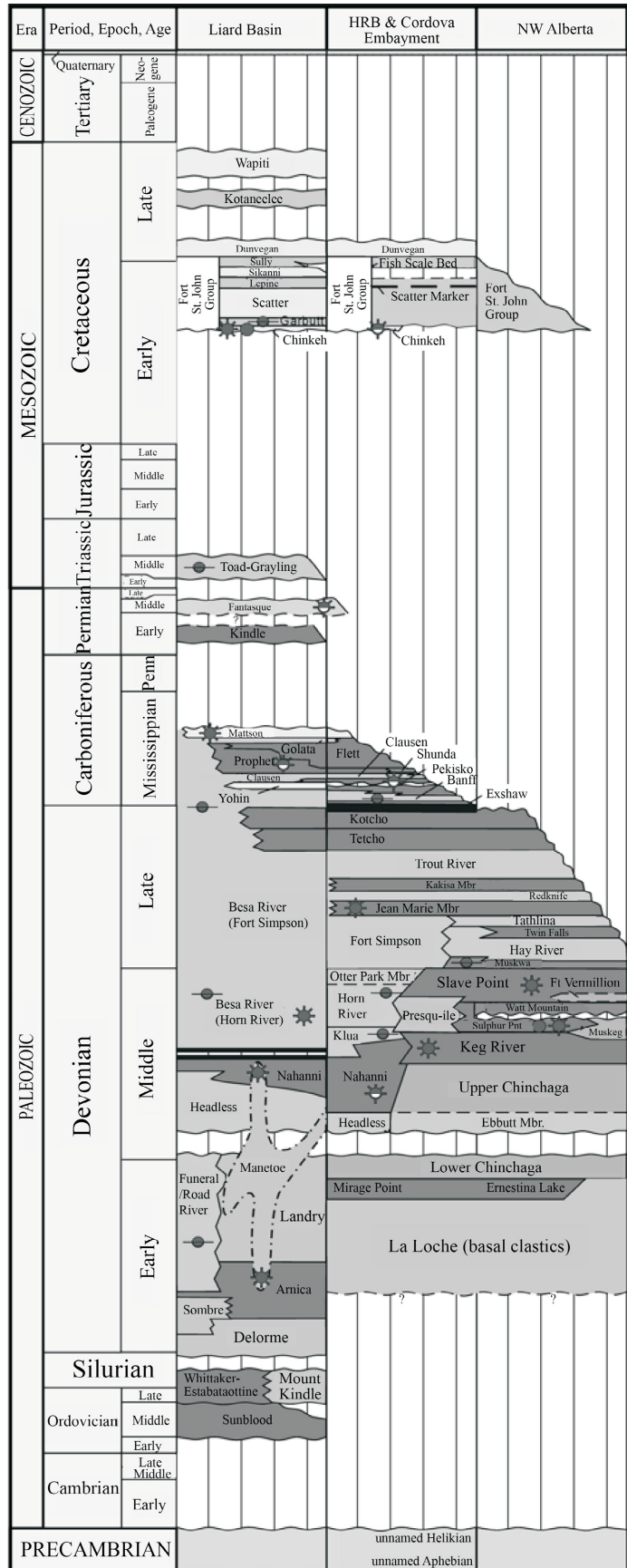
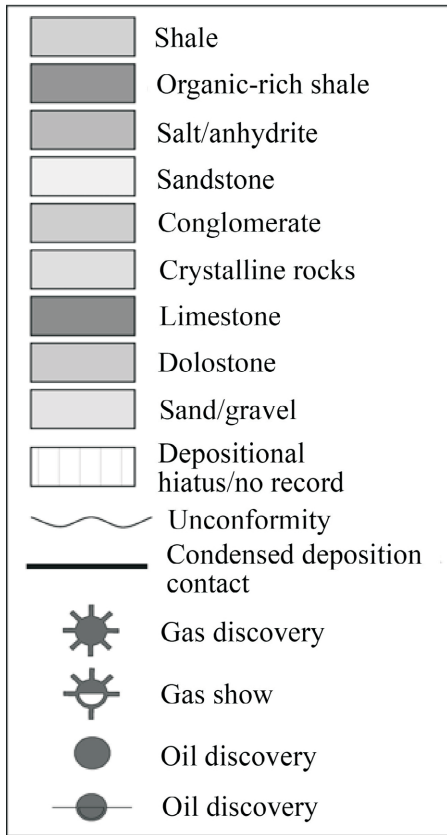
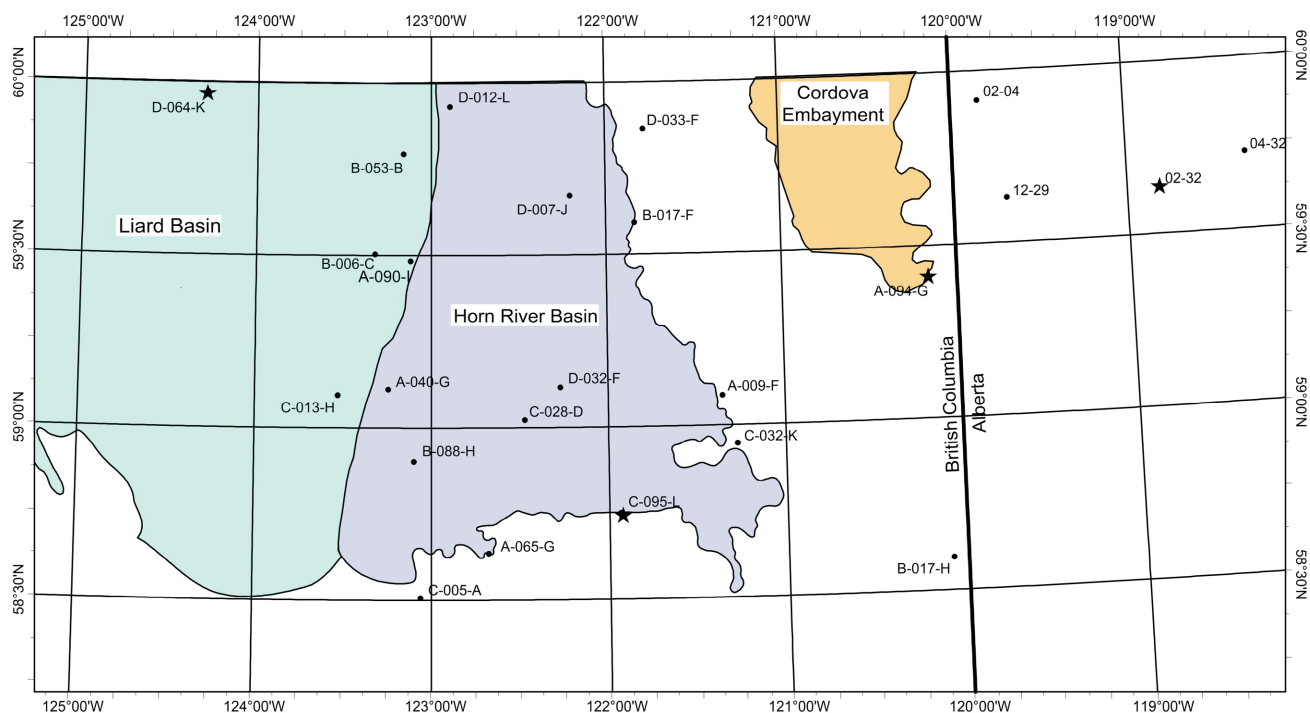


Figure 2. Phanerozoic stratigraphy of northeastern BC and Alberta (modified from Maclean and Morrow, 2004).



**Figure 3.** Location of 1-D models within the study area in northeastern BC and adjacent areas. Model locations are represented by black dots, and the models discussed in this paper are represented by black stars.

ties and ensure that the final models reflected the most likely case.

## Lithology

Accurately defining the lithology of individual stratigraphic intervals (Devonian to present) is critical during basin modelling. Different rock types exhibit different petrophysical properties (chemical, mechanical and thermal), which affect the simulation of the numerical models. User-defined rock types were created within PetroMod<sup>®</sup> for each stratigraphic unit by mixing several predefined rock types. The Lexicon of Canadian Geological Names (Natural Resources Canada, 2018) was the main source for generalized lithological descriptions. In general, the rock types were kept laterally consistent across the study area. The default Athy's law (Athy, 1930) was used as the mechanical compaction model and the default Sekiguchi model (Sekiguchi, 1984) was used for thermal conductivity. The thermal conductivity of mixed rock types is calculated internally by geometrically averaging the rock-matrix and pore-fluid values. The calculated thermal-conductivity values were used for each mixed lithology. Table 1 illustrates the stratigraphic formations and ages, and their respective rock types, and thermal and mechanical properties.

## Source Rock Properties

In the study area, the main identified Devonian-age petroleum source rocks are the Evie Member and the Muskwa and Exshaw formations (National Energy Board and BC Ministry of Energy, Mines and Petroleum Resources,

2011). The default Burnham 1989 TII kinetic model built within PetroMod<sup>®</sup> was used for all three source-rock intervals. Based on whole-rock pyrolysis analysis, hydrogen indices are generally <50 mgHC/g of rock, and TOC averages 3 wt. % for both the Muskwa and Evie intervals, and slightly higher for the Exshaw Formation (Wilson and Bustin, 2017).

## Boundary Conditions

The PetroMod<sup>®</sup> software requires three boundary conditions to be defined before any simulations can be completed. These conditions are heat flow, sediment-water interface temperature (SWIT) and paleo-water depth (PWD). Both present-day and paleo values must be defined. All of the boundary conditions help to define the thermal constraints of the model, with heat flow being the most important of the three. Figure 4 represents the generalized trend of these three parameters versus time.

### Sediment-Water Interface Temperature and Paleo-Water Depth

The SWIT values throughout the history of the basin were defined by using the Wygrala (1989) model for global mean temperature at sea level. This method is built into PetroMod<sup>®</sup> and uses present-day latitude and paleo-water-depth data to extract the temperature at sea level over a series of geological time steps. The SWIT values range from 5 to 25.3°C, with peak temperatures at 100 Ma. The PWD was based on the paleogeographic maps and the evolution history of the basin (Mossop and Shetsen, 1994; Wright et

**Table 1.** Stratigraphy, lithology, and thermal and mechanical parameters used for the model simulations.

Stratigraphic nomenclature	Depositional age (Ma)	Lithology	Thermal conductivity @ 20°C/300°C (W/[m•K])	Heat capacity @ 20°C/300°C (kcal/[kg•K])	Mechanical properties		
					Density (kg/m <sup>3</sup> )	Initial porosity (%)	Athy's factor (1/km)
Overburden	0.4	sst (subarkoze, typical)	4.55/2.90	0.21/0.29	2680	41	0.28
Upper Cretaceous	65	sltst (organic lean), sh (organic lean), siderite, kaolinite	1.87/1.85	0.21/0.3	2743.3	58.81	0.42
Fort St. John Gr.	100	sst (clay rich), sh (organic lean), sst wacke, coal, sltst (organic lean)	1.85/1.84	0.21/0.3	2717.4	46.97	0.6
Bullhead Gr.	110	Cnglm (typical), sst (typical), coal, sltst (organic lean), sh (organic lean)	2.45/2.08	0.21/0.30	2656	49.05	0.44
Doig/Toad Fm.	230	sh (organic lean), sst (typical), lmst (shaly), sltst (organic lean)	2.03/1.91	0.21/0.3	2716.9	57.17	0.59
Fantasque Fm.	252	Chert, sh (typical), sst (typical)	4.42/2.84	0.21/0.3	2663	45.65	0.41
Belloy Fm.	270	sst (typical)	3.95/2.66	0.2/0.29	2720	41	0.31
Mattson Fm.	325	sst (typical), sst (quartzite), sh (typical), dlm (typical), chert, coal	3.85/2.62	0.21/0.3	2650.7	43.49	0.34
Golata Fm.	325	sst (typical), argill. carb. mdst (marl), anhydrite, coal	3.5/2.47	0.21/0.29	2706.95	47.95	0.43
Rundle Gr.	335	Lmst (oid grainstone), dlm (typical)	3.2/2.37	0.2/0.29	2770	35	0.24
Banff Fm.	347	sh (organic lean, silty), carb-rich arg mdst, lmst (shaly), sltst (organic lean)	2.70/2.18	0.21/0.29	2716.9	58	0.63
Exshaw Fm	360	Sh. (black), pyrite, tuff (felsic)	1.00/1.51	0.22/0.31	2584.3	67.33	0.78
Kotcho Fm.	361	Carb. silic. mdst, Sh (black), carb-rich argill. mdst, lmst (micrite)	3.50/2.49	0.21/0.29	2712.85	57.6	0.61
Tetcho Fm.	362	Lmst (micrite), sh (typical), sltst (organic lean)	2.86/2.24	0.2/0.29	2737	52.15	0.54
Trout River Fm.	363	sltst (organic lean), lmst (shaly), shale (typical)	2.9/2.25	0.21/0.3	2720	55.2	0.57
Red Knife Fm.	369	lmst (shaly), sst (subarkoze, dlm rich), sltst (organic lean)	2.44/2.07	0.21/0.29	2724.5	48.55	0.47
Jean Marie Fm.	369	Dlm (organic lean, silty), lmst (micrite), lmst (mound)	3.00/2.29	0.2/0.29	2752	34.4	0.34
Fort Simpson Fm.	371	Sh (organic lean, typical), carb. silic. Mdst, sltst (organic lean), sst (typical)	3.45/2.47	0.21/0.30	2710.6	61.8	0.67
Muskwa Fm.	376	Carb. silic. mdst, sh (typical), pyrite	1.5/1.71	0.2/0.29	2781.78	60.73	0.68
Watt Mountain Fm.	376	Sh (typical), lmst (micrite), sst (arkoze, typical), dlm (typical), anhydrite	3.13/2.34	0.2/0.28	2761.5	42.4	0.44
Slave Point Fm.	376	lmst (micrite), dlm (typical), sh (typical)	3.12/2.34	0.2/0.29	2751	48.1	0.51
Otter Park Mbr.	378	Carb. silic. mdst, sh (typical), pyrite	2.8/2.21	0.21/0.29	2760.24	60.52	0.67
Evie Mbr.	380	Sh (black), sltst (organic lean), lmst (micrite), pyrite	1.27/1.62	0.22/0.3.1	2948.1	62.65	0.7
Dunedin Fm.	380	dlm (typical), sst (typical), lmst (oid grainstone)	2.9/2.24	0.2/0.29	2774.2	35.24	0.29
Muskeg Fm.	381	Salt, lmst (micrite), dlm (typical), anhydrite	4/2.68	0.2/0.28	2801	21.2	0.22
Keg River Fm.	382	dlm (typical), sst (typical), lmst (oid grainstone)	2.9/2.25	0.2/0.29	2774.2	35.24	0.29
Besa River Fm.	380-345	Sh (organic lean, typical), carb. silic. Mdst, sltst (organic lean), sst (typical)	3.45/2.47	0.21/0.30	2710.6	61.8	0.67

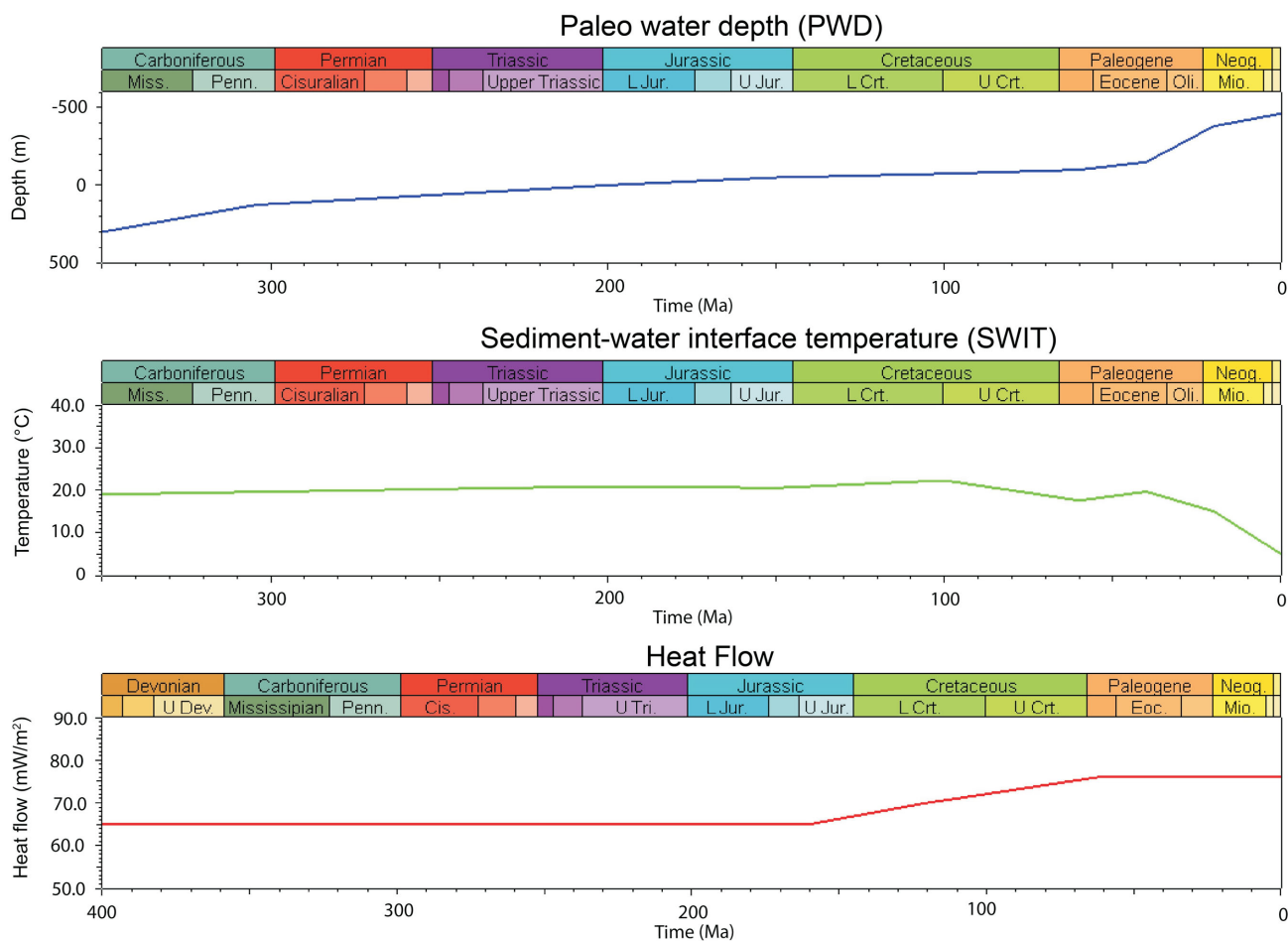


**Figure 4.** Examples of boundary conditions used for the modelling: **Top**, paleo–water depth (PWD); **Middle**, sediment-water interface temperature (SWIT); **Bottom**, heat flow (HF).

al., 1994). It is known that the PWD is an important parameter for compaction and pressure effects, along with SWIT (Bruns et al., 2016). The PWD during deposition of the Evie and Muskwa may have been in excess of 100 m (Stasiuk and Fowler, 2004); however, due to the difference in magnitude of PWD and the overall thickness of the WCSB of several kilometres, its impact is not very significant.

### Heat Flow

The SWIT and PWD define the upper thermal boundary of the basin. The lower boundary requires mapping of the heat flow. Within the study area, present-day heat flow varies significantly, with values generally the highest in the north-eastern corner of BC and lowest within the Liard Basin (Majorowicz and Jessop, 1981; Majorowicz et al., 2005). Heat flow within the Liard Basin represents a localized low (Majorowicz et al., 2005). Heat flow in the HRB, Cordova Embayment and western Alberta area are significantly elevated, reaching values near 100 mW/m<sup>2</sup>. Heat-flow maps (Majorowicz, 2005; Weides and Majorowicz, 2014) were important references for the determination of present-day heat flow (Figure 5), with the continental average value of 65 mW/m<sup>2</sup> (Allen and Allen, 2005) being used for the basin

from 350 to 65 Ma. Heat flows are often elevated during times of inversion due to the exhumation and removal of relatively hot rocks (Bruns et al., 2013), such as during the Tertiary<sup>1</sup> when heat-flow values were above 65 mW/m<sup>2</sup> in the HRB, Cordova Embayment and western Alberta. Due to the large uncertainty around heat-flow evolution through geological history, sensitivity analysis was instrumental in constraining this parameter and increasing confidence in the final models. Due to present-day elevated values, however, the ultimate impact of heat flow during the Mesozoic and Paleozoic is minimized.

### Erosion and Hiatus Events

The main tectonic event in western Canada was the uplift and erosion associated with the Laramide orogeny. Attempts at quantifying Cenozoic erosion have been made

<sup>1</sup> 'Tertiary' is an historical term. The International Commission on Stratigraphy recommends using 'Paleogene' (comprising the Paleocene to Oligocene epochs) and 'Neogene' (comprising the Miocene and Pliocene epochs). The author used the term 'Tertiary' because it was used in the source material for this report.

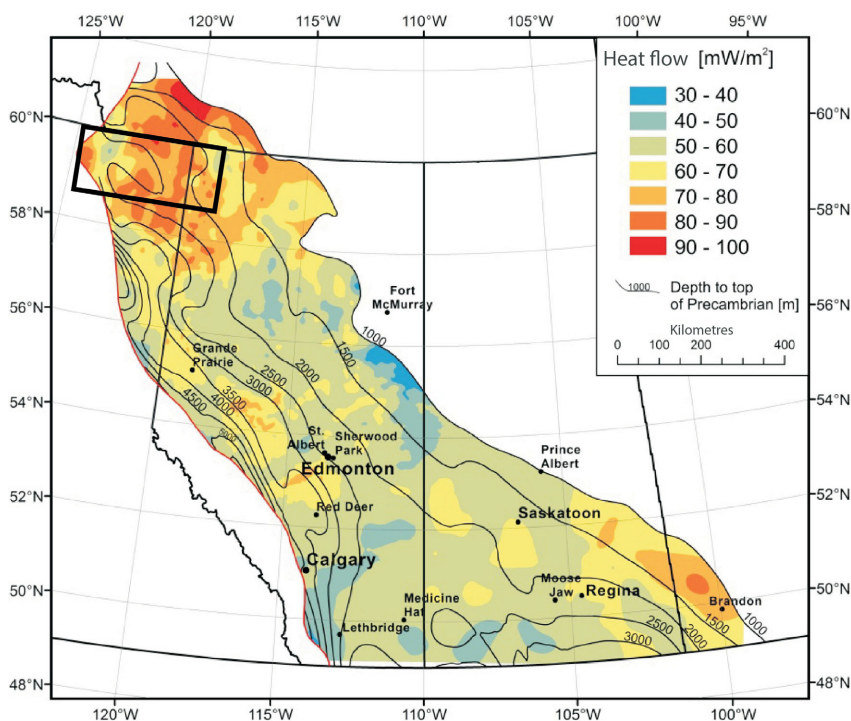


**Figure 5.** Present-day heat flow for the Western Canada Sedimentary Basin (from Weides and Majorowicz, 2014). The study area is outlined in black.

by many studies, through both compaction-based methods (Magara, 1976; Connolly, 1989; Poelchau, 2001; Aviles and Cheadle, 2015) and organic-maturity-based methods (Hacquebard, 1977; Nurkowski, 1984; England and Bustin, 1986; Osadetz et al., 1990). The limits of erosion range from 520 m (Magara, 1976) to more than 4 km (England and Bustin, 1986), depending on the method used by the researchers and the proximity of their study area to the fold-and-thrust belt. Within the Alberta Deep Basin, many of the values cluster around 1500–2000 m (Poelchau, 2001), and a basin model for the same area suggested that 2000 m of erosion was required to match the observed thermal maturity of the Cretaceous Blackstone Formation (Aviles and Cheadle, 2015). It is important to note that the tectonic regime during this time varied along the length of the fold-and-thrust belt, with a higher degree of strike-slip motion being exhibited in the northeastern BC area. This change of tectonic style may have affected the erosion. The limits for the eroded section at the modelled well locations for this study ranged from 440 to 2250 m. This range was informed by prior knowledge of geological history and results from well-defined and -calibrated models. Minor hiatus and erosion events were input throughout the model, according to the stratigraphic record.

### Thermal-Maturity Calibration Data

Calibration to thermal-maturity data is paramount for an accurate model. Since the inception of basin models in the

early 1970s, vitrinite reflectance (VR) has been the most common calibration parameter (Mukhopadhyay, 1994). Well locations for this study were preferentially picked based on the availability and number of VR data points. Unfortunately, reliable VR data are sparse throughout the study area. The main source rocks of interest were deposited in marine environments, so many of the reflectance measurements were completed on indigenous bitumen or bitumen-like substances, not vitrinite. There is sufficient support available in the literature to confidently use bitumen-reflectance values in place of vitrinite (Gentzis, 1991; Reidiger, 1991; Landis and Castano, 1995). However, the reflectance measurements from the public database do not always explain the methodology behind the values, which reduces confidence in the data. Nonetheless, these VR values are still the best calibration data available. In instances where VR data points were not available,  $T_{max}$  values were converted to %  $R_o$  values using the Jarvie et al. (2001) equation. These values should be taken with caution, since it has been shown that such formulas are not ideal, particularly when used on formations on which they were not strictly based (Wust et al., 2013). Although the study is focused on Paleozoic source rocks, data from younger formations were used when available. The assumption that the Laramide orogeny affected the entire Phanerozoic sedimentary succession warrants the use of data from younger formations when reliable Devonian data are unavailable. Table 2 shows the well locations of the 1-D models and their associated calibration data.

**Table 2.** Well locations and associated calibration data for 1-D models used in this study.

UWI	Area	Type of calibration data	Number of data points and formations
100/02-04-126-11W6/0	Alberta	Calculated Ro from Tmax	Muskwa (1)
100/02-32-122-05W6/0	Alberta	Calculated Ro from Tmax	Muskwa (4)
100/04-32-123-02W6/0	Alberta	Calculated Ro from Tmax	Muskwa (3)
100/12-29-122-10W6/0	Alberta	Calculated Ro from Tmax	Muskwa (4)
200/A-094-G/094-P-08/0	Cordova	VR in situ	Slave Point (1), Muskwa (2)
200/A-040-G/094-O-03/0	Horn River Basin	VR in situ, Calculated Ro from Tmax	Exshaw (2), Kotcho (1), Muskwa (2)
200/A-065-G/094-J-10/0	Horn River Basin	VR in situ	Fort Simpson (1)
200/B-017-F/094-P-12/0	Horn River Basin	VR in situ	Muskwa (2)
200/B-088-H/094-J-14/0	Horn River Basin	VR in situ	Muskwa (3)
200/C-028-D/094-O-01/0	Horn River Basin	VR in situ	Otter Park (1), Muskwa (1)
200/C-095-L/094-I-12/0	Horn River Basin	VR in situ	Klua (1), Redknife (1), Kotcho (1), Exshaw (1)
200/D-007-J/094-O-09/0	Horn River Basin	VR in situ	Otter Park (1)
200/D-012-L/094-O-15/0	Horn River Basin	VR in situ	Muskwa (3), Otter Park (1)
200/D-032-F/094-O-01/0	Horn River Basin	Calculated Ro from Tmax	Exshaw (3), Fort St. John (2)
200/A-090-I/094-O-06/0	Liard	VR in situ	Kotcho (3)
200/B-006-C/094-O-11/0	Liard	VR in situ	Garbutt (5)
200/B-053-B 094-O-014/0	Liard	VR in situ	Fort St. John Group (3)
200/C-013-H/094-O-14/0	Liard	VR in situ	Garbutt (3)
200/D-064-K/094-N-16/0	Liard	VR in situ	Golata (10), Banff (2), Besa/Muskwa (3)
200/A-009-F/094-P-03/0	Other	VR in situ	Muskwa (3)
200/B-017-H/094-I-09/0	Other	VR in situ	Muskwa (2)
200/C-005-A/094-J-11/0	Other	VR in situ	Slave Point (1)
200/C-032-K/094-I-14/0	Other	VR in situ	Fort Simpson (2)
200/D-033-F/094-P-13/0	Other	VR in situ	Garbutt (2)

## Sensitivity Analysis

Although basin modelling is a powerful tool, it is a probabilistic method that yields non-unique results. In order to increase confidence in the results, it is paramount to run sensitivity analysis of each model to determine the main factors that control the model and how these factors relate to one another, and to ensure that the final model represents the most likely case. For each 1-D model, dozens of iterations were completed with slight changes to variables such as boundary conditions, rock types and erosion amounts, in order to determine the influence of these variables on one another. The main iterations in this sensitivity analysis involved varying heat flow and erosion. In order to understand the importance of each variable, heat flow or erosion was held constant while the other was varied systematically. This approach allowed for the most likely solution to be modelled with confidence and provided quantitative results for the effects of heat flow and erosion on the present-day thermal maturity of the study area.

## Results

In this paper, a single model from each area—Liard Basin, HRB, Cordova Embayment and western Alberta—will be discussed. Table 3 shows an example of the primary inputs for the finalized models, including stratigraphy, age and lithology.

### Sensitivity Analysis

Heat-flow and erosion values are the two most important variables that must be constrained. Sensitivity analysis allows these variables to be determined more accurately and provides a quantitative understanding of the magnitude of impact these variables have on the overall petroleum systems. Many basin-modelling studies use some form of sensitivity analysis (Bruns et al., 2013; Grobe et al., 2015; Bruns et al., 2016), often isolating heat flow and erosion, as this study does. For each of the models discussed here, erosion values were changed in 200 m increments between iterations, and heat-flow values by 5 mW/m<sup>2</sup>. Heat flow was

**Table 3.** Example of primary inputs for the finalized models.

Age	Formations/ events	Depth (m)	Thickness (m)	Event type	Paleodeposition/ erosion	Lithology
0	hiatus	-459.6	0	Hiatus		
0.4	Overburden	-459.6	391.7	Deposition		Sandstone (arkose, typical)
10	Hiatus 10	-67.9	0	Hiatus		
25	Uplift	-67.9	0	Erosion	-1565	
55	Hiatus 9	-67.9	0	Hiatus		
65	Upper Cretaceous	-67.9	0	Deposition	790	Smoky River
88	Hiatus 8	-67.9	0	Hiatus		
95	Spirit River	-67.9	204.49	Deposition	775	Spirit River (FSJ)
115	Hiatus 7	136.59	0	Hiatus		
140	Erosion	136.59	0	Erosion	-275	
200	Hiatus 6	136.59	0	Hiatus		
230	Doig/Toad	136.59	0	Deposition	150	Toad/Doig
245	Hiatus 5	136.59	0	Hiatus		
252	Fantasque	136.59	0	Deposition	125	Fantasque
280	Hiatus 4	136.59	0	Hiatus		
290	Erosion	136.59	0	Erosion	-300	
305	Hiatus 3	136.59	0	Hiatus		
310	Mattson	136.59	0	Deposition	250	Mattson
335	Rundle Group	136.59	196.32	Deposition	50	Rundle Group
347	Banff	332.91	306.9	Deposition		Banff
360	Exshaw	639.81	8.2	Deposition		Exshaw
360.5	Hiatus 2	648.01	0	Hiatus		
362	Kotcho	648.01	81.99	Deposition		Kotcho
364	Tetcho	730	55.51	Deposition		Tetcho
366	Trout River	785.51	25.88	Deposition		Trout river
367	Hiatus 1	811.39	0	Hiatus		
368	Kakisa	811.39	14.32	Deposition		Kakisa
369	Redknife	825.71	168.59	Deposition		Redknife
369.5	Jean Marie	994.3	44.8	Deposition		Jean Marie
370	Fort Simpson	1039.1	418.49	Deposition		Fort Simpson
374	Muskwa	1457.59	13.72	Deposition		Muskwa
374.5	Otter Park	1471.31	1.8	Deposition		Otter Park
375	Slave Point	1473.11	80.8	Deposition		Slave Point
376	Watt Mountain	1553.91	2.1	Deposition		Watt Mountain
377	Muskeg	1556.01	164.29	Deposition		Muskeg
378	Klua	1720.3	96.99	Deposition		Evie
380	Keg River	1817.29				

kept constant at 65 mW/m<sup>2</sup> while erosion was varied, and heat flow was varied while erosion was held constant.

Increasing erosion thicknesses shifts the vitrinite reflectance trend to higher maturities, as the thicker overburden section would have caused the interval in question to have been buried deeper. With each increment in erosion (keeping heat flow constant), the slope of the vitrinite reflectance as a function of depth remains constant (at 0.5% R<sub>o</sub>/km) and there is a bulk shift in maturity of 0.2% R<sub>o</sub> for every 200 m increment in erosion (Figure 6a). For the example in Fig-

ure 6a, the lower and upper brackets of the eroded section are 2200 and 3200 m, which causes a range of change in maturity of 1.0% R<sub>o</sub>. The values that best fit the calibration data are erosion thicknesses of 2600–2800 m. In all iterations, however, the slope of the line must be increased in order to match the calibration, which requires an increase in heat flow. Although a constant-heat-flow scenario is unlikely due to the time span encompassed by this model and the various tectonic regimes acting through the geological history, keeping heat flow at 65 mW/m<sup>2</sup> for the entirety of

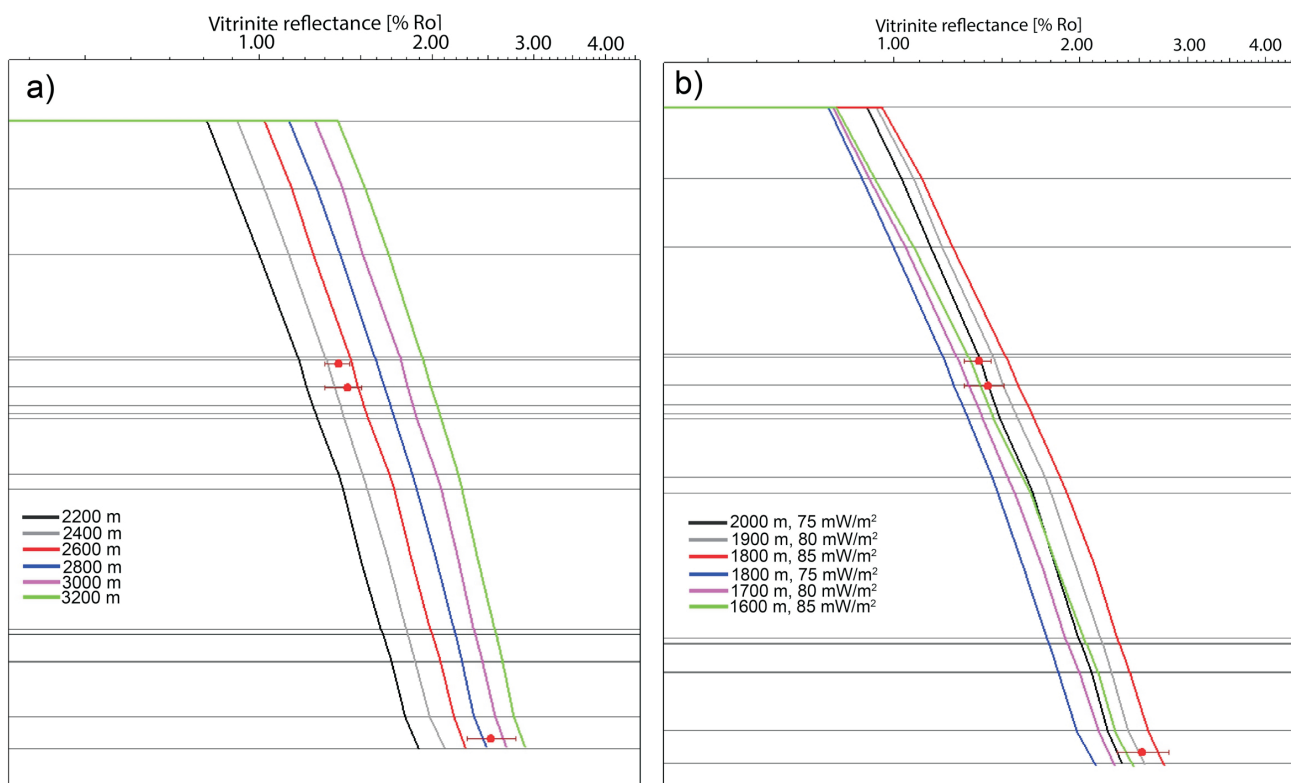


**Figure 6.** Results of sensitivity analysis for the Direct Gunnel C-095-L model: **a)** vitrinite reflectance versus depth for variable erosion thickness at a fixed heat flow of 65 mW/m<sup>2</sup>; **b)** vitrinite reflectance versus depth for variable present-day heat flow. The points on the graph represent calibration data and the lines represent the calculated vitrinite reflectance for each different iteration.

basin evolution provides insight into the quantitative importance of erosion.

Increasing heat flow also has the effect of increasing the thermal-maturity trends. However, as can be seen in Figure 6b, the maturity trends for different heat-flow values are not parallel, as the slope increases from 0.5% R<sub>o</sub>/km to 0.85% R<sub>o</sub>/km for a heat-flow change from 65 mW/m<sup>2</sup> to 80 mW/m<sup>2</sup>. Using the same erosion thickness and increasing heat flow by 5 mW/m<sup>2</sup> can shift thermal maturity by 0.3% R<sub>o</sub> in the Devonian shales. In the example illustrated in Figure 6b, the range of heat flow is from 75 to 85 mW/m<sup>2</sup>, spanning an increase of nearly 0.6% R<sub>o</sub>. The trend that most closely matches the data is associated with 1600 m of erosion and a present-day heat flow of 85 mW/m<sup>2</sup>. In the final model for this example, values of 1565 m of erosion and 88 mW/m<sup>2</sup> for heat flow were used. Based on the detailed sensitivity analysis, confidence in the erosion and heat-flow values for the final models is within 50 m and 1 mW/m<sup>2</sup>, respectively.

### Liard Basin

The Nexen Beaver D-064-K well is located in the north-central part of the Liard Basin, near the deformation front. This model uses present-day heat-flow values of 67 mW/m<sup>2</sup>. The burial history of the Upper Paleozoic comprises

several kilometres of sediment due to the thicknesses of the Besa River, Golata and Mattson formations. The organic-rich Evie and Muskwa members within the Besa River Formation were buried to depths of 3225 m and 3110 m, with corresponding temperatures of 101 and 105°C, respectively, by the end of Mattson Formation deposition (Figure 7a). These depths were obtained by backstripping the model to Carboniferous/Permian time. This model entered the oil window (0.60% R<sub>o</sub>) by 310 Ma. Throughout the Permian to Jurassic, the Fantasque and Toad formations were deposited, along with multiple hiatus/nondepositional periods. Thermal maturity was held fairly constant throughout this time, reaching 0.90% R<sub>o</sub> by Late Jurassic. During foreland subsidence, the Evie and Muskwa horizons reached maximum burial depths 5375 and 5260 m, and maximum temperatures of and 238 and 234°C, respectively. During foreland subsidence, thermal maturation increased from 0.9% R<sub>o</sub> (oil window) to 3.3% R<sub>o</sub> (overmature). By Late Cretaceous, all of the formations had reached thermal maturities necessary for hydrocarbon generation, with the majority of strata within the gas window or overmature. The erosion thickness for this model is 2250 m, corresponding to an erosion rate of 85 m/m.y. Present-day maturities range from 1.7% R<sub>o</sub> in the Mattson Formation to 3.4% R<sub>o</sub> in the Muskwa member (Figure 7b).

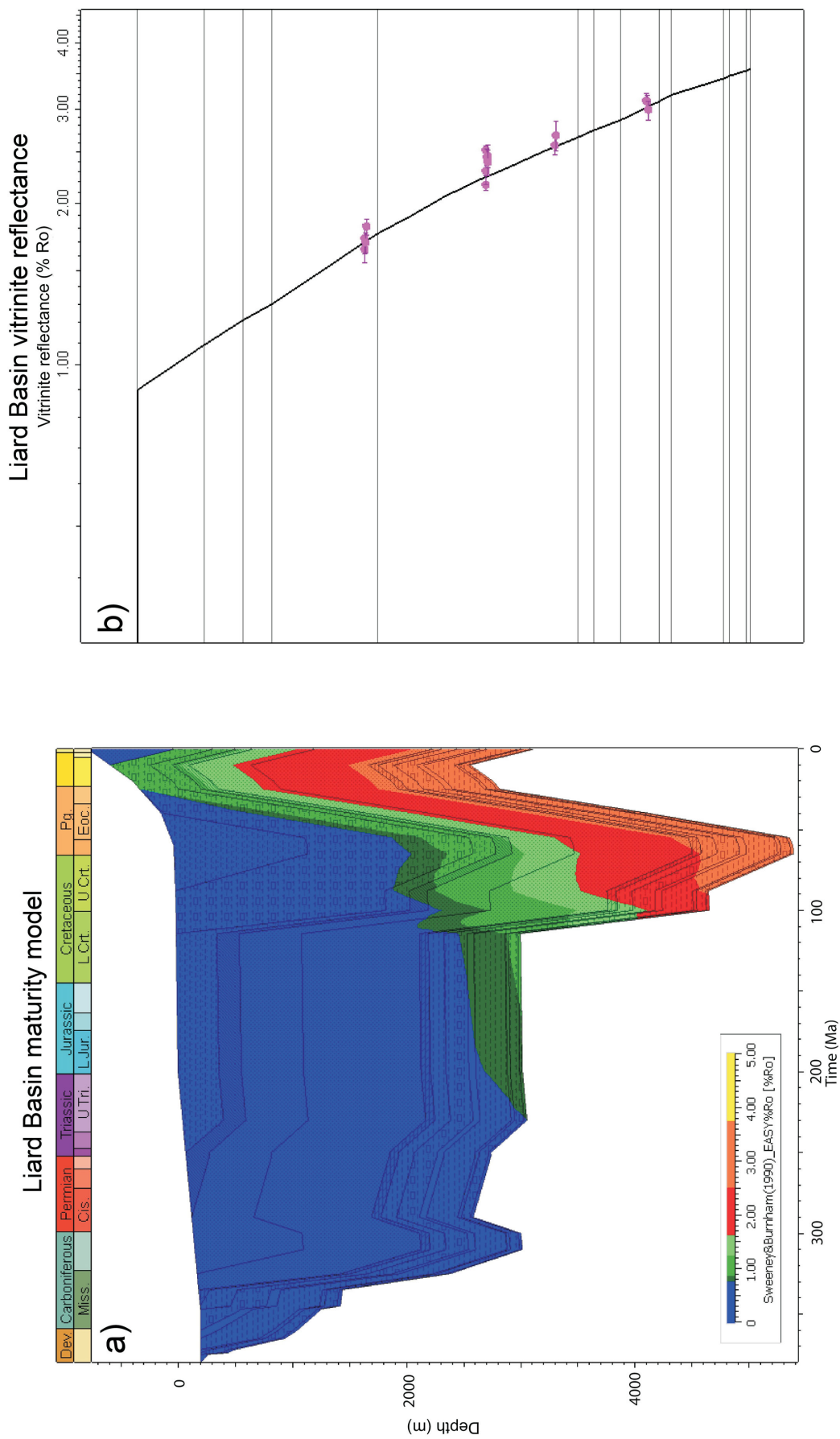


**Figure 7.** Liard Basin maturity model for the Nexen Beaver D-064-K well: **a)** burial-history plot with vitrinite-reflectance overlay; **b)** vitrinite-reflectance versus depth plot. The calculated vitrinite line (black) matches well with the calibration data points (pink).

## Horn River Basin

The Horn River Basin (HRB) model presented here (Direct Gunnel C-095-L well) is located in the southeastern portion of the basin. This model uses a present-day heat flow of  $88 \text{ mW/m}^2$ . The Muskwa Formation was buried to a depth of 2025 m and a temperature of  $83^\circ\text{C}$  by Late Carboniferous, beneath the thick accumulation of the Fort Simpson and Mattson formations (Figure 8a). The Mattson Formation was subsequently eroded due to movement along the Bovie fault, as were the Toad and Fantasque formations (Maclean and Morrow, 2004). Hydrocarbon generation began in the Lower Jurassic for the Muskwa Formation. Maximum burial depths and temperatures of 3035 m and  $195^\circ\text{C}$ , respectively, are reached during foreland subsidence. Thermal maturity for the Muskwa Formation increased from 0.6 (early-oil window) to 2.0%  $R_o$  (wet-gas window) during this time. The amount of erosion for this model is 1565 m, with an erosion rate of 52 m/m.y. Present-day maturities range from 1.4%  $R_o$  in the Exshaw Formation to 2.6%  $R_o$  in the Klua Formation (Figure 8b).

### Cordova Embayment and Adjacent Areas

The featured Cordova Embayment model (Ioe Union Shekilie A-094-G well) is located in the southern part of the embayment and uses a present-day heat-flow value of  $88 \text{ mW/m}^2$ . The burial history for this model is similar to many of the models within the HRB. During the Paleozoic, the Muskwa Formation reached depths of 1830 m, corresponding to a temperature of  $76^\circ\text{C}$  (Figure 9a). Depths remained fairly constant throughout the Permian, Triassic and Jurassic. The Klua Formation entered the oil window in the Late Triassic, and the Muskwa Formation in the early Cretaceous (at the start of foreland subsidence). Maximum burial depths and temperatures for the Muskwa Formation were of 2920 m and  $183^\circ\text{C}$ , respectively. During maximum burial, thermal maturity increased from 0.6 to 1.8%  $R_o$  (early-oil to wet-gas window). The thickness of the eroded section for this model is 1650 m, corresponding to an erosion rate of 55 m/m.y. Present-day maturities for the Muskwa and Klua formations are 1.9 and 2.1%  $R_o$ , respectively (Figure 9b).

### Western Alberta

The models in western Alberta present significantly shallower burial and therefore lower maturities than those calculated in the models in British Columbia. The 100/02-32 well, located east of  $119^\circ\text{W}$ , has a present-day heat-flow value of  $66 \text{ mW/m}^2$ . The model was buried to a depth of 1400 m and a corresponding temperature of  $70^\circ\text{C}$  during the Paleozoic (Figure 10a). As with the Cordova Embayment model, depths and temperatures stayed fairly constant throughout the Permian to Jurassic. Maximum foreland-subsidence burial depths and temperatures for the Muskwa Formation are 1830 m and  $92^\circ\text{C}$ , respectively. The Muskwa

Formation did not reach the oil window until the Latest Cretaceous. The thickness of the eroded section for this location is 525 m, corresponding to an erosion rate of only 17.5 m/m.y. The present-day maturity for this model is 0.62%  $R_o$  for the Muskwa Formation, with all younger strata remaining immature (Figure 10b).

## Discussion

### Impact of Peak Hydrocarbon Generation on Present-Day Distribution

In all of the models, peak burial depth and temperature were reached during the Late Cretaceous and beginning of the Paleocene. However, the onset of hydrocarbon generation (specifically the onset of oil generation) varies by hundreds of millions of years over the spatial extent of the study area. In the Liard Basin, the Devonian shales have been generating since the Carboniferous, reaching peak oil generation (transformation ratio = 50%) in the early Triassic (Figure 11). Conversely, the onset of oil generation in the Alberta wells occurred at 100 Ma at the earliest (if oil generation occurred at all), and peak generation occurred during the Late Cretaceous (Figure 11). Areas that have been in the maturity window for longer have a lower likelihood of containing extensive volumes of generative hydrocarbons today, since the organic matter has been generating for hundreds of millions of years. In the Liard Basin, many of the areas have reached maturities high enough, and sustained high temperatures long enough, that the organic matter no longer has any generating potential left but may still have producing potential. Age of maturation generally decreases toward the eastern and southeastern portions of the study area—in locations where production shows larger fractions of produced condensate than farther west. The temporal constraints provided by basin modelling can be used in conjunction with maturity to deduce the potential producibility of different areas. In nearly all of the well locations modelled, the transformation ratio reached 100% during foreland subsidence, which is expected due to the dominantly dry-gas nature of the Devonian petroleum system.

### Limitations of the Model

Basin modelling is a powerful tool for understanding basin evolution, burial history, thermal maturation and the multitude of dependent relationships that exist between input variables. However, because the models require that such an extensive suite of factors be defined, there is a large amount of uncertainty involved, even in well-calibrated models. The results of this study are geologically plausible but not necessarily correct. Each model provides abundant information for each stratigraphic unit and each important time step, but the nuances of variables such as lithological variability are not captured, thereby decreasing the accuracy of the modelling. This study used only 24 models to

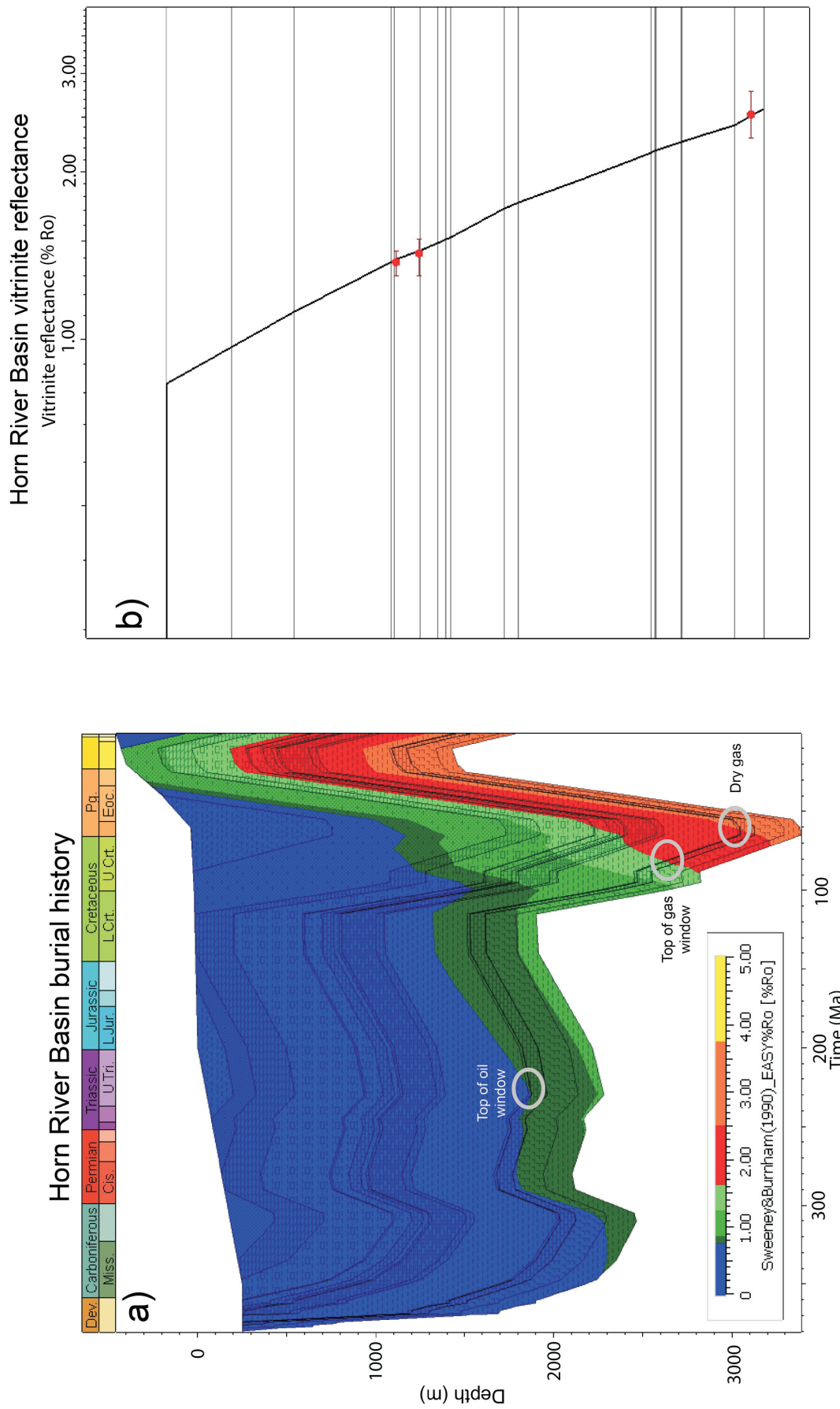


**Figure 8.** Horn River Basin maturity model for the Direct Gunnerl C-095-L well: **a)** burial-history plot with vitrinite-reflectance overlay; **b)** vitrinite-reflectance versus depth plot. The calculated vitrinite line (black) matches well with the calibration data points (red).

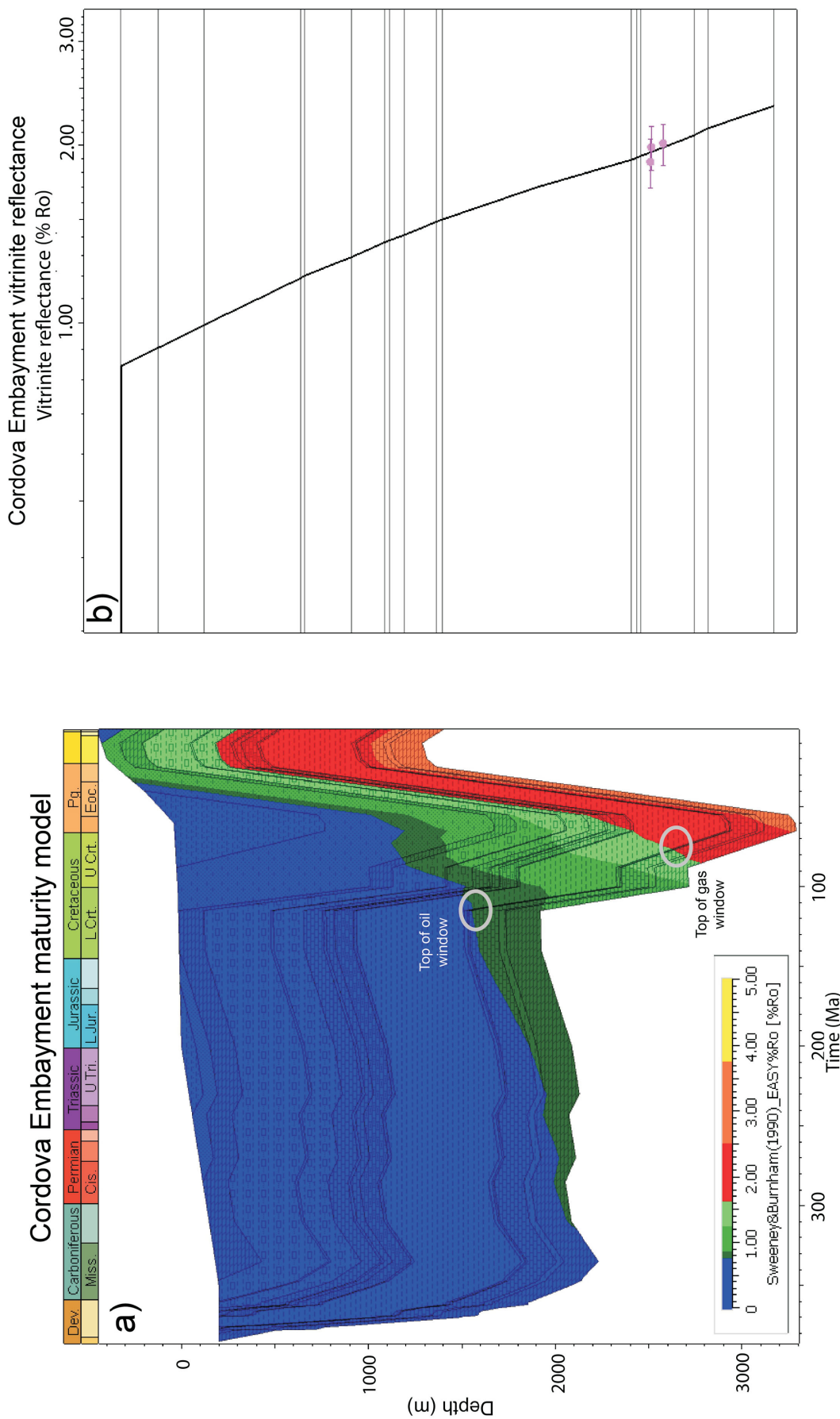


**Figure 9.** Cordova Embayment maturity model for the Ioe Union Shekille A-094-G well: **a)** burial-history plot with vitrinite reflectance overlay; **b)** vitrinite-reflectance versus depth plot. The calculated vitrinite line (black) matches well with the calibration data points (pink).

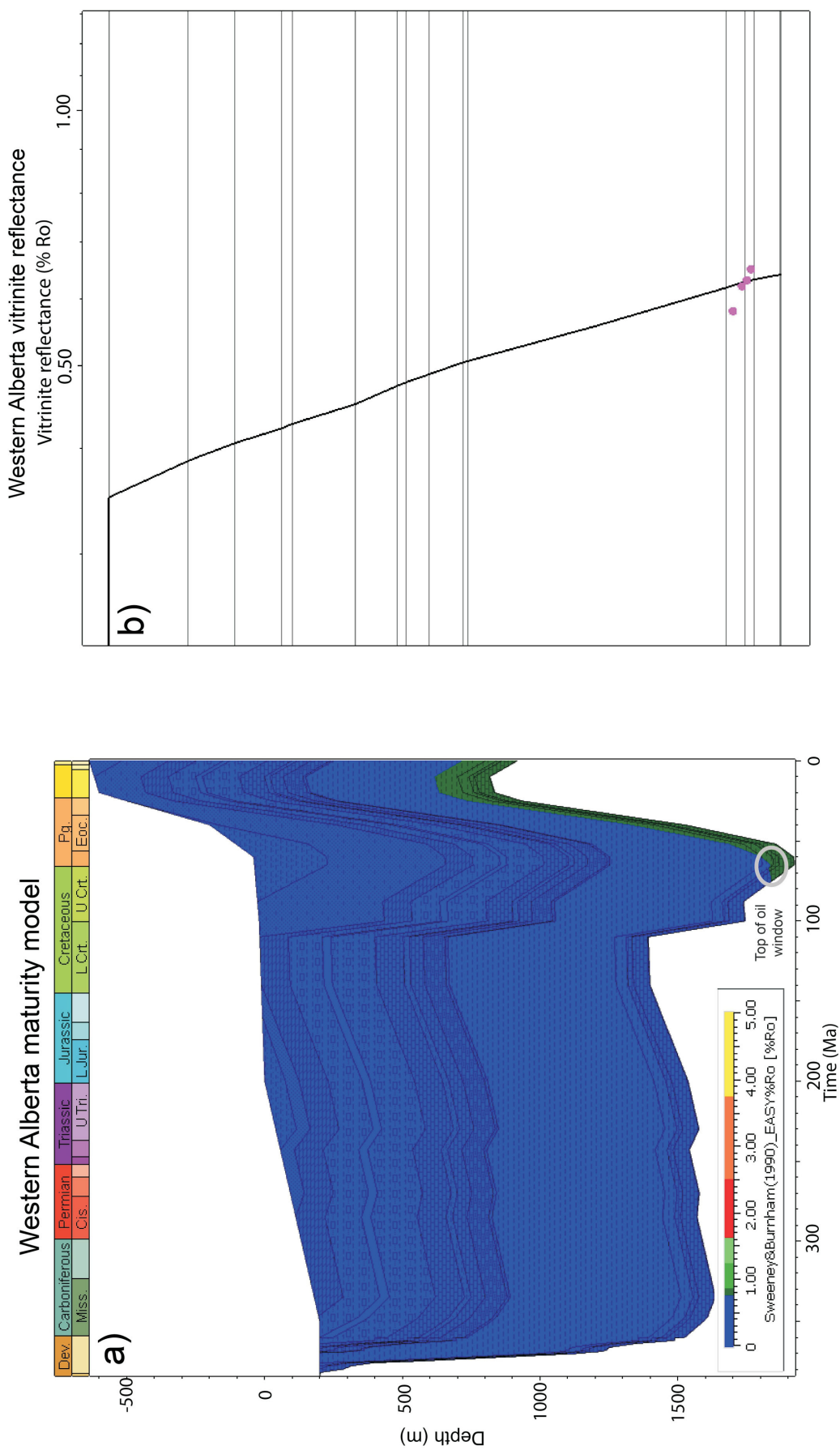


**Figure 10.** Western Alberta maturity model for the 100/02-32 well: **a)** burial-history plot with vitrinite-reflectance overlay; **b)** vitrinite-reflectance versus depth plot. The calculated vitrinite line (black) matches well with the calibration data points (pink).

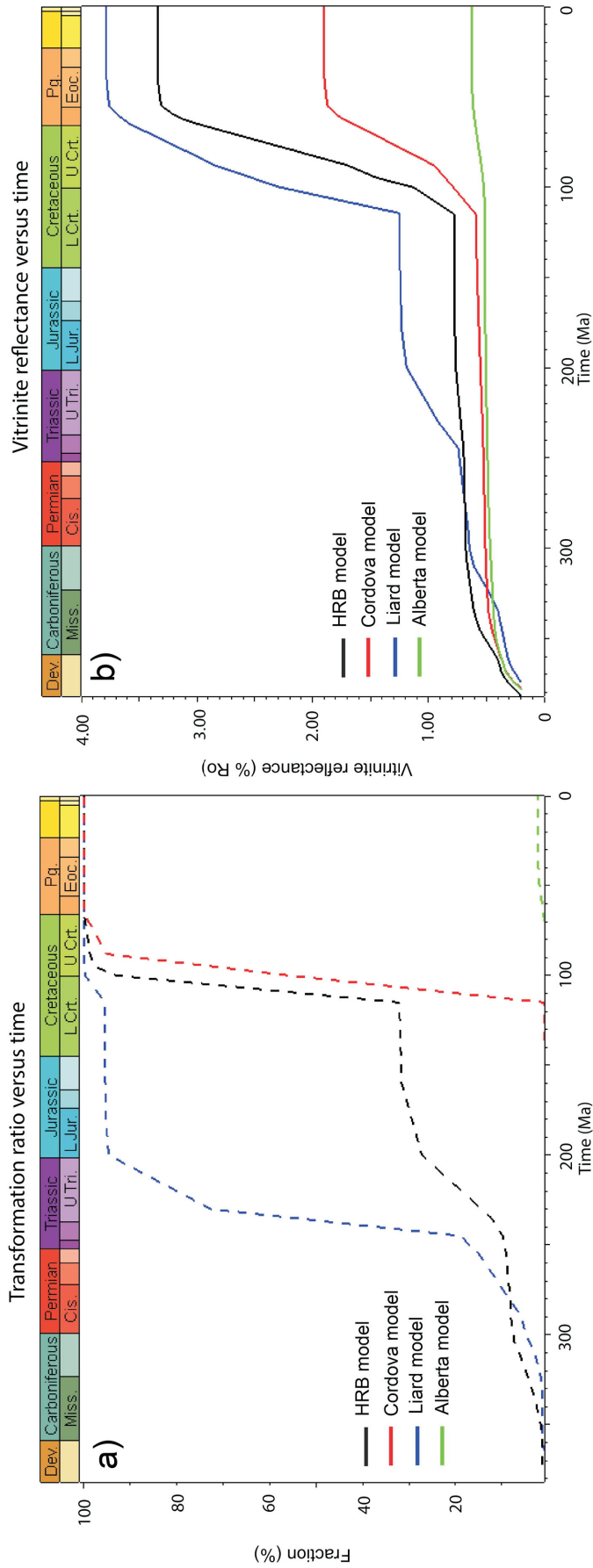


**Figure 11.** Relative timing and phases of maturation across the four main areas of this study: **a)** transformation ratio versus time, and **b)** vitrinite reflectance versus time. Dotted lines represent the calculated transformation ratios over time and solid lines represent the calculated vitrinite reflectance over time.

define an area that encompasses hundreds of square kilometres. The models provide considerable information in the direct vicinity of the well location, but caution should be taken when upscaling to a regional scale. The calibration data used for this study were relatively sparse and not all of the data could be used with complete confidence. Basin modelling can help identify suspicious and erroneous data. For example, some reported vitrinite-reflectance and pyrolysis values required erosion levels, heat flow or the thermal conductivity of formations to be outside the geologically plausible limits of the model. Although this method helps flag bad data, it is difficult to determine how accurate the ‘good’ data are and therefore how accurate the overall model is. However, basin modelling is a quantitative approach that provides valuable information even with limited data or well control.

### Conclusions and Future Work

Basin modelling of the Liard and Horn River Basins, Cordova Embayment and western Alberta provides insight into burial history, thermal maturation and how the evolution of the basin has affected the present-day Devonian petroleum systems. Important conclusions of this ongoing study include the following:

- The Devonian shales were buried to depths of 1500 to 3200 m by the end of the Carboniferous Period, and reached temperatures of up to 100°C during this time. Burial depths and temperatures are greatest within the Liard Basin, which experienced the additional accumulation and preservation of the Mattson Formation due to movement along the Bovie fault.
- Tectonism related to the Laramide orogeny was the dominant control on the present-day petroleum system. During deepening of the foreland basin and subsequent uplift and erosion, all of the models experienced rapid increase in maturity. The majority of the 1-D models experienced an increase in reflectance of approximately 2% Ro over a 50 m.y. time span.
- Based on the sensitivity analysis, confidence in the heat-flow values is within 1 mW/m<sup>2</sup> and within 50 m for erosion. Eroded-section thicknesses range from 2250 to 440 m across the study area, and heat flow ranges from 48.5 to 88 Mw/m<sup>2</sup>. Heat flow is highest within the Cordova Embayment and lowest within the Liard Basin, and erosion thicknesses generally decrease toward the east, away from the deformation front.
- Lithology has a relatively minor effect on the burial history and thermal maturation of the Western Canada Sedimentary Basin. Most of the stratigraphic interval comprises carbonate or sandstone, both of which have moderate values of thermal conductivity and therefore do not greatly impact the maturity profile.
- The timing of the onset of oil generation varies greatly across the study area. In the Liard basin, the Muskwa

member of the Besa River Formation entered the oil window in the Carboniferous and, in Alberta, the Muskwa Formation began generating oil in the Upper Cretaceous. This large time span of hydrocarbon generation affects the present-day distribution and potential of the study area. The organic matter within the Muskwa of the Liard basin has been generating hydrocarbons for hundreds of millions of years and, as a result, its production potential today is poor. Areas that have only experienced generation since the onset of foreland subsidence (eastern Horn River Basin, eastern BC and western Alberta) will have greater potential for present-day in situ production.

In order to further constrain maturity trends and quantify erosion and hydrocarbon distribution, additional 1-D models need to be simulated, along with further sensitivity analysis. Taking the 1-D models into 2-D and 3-D should be completed in future studies to further enhance the understanding of the basin and gain further insight into hydrocarbon migration in northeastern BC.

### Acknowledgments

Financial support from Geoscience BC, EnCana Corporation, Devon Energy Corporation, Husky Energy Inc., Chevron Canada Limited, Canadian Natural Resources Limited and geoLOGIC Systems Limited is greatly appreciated. This paper benefited from a careful review by P.L. Silva.

### References

- Allen, P.A. and Allen, J.R. (2005): *Basin Analysis: Principles and Applications* (Second Edition); Blackwell Publishing Ltd., Oxford, United Kingdom, 549 p.
- Athy, L.F. (1930): Density, porosity and compaction of sedimentary rocks; *American Association of Petroleum Geologists*, v. 14, p. 1–24.
- Aviles, M.A. and Cheadle, B.A. (2015): Regional study of the thickness of exhumed sediments in the foredeep section of the Western Canada Foreland Basin using the sonic compaction based technique; *Canadian Society of Petroleum Geologists, Geoconvention 2015*, Calgary, Alberta, extended abstract, 5 p.
- Balogun, A. (2014): Organic shale potential of the Muskwa–Otter Park interval within the Cordova Embayment area of northeastern British Columbia using sonic and resistivity logs; *Geoscience Reports 2014*, BC Ministry of Natural Gas Development, p. 1–6.
- Berbesi, L.A., di Primio, R., Anka, Z., Horsfield, B. and Higley, D.K. (2012): Source rock contributions to the Lower Cretaceous heavy oil accumulations in Alberta: a basin modeling study; *American Association of Petroleum Geologists Bulletin*, v. 96, no. 7, p. 1211–1234.
- Bruns, B., Di Primio, R., Berner, U. and Littke, R. (2013): Petroleum system evolution in the inverted Lower Saxony basin, northwest Germany: a 3D basin modelling study; *Geofluids*, v. 13, p. 246–271.
- Bruns, B., Littke, R., Gasparik, M., van Weest, J.D. and Nelskamp, S. (2016): Thermal evolution and shale gas potential estima-

- tion of the Wealden and Posidonia Shale in NW-Germany and the Netherlands: a 3D basin modelling study; *Basin Research*, v. 28, p. 2–33.
- CBM Solutions Ltd. (2005): Gas shale potential of Devonian strata, northeastern British Columbia; CBM Solutions Ltd., internal report.
- Chalmers, G.R.L., Ross, D.J.K. and Bustin, R.M. (2012): Geological controls on matrix permeability of Devonian gas shales in the Horn River and Liard basins, northeastern British Columbia, Canada; *International Journal of Coal Geology*, v. 103, p. 120–131.
- Connolly, C.A. (1989): Thermal history and diagenesis of the Wilrich Member shale, Spirit River Formation, northwest Alberta; *Bulletin of Canadian Petroleum Geology*, v. 37, p. 182–197.
- Dong, T. (2016): Geochemical, petrophysical and geochemical properties of stratigraphic sequences in Horn River shale, Middle and Upper Devonian, northeastern British Columbia, Canada; Ph.D. thesis, University of Alberta, Edmonton, Alberta, 258 p.
- Dong, T., Kennedy, M. and Harris, N.B. (2014): Geochemical characterization of stratigraphic sequences in the Horn River shale, Middle and Upper Devonian, northeastern British Columbia, Canada; American Association of Petroleum Geologists (AAPG), Annual Convention and Exhibition, 2013, Pittsburgh, Pennsylvania, oral presentation, 24 p.
- Dubey, S., Chakraborty, D., Mishra, S. and Fredd, C. (2017): Systemic evaluation of shale play by introducing integration of inversion geophysics, petroleum system and reservoir simulation workflows; Society of Petroleum Engineers (SPE) Middle East Oil and Gas Show and Conference 2017, Manama, Bahrain, extended abstract, 20 p.
- England, T.D.J. and Bustin, R.M. (1986): Thermal maturation of the Western Canadian Sedimentary Basin south of the Red Deer River: I) Alberta Plains; *Bulletin of Canadian Petroleum Geology*, v. 34, p. 71–90.
- Ferri, F. and Griffiths, M. (2014): Thermal maturity and regional distribution of the Muskwa Formation, northeastern British Columbia; *in Geoscience Reports 2014*, BC Ministry of Natural Gas Development, p. 37–45.
- Ferri, F., Hickin, A.S. and Huntley, D.H. (2011): Besa River Formation, western Liard Basin, British Columbia (NTS 094N): geochemistry and regional correlations; *in Geoscience Reports 2011*, BC Ministry of Energy and Mines, p. 1–18.
- Ferri, F., McMechan, M. and Creaser, R. (2015): The Besa River Formation in Liard Basin, British Columbia; *in Oil and Gas Geoscience Reports 2015*, BC Ministry of Natural Gas Development, p. 1–27.
- Fiess, K.M., Ferri, F., Fraser, T.L., Pyle, L.J. and Rocheleau, J. (2013): Liard Basin Hydrocarbon Project: shale gas potential of Devonian–Carboniferous strata in the Northwest Territories, Yukon and northeastern British Columbia; Canadian Society of Petroleum Geologists, Geoconvention 2013, Calgary, Alberta, extended abstract, 9 p.
- Gentzis, T. (1991): Regional maturity and source-rock potential of Paleozoic and Mesozoic strata, Melville Island, Arctic Canada; Ph.D. thesis, Newcastle University, Newcastle, United Kingdom, 476 p.
- Grobe, A., Littke, R., Sachse, V. and Leythaeuser, D. (2015): Burial history and thermal maturity of Mesozoic rocks of the Dolomites, northern Italy; *Swiss Journal of Geoscience*, v. 108, p. 253–271.
- Hacquebard, P.A. (1977): Rank of coal as an index of organic metamorphism for oil and gas in Alberta; *in The Origin and Migration of Petroleum in the Western Canadian Sedimentary Basin, Alberta: A Geochemical and Thermal Maturation Study*, G. Deroo, T.G. Powell, B. Tissot and R.G. McCrossan (ed.), Geological survey of Canada, Bulletin 262, 136 p.
- Harris, N.B. and Dong, T. (2013): Characterizing porosity in the Horn River shale, northeastern British Columbia; *in Geoscience Reports 2013*, British Columbia Ministry of Natural Gas Development, p. 33–40.
- Higley, D.K., Lewan, M.D., Roberts, L.N.R. and Henry, M. (2009): Timing and petroleum sources for the Lower Cretaceous Mannville Group oil sands of northern Alberta based on 4-D modeling; *American Association of Petroleum Geologists (AAPG) Bulletin*, v. 93, p. 203–230.
- Jarvie, D.M., Claxton, B.L., Henk, F. and Breyer, J.T. (2001): Oil and shale gas from the Barnett Shale, Fort Worth basin, Texas; AAPG National Convention, 2001, Denver, Colorado, American Association of Petroleum Geologists (AAPG) Bulletin, v. 85, p. A100.
- Kalkreuth, W. and McMechan, M. (1988): Burial history and thermal maturation, Rock Mountain front ranges, foothills and foreland, east central British Columbia and adjacent Alberta, Canada; *American Association of Petroleum Geologists (AAPG) Bulletin*, v. 72, p. 1395–1410.
- Kent, D.M. (1994): Paleogeographic evolution of the cratonic platform – Cambrian to Triassic; *in Geological Atlas of the Western Canada Sedimentary Basin*, G.D. Mossop and I. Shetsen (comp.), Canadian Society of Petroleum Geologists, Calgary, Alberta and Alberta Research Council, Edmonton, Alberta, p. 69–86.
- Landis, C.R. and Castano, J.R. (1995): Maturation and bulk chemical properties of a suite of solid hydrocarbons; *Organic Geochemistry*, v. 22, p. 137–149.
- MacLean, B.C. and Morrow, D.W. (2004): Bovie Structure: its evolution and regional context; *Bulletin of Canadian Petroleum Geology*, v. 52, p. 302–324.
- Magara, K. (1976): Thickness of removed sedimentary rocks, paleopore pressure, and paleotemperature, southwestern part of Western Canada Basin; *American Association of Petroleum Geologists (AAPG) Bulletin*, v. 60, p. 554–565.
- Majorowicz, J.A. and Jessop, A.M., (1981): Regional heat flow patterns in the Western Canadian Sedimentary Basin; *Tectonophysics*, v. 74, p. 209–238.
- Majorowicz, J.A., Jessop A.M. and Lane, L.S. (2005): Regional heat flow pattern and lithospheric geotherms in northeastern British Columbia and adjacent Northwest Territories, Canada; *Bulletin of Canadian Petroleum Geology*, v. 53, p. 51–66.
- Morrow, D.W., Potter, J., Richards, B. and Goodarzi, F. (1993): Paleozoic burial and organic maturation in the Liard Basin region, northern Canada; *Bulletin of Canadian Petroleum Geology*, v. 41, p. 17–31.
- Mossop, G.D. and Shetsen, I., compilers (1994): Geological Atlas of the Western Canada Sedimentary Basin; Canadian Society of Petroleum Geologists, Calgary, Alberta and Alberta Research Council, Edmonton, Alberta, 510 p.
- Mukhopadhyay, P.K. (1994): Vitrinite reflectance as maturity parameter: petrographic and molecular characterization and its

- applications to basin modelling; Chapter 1 *in* Vitrinite Reflectance as a Maturity Parameter: Applications and Limitations, P.K. Mukhopadhyay and W.G. Dow (ed.), American Chemical Society, ACS Symposium Series, p. 1–24.
- National Energy Board and BC Ministry of Energy, Mines and Petroleum Resources (2011): Ultimate potential for unconventional natural gas in northeastern British Columbia's Horn River Basin; National Energy Board and BC Ministry of Energy, Mines and Petroleum Resources, 50 p.
- Natural Resources Canada (2018): WEBLEX Canada – lexicon of Canadian geological names on-line; Natural Resources Canada, URL <[https://weblex.rncan.gc.ca/weblexnet4/Weblex\\_e.aspx](https://weblex.rncan.gc.ca/weblexnet4/Weblex_e.aspx)> [November 2018].
- Nurkowski, J.R. (1984): Coal quality, coal rank variation and its relation to reconstructed overburden, Upper Cretaceous and Tertiary plains coals, Alberta, Canada; American Association of Petroleum Geologists (AAPG) Bulletin, v. 68, p. 285–295.
- Osadetz, K.G., Pearson, D.E. and Stasiuk, L. (1990): Paleogeothermal gradients and changes in the geothermal gradient field of the Alberta Plains; *in* Current Research, Part D, Geological Survey of Canada, Paper 90-1D, p. 165–178.
- Poelchau, H.S. (2001): Modeling an exhumed basin: a method for estimating eroded overburden; Natural Resources Research, v. 10, p. 73–84.
- Potter, J. (1998): Organic petrology, maturity, hydrocarbon potential and thermal history of the Upper Devonian and Carboniferous in the Liard Basin, northern Canada; Ph.D. thesis, University of Newcastle, Newcastle, United Kingdom, 363 p.
- Price, R.A. (1994): Cordilleran tectonics and the evolution of the Western Canada Sedimentary Basin; *in* Geological Atlas of the Western Canadian Sedimentary Basin, G.D. Mossop and I. Shetsen (comp.), Canadian Society of Petroleum Geologists, Calgary, Alberta and Alberta Research Council, Edmonton, Alberta, p. 13–24.
- Reidiger, C.L. (1991): Lower Mesozoic hydrocarbon source rocks, Western Canada Sedimentary Basin; Ph.D. thesis, University of Waterloo, Waterloo, Ontario, 602 p.
- Richards, B.C. (1989): Upper Kaskaskia Sequence: uppermost Devonian and Lower Carboniferous; Chapter 9 *in* Western Canada Sedimentary Basin, a Case History, B.D. Ricketts (ed.), Canadian Society of Petroleum Geologists, p. 165–201.
- Richards, B.C., Bryan, D., Hartling, A., Henderson, C.M. and Hinds, R.C. (1994): Carboniferous strata of the Western Canada Sedimentary Basin; *in* Geological Atlas of the Western Canadian Sedimentary Basin, G.D. Mossop and I. Shetsen (comp.), Canadian Society of Petroleum Geologists, Calgary, Alberta and Alberta Research Council, Edmonton, Alberta, p. 221–250.
- Ross, D.J.K. (2007): Investigation into the importance of geochemical and pore structural heterogeneities for shale gas reservoir evaluation; Ph.D. thesis, The University of British Columbia, Vancouver, British Columbia, 410 p.
- Ross, D.J.K., and Bustin, R.M. (2008): Characterizing the shale gas resource potential of Devonian–Mississippian strata in the Western Canada Sedimentary Basin: application of an integrated formation evaluation; American Association of Petroleum Geologists (AAPG) Bulletin, v. 92, p. 87–125.
- Ross, D.J.K., and Bustin, R.M. (2009a): Investigating the use of sedimentary geochemical proxies for paleoenvironment interpretation of thermal mature organic rich strata: examples from the Devonian–Mississippian shales, Western Canadian Sedimentary Basin; Chemical Geology, v. 260, p. 1–19.
- Ross, D.J.K., and Bustin, R.M. (2009b): The importance of shale composition and pore structure upon gas storage potential of shale gas reservoirs; Marine and Petroleum Geology, v. 26, p. 916–927.
- Sekiguchi, K. (1984): A method for determining terrestrial heat flow in oil basin areas; Tectonophysics, v. 103, no. 1–4, p. 67–79.
- Stasiuk, L.D. and Fowler, M.G. (2004): Organic facies in Devonian and Mississippian strata of Western Canada Sedimentary Basin: relation to kerogen type, paleoenvironment, and paleogeography; Bulletin of Canadian Petroleum Geology, v. 52, p. 234–255.
- Stott, D.F. (1982): Lower Cretaceous Fort St. John and Upper Cretaceous Dunvegan of the foothills and plains of Alberta, British Columbia, District of Mackenzie and Yukon Territory; Geological Survey of Canada, Bulletin 328, p. 241–249.
- Sweeney, J.J. and Burnham, A.K. (1990): Evaluation of a simple model of vitrinite reflectance based on chemical kinetics; American Association of Petroleum Geologists (AAPG) Bulletin, v. 74, p. 1559–1570.
- Switzer, S.B., Holland, W.G., Christie, D.S., Graf, G.C., Hedinger, A.S., McAuley, R.J., Wierzbicki, R.A. and Packard, J.J. (1994): Devonian Woodbend–Winterburn strata of the Western Canada Sedimentary Basin; *in* Geological Atlas of the Western Canadian Sedimentary Basin, G.D. Mossop and I. Shetsen (comp.), Canadian Society of Petroleum Geologists, Calgary, Alberta and Alberta Research Council, Edmonton, Alberta, p. 165–202.
- Weides, S. and Majorowicz, J. (2014): Implications of spatial variability in heat flow for geothermal resource evaluation in large foreland basins: the case of the Western Canada Sedimentary Basin; Energies, v. 7, p. 2573–2594.
- Wilson, T.K. and Bustin, R.M. (2017): Unconventional petroleum systems analysis on Upper Devonian organic-rich shales in the Horn River and Liard basins, and adjacent western Alberta: preliminary report; *in* Geoscience BC Summary of Activities 2016, Geoscience BC, Report 2017-1, p. 29–36.
- Wright, G.N., McMechan, M.E. and Potter, D.E.G. (1994): Structure and architecture of the Western Canadian Sedimentary Basin; *in* Geological Atlas of the Western Canadian Sedimentary Basin, G.D. Mossop and I. Shetsen (comp.), Canadian Society of Petroleum Geologists, Calgary, Alberta and Alberta Research Council, Edmonton, Alberta, p. 25–39.
- Wust, R.A.J., Hackley, P.C., Nassichuk, B.R., Willment, N. and Brozovski, R. (2013): Vitrinite reflectance versus pyrolysis Tmax data: assessing thermal maturity in shale plays with special reference to the Duvernay shale play of the Western Canadian Sedimentary Basin, Alberta, Canada; SPE Unconventional Resources Conference and Exhibition–Asia Pacific, Brisbane, Society of Petroleum Engineers, extended abstract, 11 p.
- Wygrala, B.P. (1989): Integrated study of an oil field in the southern Po basin, northern Italy; Ph.D. thesis, University of Cologne, Germany, 328 p.



# Variability and Controls on the Matrix Permeability of the Doig Formation in Northeastern British Columbia

P.L. Silva, The University of British Columbia, Vancouver, BC, [pablols@alumni.ubc.ca](mailto:pablols@alumni.ubc.ca)

R.M. Bustin, The University of British Columbia, Vancouver, BC

---

Silva, P.L. and Bustin, R.M. (2019): Variability and controls on the matrix permeability of the Doig Formation in northeastern British Columbia; in Geoscience BC Summary of Activities 2018: Energy and Water, Geoscience BC, Report 2019-1, p. 21–28.

## Introduction

The Lower to Middle Triassic Doig Formation of the Western Canada Sedimentary Basin (WCSB) extends continuously across northeastern British Columbia (BC) and west-central Alberta. Historically, the Doig and the underlying Montney formations were viewed as source rocks for other conventional reservoirs in the basin, mainly in other Triassic, and Cretaceous strata (Du Rouchet, 1985; Creaney and Allan, 1990; Riediger et al., 1990; Edwards et al., 1994). There has also been some limited hydrocarbon production from the conventional sandstone bodies in the Doig (Marshall et al., 1987; Walsh et al., 2006; Chopra et al., 2014). With the industry shifting the focus of development to unconventional reservoirs, the Doig Formation has been recognized as an important resource of gas and natural-gas liquids (NGL). The Gas Technology Institute (Faraj et al., 2002) estimated the Doig total gas-in-place at 4 trillion m<sup>3</sup> (140 tcf), while Walsh et al. (2006) estimated it as ranging from 1.1 to 5.7 trillion m<sup>3</sup> (40–200 tcf). A more recent study by the United States Energy Information Administration (2013) estimated 2.8 trillion m<sup>3</sup> (100 tcf) of gas-in-place for the Doig Phosphate Zone alone. The unconventional portion of the Doig is a relatively new play and thus, the distribution of its properties has not been extensively studied nor is it well understood. Basin-scale studies that focus on the entire Doig succession and the variation in its properties are notably absent in the literature. The present study aims to characterize the range and variability of the matrix permeability of the Doig Formation, as well as explain the geological factors that control this variability in terms of lithology, mineralogy, organic matter, porosity and pore-size distribution.

## Geological Framework

The sedimentation in the Triassic of the WCSB is marked by a transition from carbonate-dominated intra-cratonic and passive-margin conditions, predominant during the Paleozoic, to a siliciclastic-dominated relatively active em-

bryonic foreland basin. The general paleogeographic configuration of the Triassic in the WCSB was that of a westward-deepening continental shelf margin. This westward facing margin under the influence of trade winds, seasonal climatic aridity and coastal cold-water oceanic upwelling, was characterized by low fluvial input, dominantly fine-grained siliciclastic sedimentation in marine shelves and ramps, with extensive associated eolian and evaporitic environments (Marshall et al., 1987; Henderson, 1989; Davies, 1997).

The Middle Triassic Doig Formation is part of the Diaber Group along with the underlying Montney Formation (Figure 1). This group was defined by Armitage (1962), who re-defined the original Toad–Grayling Formation equivalents in the subsurface as the Doig and Montney formations. The lower boundary of the Doig corresponds to the base of a phosphatic zone, which was later informally named Doig Phosphate Zone (DPZ) by Creaney and Allan (1990). The Triassic succession was deposited in a series of three major third- or fourth-order transgressive-regressive cycles (Gibson and Barclay, 1989; Edwards et al., 1994). The interval from the Doig through the Halfway and Charlie Lake formations corresponds to the second cycle and the DPZ represents a condensed section formed during the initial transgression of the second cycle (Gibson and Barclay, 1989).

The main structural elements that influenced the distribution of the WCSB Triassic interval were the underlying Devonian Leduc and Swan Hills reefs, and the Mesozoic reactivation of the Mississippian Dawson Creek graben complex (DCGC), which includes the Fort St. John graben (FSJG) and the Hines Creek graben. The DCGC formed in response to localized subsidence in the Peace River Embayment. The DCGC faults continued to be active during the Triassic, imposing significant controls on the distribution of sediments (Marshall et al., 1987; Barclay et al., 1990; Davies, 1997; Eaton et al., 1999). The Devonian reefs exerted a topographic influence on Triassic sedimentation by controlling facies change (Davies, 1997), and may also have influenced subsidence rates and, hence, thickness variation.

---

*This publication is also available, free of charge, as colour digital files in Adobe Acrobat® PDF format from the Geoscience BC website: <http://www.geosciencebc.com/s/SummaryofActivities.asp>.*

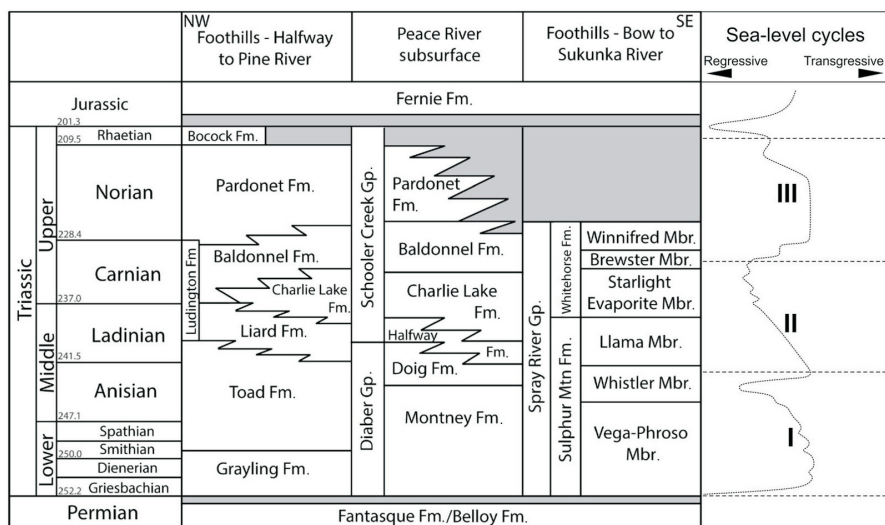


**Figure 1.** Stratigraphic chart of the Triassic, correlating the surface and subsurface relationships of British Columbia and the surface relationships of Alberta (after Gibson and Barclay, 1989; Golding et al., 2015). Eustatic level based on Hardenbol et al. (1998). Abbreviations: Fm., Formation; Gp., Group.

The Doig Formation consists of mudstone, siltstone and subordinate sandstone, bioclastic packstone and grainstone, deposited under marine conditions in environments ranging from shoreface through offshore (Evoy and Moslow, 1995). The Doig Formation can be informally subdivided into three units, as proposed by Chalmers and Bustin (2012): the basal unit, Doig A, also widely referred to as the DPZ, is composed of organic-rich radioactive dark mudstone with common phosphate granules and nodules, and generally easily distinguished in well logs by its high gamma-ray signature; the intermediate Doig B, primarily composed of medium to dark grey argillaceous siltstone and mudstone intercalated with localized sandstone beds; and the upper Doig C, composed of relatively organic-lean (less than 2%) siltstone and argillaceous fine-grained sandstone.

### Material and Methods

Permeability measurements were performed on a total of 60 core plugs 30 mm in diameter and between 20 and 60 mm in length. The plugs were cut from full diameter core, both parallel and perpendicular to bedding, from 14 wells located across the entire extent of the Doig subcrop area in northeastern BC (Figure 2). The samples were taken from a wide range of lithofacies stratigraphically distributed through all Doig informal sub-zones defined in Chalmers and Bustin (2012).

The plug samples were cleaned of soluble hydrocarbons and any residual connate brine through distillation extraction with Dean–Stark-type apparatuses, using toluene as a solvent. Each sample was cleaned for approximately one week and oven-dried at 110°C for another week. The sample mass was measured before and after solvent extraction, with an observed mass loss of 0.1 to 0.5% of the initial mass. The ends of all plugs were trimmed to minimize mud-filtrate invasion effects. Plug-end surfaces were then milled in a surface grinder to create smooth, parallel faces on both ends.

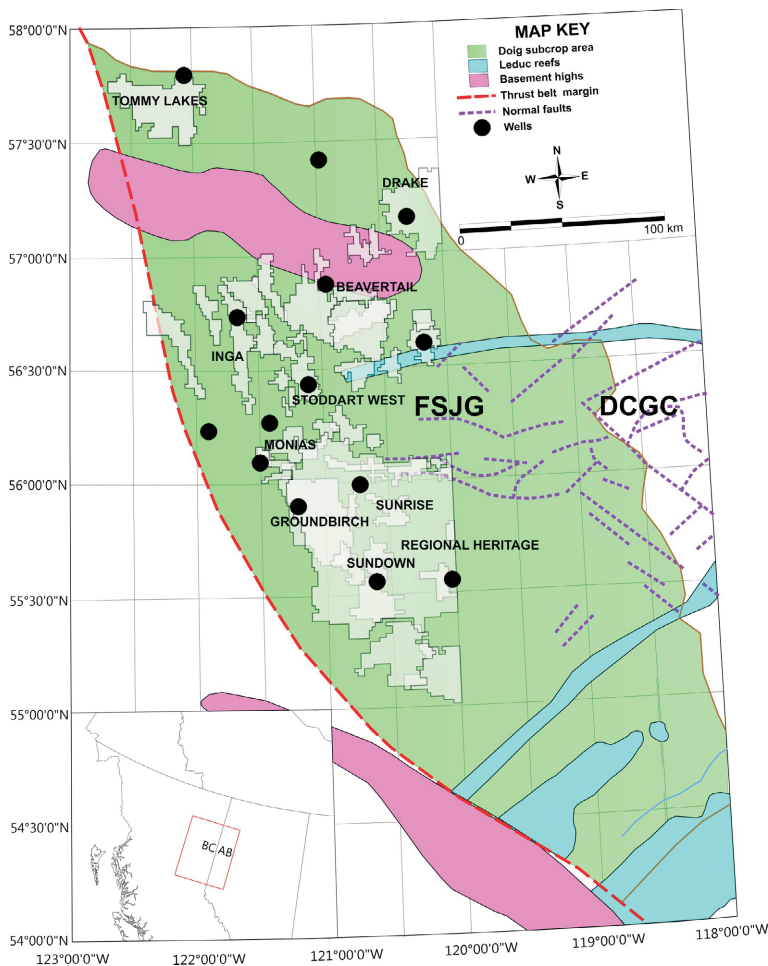


**Figure 2.** Location of wells from which core samples were analyzed for this study of the Doig Formation, northeastern British Columbia, against a backdrop of the Doig subcrop and main structural elements that influenced the Triassic deposition (structural elements after Davies, 1997). Abbreviations: DCGC, Dawson Creek graben complex; FSJG, Fort St. John graben.

Approximately 10 g of rock from a companion sample to the plugs, was crushed to a particle size of 4.8 to 2.4 mm (4–8 mesh) for mercury intrusion porosimetry. The choice of particle size is a compromise between the more limited pore accessibility of whole plugs and the larger compressibility and closure effects on more finely crushed rock (Comisky et al., 2007; Munson, 2015). These samples were also cleaned for seven days using the Dean–Stark method of distillation extraction with toluene and then oven dried for 3 days. Approximately 30 g of 500–841  $\mu\text{m}$  (20 to 35 mesh) particle-size, oven-dried crushed rock was used for helium pycnometry, and another sample measuring between 30 and 50 g was used to measure bulk density by immersion in mercury. Companion samples from the remaining whole core were also collected and powdered for mineralogy and pyrolysis.

Thin sections of select samples were studied to visualize the pore structure and resolve the relationship of texture on permeability and pore-size distribution. Thin sections were impregnated with a blue-dye epoxy to highlight porosity and a dual staining technique was used to identify carbonate minerals (Huegi, 1945; Warne, 1962; Evamy, 1963; Dickson, 1965) and feldspars (Bailey and Stevens, 1960).

### Pulse-Decay Permeability

Gas permeability was obtained through a pulse-decay permeameter, using helium as the probe fluid. The solvent-extracted plugs were oven-dried at 60°C for at least three days immediately before the analysis and confined in a hydrostatic Hoek-type core-cell holder, where they were initially subjected to approximately 17 MPa (2500 psi) confining pressure and 7 MPa (1000 psi) pore pressure to reproduce the lowest possible range of in situ net confining stress (NCS). A differential pressure  $\Delta p$  of approximately 1 MPa (150 psi) was established between the upstream and downstream ends of the core-cell holder, and the permeability was calculated based on the  $\Delta p$  decay with time, according to methods outlined in Cui et al. (2009). The confining pressure was then increased, in increments of approximately 7 MPa (1000 psi), to 45 MPa (6500 psi), while keeping the pore pressure constant, and the measurement was repeated to capture the upper in situ NCS limit. At least three measurements were made at different net confining pressure values. A linear fit through the permeability as a function of NCS allowed the calculation of permeability at the in situ NCS for each sample and the estimation of permeability reduction with increasing stress. The NCS was determined for every sample, by assuming a mean total stress of 93% of the overburden, which is based on estimations of horizontal stresses for the WCSB (Bell et al., 1994), and subtracting the pore pressure from the mean. The overburden pressure was calculated as the integration with depth of the bulk density well log, filling the gaps in log coverage with a linear regression of bulk density as a

function of vertical depth extrapolated to the surface. The pore pressure is a simple integration of the hydrostatic gradient with depth.

### Mercury-Intrusion Porosimetry

Mercury-intrusion data was collected from the companion sample of every plug, using a Micromeritics® Autopore IV 9500 Series, to a maximum pressure of 414 MPa (60 000 psi). Mercury intrusion provides a pore-throat-size distribution curve with a lower limit of 3 nm, as well as a total porosity value. The intrusion and extrusion volumes were corrected for closure and compressibility effects. Pore-throat diameter was then calculated from the corrected data for each pressure step through the modified Young-Laplace equation proposed by Washburn (1921), assuming cylindrical pore geometry, a surface-tension value of 0.485 N/m after Adam (1941) and an advancing contact angle of 130°, established by Ellison et al. (1967) for a mercury–air–quartz system. The pore-size classification terminology used here follows the scheme defined by the International Union of Pure and Applied Chemistry, according to which micropores are defined as smaller than 2 nm, mesopores range between 2 and 50 nm and macropores are larger than 50 nm (Rouquerol et al., 1994).

### Unstressed Porosity

Unstressed porosity was determined on the companion sample to the core plugs by a combination of dual chamber helium pycnometry grain volume and mercury buoyancy–mercury immersion bulk volume measurements, in accordance with the American Petroleum Institute (1998) standard. Pycnometry values were averaged over four repeated measurements for each sample. The unstressed porosity values were used as a reference to calculate stressed porosity from mercury intrusion porosimetry tests.

### X-Ray–Diffraction Mineralogy

Mineralogy was obtained by X-ray diffraction using powdered samples smear mounted on glass slides, prepared according to the method outlined by Munson et al. (2016). This method was demonstrated by the authors to be a viable alternative to methods requiring much longer processing times for obtaining quantitative bulk mineralogy. However, this method does not allow to distinguish between the peaks of illite and those of muscovite. The analysis was performed using normal-focus  $\text{CoK}\alpha$  radiation on a Bruker® D8 Focus with diffraction patterns obtained over a  $2\theta$  range of 3–70° with a step size of 0.03° and a step time of 0.8 s. Analysis of the mineral phases was quantified using the Rietveld full-pattern fitting method (Rietveld, 1967) on the Bruker® AXS TOPAS v3.0 software.

## Rock-Eval Pyrolysis

Samples for whole-rock pyrolysis were analyzed using a HAWK™ instrument from Wildcat Technologies, with the standard Rock-Eval pyrolysis method after Espitalié et al. (1977). Approximately 70 mg of powdered sample was pyrolyzed at a temperature rate of 25°C per minute to a peak temperature of 650°C, followed by a temperature decrease and oxidation stage at 730°C.

## Results and Discussion

The Doig Formation is very heterogeneous in terms of lithofacies, mineralogy, porosity and pore size distributions. Although it is subdivided into the basal phosphatic Doig A, the intermediate mudstone Doig B and the coarser-grained siltstone Doig C, significant variability within each zone causes the matrix permeability to vary by multiple orders of magnitude in less than 20 cm. The permeability of the Doig is controlled by a complex interplay between total porosity, pore-size distribution and clay content. The phosphatic oolitic packstone and grainstone of the Doig A and the quartz-rich siltstone of Doig C tend to have the highest porosity and more favourable balance of macro- to mesopores, which make these lithofacies the best reservoirs in terms of flow capacity.

There is a large spread in matrix permeability, spanning four orders of magnitude from  $10^{-5}$  to  $10^{-1}$  millidarcies (mD), for a porosity range of less than 1% to nearly 15% (Figure 3). Based on this crossplot, the rocks can be divided into two groups: rocks with porosity larger than 5% have permeabilities of  $10^{-3}$  to  $10^{-1}$  mD, and are essentially composed of quartz-rich siltstone to very fine sandstone (illustrated by samples TG19 and TB1) and phosphatic oolitic packstone to grainstone (illustrated by samples CD15 and MH7): the rocks of the second group have porosities ranging from just under 1 to 5% and a larger spread in permeability, ranging from  $10^{-5}$  to  $10^{-1}$  mD. This spread is attributed to enhanced permeability due to microfractures and degrades the correlation between porosity and permeability, which has an  $R^2$  value of 0.27 for the linearized permeability using its logarithm. However, there is a clear trend of increasing permeability with porosity and, for all the properties measured, porosity is still the best single predictor for permeability. Pore-size distribution and, more subordnately, clay content comprise a second order control on permeability. Clay mineralogy is predominantly composed of illite, followed in importance by chlorite in the Doig C interval.

The range of permeabilities found in this study is higher than previously reported ranges of  $10^{-7}$  to  $10^{-3}$  mD (Chalmers and Bustin, 2012; Chalmers et al., 2012) using methane. The higher permeabilities of this study may be due to the solvent extraction process, which clears additional pathways for gas flow and/or to the smaller kinetic diam-

eter of helium compared to methane. This study confirms the observation by Chalmers and Bustin (2012) that there is no obvious relationship between mineralogy and permeability, with the exception of clay content (Figure 4). The highest porosities and permeabilities ( $10^{-3}$  to  $10^{-1}$  mD) are associated with the siltstone to very fine sandstone of Doig C in the Groundbirch and Beavertail areas, and the phosphatic oolitic packstone to grainstone of Doig A in the Drake and Regional Heritage fields. The relationship between permeability and mineralogy is further obscured by the occurrence of clay and extensive carbonate replacement associated with the phosphatic oolitic packstone and grainstone, which may also be associated with relatively high total organic carbon (TOC). Hence, there is no relationship between TOC and permeability. Furthermore, the quartz-rich siltstone and very fine sandstone contain a significant amount of carbonate cement. Thus, high permeabilities occur in carbonate-rich, quartz-rich and even in relatively clay-rich samples, with up to 20 wt. % clay content.

In the Groundbirch sample (TG19), porosity is mainly primary intergranular, whereas in the Beavertail sample (TB1), porosity is intergranular but mainly secondary due to dissolution of feldspar. The Groundbirch field is located at a deeper part of the basin than the Beavertail. At a burial depth of 2540 m, the porosity of sample TG19 is less than half that of sample TB1, which was retrieved from 1310 m. This helps explain the difference in permeability of one order of magnitude for these lithologically similar samples. Another factor influencing the higher permeability of TB1 is the higher proportion of macropores as opposed to mesopores (Figure 5). Both high permeability samples have over 80% of their total pore volume accessible by pore throats larger than the macropore–mesopore boundary of 50 nm. The phosphatic oolitic packstone and grainstone have pore-size distributions shifted toward the mesoporous region. However, the distributions are either broader (MH7) or weakly bimodal (CD15), which enhances permeability, likely due to the interconnectedness of macropores through mesopores. This bimodality is a result of the presence of macropores produced by partial grain dissolution of ooids and mesoporous intergranular porosity. The low permeability rocks ( $<10^{-3}$  mD) have 50% or more of their total pore volume accessible through the mesoporous region or finer and are composed mostly of finer grained siltstone with highly variable proportions of clay, carbonate in the form of cement and bioclasts, and organic matter. Although mercury porosimetry is limited to pore-throat diameters larger than 3 nm, the HM1 and PA7 samples may have a significant contribution to their pore volume from micropores, as suggested by the asymptotic character of their cumulative pore-size distribution curve at the micropore–mesopore boundary.

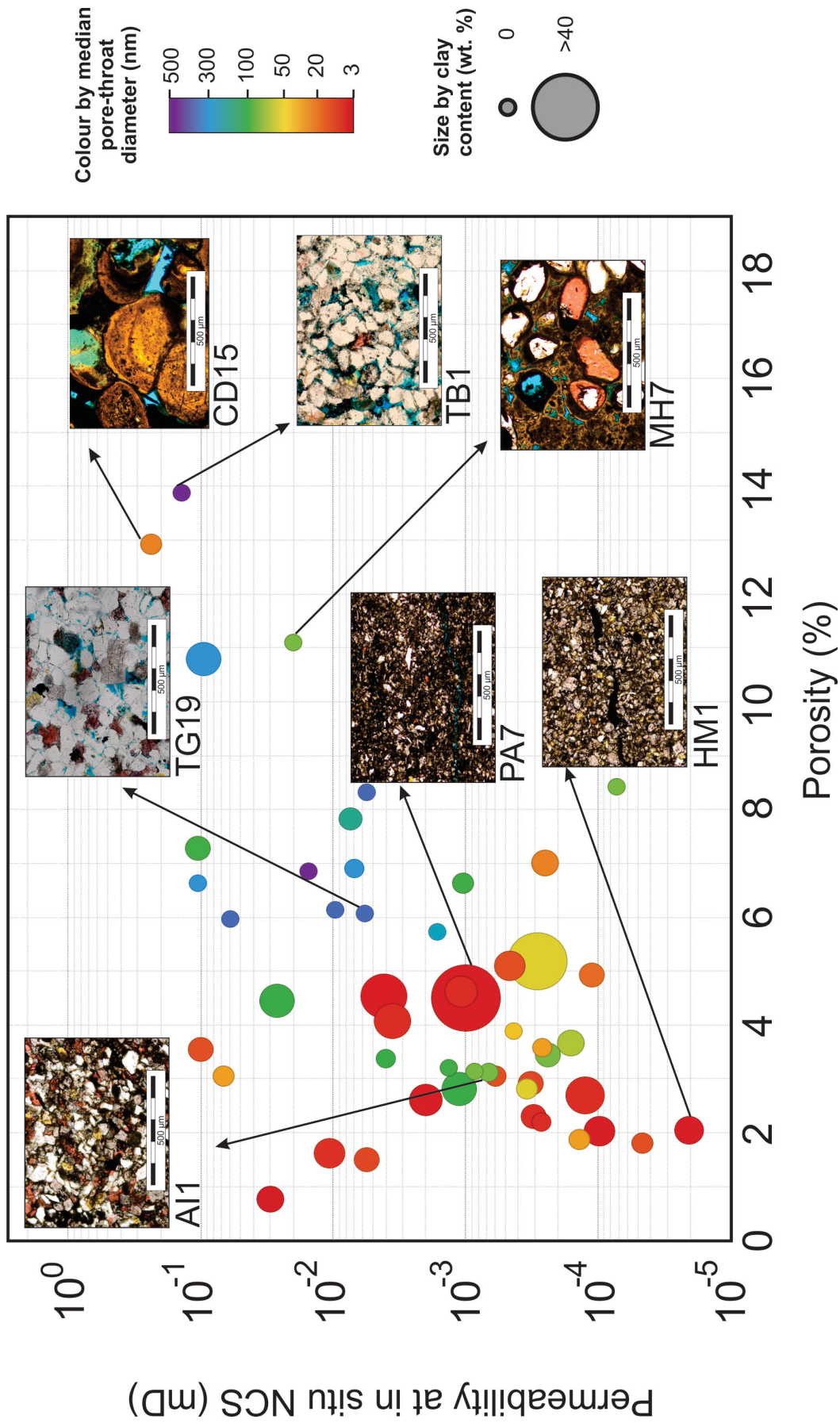


**Figure 3.** Crossplot of gas permeability at in situ net confining stress (NCS) versus porosity in samples analyzed for this study of the Doig Formation, northeastern British Columbia. Circle size is proportional to the total amount of clay and colour represents the median pore-throat diameter. Selected samples are highlighted to illustrate the textural variability, and its influence on porosity and permeability. Abbreviation: mD, millidarcy.

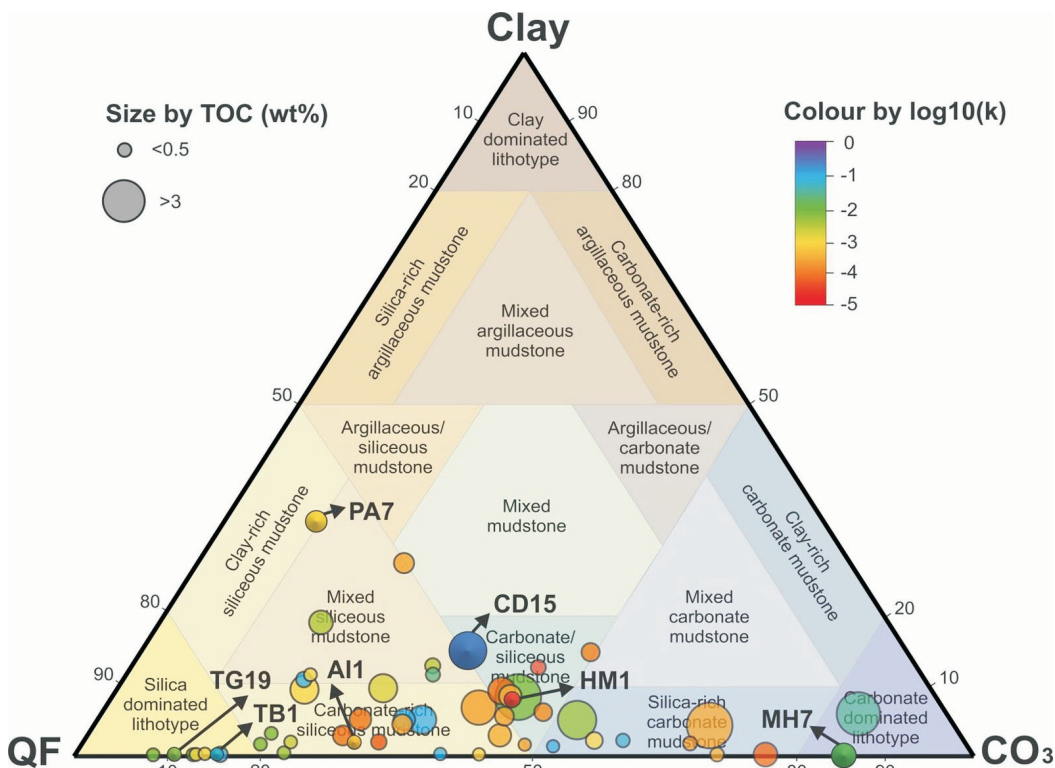


**Figure 4.** Ternary diagram of whole-rock mineralogy normalized to clay, carbonate and quartz-feldspar-plagioclase (QF; after Gamero-Diaz et al., 2012) of samples analyzed for this study of the Doig Formation, northeastern British Columbia. Total organic carbon (TOC) is represented by the size of the circles and the logarithm of gas permeability is represented as a colour gradient. Samples highlighted in Figures 3 and 5 are labelled.

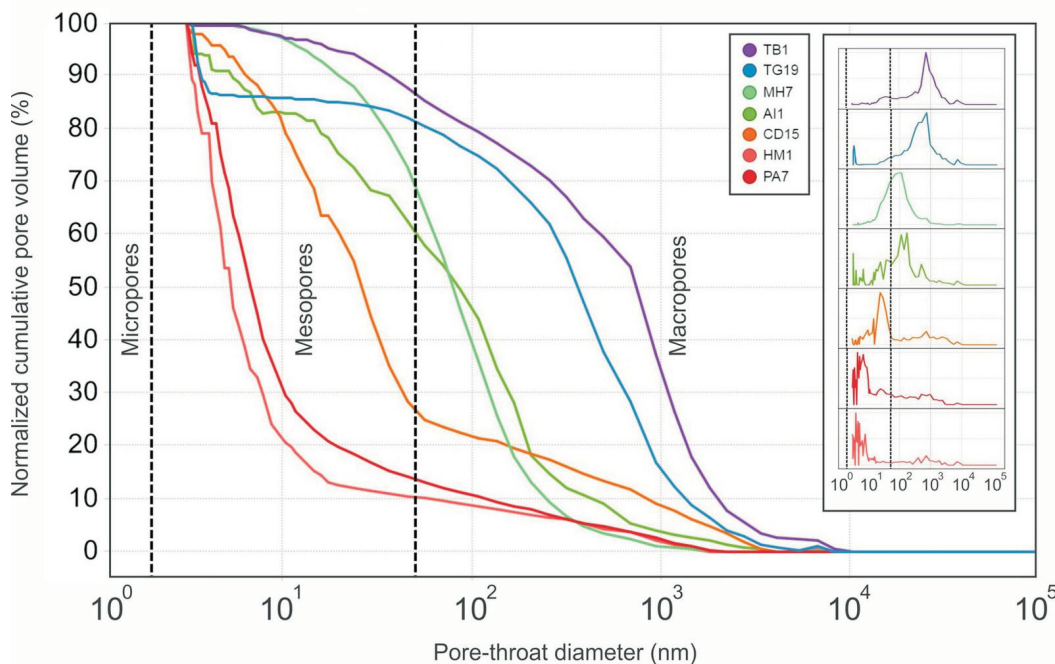


**Figure 5.** Curves of cumulative pore-throat diameter normalized to total pore volume of the selected samples highlighted in Figure 3 for this study of the Doig Formation, northeastern British Columbia. Inset shows their respective frequency distributions sorted by pore size, in descending order from the top.

## Ongoing Work

This study is part of a larger research project aimed at characterizing the Doig Formation through a petroleum system analysis approach and evaluating its potential (Silva, 2017). The project includes an assessment of the source-rock organic geochemical properties, storage and flow properties, geomechanical behaviour, and basin modelling focused on the reconstruction of the thermal history and timing of hydrocarbon generation. Besides the other components of the project, the next steps in characterizing the permeability are:

- inspecting for fractures under the microscope and through acetone imbibition, on the anomalously high permeabilities exhibited by dominantly clay-rich mesoporous samples that plot off trend;
- understanding the impact of the solvent-extraction process on the gas-permeability measurements, which may help explain the discrepancy between the range of permeabilities found in this study and the ones from previous studies, besides providing important information on sample-preparation procedures for mudrock, which currently lack consensus and data;
- characterizing the microporous portion of pore-size distributions of lower permeability ( $10^{-5}$  to  $10^{-3}$  mD) samples, which is below the resolution of mercury porosimetry, through low-pressure isotherms; and
- carrying out additional matrix-permeability measurements on samples from different lithofacies, which will assist in better understanding the impact on permeability of the interplay between porosity, pore-size distribution, mineralogy and lithology, and which may help in defining distinct porosity–permeability functions for difference lithofacies.

## Acknowledgments

The authors acknowledge financial support from Geoscience BC, Canadian Natural Resources Limited, Chevron Canada Limited, Devon Energy Corporation, EnCana Corporation, geoLOGIC systems ltd., Husky Energy Inc. and AGAT Laboratories. The donation of software by geoLOGIC systems ltd. and Paradigm Geophysical Canada Limited was also instrumental in handling the well and core data, and greatly appreciated. The authors would also like to acknowledge the time and effort dedicated to the thorough review of the manuscript by G. Chalmers, research associate at The University of British Columbia.

## References

Adam, N.K. (1941): *The Physics and Chemistry of Surfaces* (3rd edition); Oxford University Press, Oxford, 448 p.

American Petroleum Institute (1998): *Recommended Practice RB40: Recommended Practices for Core Analysis*; API

Publishing Services, Washington, DC, 236 p., URL <<http://w3.energistics.org/RP40/rp40.pdf>> [October 2018].

Armitage, J.H. (1962): Triassic oil and gas occurrences in north-eastern British Columbia, Canada; *Journal of the Alberta Society of Petroleum Geologists*, v. 10, p. 35–56.

Bailey, E.H. and Stevens, R.E. (1960): Selective staining of K-feldspar and plagioclase on rock slabs and thin sections; *The American Mineralogist*, v. 45, p. 1020–1025.

Barclay, J.E., Krause, F.F., Campbell, R.I. and Utting, J. (1990): Dynamic casting of the Dawson Creek Graben Complex: Carboniferous-Permian Peace River Embayment, western Canada; *Bulletin of Canadian Petroleum Geology*, v. 38(A), p. 115–145.

Bell, J.S., Price, P.R. and McLellan, P.J. (1994): In-situ stress in the Western Canada Sedimentary Basin; *in Geological Atlas of the Western Canada Sedimentary Basin*, G.D. Mossop and I. Shetsen (comp.), Canadian Society of Petroleum Geologists and Alberta Research Council, Edmonton, Alberta, p. 439–446, URL <[https://www.cspg.org/documents/Publications/Atlas/geological/atlas\\_29\\_in-situ\\_stress\\_in\\_the\\_WCSB.pdf](https://www.cspg.org/documents/Publications/Atlas/geological/atlas_29_in-situ_stress_in_the_WCSB.pdf)> [October 2018].

Chalmers, G.R.L. and Bustin, R.M. (2012): Geological evaluation of Halfway-Doig-Montney hybrid gas shale-tight gas reservoir, northeastern British Columbia; *Marine and Petroleum Geology*, v. 38, no. 1, p. 53–72.

Chalmers, G.R.L., Bustin, R.M. and Bustin, A.A.M. (2012): Geological controls on matrix permeability of the Doig-Montney hybrid shale-gas-tight-gas reservoir, northeastern British Columbia (NTS 093P); *in Geoscience BC Summary of Activities 2011*, Geoscience BC Report 2012-1, p. 87–96, URL <[https://cdn.geosciencebc.com/pdf/SummaryofActivities2011/SoA2011\\_Chalmers.pdf](https://cdn.geosciencebc.com/pdf/SummaryofActivities2011/SoA2011_Chalmers.pdf)> [October 2018].

Chopra, S., Kumar Sharma, R. and Keay, J. (2014): Mapping Middle Triassic Doig sandstone reservoirs in northeast British Columbia using seismic attributes; *Society of Exploration Geophysicists, 2013 SEG Annual Meeting*, September 22–27, 2013, Houston, Texas, SEG-2013-0170, URL <<https://www.onepetro.org/conference-paper/SEG-2013-0170>> [October 2018].

Comisky, J.T., Newsham, K.E., Rushing, J.A. and Blasingame, T.A. (2007): A comparative study of capillary-pressure-based empirical models for estimating absolute permeability in tight gas sands; *Society of Petroleum Engineers, 2007 SPE Annual Technical Conference and Exhibition*, November 11–14, 2007, Anaheim, California, SPE-110050-MS, URL <<https://www.onepetro.org/conference-paper/SPE-110050-MS>> [October 2018].

Creaney, S. and Allan, J. (1990): Hydrocarbon generation and migration in the Western Canada Sedimentary Basin; *in Classic Petroleum Provinces*, J. Brooks (ed.), Geological Society of London, Geological Society Special Publications 50, p. 189–202.

Cui, X., Bustin, A.M.M. and Bustin, R.M. (2009): Measurements of gas permeability and diffusivity of tight reservoir rocks: different approaches and their applications; *Geofluids*, v. 9, p. 208–223.

Davies, G.R. (1997): The Triassic of the Western Canada Sedimentary Basin: tectonic and stratigraphic framework, paleogeography, paleoclimate and biota; *Bulletin of Canadian Petroleum Geology*, v. 45, no. 4, p. 434–460.

Dickson, J.A.D. (1965): A modified staining technique for carbonates in thin section; *Nature*, v. 205, p. 587.

- Du Rouchet, J. (1985): The origin and migration paths of hydrocarbons accumulated in the Lower Cretaceous sandstone ‘giant’ tar accumulations of Alberta—Part II; *Journal of Petroleum Geology*, v. 8, no. 1, p. 101–114.
- Eaton, D.W., Ross, G.M. and Hope, J. (1999): The rise and fall of a cratonic arch: a regional seismic perspective on the Peace River Arch, Alberta; *Bulletin of Canadian Petroleum Geology*, v. 47, no. 4, p. 346–361.
- Edwards, D.E., Barclay, J.E., Gibson, D.W., Kville, G.E. and Halton, E. (1994): Triassic strata of the Western Canada Sedimentary Basin; Chapter 16 in *Geological Atlas of the Western Canada Sedimentary Basin*, G.D. Mossop and I. Shetsen (comp.), Canadian Society of Petroleum Geologists and Alberta Research Council, Edmonton, Alberta, p. 257–275, URL <<https://ags.aer.ca/publications/chapter-16-triassic-strata>> [October 2018].
- Ellison, A.H., Klemm, R.B., Schwartz, A.M., Grubb, L.S. and Petrash, D.A. (1967): Contact angles of mercury on various surfaces and the effect of temperature; *Journal of Chemical and Engineering Data*, v. 12, no. 4, p. 607–609.
- Espitalié, J., Laporte, J.L., Madec, M., Marquis, F., Leplat, P., Paulet, J. and Boutefeu, A. (1977): Méthode rapide de caractérisation des roches mères, de leur potentiel pétrolier et de leur degré d’évolution; *Revue de l’Institut Français du Pétrole*, v. 32, no. 1, p. 23–42.
- Evamy, B.D. (1963): The application of a chemical staining technique to a study of dedolomitisation; *Sedimentology*, v. 2, p. 164–170.
- Evoy, R.W. and Moslow, T.F. (1995): Lithofacies associations and depositional environments in the Middle Triassic Doig Formation, Buick Creek Field, northeastern British Columbia; *Bulletin of Canadian Petroleum Geology*, v. 43, no. 4, p. 461–475.
- Faraj, B., Harold, W., Addison, G., McKinstry, B., Donaleshen, R., Sloan, G., Lee, J., Anderson, T., Leal, R., Anderson, C., Lafleur, C. and Ahlstrom, A. (2002): Shale gas potential of selected Upper Cretaceous, Jurassic, Triassic and Devonian shale formations in the WCSB of Western Canada: implications for shale gas production; *Gas Technology Institute, Report GRI-02/0233*, 258 p.
- Gamero-Díaz, H., Miller, C. and Lewis, R. (2012): sCore: A classification scheme for organic mudstones based on bulk mineralogy; *American Association of Petroleum Geologists, AAPG Southwest Section Convention*, May 19–22, 2012, Fort Worth, Texas, AAPG Search and Discovery article 40951, 18 p., URL <[https://www.searchanddiscovery.com/documents/2012/40951diaz/ndx\\_diaz.pdf](https://www.searchanddiscovery.com/documents/2012/40951diaz/ndx_diaz.pdf)> [October 2018].
- Gibson, D.W. and Barclay, J.E. (1989): Middle Absaroka sequence—the Triassic stable craton; in *Western Canada Sedimentary Basin—a Case History*, B.D. Ricketts (ed.), Canadian Society of Petroleum Geologists, Calgary, Special Publication, p. 219–232.
- Golding, M.L., Orchard, M.J., Zonneveld, J.P. and Wilson, N.S.F. (2015): Determining the age and depositional model of the Doig phosphate zone in northeastern British Columbia using conodont biostratigraphy; *Bulletin of Canadian Petroleum Geology*, v. 63, no. 2, p. 143–170.
- Hardenbol, J., Thierry, J., Farley, M.B., Jacquin, T., De Graciansky, P.-C. and Vail, P.R. (1998): Cenozoic sequence chronostratigraphy; in *Mesozoic and Cenozoic Sequence Chronostratigraphic Framework of European Basins*, P.C. De Graciansky, J. Hardenbol, T. Jacquin and P.R. Vail (ed.), *Society for Sedimentary Geology, SEPM Special Publication 60*, p. 3–13.
- Henderson, C.M. (1989): The lower Absaroka Sequence: Upper Carboniferous and Permian; in *Western Canada Sedimentary Basin—a Case History*, Special Publication, B.D. Ricketts (ed.), Canadian Society of Petroleum Geologists, Calgary, p. 203–217.
- Huegi, T. (1945): Gesteinbildend wichtige karbonate und deren nachweis mittels farbmethode; *Schweizerische Mineralogische und Petrographische Mitteilungen*, v. 25, p. 114–140.
- Marshall, G.M., Noble, I.A.R. and Tang, C.W. (1987): Triassic/Jurassic fields; Chapter 7 in *Geophysical Atlas of Western Canadian Hydrocarbon Pools*, N.L. Anderson, L.V. Hills and D.A. Cederwall (ed.), Canadian Society of Exploration Geophysicists and Canadian Society of Petroleum Geologists, Calgary, Alberta, p. 187–215, URL <[https://www.cspg.org/cspg/documents/Publications/Atlas/geophysical/L\\_Chapter\\_7.pdf](https://www.cspg.org/cspg/documents/Publications/Atlas/geophysical/L_Chapter_7.pdf)> [October 2018].
- Munson, E.O. (2015): Reservoir characterization of the Duvernay Formation, Alberta: a pore- to basin-scale investigation; Ph.D. thesis, University of British Columbia, 266 p.
- Munson, E.O., Chalmers, G.R.L., Bustin, R.M. and Li, K. (2016): Utilizing smear mounts for X-ray diffraction as a fully quantitative approach in rapidly characterizing the mineralogy of shale gas reservoirs; *Journal of Unconventional Oil and Gas Resources*, v. 14, p. 22–31.
- Riediger, C.L., Fowler, M.G., Brooks, P.W. and Snowdon, L.R. (1990): Triassic oils and potential Mesozoic source rocks, Peace River Arch area, Western Canada Basin; *Organic Geochemistry*, v. 16, no. 1–3, p. 295–305.
- Rietveld, H.M. (1967): Line profiles of neutron powder-diffraction peaks for structure refinement; *Acta Crystallographica*, v. 22, p. 151–152.
- Rouquerol, J., Avni, D., Fairbridge, C.W., Everett, D.H., Haynes, J.M., Pernicone, N., Ramsay, J.D.F., Sing, K.S.W. and Unger, K.K. (1994): Recommendations for the characterization of porous solids; *International Union of Pure and Applied Chemistry*, v. 68, no. 8, p. 1739–1758.
- Silva, P.L. (2017): Status report on petroleum system analysis study of the Triassic Doig Formation, Western Canada Sedimentary Basin, northeastern British Columbia; in *Geoscience BC Summary of Activities 2011*, *Geoscience BC Report 2017-1*, p. 25–28, URL <[https://cdn.geosciencebc.com/pdf/SummaryofActivities2016/SoA2016\\_Silva.pdf](https://cdn.geosciencebc.com/pdf/SummaryofActivities2016/SoA2016_Silva.pdf)> [October 2018].
- United States Energy Information Administration (2013): Technically recoverable shale oil and shale gas resources: Canada; United States Department of Energy, 29 p., URL <<https://www.eia.gov/analysis/studies/worldshalegas/pdf/overview.pdf>> [October 2018].
- Walsh, W., Adams, C., Kerr, B. and Korol, J. (2006): Regional “shale gas” potential of the Triassic Doig and Montney formations, northeastern British Columbia; BC Ministry of Energy, Mines and Petroleum Resources, Oil and Gas Division, Resource Development and Geoscience Branch, Open File 2006-0, 19 p., URL <<https://www2.gov.bc.ca/assets/gov/farming-natural-resources-and-industry/natural-gas-oil/petroleum-geoscience/petroleum-open-files/pgof20062.pdf>> [October 2018].
- Warne, S.S.J. (1962): A quick field or laboratory staining scheme for the differentiation of the major carbonate minerals; *Journal of Sedimentary Petrology*, v. 32, p. 29–38.
- Washburn, E.W. (1921): Note on a method of determining the distribution of pore sizes in a porous material; in *Proceedings of the National Academy of Sciences of the United States of America*, v. 7, no. 4, p. 115–116.

# Preliminary Characterization of Early Jurassic Source Rocks and Ocean-Redox Conditions Based on Trace-Metal and Organic Geochemistry of the Gordondale and Poker Chip Shale Members, Fernie Formation, Northeastern British Columbia

A. Kunert, University of Waterloo, Waterloo, ON, [akunert@uwaterloo.ca](mailto:akunert@uwaterloo.ca)

B. Kendall, University of Waterloo, Waterloo, ON

T.F. Moslow, Petronas Canada, Calgary, AB

G. Nyberg, Petronas Canada, Calgary, AB

B. Pedersen, Petronas Canada, Calgary, AB

C. Smith, Sasol Canada, Calgary, AB

---

Kunert, A., Kendall, B., Moslow, T.F., Nyberg, G., Pedersen, B. and Smith, C. (2019): Preliminary characterization of Early Jurassic source rocks and ocean-redox conditions based on trace-metal and organic geochemistry of the Gordondale and Poker Chip Shale members, Fernie Formation, northeastern British Columbia; *in* Geoscience BC Summary of Activities 2018: Energy and Water, Geoscience BC, Report 2019-2, p. 29–42.

## Introduction

The Gordondale member (Asgar-Deen et al., 2004; previously the ‘Nordegg Member’ of Spivak, 1949) of the Lower Jurassic Fernie Formation in the subsurface of northeastern British Columbia (NEBC) has attracted interest for its hydrocarbon potential since the early 1990s (e.g., Creaney and Allan, 1990; Riediger et al., 1991). The Poker Chip Shale, another Lower Jurassic member in the Fernie Formation, overlies the Gordondale member in some areas and has also shown hydrocarbon potential (Riediger, 2002). With increasing oil and gas exploration in NEBC, especially in unconventional reservoirs, new source-rock plays like the Gordondale and Poker Chip Shale members may become viable targets for expansion of British Columbia’s hydrocarbon resource base.

While there exists limited production from the Gordondale and Poker Chip Shale members in the Fort St. John area of NEBC, advancements in exploration and development activity may be achieved through a better understanding of geological and geochemical parameters of these formations. This study is designed to address this issue. Previous studies in NEBC and Alberta have included organic geochemistry and source-rock characterization (e.g., Riediger et al., 1991; Ibrahimbas and Riediger, 2004; Ross and Bustin, 2007; Kondla et al., 2017), biostratigraphy (e.g., Asgar-Deen et al., 2004; Them et al., 2017a), inorganic geochemistry (e.g., Ross and Bustin, 2006) and carbon-isotope geochemistry (e.g., Them et al., 2017a). This study examines in detail a 45.7 m core of the uppermost Pardonet Formation

(Upper Triassic), Gordondale member and Poker Chip Shale (Lower Jurassic), and lowermost upper Fernie Formation shales (Upper Jurassic) from the Altares field (Figure 1) employing detailed organic and inorganic trace-metal geochemistry analyses.

The goal of this project is to identify spatial and temporal trends in paleoredox, paleoproductivity and paleohydrographic conditions during deposition of the Gordondale member and the Poker Chip Shale. This will help to constrain intervals that show the greatest potential for resource development in the study area, based on their potential for organic-matter deposition and preservation. The results of this study can hopefully be used to enhance prediction of reservoir parameters in these units in other parts of the Western Canada Sedimentary Basin. Another objective is to search for geochemical evidence of the Toarcian Oceanic Anoxic Event (T-OAE) in the Gordondale member or the overlying Poker Chip Shale. Identification of this event is necessary to constrain the impact of changes in global ocean-redox conditions on depositional geochemical signatures and thus aid with understanding geochemical differences between the two hydrocarbon source rocks in this region. Further analysis will include organic carbon-isotope ( $\delta^{13}\text{C}_{\text{org}}$ ) geochemistry to test this hypothesis, as marine sedimentary rocks of Toarcian age worldwide contain negative  $\delta^{13}\text{C}_{\text{org}}$  excursions that mark the T-OAE. This paper will highlight preliminary results of X-ray diffraction (XRD), major-element (CaO,  $\text{P}_2\text{O}_5$ ,  $\text{TiO}_2$  and  $\text{Al}_2\text{O}_3$ ), molybdenum (Mo), uranium (U), rhenium (Re) and carbon content (organic and inorganic) analysis and the use of these results in identifying paleoredox and paleohydrographic trends. Future research directions are discussed.

---

*This publication is also available, free of charge, as colour digital files in Adobe Acrobat® PDF format from the Geoscience BC website: <http://www.geosciencebc.com/s/SummaryofActivities.asp>.*

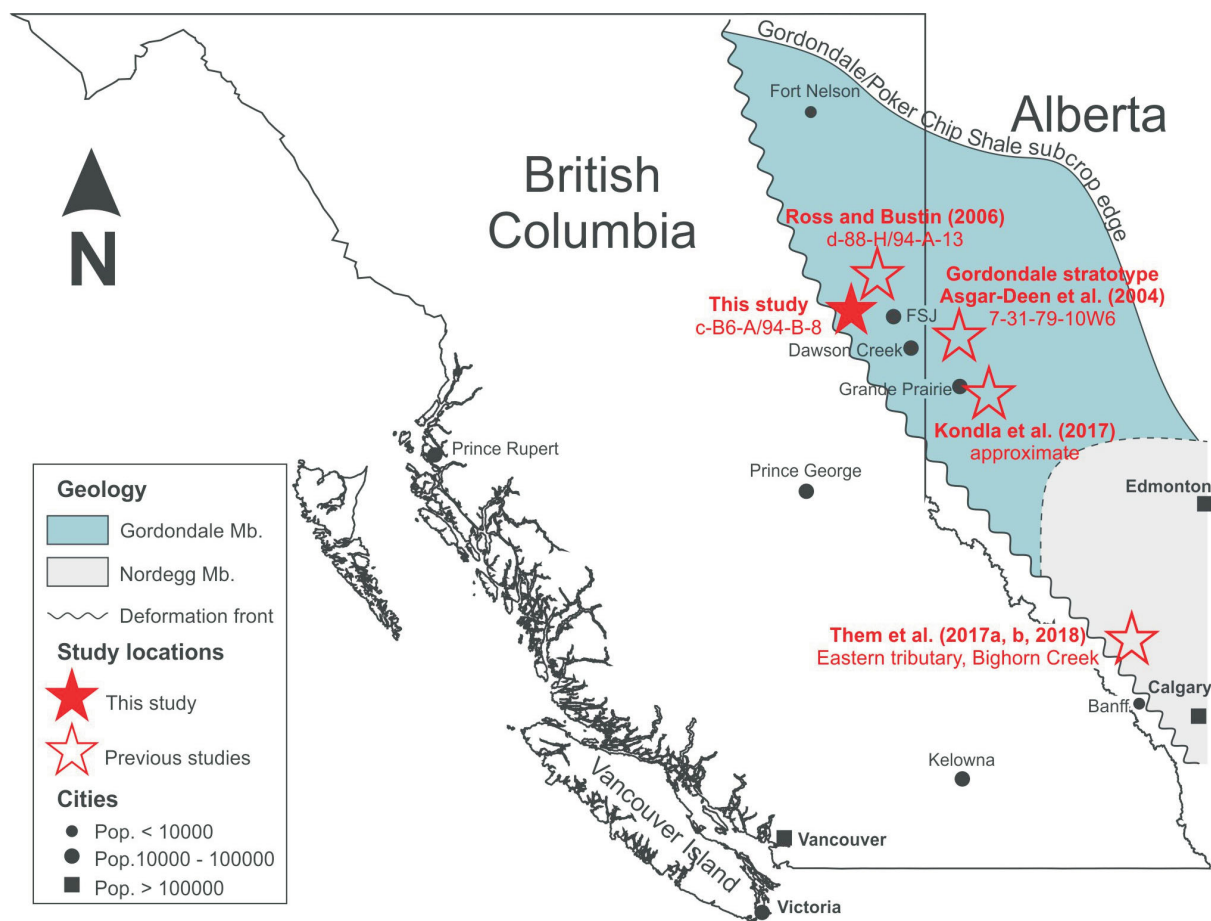


**Figure 1.** Location of study area in northeastern BC, with core and outcrop locations from previous studies. The red star indicates the location of the Progress HZ Altares c-B6-A/94-B-8 well (BC Oil and Gas Commission, 2018), core from which was examined in this study; empty stars indicate core and outcrop locations that have been examined by other authors (Asgar-Deen et al., 2004; Ross and Bustin, 2006; Kondla et al., 2017; Them et al., 2017a, b, 2018). Gordondale (formerly Nordegg) member coverage, transition to true Nordegg and subcrop are approximated from Asgar-Deen et al. (2004). The Poker Chip Shale can be found throughout the area covered by the Gordondale (blue) and Nordegg (grey) members, and the subcrop is inferred to coincide with that of the Gordondale member (Riediger, 2002).

## Geological and Geochemical Background

### Jurassic Strata of Northeastern BC

The basal Gordondale member of the Jurassic Fernie Formation in NEBC is an organic-rich, calcareous and variably phosphatic black shale. The unit is recognized petrophysically by its high gamma-ray log response with a ‘doublet’ (dual gamma-ray peak) feature. The gamma peaks correspond to units 1 and 3 of Asgar-Deen et al. (2004), or units B and D of Ross and Bustin (2006). The Gordondale member reaches thicknesses of up to 40 m over the depocentre (north-northwest trend) and thins to the west and east both depositionally and erosionally, although not equally in either direction (Poulton et al., 1994). The Gordondale member in NEBC ranges between 15 and 25 m in thickness (Asgar-Deen et al., 2004) and is underlain by the sub-Jurassic unconformity and truncated by progressively older strata from west to east (Poulton et al., 1994). The subsurface Gordondale member of NEBC is time

equivalent to the Red Deer Member, Poker Chip Shale and Nordegg Member cherty-carbonate facies of the Alberta foothills outcrop belt (Asgar-Deen et al., 2004). In NEBC, the Gordondale member is typically underlain by the dolomitic Triassic Pardonet Formation, which subcrops to the east where the Gordondale member immediately overlies the older Triassic Baldonnel Formation dolomite. The Gordondale member in NEBC is likely overlain by the Toarcian Poker Chip Shale (Riediger, 2002). Figure 2 outlines the Jurassic stratigraphy in NEBC.

Deposition of the Gordondale member occurred during a major marine transgression (Creaney and Allen, 1990). Eustatic lowstand caused periods of restriction in the Gordondale basin (Poulton et al., 1994) due to the presence of physical sills, thus promoting the development of anoxic or euxinic bottom-water conditions (Riediger et al., 1990; Riediger and Bloch, 1995). Convergent tectonism (Columbian orogeny) may have led to decreased ocean circulation



Shale A strata have TOC contents of 1.0–2.5% and contain oil-prone type II kerogens (Riediger, 2002).

Recent geochronology of the Gordondale member and equivalent units to the south has provided ages for the upper and lower contacts. Paná et al. (2018) performed Re-Os geochronology on cores in northwestern Alberta. Organic-rich shales from the base of the Gordondale member yielded an isochron age of  $192.0 \pm 1.4$  Ma (near the Sine-murian–Pliensbachian boundary), whereas shales from the base of the Poker Chip Shale yielded an age of  $182.0 \pm 2.5$  Ma (approx. Pliensbachian–Toarcian boundary). These ages are in agreement with ammonite biostratigraphy (e.g., Asgar-Deen et al., 2004; Them et al., 2017a) and U-Pb zircon ages (e.g., Paná et al., 2017). The thickness of the dated interval was approximately 24.7 m, implying a minimum average sedimentation rate for the Gordondale member of 2.5 m/m.y.

### Inorganic Geochemistry

Multi-element redox studies provide important information on ancient bottom-water  $O_2$  levels, porewater chemistry and extent of basin restriction in terms of water exchange with the open ocean. Bottom-water conditions are divided into oxic ( $>2.0$  ml  $O_2$  per L water), suboxic (0.2–2.0 ml  $O_2$  per L water) and anoxic (0 ml  $O_2$  per L water; after Tribovillard et al., 2006). Additionally, anoxic waters can be subdivided into ferruginous (0 ml  $O_2$  per L water, 0 ml  $H_2S$  per L water) or euxinic (0 ml  $O_2$  per L water,  $>0$  ml  $H_2S$  per L water). Modern oceans are widely oxic; however, there are several locations where anoxia and euxinia occur either seasonally or year-round. Extensively studied modern anoxic basins include the Black Sea (eastern Europe), Framvaren Fjord (Norway), Cariaco Basin (Venezuela), Saanich Inlet (British Columbia) and eastern tropical-Pacific open-ocean oxygen minimum zones along the California, Mexico and Peru continental margins. A shared feature of these basins is their restriction from consistent deep-marine circulation by seasonal changes in circulation, geographic configuration and/or submarine sills. Sediment- and water-column analysis in these basins has provided a catalogue of the chemistry defining these environments (e.g., Algeo and Lyons, 2006; Algeo and Tribovillard, 2009), which can now be compared with geochemical data from ancient anoxic marine strata, such as the Gordondale member, to identify similar past depositional settings.

Molybdenum is a trace metal with a low upper-crustal concentration of 1.5 ppm (McLennan, 2001) but is found in abundance in oxic seawater (105 nmol/kg; Tribovillard et al., 2006). Sediments deposited from well-oxygenated bottom waters have low authigenic Mo enrichments that approach crustal concentrations. Modern sediments and sedimentary rocks deposited from euxinic waters have pronounced Mo enrichments (several tens to hundreds of

parts per million; Scott and Lyons, 2012) because molybdate converts to thiomolybdate and to particle-reactive polysulphides that are removed to the sediments (Dahl et al., 2013). Mild authigenic Mo enrichment can occur in marine environments where bottom waters are mildly oxygenated to ferruginous and the sediment pore fluids just below the sediment-water interface contain dissolved sulphide. Molybdenum enrichment in sediments is further enhanced if Fe-Mn oxyhydroxides are delivered to sediments. Adsorption of molybdate to Fe-Mn oxyhydroxides can occur in the oxic upper-water column and, upon deposition in anoxic settings, the Mo species are desorbed once the Fe-Mn particulates are dissolved. The released Mo can be captured by organic matter and sulphide minerals, thus enhancing Mo enrichments in anoxic sediments (Tribovillard et al., 2006).

Scott and Lyons (2012) compiled Mo concentration data for modern marine sediments. Sediments deposited under non-euxinic bottom waters with active Fe-Mn oxyhydroxide shuttles and porewater  $H_2S$  have Mo concentrations above crustal values but below 25 ppm. Sediments deposited under year-round Mo-replete euxinic bottom waters have Mo  $>100$  ppm. Intermediate concentrations (25–100 ppm) were linked to four possible nonexclusive conditions: 1) seasonal euxinia, 2) high sedimentation rates (dilution effect), 3) depletion of aqueous Mo in restricted marine settings, and 4) pH effects. Alternatively, Scholz et al. (2017) stated that intensely suboxic (i.e., nitrogenous) conditions of the Peruvian margin oxygen-minimum zone have Mo enrichments ( $\sim 70$ –100 ppm) in sediments similar to those found in euxinic basins. Hardisty et al. (2018) also demonstrated that significant overlap in sediment Mo concentrations may occur under various redox conditions, which may confuse interpretation of paleoredox environments. In all cases, alternative proxies should be used to further strengthen interpretations in constraining the local redox environment.

Uranium is a redox-sensitive trace metal that, like Mo, has a low upper-crustal concentration (2.8 ppm; McLennan, 2001) and is present as dissolved uranyl carbonate complexes in seawater with an average concentration of 13.4 nmol/kg (Tribovillard et al., 2006). Oxic sediments have low U concentration, typically near crustal concentrations. Unlike Mo, enrichment of U in anoxic environments does not require the presence of free  $H_2S$  (although enrichment is not deterred by its presence) in the water column and typically occurs within the sediment rather than at the sediment-water interface (Tribovillard et al., 2006). Once U is diffused into sediments, enrichment under anoxic conditions is facilitated by abiotic or microbial reduction (e.g., sulphate/iron-reducing or fermenting bacteria; Stylo et al., 2015) of U(VI) to U(IV), resulting in sedimentary U  $>10$  ppm (Partin et al., 2013). Uranium adsorption to Fe-Mn particulates is much weaker than that of Mo (Algeo and

Tribovillard, 2009). Uranium enrichments can correlate with organic-matter content in sediments (McManus et al., 2006). Other factors influencing U enrichments in sediments are the depth of O<sub>2</sub> penetration below the sediment-water interface, sedimentation rate and oxic remobilization.

Like Mo and U, Re is a redox-sensitive trace metal with very low upper-crustal abundance (0.4 ppb; McLennan, 2001; Sheen et al., 2018) but high seawater concentrations (39.8 ± 0.1 pmol/kg at 1σ<sup>1</sup>; Anbar et al., 1992). Oxidic sediments do not show Re enrichments, but retain concentrations near the crustal average. The main Re sink is anoxic sediments, with Re typically >5.0 ppb (Sheen et al., 2018). Euxinic sediments are a sink for Re, but its enrichment is independent of H<sub>2</sub>S availability, so no threshold for euxinia is defined in terms of Re concentration (Sheen et al., 2018). Rhenium adsorption to Fe-Mn oxyhydroxides is weak and therefore not an important control on delivery of Re to sediments, and enrichment is thought to occur below the sediment-water interface (Crusius et al., 1996).

In combination, Mo and U covariations show a relationship with basin restriction and sediment trace-metal enrichment mechanisms (Algeo and Tribovillard, 2009). Algeo and Tribovillard (2009) examined this relationship by observing Mo<sub>EF</sub>/U<sub>EF</sub> ratios (EF, enrichment factor; see ‘Methods’ section for calculation) in three anoxic-euxinic locations: 1) the eastern tropical Pacific (California, Mexico and Peru margins), 2) the Cariaco Basin, and 3) the Black Sea. The eastern tropical Pacific is a productive upwelling zone of predominantly open-ocean characteristics but with localized sills leading to partially restricted, euxinic deep-water masses. Along these coasts, sediments exhibit a range of redox environments from suboxic (marginal) to anoxic and euxinic (basinal). The Cariaco Basin is a tectonic depression located off the coast of Venezuela in the Gulf of Mexico with a sill at 120–150 m that weakly restricts deep-water exchange with the open ocean, creating a mildly euxinic bottom-water layer. An Fe-Mn-oxyhydroxide particulate shuttle operates in the Cariaco Basin, delivering Mo to the sediment-water interface and producing pronounced Mo enrichments relative to U (because U removal to particulates is less efficient) and thus increased Mo<sub>EF</sub>/U<sub>EF</sub> ratios in sediments. The Black Sea is a highly restricted, pervasively anoxic, intensely stratified basin with a shallow sill connecting it to the Mediterranean Sea that limits O<sub>2</sub> penetration in deep waters. High sulphate and organic-matter fluxes lead to sustained microbial sulphate reduction and scavenging of reactive iron by sulphide, resulting in euxinic bottom waters. Renewal times of deep-water masses in the Black Sea are long (500–2000 years) compared to those of the Cariaco Basin (50–100 years), which limits the re-

plenishment of aqueous chemical species. As drawdown of redox-sensitive metals into euxinic Black Sea sediments occurs, the water-mass trace-metal chemistry evolves to lower aqueous concentrations. Due to the faster rate of reduction and removal of Mo from euxinic waters to sediments compared with U, the Mo<sub>EF</sub>/U<sub>EF</sub> decreases over time until steady-state conditions are achieved or aqueous species are replenished (Algeo and Tribovillard, 2009).

The extent of basin restriction can be inferred from organic-rich mudrocks deposited in restricted basins by the degree of Mo enrichment normalized to TOC content (Algeo and Lyons, 2006). Based on Mo and TOC concentrations from four modern anoxic basins, Algeo and Lyons (2006) illustrated that the slope (*m*) of a Mo–TOC covariation trend infers the relative extent of basin restriction, where a steep slope (higher Mo/TOC) implies weaker restriction than a shallow slope (lower Mo/TOC). Their study examined four anoxic marine basins with varied water-exchange restriction, from least to most restricted: 1) Saanich Inlet (*m* = 45 ppm/wt. %), 2) the Cariaco Basin (*m* = 25 ppm/wt. %), 3) Framvaren Fjord (*m* = 9 ppm/wt. %), and 4) the Black Sea (*m* = 4.5 ppm/wt. %). Saanich Inlet is a small, seasonally euxinic (annual renewal of deep-water mass) and silled fiord located on Vancouver Island, connected to the Georgia and Haro straits. Framvaren Fjord is a redox-stratified basin with a very long and shallow sill (2.5 m depth) connecting it to the ocean via Helvikfjord and Lyngdalsfjord (Algeo and Lyons, 2006).

## Methods

Two sample sets have been collected and analyzed from the 45.7 m Progress HZ Altares c-B6-A/94-B-8 Jurassic cored well drilled 75 km west of Fort St. John. The first sample set (*n*<sub>1</sub> = 45) was collected in 2016 and included XRD analysis, which guided initial stratigraphic correlation and selection of the second sample set (*n*<sub>2</sub> = 46) in 2018. This second set has been analyzed for major and minor elements, redox-sensitive trace-metal concentrations and carbon content. The cored well contains (from base to top): uppermost Pardonet Formation, Gordondale member, Poker Chip Shale and lowermost upper Fernie Formation shales. The samples included rocks from the Pardonet Formation (*n*<sub>1</sub> = 2; *n*<sub>2</sub> = 3), Gordondale member (*n*<sub>1</sub> = 21; *n*<sub>2</sub> = 22), Poker Chip Shale (*n*<sub>1</sub> = 15; *n*<sub>2</sub> = 19) and upper Fernie Formation shales (*n*<sub>1</sub> = 7; *n*<sub>2</sub> = 2). The black shales of the Gordondale member and Poker Chip Shale are the focus of the analysis.

## X-ray Diffraction (XRD)

Analysis of the first sample set, including the XRD analysis, was completed at Argile Analytica (Calgary, Alberta). Bulk-analysis XRD was conducted on 1.5 g samples that were crushed for 3 minutes in a Retsch ball mill and subsequently by hand in an agate mortar to homogenize grain size. Sample powder was packed into a sample holder to

<sup>1</sup>one standard deviation

avoid preferential orientation and scanned from 4° to 60° 2θ (where θ is the angle of the incident X-ray beam with a crystallographic plane; Stefani, 2016).

### Sample Collection and Preparation for Elemental Analysis

The second set of core samples was collected at Weatherford Labs (Calgary, Alberta) in January 2018. Sampling was completed at ~1 m intervals, targeting black shales where lithology was consistent; if rock type varied over short intervals, each lithology was sampled. Several features were avoided during sampling, including veins (calcite or quartz), macroscopic pyrite nodules, fossils and bedding contacts, to reduce the influence of diagenetic and biological effects on depositional geochemical signals. Samples were mainly black shales (i.e., dark, finely laminated, fissile, organic-rich mudstone); however, other rocks such as turbidites, ash beds and siltstones were collected to derive geochemical information about background detrital sedimentation and volcanogenic contributions.

Bagged samples were photographed, catalogued and returned to the University of Waterloo for analytical preparation. Samples were cut to remove unwanted material (e.g., core paint, chisel marks), manually crushed using a rubber mallet and powdered using an automated ball mill with agate grinding jars to avoid metal contamination. Powdered samples were separated into multiple aliquots for elemental and carbon analysis.

### Elemental Analysis

Powdered samples were weighed (100 ± 20 mg per sample) and ashed overnight at 550°C to oxidize organic matter. Ashed powders were digested through iterative dissolution in trace-metal grade HCl-HNO<sub>3</sub>-HF in a clean room at the Metal Isotope Geochemistry Laboratory, Department of Earth and Environmental Sciences, University of Waterloo. Aliquots of sample solutions were diluted by factors of 6000 (for major, minor and most trace elements) and 400 (for Cd, Re and heavy rare-earth elements) for analysis on an Agilent 8800 triple-quadrupole inductively coupled plasma-mass spectrometer (QQQ-ICP-MS). An internal standard solution of Sc, Ge, In and Bi was employed to monitor and correct for instrument signal drift. A set of multi-element calibration standards, designed to be representative of black shale chemistry, was used to define calibration curves for each element undergoing analysis. Each element for a single sample was analyzed three times per QQQ-ICP-MS session, providing an averaged concentration and relative standard deviation (RSD), which was typically less than 4%. Three shale standards (USGS SBC-1, SDO-1 and SGR-1b) were prepared and analyzed in the same manner as the core samples. During each analytical session, these standards were analyzed multiple times to

verify instrument accuracy, which was determined to be 90–110% calculated as percent recovery compared to certified standard values. Procedural blanks were prepared with the samples during dissolution to monitor background elemental contamination levels. Blanks were typically less than 0.01% of sample-element content. Replicate analysis was completed for eight samples from splits of un-ashed powder to monitor analytical precision. Reproducibility was typically better than 5% on all elements; however, Re was an exception with a mean reproducibility of 8%.

### Enrichment Factors

Normalization of trace-element concentrations to a detrital proxy was completed by calculating enrichment factors (EF) to account for dilution by chemical/biochemical components (e.g., opal and carbonate; equation 1). To avoid spurious correlations, Van der Weijden (2002) outlined requirements for using Al for EF normalization, including 1) the need for low Al RSD compared to the RSD of the trace metal, 2) exclusion of samples with very low detrital-mineral content, and 3) limited excess Al in relation to other detrital elements such as Ti. The EF normalization compares the ratio between a given trace-metal (X) and the Al content in a sample to that ratio in a standard material or rock type:

$$X_{EF} = (X/Al)_{\text{sample}} / (X/Al)_{\text{standard}} \quad (1)$$

An  $X_{EF}$  of ~1 indicates negligible enrichment, values between 1 and 10 show slight enrichment, and values greater than 10 show substantial enrichment relative to the standard. This scaling is also used to determine relative depletion, where  $X_{EF}$  between 1 and 0.1 indicates slight depletion in the trace metal and values of less than 0.1 indicate substantial depletion. Two standard values were used for normalization: 1) average upper continental crust (UCC) concentrations of McLennan (2001), and 2) Post-Archean Australian Average Shale (PAAS) for direct comparison with the  $Mo_{EF}$ - $U_{EF}$  covariation trends identified by Algeo and Tribovillard (2009). Table 1 presents the UC and PAAS values for the elements of interest in this paper.

### Carbon Content

Forty-two of the 46 samples were analyzed for carbon content at the Agriculture and Food Laboratory, University of Guelph. Excluded samples were the three volcanic-ash beds and one Pardonet Formation sample that had inadequate sample-powder mass for analysis. Following the procedure described in Wang (2018), 1 g of powdered sample was divided into two splits to determine total inorganic carbon (TIC) and total carbon (TC) contents. To measure TIC, sample splits were ashed at 475°C for 3 hours to oxidize organic matter. They were then combusted in an Elementar Vario Macro Cube CN catalytic combustor at 960°C; resulting gases were measured using a thermal-conductivity detector. Total carbon was measured in the same manner,

but the splits were not ashed before analysis. Total organic carbon is calculated as the difference between the TC and TIC contents. Two shale standards (USGS SBC-1 and SGR-1b) and two replicate samples were included for analysis to verify accuracy and precision.

**Table 1.** Normalization standards for enrichment-factor calculations: **PAAS**, Post-Archean Australian Average Shale (PAAS) concentrations from Tribovillard et al. (2006); **UCC**, upper continental crust concentrations from McLennan (2001).

Parameter	UCC	PAAS
<i>Major elements (wt.%):</i>		
CaO	4.2	-
P <sub>2</sub> O <sub>5</sub>	0.3	-
TiO <sub>2</sub>	0.7	-
Al <sub>2</sub> O <sub>3</sub>	15.2	15.9
TiO <sub>2</sub> /Al <sub>2</sub> O <sub>3</sub> *	0.045	-
<i>Trace metals:</i>		
Mo (ppm)	1.5	1
U (ppm)	2.8	0.91
Re (ppb)	0.4	-

\*wt.%/wt.% ratio

## Results

The majority of the samples analyzed ( $n = 34$ ) are black shales of the Gordondale member ( $n = 18$ ) and the Poker Chip Shale ( $n = 16$ ). Samples from the underlying Pardonet Formation dolomitic siltstones ( $n=3$ ), upper Fernie Formation fissile shales ( $n = 2$ ), and volcanic ash beds ( $n = 3$ ), turbidites ( $n = 2$ ) and siltstones ( $n = 2$ ) within the Gordondale member and Poker Chip Shale were also analyzed. This paper focuses on the black shales of the Gordondale member and Poker Chip Shale; interpretations for other samples will be integrated with future work and will enable identification of geochemical changes associated with stratigraphic boundaries (Pardonet, upper Fernie), volcanic inputs (volcanic ash beds) and local detrital composition (turbidites and siltstones).

### XRD Mineralogy and Major Elements

The first set of samples was analyzed for XRD mineralogy. The analysis revealed an abrupt change approximately midway in the core (~1575 m) from calcareous (high calcite content) and variably phosphatic (variable apatite content) below the contact to virtually calcite and apatite free and siliceous (quartz rich) above the contact. Based on the con-

**Table 2.** Average XRD calcite, apatite and quartz mineralogy; concentrations of major elements CaO, P<sub>2</sub>O<sub>5</sub>, TiO<sub>2</sub> and Al<sub>2</sub>O<sub>3</sub>, and TiO<sub>2</sub>/Al<sub>2</sub>O<sub>3</sub> ratio; trace-metal concentrations and enrichment factors (EF); and total inorganic (TIC) and organic (TOC) carbon content in the black shales of the Gordondale member and Poker Chip Shale.

Parameter	Poker Chip Shale	Gordondale Member	All black shale samples
<i>XRD mineralogy (wt.%):</i>			
Quartz	49.1 ± 9.8	35.5 ± 29.8	41.2 ± 24.3
Calcite	0.2 ± 0.4	44.1 ± 32.5	25.8 ± 32.9
Apatite	0 ± 0	7.2 ± 11.7	4.2 ± 9.6
<i>Major-element concentrations (wt.%):</i>			
CaO	1.4 ± 0.7	20.7 ± 9.5	11.6 ± 11.9
P <sub>2</sub> O <sub>5</sub>	0.2 ± 0.1	2.0 ± 2.5	1.2 ± 2.0
TiO <sub>2</sub>	0.5 ± 0.1	0.2 ± 0.1	0.4 ± 0.2
Al <sub>2</sub> O <sub>3</sub>	12.4 ± 2.0	5.1 ± 2.3	8.5 ± 4.3
TiO <sub>2</sub> /Al <sub>2</sub> O <sub>3</sub> *	0.038 ± 0.004	0.048 ± 0.008	0.043 ± 0.008
<i>Trace-metal concentrations:</i>			
Mo (ppm)	14.6 ± 11.0	120.4 ± 95.7	70.6 ± 87.5
U (ppm)	4.4 ± 2.2	14.4 ± 7.9	9.7 ± 7.7
Re (ppb)	122.5 ± 85.1	220.5 ± 92.9	174.4 ± 101.0
<i>Trace-metal enrichment factors:</i>			
Mo <sub>EF</sub> (UC)	11.9 ± 9.5	333 ± 355	182 ± 302
U <sub>EF</sub> (UC)	2.0 ± 1.0	20.1 ± 16.0	11.6 ± 14.7
Mo <sub>EF</sub> (PAAS)	18.6 ± 14.9	521 ± 556	285 ± 474
U <sub>EF</sub> (PAAS)	6.4 ± 3.1	64.5 ± 51.3	37.2 ± 47.2
Mo <sub>EF</sub> /U <sub>EF</sub> (PAAS)	3.2 ± 1.8	7.5 ± 4.7	5.5 ± 4.2
Re <sub>EF</sub>	346 ± 250	1811 ± 1122	1122 ± 1108
<i>Carbon content (wt.%):</i>			
TOC	4.2 ± 0.8	6.2 ± 2.0	5.3 ± 1.8
TIC	0.5 ± 0.3	4.9 ± 2.2	2.8 ± 2.7

\*wt.%/wt.% ratio

tact ages given by Paně et al. (2018) and the position of the Gordondale member interval in the core, from approximately 1595.8 to 1575.0 m (thickness of 20.8 m), Gordondale member sedimentation occurred at a minimum average rate of 2.1 m/m.y.

The second set of samples was analyzed for Ca, P, Fe, Ti, Al, Mg, Na, K and Mn. Presented in this paper are the concentrations of the major elements CaO, P<sub>2</sub>O<sub>5</sub>, TiO<sub>2</sub> and Al<sub>2</sub>O<sub>3</sub>, as well as the TiO<sub>2</sub>/Al<sub>2</sub>O<sub>3</sub> ratio (Table 2). The observation that all black shales have MnO concentrations well below the crustal average concentration (0.08 wt. %; McLennan, 2001) implies that the samples were exposed to an anoxic water column and/or pore waters during and/or following deposition (Tribovillard et al., 2006). Profiles of the XRD mineralogy and major-element distributions are illustrated in Figure 3. Calcium and P vary strongly through the black shales in this core, where mean CaO content is 11.6 ± 11.9 wt. % (1σ) and mean P<sub>2</sub>O<sub>5</sub> content is 1.2 ± 2.0 wt. % (1σ). Mean CaO and P<sub>2</sub>O<sub>5</sub> contents in the Gordondale member are 20.7 ± 9.5 wt. % (1σ) and 2.0 ± 2.5 wt. % (1σ), respectively. Variability in P<sub>2</sub>O<sub>5</sub> content of the Gordondale member is still apparent, with two peaks at 1590.25 m (P<sub>2</sub>O<sub>5</sub> = 9.1 wt. %) and 1582.14 m (P<sub>2</sub>O<sub>5</sub> = 7.0 wt. %) and a minimum at 1584.18 m (P<sub>2</sub>O<sub>5</sub> = 0.05 wt. %). Mean CaO and P<sub>2</sub>O<sub>5</sub> contents in the Poker Chip Shale are 1.4 ± 0.7 wt. % (1σ) and 0.2 ± 0.1 wt. % (1σ), respectively, which are both more than an order of magnitude lower compared to the Gordondale member. Additionally, both Al<sub>2</sub>O<sub>3</sub> and TiO<sub>2</sub> show a steady uphole increase in concentration that corresponds to the decrease in CaO and P<sub>2</sub>O<sub>5</sub> and increase in quartz content.

To evaluate the appropriateness of using Al for EF normalization of redox-sensitive trace-metal contents, the RSD of Al and the trace metals was calculated. The RSD for Al in the black shale sample set is 50%, while trace metals reported in this paper have RSDs ranging from 58% (Re) to 123% (Mo). Additionally, a cross-plot of TiO<sub>2</sub> versus Al<sub>2</sub>O<sub>3</sub> for the black shale samples shows a strong correlation ( $r^2 = 0.91$ ) and a mean of 0.043 ± 0.008 (1σ;  $n = 34$ ) that is near the crustal average of 0.045 (McLennan, 2001). The criteria noted in Van der Weijden (2002) for working with EFs are met for this sample set.

### Redox-Sensitive Trace-Metal Content

The elemental content and enrichment ( $X_{EF}$ ) of Mo, U and Re were examined in detail (Table 2). The  $Mo_{EF}$ ,  $U_{EF}$ , and  $Re_{EF}$  values for the Gordondale member (Figure 4) are high with respect to upper continental crust ( $EF > 1$ ) and typically strongly enriched ( $EF > 10$ ), with mean  $Mo_{EF}$  of 332.7 ± 354.9 (1σ; range = 22.4–1002.8),  $U_{EF}$  of 20.1 ± 16.0 (1σ; range = 4.0–57.6) and  $Re_{EF}$  of 1810.7 ± 1122.2 (1σ; range = 501.4–4456.0). The magnitude of trace-metal enrichments in the Gordondale member is highest at the base of the

member and steadily decreases toward the upper contact with the Poker Chip Shale at ~1575 m. Trace-metal enrichments in the Poker Chip Shale are smaller than in the Gordondale member and do not vary as greatly, with mean  $Mo_{EF}$  of 11.9 ± 9.5 (1σ; range = 3.9–35.8),  $U_{EF}$  of 2.0 ± 1.0 (1σ; range = 0.9–4.0) and  $Re_{EF}$  of 346.3 ± 250.1 (1σ; range = 110.9–1032.3). The interval in the Poker Chip Shale containing samples 1562.93 m, 1563.90 m and 1564.28 m shows a slightly increased enrichment ( $Mo_{EF} = 12.8–35.8$ ,  $U_{EF} = 2.7–4.0$ ,  $Re_{EF} = 432.9–1032.3$ ).

### Carbon Content

The TOC and TIC contents were determined for the black shales of the Gordondale member and Poker Chip Shale (Table 2). The TOC contents for all black shale samples ranged from 2.5 to 10.9 wt. %, with a mean of 5.3 ± 1.8 wt. % (1σ;  $n = 34$ ; Figure 4). The TIC content ranged from 0.2 to 8.8 wt. % with a mean of 2.8 ± 2.7 wt. % (1σ; Figure 3) and is strongly and positively correlated with Ca content ( $r^2 = 0.96$ ) throughout the core, indicating that much of the TIC is associated with Ca in carbonate. Mean TOC and TIC contents for the Gordondale member are 6.2 ± 2.0 wt. % (1σ) and 4.9 ± 2.2 wt. % (1σ), respectively. The Poker Chip Shale has mean TOC and TIC contents of 4.2 ± 0.8 wt. % (1σ) and 0.5 ± 0.3 wt. % (1σ), respectively.

### Mo-U and Mo-TOC Covariance

Using a cross-plot of PAAS-normalized  $Mo_{EF}$  versus  $U_{EF}$ , ancient black shales can be compared to sediment data from modern marine environments to infer the basin-restriction regime, local redox conditions and presence/absence of an Fe-Mn particulate shuttle. Figure 5 depicts the  $Mo_{EF}$ - $U_{EF}$  covariation for the Gordondale member and Poker Chip Shale. A strong correlation between  $Mo_{EF}$  and  $U_{EF}$  exists for all samples from both the Gordondale member and Poker Chip Shale ( $r^2 = 0.80$ ;  $n = 34$ ). Individually, Gordondale member samples show moderate correlation ( $r^2 = 0.55$ ;  $n = 18$ ), whereas Poker Chip Shale samples show poor correlation ( $r^2 = 0.10$ ;  $n = 16$ ) between  $Mo_{EF}$  and  $U_{EF}$ . When compared to the modern environments studied by Algeo and Tribovillard (2009), the black shales have a covariation trend similar to that of sediments from the eastern tropical Pacific. The Gordondale member is more enriched in both Mo and U, and the mean  $Mo_{EF}/U_{EF}$  is 7.1 ± 4.5 (1σ), more than two times greater than the weight average of 3.1 for Mo/U in modern Pacific seawater. The Poker Chip Shale is less enriched in Mo and U, and has a lower mean  $Mo_{EF}/U_{EF}$  of 3.8 ± 3.1 (1σ).

Covariation between Mo and TOC (Figure 6) for the Gordondale member yields a moderate slope ( $m = 24$  ppm/wt. %), whereas the Poker Chip Shale defines a shallow slope ( $m = 4.9$  ppm/wt. %). However, neither the Gordondale member nor the Poker Chip Shale shows good correla-

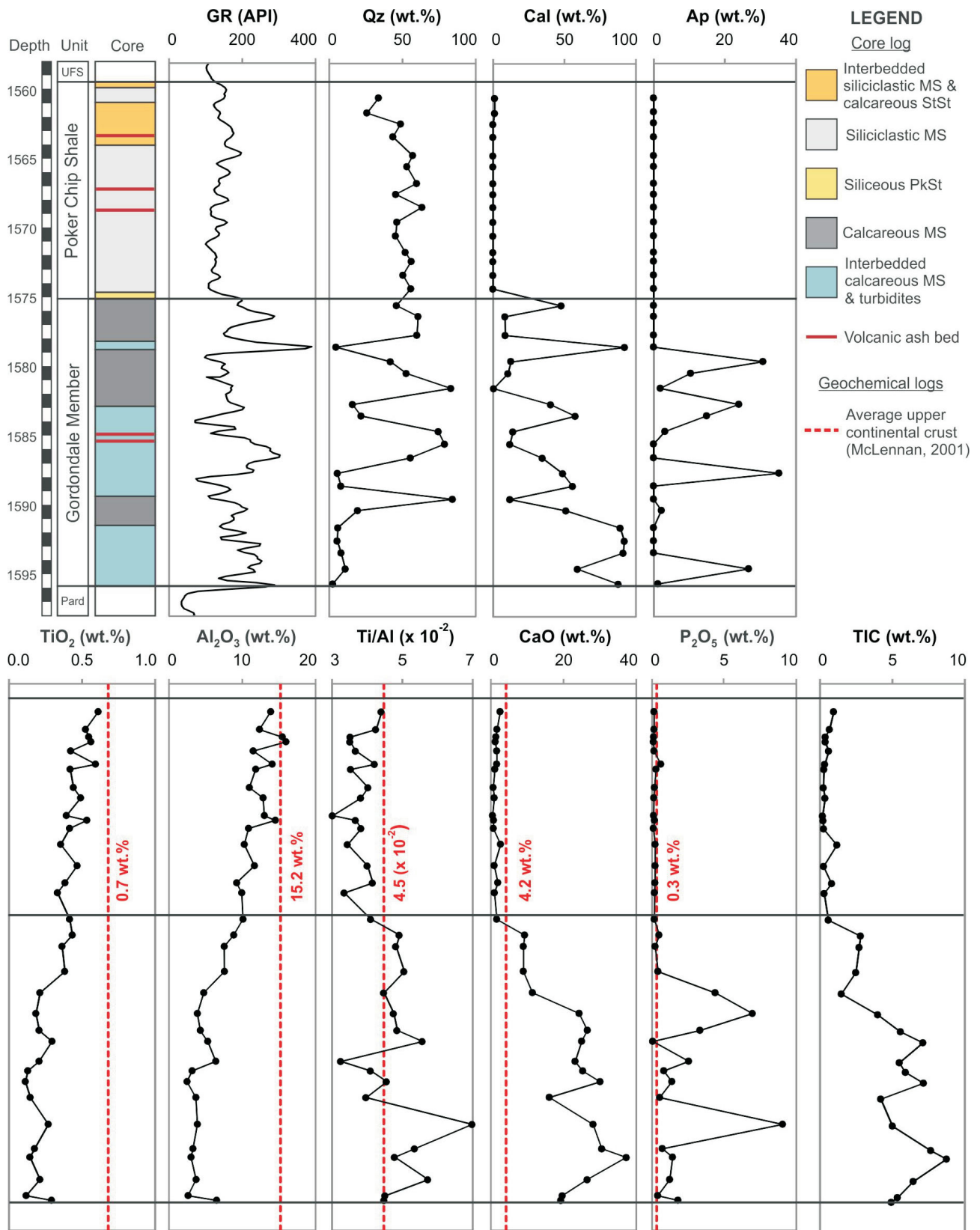


**Figure 3.** Stratigraphic and lithological units; gamma-ray (GR) log; quartz (Qz), calcite (Cal) and apatite (Ap) XRD mineralogy; TiO<sub>2</sub>, Al<sub>2</sub>O<sub>3</sub>, CaO and P<sub>2</sub>O<sub>5</sub> concentrations; Ti/Al oxide ratio; and total inorganic carbon (TIC) in black shale samples of the Gordondale member and Poker Chip Shale in the Progress HZ Altares c-B6-A/94-B-8 core. Average upper continental crust concentrations for the major-element oxides are denoted (red dashed lines; McLennan, 2001). Other abbreviations: MS, mudstone; Pard, Pardonet Formation; PkSt, packstone; StSt, siltstone; UFS, upper Fernie shales.

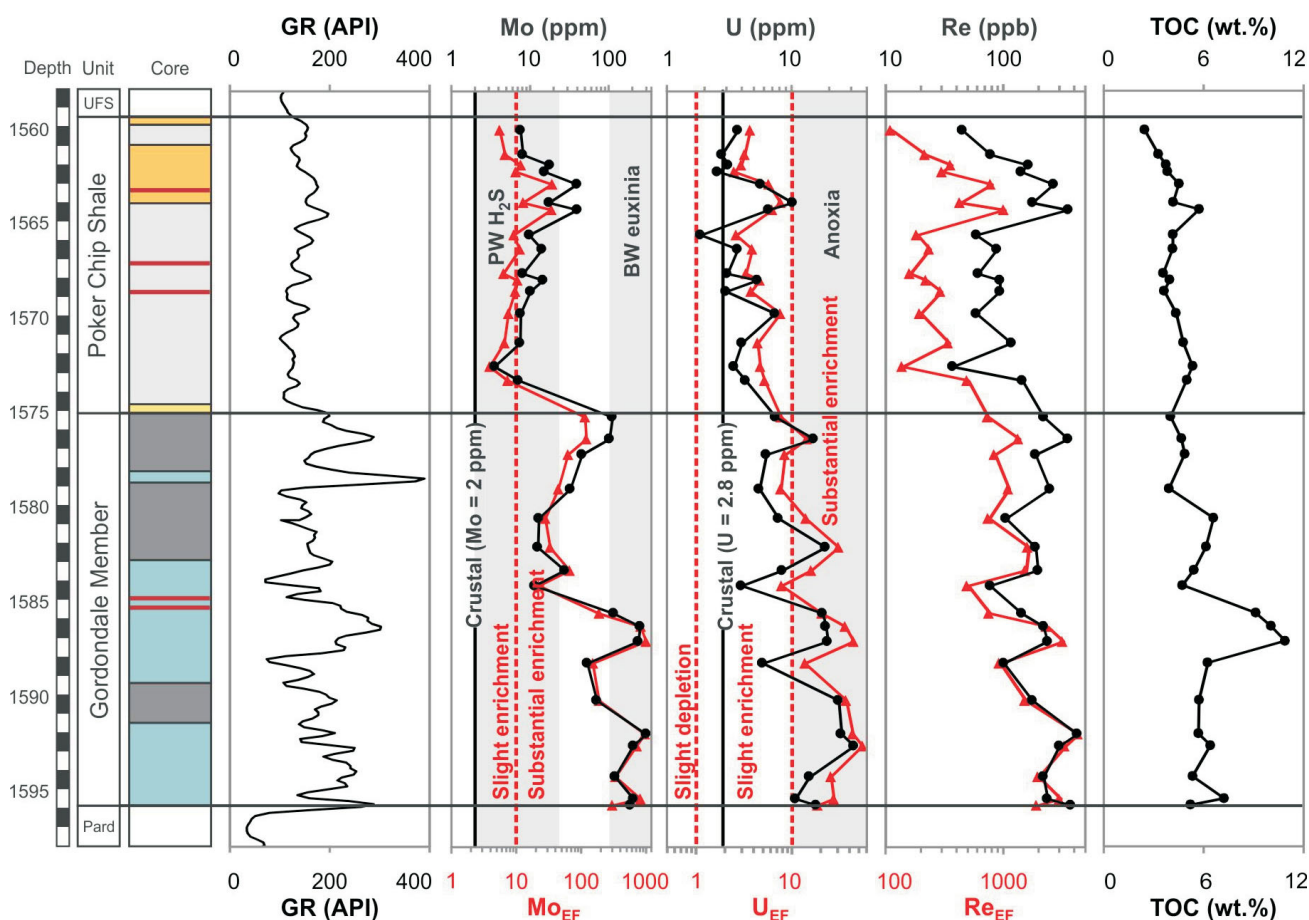


**Figure 4.** Stratigraphic and lithological units; gamma-ray (GR) log; trace-metal concentrations (black) and enrichment factors (EF; red) normalized to upper continental crust of McLennan (2001) for Mo, U and Re; and total organic carbon (TOC) content in the Progress HZ Altares c-B006-A/094-B-08 core. Grey fields represent sediment Mo concentrations where sulphidic porewater (PW H<sub>2</sub>S) and bottom-water (BW) euxinia develop (Scott and Lyons, 2012), and sediment U concentrations for bottom-water anoxia from Partin et al. (2013). White field in Mo track represents a transition zone between PW H<sub>2</sub>S and euxinia. Red dashed lines mark boundaries between slight depletion and slight enrichment (EF = 1), and slight enrichment and substantial enrichment (EF = 10). All Re samples are substantially enriched (Re<sub>EF</sub> > 10) and represent anoxia (Re > 5 ppb; Sheen et al., 2018), so no fields or dividers are presented. See Figure 3 for core-lithology legend. Abbrevia-

tion ( $r^2$  of 0.25 and 0.13, respectively), in contrast to data from modern anoxic basins (Algeo and Lyons, 2006).

### Preliminary Interpretations

#### First-Order Variations in Gordondale–Poker Chip Shale Geochemistry

Geochemical analysis revealed that the Gordondale member black shales are more enriched in Mo, U and Re than shales in the overlying Poker Chip Shale. Hence, the Gordondale member was likely deposited in an environment conducive to trace-metal enrichment in sediments, such as lower bottom-water O<sub>2</sub> levels, higher H<sub>2</sub>S levels or higher water-mass trace-metal concentrations compared to the Poker Chip Shale. This first-order trend to lower redox-sensitive metal enrichments upsection in the core corresponds to a decrease in calcite, apatite, TOC, CaO and P<sub>2</sub>O<sub>5</sub> content from the Gordondale member to the Poker Chip Shale. Poker Chip Shale Mo concentrations fall into the lower (<25 ppm) and intermediate (25–100 ppm) bins of

Scott and Lyons (2012), indicating that any of several factors may have influenced the degree of Mo enrichment. The contrast between the units implies major changes in the depositional environment, which may include one or more of the following conditions: enhanced detrital input or sedimentation, local bottom-water redox variation, basin restriction or global ocean-redox conditions.

The first possible explanation for the reduced enrichments in the Poker Chip Shale is the apparent increase in the input of siliciclastic material. This is observed through 1) a change from calcite to quartz enrichment in XRD profiles, 2) an increase in Al<sub>2</sub>O<sub>3</sub> and TiO<sub>2</sub> contents upsection, and hence 3) a potentially enhanced sedimentation rate for siliciclastic material. All three may have had a dilution effect on the concentration of trace metals and TOC, resulting in muted enrichments.

A strong correlation between the Mo<sub>EF</sub>-U<sub>EF</sub> covariation trend for the Gordondale member and Poker Chip Shale (Figure 5) indicates that there may have been a stable and

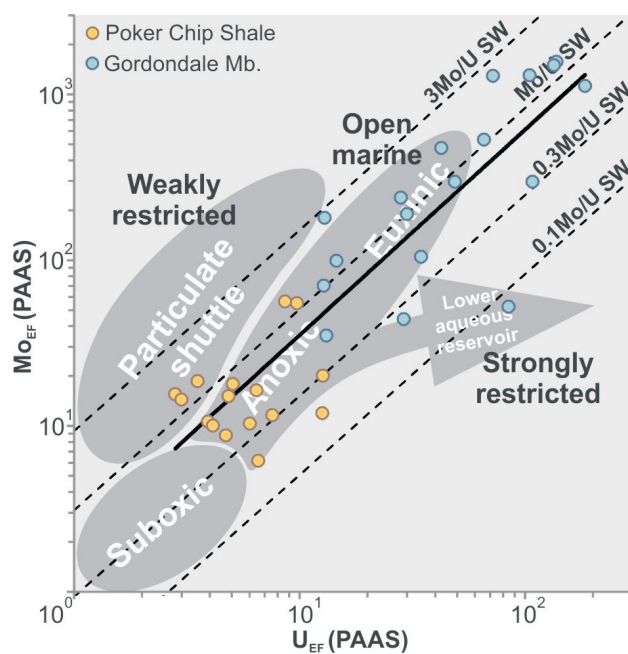


**Figure 5.** Covariation diagram for  $Mo_{EF}$  and  $U_{EF}$  of the Gordondale member (blue) and Poker Chip Shale (orange). Enrichment factors (EF) are normalized to Post-Archean Australian Average Shale (PAAS; Tribouvillard et al., 2006). There is moderate correlation between Gordondale member samples ( $r^2 = 0.55$ ) and poor correlation between Poker Chip Shale samples ( $r^2 = 0.10$ ) independently (trends not depicted), but a strong correlation ( $r^2 = 0.80$ ) exists between all black shale samples from both members (solid black line). Modern marine redox trends for weakly restricted (e.g., Cariaco Basin), open-marine (e.g., eastern tropical Pacific) and strongly restricted (e.g., Black Sea) basins are approximated from Algeo and Tribouvillard (2009). Modern Pacific seawater (SW) Mo/U (weighted average = 3.1) is depicted at factors of 0.1, 0.3, 1 and 3 (black dashed lines).

continuous redox transition from anoxic and/or euxinic (Gordondale) to suboxic (Poker Chip Shale), similar to the modern eastern tropical-Pacific margin (Algeo and Tribouvillard, 2009). The mechanisms for the transition might include 1) a decrease in primary productivity, or 2) a transition from basinal to marginal deposition.

It is also possible that the aqueous chemistry began to evolve due to intense drawdown of trace metals into the sediments without replenishment from exchange between deep water and the open ocean, such as occurs in a strongly restricted basin like the Black Sea. A Mo-TOC covariation diagram (Figure 6) helps to illustrate the extent of restriction in the basin in which sediments were deposited. Whereas both the Gordondale member and the Poker Chip Shale have poor correlations between Mo and TOC contents, a shallowing between their covariation slopes is observed ( $m_{Gordondale} = 24 \text{ ppm/wt. \%}$ ;  $m_{Poker\ Chip} = 4.9 \text{ ppm/wt. \%}$ ), suggesting that the basin may have transitioned from being weakly restricted, similar to the modern Cariaco Basin, to strongly restricted, like the modern Black Sea. If correct, this change toward strong restriction would pro-

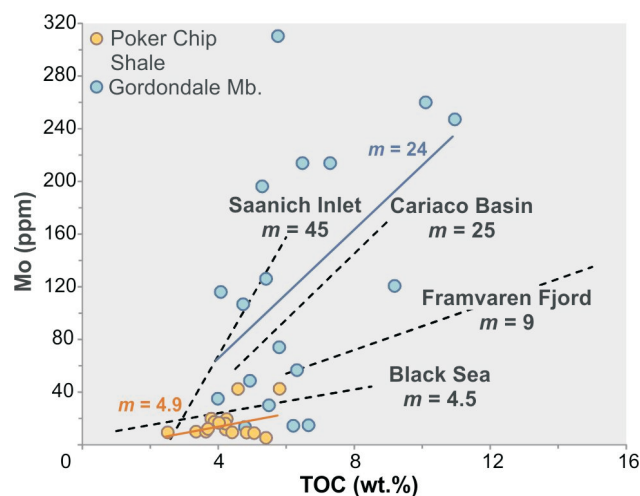


**Figure 6.** Covariation diagram for Mo and TOC of the Gordondale member (blue) and Poker Chip Shale (orange), superimposed on trends for modern anoxic basins (Algeo and Lyons, 2006). The Gordondale trend slope of 24 ppm/wt. % is similar to that of the weakly restricted Cariaco Basin, whereas the Poker Chip Shale slope of 4.9 ppm/wt. % is similar to that of the Black Sea. Correlations are poor (Gordondale  $r^2 = 0.25$ , Poker Chip Shale  $r^2 = 0.13$ ), so the trends depicted are not definitive.

mote intense drawdown of trace metals into anoxic seafloor sediments while depleting the water column. This process tends to lead to lower sediment  $Mo_{EF}/U_{EF}$  ratios. A decreased  $Mo_{EF}/U_{EF}$  ratio is evident between the Gordondale and Poker Chip Shale members, with the latter having a ratio less than half that of the former. If further evidence of increased basin restriction is identified, this may indicate a western landmass during the Early Jurassic through initiation of a foreland basin (Riediger and Coniglio, 1992; Paná et al., 2017) that inhibited communication between the Gordondale and/or Poker Chip Shale basins and the open ocean. However, the poor Mo-TOC correlation does not provide a robust justification for these interpretations. The low  $r^2$  values may be a result of dynamic changes in the depositional environment or diagenetic processes (e.g., sedimentation rates, water-column pH, water-column Mo concentrations, bottom-water redox conditions and/or over-maturation).

Another factor to consider is the Toarcian Oceanic Anoxic Event (T-OAE), which may have resulted in a global areal increase in anoxic bottomwater conditions (Them et al., 2018). The T-OAE is readily identified in core and outcrop sections globally based on a distinct negative  $\delta^{13}C_{org}$  excursion, but there are currently no C-isotope data available for this core. This event may coincide with Poker Chip Shale deposition in NEBC, given that the C-isotope expression of the T-OAE was found in the lower Poker Chip Shale in Alberta (Them et al., 2017a, b, 2018). During the T-OAE, a global drawdown of trace metals into an expansive area of anoxic and euxinic sediments may have occurred. Hence, the lower redox-sensitive metal enrichments observed in

the Poker Chip Shale may not reflect strong basin restriction, but rather a lower global oceanic reservoir of these metals, if the T-OAE occurred during deposition of the Poker Chip Shale (e.g., Owens et al., 2016).

### Implications for Source-Rock Potential

From the geochemical analysis and preliminary interpretations completed thus far, the following can be said regarding possible implications for the Gordondale and Poker Chip Shale source-rock potential:

- The TOC contents in the black shales of both the Gordondale member and the Poker Chip Shale support enhanced source potential. The Gordondale member is the more attractive unit, based on higher mean TOC of 6.2 wt. % (maximum of 10.9 wt. %), compared to the Poker Chip Shale (mean TOC of 4.2 wt. %).
- Increased sedimentation rates may have occurred in the Poker Chip Shale, thus diluting organic-matter concentrations.
- Open or weakly restricted basin conditions during deposition of the Gordondale member suggest that anoxia/euxinia was driven by increased primary productivity, implying an enhanced nutrient supply (consistent with higher TOC and P contents);
- Global expansion of anoxia and/or euxinia during the T-OAE may have resulted in widespread conditions for organic-matter preservation, potentially including the Poker Chip Shale.

Some limitations in this study area are the indication of thermal overmaturity (Creaney and Allen, 1990) and extensive structural deformation due to its proximity to the Rocky Mountain deformation front. Additionally, type II-S kerogens in the Gordondale member that have resulted from euxinic conditions could pose a hazard during drilling operations due to the presence and release of sour gas (H<sub>2</sub>S).

### Conclusions

A preliminary examination of XRD mineralogy and major element (CaO, P<sub>2</sub>O<sub>5</sub>, TiO<sub>2</sub>, Al<sub>2</sub>O<sub>3</sub>), trace-metal (Mo, U, Re) and carbon (TOC, TIC) data was presented for one of the very few continuous, full-diameter, Early Jurassic cores in NEBC. The core covered the Gordondale member and Poker Chip Shale of the Fernie Formation. The calcite/CaO and apatite/P<sub>2</sub>O<sub>5</sub> concentrations showed a significant decline from the Gordondale member to the Poker Chip Shale, indicating substantial changes to the depositional environment, specifically increased siliciclastic and decreased carbonate sedimentation. Redox-sensitive trace-metal concentrations suggest the Gordondale member experienced periodic water-column euxinia based on peaks of Mo (>100 ppm) and anoxia (U >10 ppm and Re >>5 ppb). The Poker Chip Shale did not exhibit such high metal con-

centrations. Four scenarios are proposed to explain the lower metal enrichments in the Poker Chip Shale:

- Sedimentation rates increased with the input of siliciclastic material, which had a dilution effect on the trace-metal and TOC concentrations in the Poker Chip Shale.
- A transition of local bottom-water redox state from intensely suboxic-anoxic and periodically euxinic (Gordondale member) to dominantly suboxic (Poker Chip Shale) conditions would be accompanied by less efficient burial of redox-sensitive trace metals in sediments.
- Strong basin restriction with slow rates of deep-water renewal depleted the stock of aqueous trace-metal species following intense drawdown into euxinic sediments.
- Global drawdown of the trace-metal inventory from seawater to sediments occurred during the T-OAE, when the area of bottom-water euxinia was expansive.

Paleoenvironmental factors such as primary productivity and bottom-water redox conditions are linked to current source-rock potential of the Gordondale and Poker Chip Shale members. Gordondale member TOC indicates excellent source-rock potential (up to 10.90 wt. %), while the Poker Chip Shale has moderate source potential with TOC up to 5.74 wt. %, mirroring the decreasing trace-metal content. Environmental changes likely had an effect on source potential and may include an increased sedimentation rate diluting organic matter/TOC, a shift in bottom-water redox conditions from euxinic/anoxic to suboxic decreasing organic-matter preservation, or an extinction event due to ocean anoxia (T-OAE) leading to the widespread decline in primary productivity and organic-matter deposition. These factors occur at local, regional and global scales, respectively. Deduction of paleoenvironmental conditions from detailed organic and inorganic geochemistry will aid in hydrocarbon exploration efforts, having implications for the areal extent, quantity and quality of the source potential in the Early Jurassic of NEBC.

### Future Work

This paper focused on preliminary interpretation of geochemical data for black shales of the Gordondale member and Poker Chip Shale intersected in a core within the Altares field of NEBC (Progress HZ Altares c-B6-A/94-B-8 well). Analyses of these samples included more minor and trace metals (including rare-earth elements) than are discussed in this paper; these will be examined in the future to provide a full picture of the paleoredox, paleoproductivity and paleohydrography of the stratigraphy covered in the core. Sedimentary Fe-speciation data (Raiswell et al., 2018) may also be acquired to provide independent constraints on local bottom-water redox conditions during deposition. Additionally, organic carbon-isotope data will be collected at the University of Waterloo's Environmental

Isotope Laboratory to search for the presence of the Toarcian Oceanic Anoxic Event (T-OAE), which is marked by a strong negative organic C-isotope excursion in sedimentary rocks at other localities worldwide, including the Poker Chip Shale in Alberta (e.g., Them et al., 2017a, b, 2018). This will not only provide information in the context of the T-OAE but will also further constrain the age of the core in NEBC if the excursion is present. Once C-isotope analyses are completed, intervals of interest will be chosen from which to complete higher resolution sampling and geochemical analysis in early 2019.

## Acknowledgments

The authors acknowledge the financial support of Geoscience BC, Petronas Canada, Sasol Canada and Mitacs (through the Mitacs Accelerate program). The Metal Isotope Geochemistry Laboratory at Waterloo was funded, in part, by the Canada Foundation for Innovation (John R. Evans Leaders Fund) and the Ontario Research Fund (Research Infrastructure Program). The authors thank reviewers T.R. Them, II and S. Georgiev for their helpful and constructive feedback on the manuscript.

## References

- Algeo, T.J. and Lyons, T.W. (2006): Mo–total organic carbon covariation in modern anoxic marine environments: implications for analysis of paleoredox and paleohydrographic conditions; *Paleoceanography*, v. 21, PA1016, 23 p.
- Algeo, T.J. and Tribouillard, N. (2009): Environmental analysis of paleoceanographic systems based on molybdenum-uranium covariation; *Chemical Geology*, v. 268, p. 211–225.
- Anbar, A.D., Creaser, R.A., Papanastassiou, D.A. and Wasserburg, G.J. (1992): Rhenium in seawater: confirmation of generally conservative behaviour; *Geochimica et Cosmochimica Acta*, v. 56, p. 4099–4103.
- Asgar-Deen, M., Hall, R., Craig, J. and Riediger, C.L. (2003): New biostratigraphic data from the Lower Jurassic Fernie Formation in the subsurface of west-central Alberta and their stratigraphic implications; *Canadian Journal of Earth Sciences*, v. 40, p. 45–63.
- Asgar-Deen, M., Riediger, C. and Hall, R. (2004): The Gordondale Member: designation of a new member in the Fernie Formation to replace the informal “Nordegg Member” nomenclature of the subsurface of west-central Alberta; *Bulletin of Canadian Petroleum Geology*, v. 52, no. 3, p. 201–214.
- BC Oil and Gas Commission (2018): Well lookup and reports; BC Oil and Gas Commission, web application, URL <<http://www.bcogc.ca/online-services>> [November 2018].
- Creaney, S. and Allan, J. (1990): Hydrocarbon generation and migration in the Western Canada Sedimentary Basin; in *Classic Petroleum Provinces*, J. Brooks (ed.), Geological Society of London, Special Publications, v. 50, p. 189–202.
- Crusius, J., Calvert, S., Pedersen, T. and Sage, D. (1996): Rhenium and molybdenum enrichments in sediments as indicators of oxic, suboxic and sulfidic conditions of deposition; *Earth and Planetary Science Letters*, v. 145, p. 65–78.
- Dahl, T.W., Chappaz, A., Fitts, J.P. and Lyons, T.W. (2013): Molybdenum reduction in a sulfidic lake: evidence from X-ray absorption fine-structure spectroscopy and implications for the Mo paleoproxy; *Geochimica et Cosmochimica Acta*, v. 103, p. 213–231.
- Hardisty, D.S., Lyons, T.W., Riedinger, N., Isson, T.T., Owens, J.D., Aller, R.C., Rye, D.M., Planavsky, N.J., Reinhard, C.T., Gill, B.C., Masterson, A.L., Asael, D. and Johnston, D.T. (2018): An evaluation of sedimentary molybdenum and iron as proxies for pore fluid paleoredox conditions; *American Journal of Science*, v. 318, p. 527–556.
- Ibrahimbas, A. and Riediger, C. (2004): Hydrocarbon source rock potential as determined by Rock-Eval 6/TOC pyrolysis, northeast British Columbia and northwest Alberta; in *Summary of Activities 2004*, British Columbia Ministry of Energy, Mines and Petroleum Resources, Resource Development and Geoscience Branch, p. 7–18, URL <[https://www2.gov.bc.ca/assets/gov/farming-natural-resources-and-industry/natural-gas-oil/petroleum-geoscience/geoscience-reports/2004/ibrahimbass\\_riediger.pdf](https://www2.gov.bc.ca/assets/gov/farming-natural-resources-and-industry/natural-gas-oil/petroleum-geoscience/geoscience-reports/2004/ibrahimbass_riediger.pdf)> [November 2018].
- Kondla, D., Sanei, H., Clarkson, C.R. and Goodarzi, F. (2017): High resolution characterization of a core from the Lower Jurassic Gordondale Member, Western Canada Sedimentary Basin; *Marine and Petroleum Geology*, v. 83, p. 50–59.
- McLennan, S.M. (2001): Relationships between the trace element composition of sedimentary rocks and upper continental crust; *Geochemistry, Geophysics, Geosystems*, v. 2, 24 p.
- McManus, J., Berelson, W.M., Severmann, S., Poulson, R.L., Hammond, D.E., Klinkhammer, G.P. and Holm, C. (2006): Molybdenum and uranium geochemistry in continental margin sediments: paleoproxy potential; *Geochimica et Cosmochimica Acta*, v. 70, p. 4643–4662.
- Owens, J.D., Reinhard, C.T., Rohrssen, M., Love, G.D. and Lyons, T.W. (2016): Empirical links between trace metal cycling and marine microbial ecology during a large perturbation to Earth’s carbon cycle; *Earth and Planetary Science Letters*, v. 449, p. 407–417.
- Pană, D.I., Creaser, R.A., Toma, J., Playter, T.L., Corlett, H.J., Hauck, T.E., Peterson, J.T., Grobe, M. and Poulton, T. (2018): Geochronology in support of the Alberta Table of Formations: rhenium-osmium isotope dating of selected Devonian and Jurassic core samples from central and northern Alberta; Alberta Energy Regulator, AER/AGS Open File Report 2018-06, 25 p., URL <[https://ags.aer.ca/document/OFR/OFR\\_2018\\_06.pdf](https://ags.aer.ca/document/OFR/OFR_2018_06.pdf)> [November 2018].
- Pană, D.I., Poulton, T.P. and DuFrane, A. (2017): U-Pb detrital zircon geochronology of the Jurassic through Lower Cretaceous strata of the Rocky Mountains, southwestern Alberta; Alberta Energy Regulator, AER/AGS Open File Report 2017-01, 6 p. URL <[https://ags.aer.ca/document/OFR/OFR\\_2017\\_01.pdf](https://ags.aer.ca/document/OFR/OFR_2017_01.pdf)> [November 2018].
- Partin, C.A., Bekker, A., Planavsky, N.J., Scott, C.T., Gill, B.C., Li, C., Podkovyrov, V., Maslov, A., Konhauser, K.O., Lalonde, S.V., Love, G.D., Poulton, S.W. and Lyons, T.W. (2013): Large-scale fluctuations in Precambrian atmospheric and oceanic oxygen levels from the record of U in shales; *Earth and Planetary Science Letters*, v. 369–370, p. 284–293.
- Poulton, T.P., Christopher, J.E., Hayes, B.J.R., Losert, J., Tittermore, J. and Gilchrist, R.D. (1994): Jurassic and lowermost Cretaceous strata of the Western Canada Sedimentary Basin; Chapter 18 in *Geological Atlas of the Western Canada Sedimentary Basin*, G. Mossop and I. Shetsen (ed.), Canadian Society of Petroleum Geologists, Calgary, Alberta

- and Alberta Research Council, Edmonton, Alberta, p. 297–316.
- Raiswell, R., Hardisty, D.S., Lyons, T.W., Canfield, D.E., Owens, J.D., Planavsky, N.J., Poulton, S.W. and Reinhard, C.T. (2018): The iron paleoredox proxies: a guide to the pitfalls, problems, and proper practice; *American Journal of Science*, v. 318, p. 491–526.
- Riediger, C.L. (2002): Hydrocarbon source rock potential and comments on correlation of the Lower Jurassic Poker Chip Shale, west-central Alberta; *Bulletin of Canadian Petroleum Geology*, v. 50, no. 2, p. 263–276.
- Riediger, C.L. and Bloch, J.D. (1995): Depositional and diagenetic controls on source rock characteristics of the Lower Jurassic ‘Nordegg Member’, Western Canada; *Journal of Sedimentary Research*, v. A65, no. 1, p. 112–126.
- Riediger, C.L. and Coniglio, M. (1992): Early diagenetic calcites and associated bitumens in the ‘Nordegg Member’: implications for Jurassic paleogeography of the Western Canada Sedimentary Basin; *Bulletin of Canadian Petroleum Geology*, v. 40, no. 4, p. 381–394.
- Riediger, C.L., Fowler, M.G. and Brooks, P.W. (1991): The Lower Jurassic ‘Nordegg Member’, Western Canada Sedimentary Basin; in *Organic Geochemistry: Advances and Applications in the Natural Environment*, D.A.C. Manning (ed.), Manchester University Press, Manchester, United Kingdom, p. 92–94.
- Riediger, C.L., Fowler, M.G., Snowdon, L.R., Goodarzi, F. and Brooks, P.W. (1990): Source rock analysis of the Lower Jurassic ‘Nordegg Member’ and oil–source rock correlations in northwestern Alberta and northeastern British Columbia; *Bulletin of Canadian Petroleum Geology*, v. 38A, no. 1, p. 236–249.
- Ross, D.J.K. and Bustin, R.M. (2006): Sediment geochemistry of the Lower Jurassic Gordondale Member, northeastern British Columbia; *Bulletin of Canadian Petroleum Geology*, v. 54, no. 4, p. 337–365.
- Ross, D.J.K. and Bustin, R.M. (2007): Shale gas potential of the Lower Jurassic Gordondale Member, northeastern British Columbia; *Bulletin of Canadian Petroleum Geology*, v. 55, no. 1, p. 51–75.
- Scholz, F., Siebert, C., Dale, A.W. and Frank, M. (2017): Intense molybdenum accumulation in sediments underneath a nitrogenous water column and implications for the reconstruction of paleo-redox conditions based on molybdenum isotopes; *Geochimica et Cosmochimica Acta*, v. 213, p. 400–417.
- Scott, C. and Lyons, T.W. (2012): Contrasting molybdenum cycling and isotopic properties in euxinic versus non-euxinic sediments and sedimentary rocks: refining the paleoproxies; *Chemical Geology*, v. 324–325, p. 19–27.
- Sheen, A.I., Kendall, B., Reinhard, C.T., Creaser, R.A., Lyons, T.W., Bekker, A., Poulton, S.W. and Anbar, A.D. (2018): A model for the oceanic mass balance of rhenium and implications for the extent of Proterozoic ocean anoxia; *Geochimica et Cosmochimica Acta*, v. 227, p. 75–95.
- Spivak, J. (1949): Nordegg Member (of Fernie Formation) Jurassic, Alberta, Canada; *American Petroleum Geologists Bulletin*, v. 38, no. 4, p. 535.
- Stefani, V. (2016): X-ray diffraction report on the c-B006-A/094-B-08 for Progress Energy Ltd.; Argile Analytica, Calgary, Alberta, unpublished report, 111 p.
- Stylo, M., Neubert, N., Wang, Y., Monga, N., Romaniello, S.J., Weyer, S. and Bernier-Latmani, R. (2015): Uranium isotopes fingerprint biotic reduction; *Proceedings of the National Academy of Sciences of the United States of America*, v. 112, p. 5619–5624.
- Them T.R., II, Gill, B.C., Caruthers, A.H., Gröcke, D.R., Tulsy, E.T., Martindale, R.C., Poulton, T.P. and Smith, P.L. (2017a): High-resolution carbon isotope records of the Toarcian Oceanic Anoxic Event (Early Jurassic) from North America and implications for the global drivers of the Toarcian carbon cycle; *Earth and Planetary Science Letters*, v. 459, p. 118–126.
- Them T.R., II, Gill, B.C., Selby, D., Gröcke, D.R., Friedman, R.M. and Owens, J.D. (2017b): Evidence for rapid weathering response to climatic warming during the Toarcian Oceanic Anoxic Event; *Nature Scientific Reports*, v. 7, article 5003.
- Them T.R., II, Gill, B.C., Caruthers, A.H., Gerhardt, A.M., Gröcke, D.R., Lyons, T.W., Marroquin, S.G., Trabucho Alexandre, J.P. and Owens, J.D. (2018): Thallium isotopes reveal protracted anoxia during the Toarcian (Early Jurassic) associated with volcanism, carbon burial, and mass extinction; *Proceedings of the National Academy of Sciences of the United States of America*, v. 115, p. 6596–6601.
- Tribouillard, N., Algeo, T.J., Lyons, T. and Riboulleau, A. (2006): Trace metals as paleoredox and paleoproductivity proxies: an update; *Chemical Geology*, v. 232, p. 12–32.
- Van der Weijden, C.H. (2002): Pitfalls of normalization of marine geochemical data using a common divisor; *Marine Geology*, v. 184, p. 167–187.
- Wang, S. (2018): Development of molybdenum isotopes as petroleum tracers: the Phosphoria petroleum system, Bighorn Basin, U.S.A.; M.Sc. thesis, University of Waterloo, Waterloo, Ontario, 84 p., URL <<http://hdl.handle.net/10012/13333>> [November 2018].

# Stratigraphic and Lateral Distribution of Hydrogen Sulphide within the Triassic Montney Formation, Northern Regional Play Area, Northeastern British Columbia and Northwestern Alberta

G.R.L. Chalmers, The University of British Columbia, Vancouver, BC, [gchalmers@eoas.ubc.ca](mailto:gchalmers@eoas.ubc.ca)

R.M. Bustin, The University of British Columbia, Vancouver, BC

A.A. Bustin, The University of British Columbia, Vancouver, BC

---

Chalmers, G.R.L., Bustin, R.M. and Bustin, A.A. (2019): Stratigraphic and lateral distribution of hydrogen sulphide within the Triassic Montney Formation, northern regional play area, northeastern British Columbia and northwestern Alberta; *in* Geoscience BC Summary of Activities 2018: Energy and Water, Geoscience BC, Report 2019-2, p. 43–46.

## Introduction

The Triassic Montney Formation is the most significant gas deposit in British Columbia (BC) and accounts for 59% of the province's total gas-in-place resource estimation (BC Oil and Gas Commission, 2015). The Montney Formation is a tight liquids-rich gas reservoir in northeastern BC with a gas-in-place estimate of 55 642 billion cubic metres (1965 tcf; BC Oil and Gas Commission, 2015). The Montney Formation contains nonhydrocarbon gases such as hydrogen sulphide (H<sub>2</sub>S) and carbon dioxide (CO<sub>2</sub>), which create both an economic and health and safety impact when developing the hydrocarbon play. Hydrogen sulphide in produced gas, even in trace amounts (i.e., ppm), impacts the economics of drilling, production, treatment, and marketing of gas and associated liquids. The occurrence of H<sub>2</sub>S in produced fluids is one of the most important environmental hazards and risks to resource development. The stratigraphic and lateral variation in H<sub>2</sub>S varies across Montney gas play areas in BC and the distribution, in some areas, can be inexplicable and there are multiple reasons why H<sub>2</sub>S is present in some Montney Formation producing wells. Hydrogen sulphide comes from mixed sources, which include it being a product of 1) bacterial sulphate reduction; 2) thermal sulphate reduction; 3) kerogen cracking; and 4) sulphide oxidation and/or decomposition of surfactants used for well completions. Understanding H<sub>2</sub>S distribution is further complicated by the fact that H<sub>2</sub>S can be produced in situ within the Montney reservoir or may have migrated up-dip through more permeable parasequences within the formation or fracture networks.

To reduce the uncertainty of producing H<sub>2</sub>S from the Montney reservoir, the source and processes that generate H<sub>2</sub>S need to be understood, which will require: a) mapping lateral and stratigraphic distributions of H<sub>2</sub>S; b) determining

the sulphur isotopic composition of H<sub>2</sub>S gas as well as the potential sulphur sources (kerogen, pyrite, anhydrite); and c) determining the timing of souring (i.e., did H<sub>2</sub>S initially spike then decrease or gradually increase over time?), which will provide additional information on likely sources of the H<sub>2</sub>S.

## Preliminary Results

This research, initiated in summer 2018, began by mapping the H<sub>2</sub>S distributions within the northern regional Montney play area of BC (Figure 1). Using geoLOGIC systems ltd.'s geoSCOUT version 8.8 GIS software, well search criteria was set to identify Montney producers that have tested or produced sour gas (presence of H<sub>2</sub>S). The Montney Formation is over 200 m thick within the study area and the authors have informally subdivided the formation into the upper, middle and lower Montney Formation (Figure 2). These subdivisions are based on the sequence-stratigraphic-based boundaries of Davies et al. (2018).

## Hydrogen Sulphide Distribution within the Montney Formation

A total of 153 wells have been identified that either tested or produced sour gas within the study area (Figure 3). The H<sub>2</sub>S concentrations vary widely across the study area and range from 24 000 ppm (2.4%) to <10 ppm. The presence of H<sub>2</sub>S also varies stratigraphically with the majority of sour horizontal wells being drilled in the upper and middle Montney Formation (Figures 2, 4). Wells that have no H<sub>2</sub>S present are referred to as sweet gas wells (green symbol, Figure 4). Preliminary data indicate that wells that are drilled within the top 100 m of the formation (upper Montney Formation, upper portion of the middle Montney Formation) have a higher risk of producing sour gas than the wells that are drilled in the lower Montney Formation (i.e., >150 m below the top of the formation). Migration of H<sub>2</sub>S gas may be the reason for this observation but other processes cannot be ruled out until further analyses have been completed to identify the isotopic composition of sulphur and its poten-

---

*This publication is also available, free of charge, as colour digital files in Adobe Acrobat® PDF format from the Geoscience BC website: <http://www.geosciencebc.com/s/SummaryofActivities.asp>.*

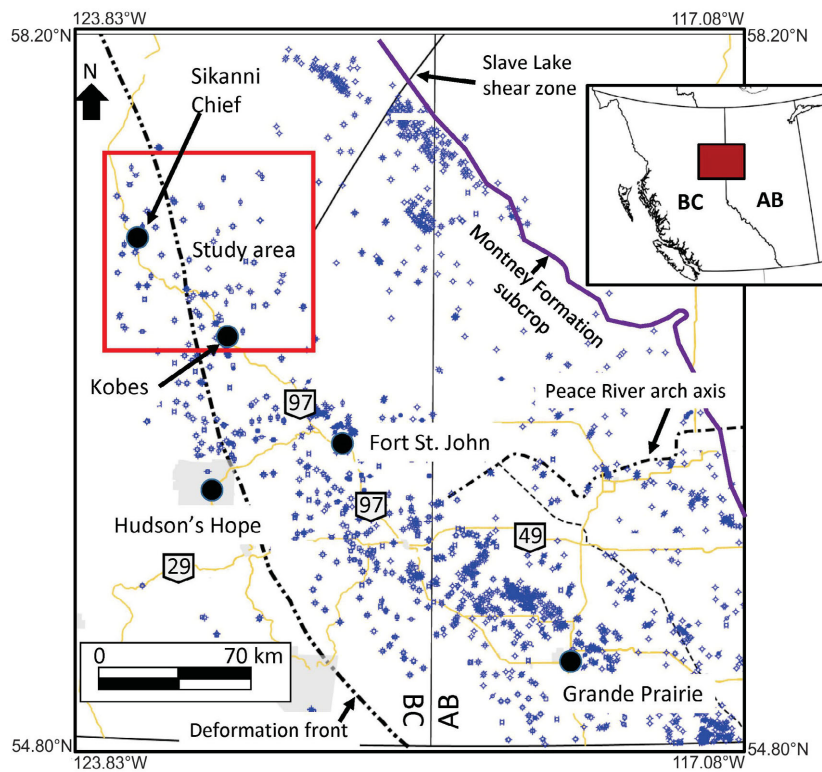


**Figure 1.** Location of the study area (red box) within northeastern British Columbia. Cored Montney Formation wells are shown as blue well symbols. Data sourced from geoLOGIC systems ltd. (2018).

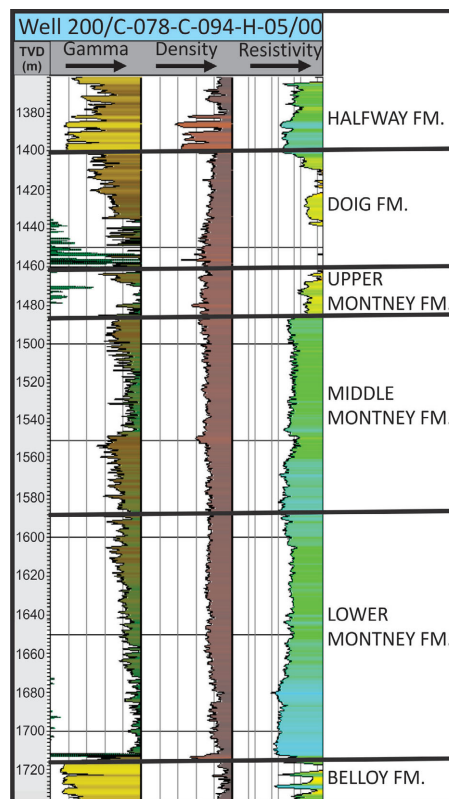


**Figure 2.** Stratigraphy and log response of the Halfway, Doig, Montney and Belloy formations in well 200/C-078-C-094-H-05/00 (geoLOGIC systems ltd., 2018). The Montney Formation is informally subdivided into the upper, middle and lower Montney Formation based on sequence stratigraphic model of Davies et al. (2018). Abbreviation: TVD, total vertical depth.

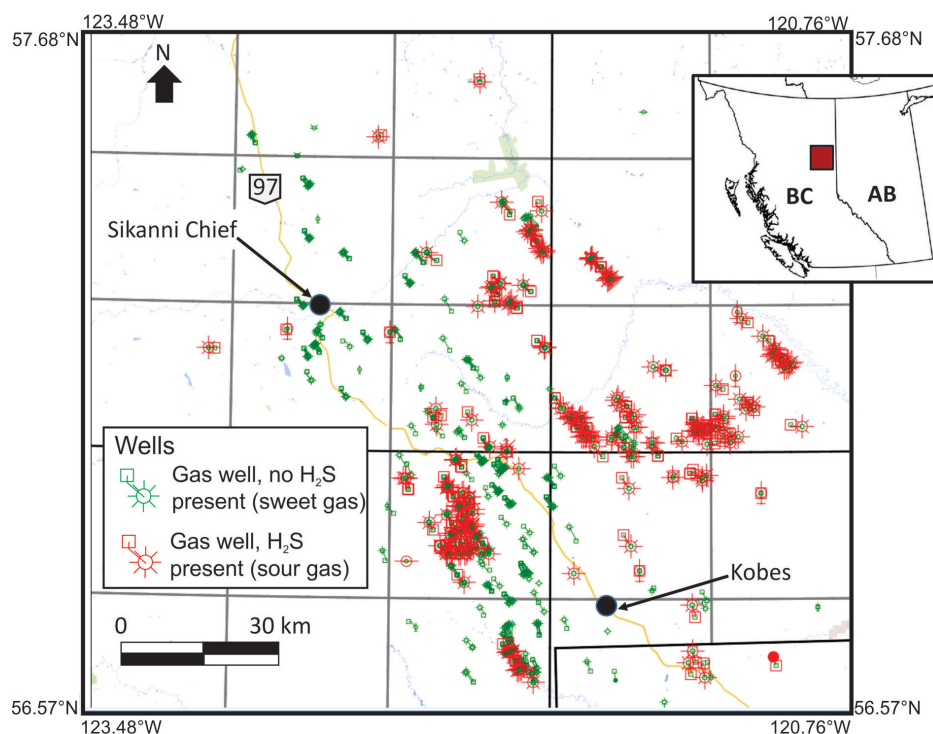


**Figure 3.** Location map of wells (only the red boxed area in Figure 1) that penetrate the Doig and Montney formations that have H<sub>2</sub>S present within the tested or producing hydrocarbons, northeastern British Columbia. Hydrogen sulphide concentrations vary from 24 000 ppm (2.4%) to <10 ppm. Data sourced from geoLOGIC systems ltd. (2018).

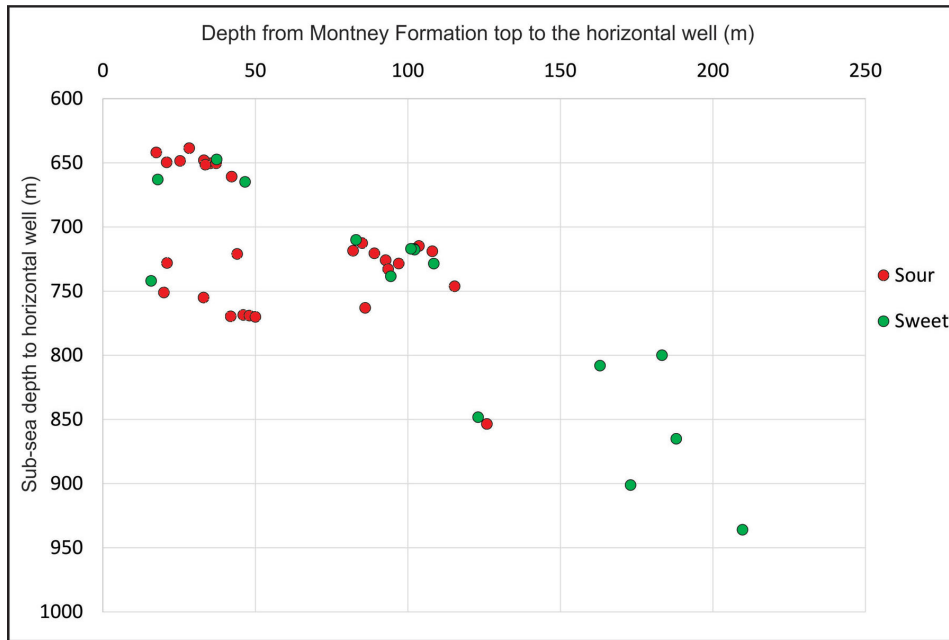


**Figure 4.** Cross-plot of selected sour (red circles) and sweet (green circles) Montney Formation horizontal wells with respect to their subsea total vertical depth (SSTVD) and their location within the Montney Formation (depth from the top of the Montney Formation). There is a higher risk of Montney Formation wells souring if the horizontal well is placed in the upper Montney Formation or the upper portion of the middle Montney Formation compared to wells that are drilled into the lower Montney Formation (see Figure 2 for stratigraphy).

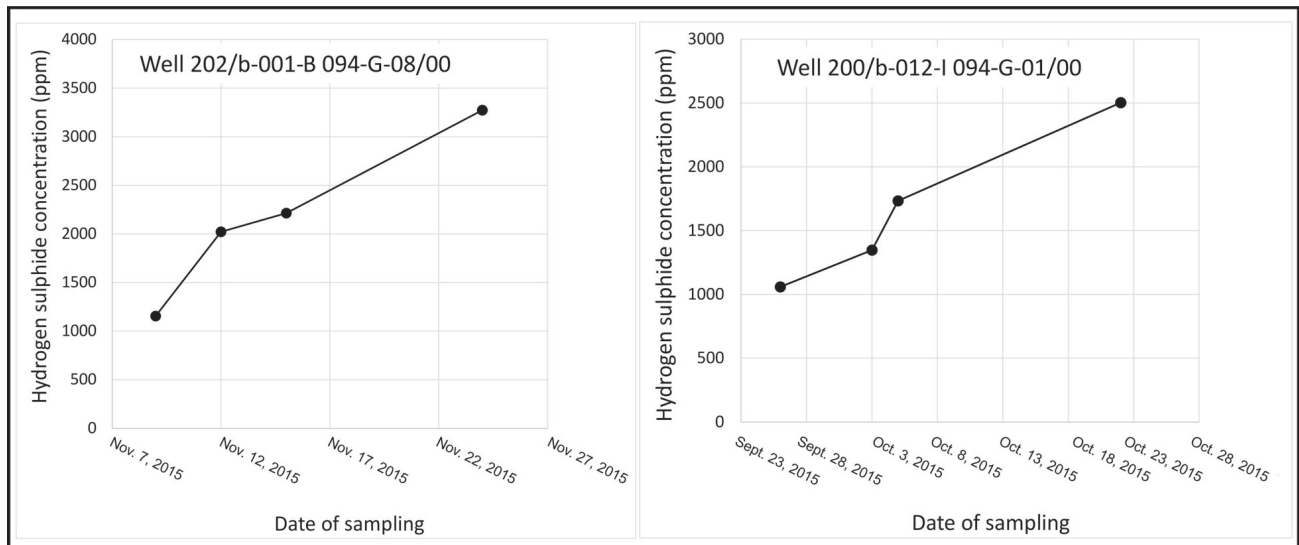


**Figure 5.** Two examples of changing hydrogen sulphide ( $H_2S$ ) concentration through time. Preliminary investigation shows wells (202/B-001-B-094-G-08/00 and 200/B-012-I-094-G-01; geoLOGIC systems Ltd., 2018) with multiple sampling of  $H_2S$  over time have increasing  $H_2S$  concentration over time or show no change in concentration.

tial sources (i.e., kerogen, fracturing fluid, pyrite, anhydrite).

### Time Series Analysis of H<sub>2</sub>S Concentrations

A preliminary investigation into the change in H<sub>2</sub>S concentration over time has shown that for wells that have multiple sample points through time, there is a general trend of increasing H<sub>2</sub>S concentration (Figure 5) or no change in concentration. A more detailed investigation is being performed to understand why the H<sub>2</sub>S concentration changes over time.

### Future Work

Inline samples from flowing Montney Formation wells are being analyzed to determine the isotopic composition of the sulphur from the H<sub>2</sub>S gas. Rock samples will also be obtained from these wells to determine the sulphur isotopic composition of kerogen, pyrite and anhydrite grains. Currently, a search for a suitable laboratory to perform these measurements is being undertaken. Comparison of the range of sulphur isotopic compositions will help determine the sources of H<sub>2</sub>S and build a geological model for the Montney play. This geological model will provide the information companies need to incorporate into their development plans to reduce economic, health and environmental risks.

### Conclusions

The study into the lateral and stratigraphic H<sub>2</sub>S distribution within the Montney Formation in British Columbia began in the summer of 2018. Preliminary results indicate that

wells that target the upper portions of the Montney Formation in the northern region of the Montney play are at a higher risk of souring compared to wells that are placed in the lower portions (i.e., lower Montney Formation).

### Acknowledgments

The authors would like to thank P. Lacerda-Silva for reviewing this paper. The authors would like to thank the industry partners Saguaro Resources Ltd., Crew Energy Inc., Encana Corporation, Chevron Corporation and Canbriam Energy Inc. for their support of this project. The authors would also like to acknowledge geoLOGIC systems ltd. for the use of geoSCOUT GIS program to search and analyze the well data for this study.

### References

- BC Oil and Gas Commission (2015): British Columbia's oil and gas reserves and production report, 2015; BC Oil and Gas Commission, 35 p., URL <<https://www.bcogc.ca/node/13607/download>> [October 2018].
- Davies, G., Watson, N., Moslow, T. and MacEacher, J. (2018): Regional subdivisions, sequences, correlations and facies relationships of the Lower Triassic Montney Formation, west-central Alberta to northeastern British Columbia, Canada — with emphasis on role of paleostructure; Bulletin of Canadian Petroleum Geology, v. 66, p. 23–92, URL <<https://pubs.geoscienceworld.org/cspg/bcpg/article/66/1/23/538508/regional-subdivisions-sequences-correlations-and>> [October 2018].
- geoLOGIC systems ltd. (2018): geoSCOUT version 8.8; geoLOGIC systems ltd., mapping, data management and analysis software, URL <<https://www.geologic.com/products/geoscout/>> [August, 2018].

# Local Magnitude Scale for Earthquakes in the Western Canada Sedimentary Basin, Northeastern British Columbia and Northwestern Alberta

A. Babaie Mahani, Geoscience BC, Vancouver, BC, ali.mahani@mahangeo.com

H. Kao, Natural Resources Canada, Geological Survey of Canada–Pacific, Sidney, BC

Babaie Mahani, A. and Kao, H. (2019): Local magnitude scale for earthquakes in the Western Canada Sedimentary Basin, northeastern British Columbia and northwestern Alberta; *in* Geoscience BC Summary of Activities 2018: Energy and Water, Geoscience BC, Report 2019-2, p. 47–54.

## Introduction

Accurate determination of local magnitude ( $M_L$ ) for induced earthquakes caused by fluid injection is a vital task for regional seismograph network operators in the Western Canada Sedimentary Basin (WCSB). Specific mitigation measures are required by government regulations when the induced events exceed a predefined  $M_L$  threshold (Kao et al., 2016). In case of an event with  $M_L$  4.0 or larger, regulators in both British Columbia (BC) and Alberta issue suspension orders to temporarily stop injection operations.

Richter (1935) proposed the first systematic measure of magnitude using a small dataset from earthquakes in southern California. It was based on the maximum zero-to-peak horizontal amplitude of ground displacement, regardless of the wave type, on the Wood-Anderson (WA) torsion seismometer. This method of determining the magnitude is given as

$$M_L = \log(A) - \log(A_0) + S \quad (1)$$

where  $\log(A)$  is the recorded WA amplitude, in millimetres, whereas  $-\log(A_0)$  is the distance correction term for the recorded amplitude. In equation (1),  $S$  is a correction term for each station, which is based on the average (over all events) of deviations between  $M_L$  at each station and event  $M_L$  (Richter, 1935). A positive value for  $S$  means that, on average, the station has a higher magnitude than the event magnitude and vice versa. Richter (1935) obtained  $-\log(A_0)$  at each distance by defining the zero magnitude at a distance of 100 km. At this distance (ignoring the  $S$  term), the ground-motion amplitude is 0.001 mm ( $\log(A)$  of  $-3$ ), therefore  $-\log(A_0)$  would be 3. Since 1935, this method has been extensively used around the globe. The aim of this study is to preserve the method's original configuration (the type of sensor and the definition of zero-magnitude), but amend it with region- and station-specific correction terms ( $-\log(A_0)$  and  $S$ ; Savage and Anderson, 1995; Bobbio

et al., 2009; Uhrhammer et al., 2011; Ottemoller and Sargeant, 2013; Ristau et al., 2016). To preserve the original sensor type, WA amplitudes are synthetically obtained through deconvolution of the recording sensor's instrument response (non-WA sensors) from the recorded waveform and convolution with the WA-type instrument response.

For WCSB, where widespread oil and gas activities have caused a significant increase in the rate of seismicity in the past decade (Atkinson et al., 2016; Babaie Mahani et al., 2016), Natural Resources Canada (NRCan) follows the original Richter approach to calculate the  $M_L$  value of a seismic event with two differences. First, NRCan uses the vertical component instead of the horizontal components (Ristau et al., 2003). Second, a window encompassing the S phase is used and the maximum amplitude within this window is read from the synthetic WA seismograms (Ristau et al., 2003). Even though the static magnification and damping ratio of WA sensors have been found by some researchers to be different than the ones assumed in Richter (1935), NRCan uses the original values. Uhrhammer and Collins (1990) showed that the damping ratio and static magnification of WA sensors are 0.7 and 2080, respectively, which are different than the values of 0.8 and 2800 reported by Anderson and Wood (1925) and used by Richter (1935). Using the static magnification of 2800 instead of 2080 will result in a systematic overestimation of  $M_L$  by an average of 0.13 unit (Uhrhammer and Collins, 1990; Bona, 2016). The distance correction term was originally provided for the epicentral distance range of 25–600 km (Richter, 1935), but was later extended to 0 distance by Gutenberg and Richter (1942). The problem with using the epicentral distance is that it ignores the effect of focal depth, resulting in under- and over-estimation at short and large distances (Boore, 1989), and therefore, hypocentral distance is a better distance metric in the modification to the Richter's distance correction term for other regions.

For this study, several distance correction terms, which were obtained for different regions including WCSB, are compared. Using a database of WA amplitudes from small-to-moderate earthquakes in northeastern BC and

*This publication is also available, free of charge, as colour digital files in Adobe Acrobat® PDF format from the Geoscience BC website: <http://www.geosciencebc.com/s/SummaryofActivities.asp>.*

northwestern Alberta, a new distance correction term for WCSB is also obtained to maintain NRCan’s magnitude estimation routine.

## Database and Methodology

The database used in this study includes the vertical component of WA amplitudes from Visser et al. (2017), who compiled a comprehensive earthquake catalogue for WCSB for the period of 2014 to 2016. Over all, there are 4182 events from 39 stations with 18 918 WA amplitudes. Figure 1 shows the distribution of events and seismograph stations and Figure 2a and b shows the event and station  $M_L$  versus depth and hypocentral distance, respectively. In Figure 2, the event  $M_L$  is the median of the station  $M_L$  values. The  $M_L$  for each station was calculated from the vertical component of WA amplitudes based on the Richter (1958) distance correction term. For this study, the station  $M_L$  values were not corrected for any site/station effect ( $S$  in equation 1).

Although depth is a poorly constrained parameter in the regional earthquake catalogues, the maximum depth of the events is ~25 km. Therefore, events are all within the crust

(the crust thickness will be determined later in this section). As observed by Yenier (2017) and shown in Figure 2b, the station  $M_L$  shows an increasing trend with distance pointing out that the original distance correction term by Richter (1958) is not suitable to account for the regional characteristics of attenuation in WCSB. In Figure 2b the increasing trend in station  $M_L$  with distance can be visualized for an individual event: the August 17, 2015 induced event in the northern Montney play of northeastern BC with moment magnitude of 4.6 (star in Figure 2a; Babaie Mahani et al., 2017). Visser et al. (2017) assigned a  $M_L$  of 5 for this event.

Figure 3a shows comparison of  $-\log(A_0)$  versus hypocentral distance from Richter (1958), Hutton and Boore (1987), Brazier et al. (2008), Bona (2016) and Yenier (2017). Whereas the Richter (1958) and Hutton and Boore (1987) terms are for southern California, Brazier et al. (2008), Bona (2016) and Yenier (2017) terms are for Ethiopia plateau, Italy and WCSB, respectively. These distance correction terms were all obtained for the horizontal component using hypocentral (Hutton and Boore, 1987; Brazier et al., 2008; Yenier, 2017) and epicentral (Richter, 1958; Bona, 2016) distance metrics. Whereas Richter (1958), Hutton and Boore (1987) and Bona (2016) assumed a static magnification of 2800 for the WA sensors, Brazier et al. (2008) and Yenier (2017) used a value of 2080. In Figure 3a, dots represent the observed WA amplitudes, which were normalized based on the reference distance bin 90–110 km. For each distance, amplitudes were divided by the geometric mean of the amplitudes in the reference bin. The data was then forced to pass through 0.001 mm ( $-\log(A_0)$  of 3 in Figure 3a) at 100 km distance.

Following Rezapour and Rezaei (2011), a parametric equation for distance correction term can be written as

$$-\log(A_0) = n \times \log\left(\frac{R_{hypo}}{100}\right) + k \times (R_{hypo} - 100) + 3.0 \quad (2)$$

where  $R_{hypo}$  is hypocentral distance, and  $n$  and  $k$  are the correction for geometrical spreading and an elastic attenuation, respectively.

Equation (2) is written in such a way that for the reference distance of 100 km, amplitudes hold a value of 0.001 mm ( $-\log(A_0)$  of 3) to maintain the consistency with the original definition of Richter magnitude. From Figure 3a it is observed that Bona (2016) has the highest correction for  $n$  whereas Brazier et al. (2008) has the lowest (note the difference between the slopes of correction terms below

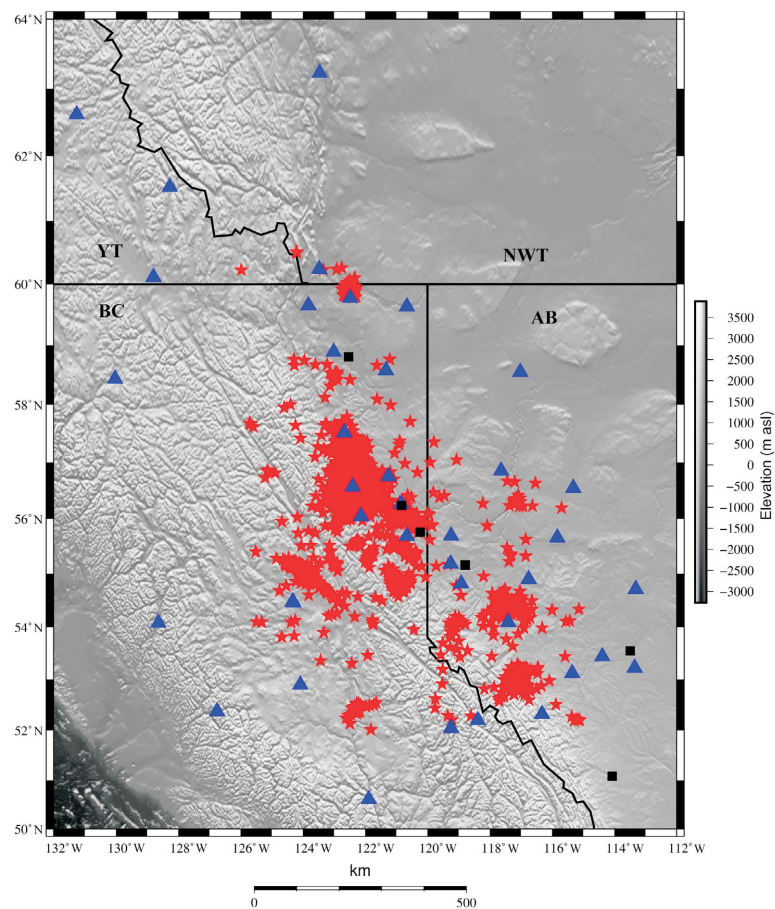


**Figure 1.** Distribution of earthquakes and seismograph stations from Visser et al. (2017) database used in this study. Stars are the earthquakes, triangles are the stations and squares are the cities and populated areas.

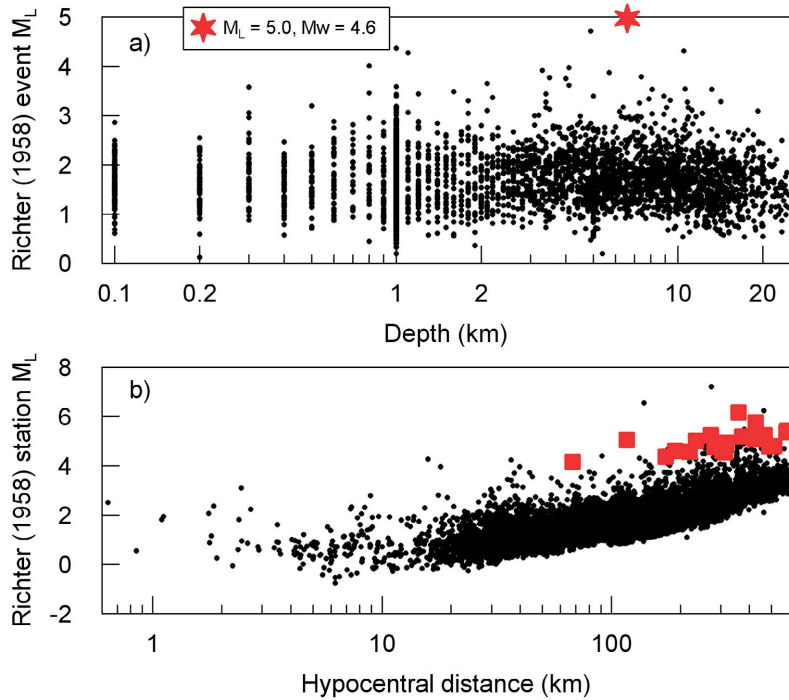


**Figure 2.** a) Event local magnitude ( $M_L$ ) versus depth and b) station  $M_L$  versus hypocentral distance. The  $M_L$  values were calculated using the vertical component of Wood-Anderson amplitudes based on the Richter (1958) distance correction term without correcting for the station term ( $S$  in equation 1). Event  $M_L$  is the median of station  $M_L$  values. Red star in a) is the August 17, 2015, induced earthquake in the northern Montney play of northeastern British Columbia with moment magnitude ( $M_w$ ) of 4.6 (Babaie Mahani et al., 2017). Red squares in b) show the station  $M_L$  for this event across recording distances.

100 km distance). The  $n$  is 1.7 for Bona (2016) and 0.7 for Brazier et al. (2008). The effect of  $n$  on the estimates of  $M_L$  can be seen from Figure 3b, which shows the average of the difference between station and event local magnitudes (median from all stations) in equally log-spaced distance bins versus hypocentral distance. Magnitudes were calculated without the  $S$  term (equation 1). Except Brazier et al. (2008), all other distance correction terms give low station magnitudes at short hypocentral distance ( $<100$  km) and high station magnitudes at hypocentral distance  $>100$  km (Figure 3b). This is important for small-magnitude events as these events are recorded at shorter distances than larger events.

The result of combing and rearranging equations (1) and (2) is

$$\log(A) + 3.0 = -n \times \log\left(\frac{R_{\text{hypo}}}{100}\right) - k \times (R_{\text{hypo}} - 100) + M_L - S + \epsilon \quad (3)$$

where  $\epsilon$  is the residual (observed minus predicted). The  $n$ ,  $k$ ,  $M_L$  and  $S$  parameters are obtained by constructing the linear inverse equation of  $d = Gm$  (Menke, 1984), where  $d$  is observed data ( $\log(A) + 3.0$ ) and  $m$  is the model parameter ( $n, k, M_L, S$ ) to be determined,  $G$  is the kernel matrix that relates  $d$  to  $m$ . In solving for the model parameters, the correc-

tion term for each station ( $S$ ), which represents the overall discrepancy in WA amplitudes between stations located at different site conditions, is obtained simultaneously. Site effects are typically determined relative to a known site condition to avoid trade-offs between source and site terms. In this study, however, site conditions are unknown for the recording stations. Thus, correction factors are computed relative to the average site condition by constraining the  $S$  terms to attain zero when averaged over all stations. This allows consistent  $M_L$  estimations with reduced overall scatter of predictions across different stations (Yenier, 2017).

In determination of  $-\log(A_0)$ , the most important factor is the shape or functional form of geometrical spreading attenuation, which is characterized by  $n$ . Although attenuation can be parameterized using a linear, bilinear or trilinear function, Babaie Mahani and Atkinson (2012) found that although the trilinear forms are statistically preferred in many cases, the differences between the forms (linear, bilinear, trilinear) are not sufficiently significant to prefer one over another. For this study, a bilinear function was used to model the distance correction due to geometrical spreading. The bilinear function is simpler because one less

parameter needs to be determined in the inversion process yet it is still complex enough to separate direct waves from refracted or head waves travelling along the Moho discontinuity.

Figure 4 shows the P-wave travel time versus epicentral distance, which was obtained by manually picking the onset of the P-wave on the vertical component for selected events with  $M_L \geq 3$ . Two wave types are shown in Figure 4. The  $P_g$  is the direct P-wave, which travels within the crust with velocity  $v_0$ , whereas  $P_n$  is the head (refracted) P-wave, which travels along the Moho discontinuity with uppermost mantle velocity  $v_1$ . From Figure 4, it can be seen that the crossover distance  $x_D$  is 200 km. The crossover distance is the distance beyond which the first arrival waves are always head waves. Using the velocities  $v_0$  (6.5 km/s) and  $v_1$  (8.2 km/s), which are the reciprocals of the slope of the direct and head P-wave travel times, and the intercept  $\tau$  (6.4 s), which is the head P-wave travel time at zero distance, the thickness of the crust ( $h_0$ ) can be estimated as (Stein and Wysession, 2003)

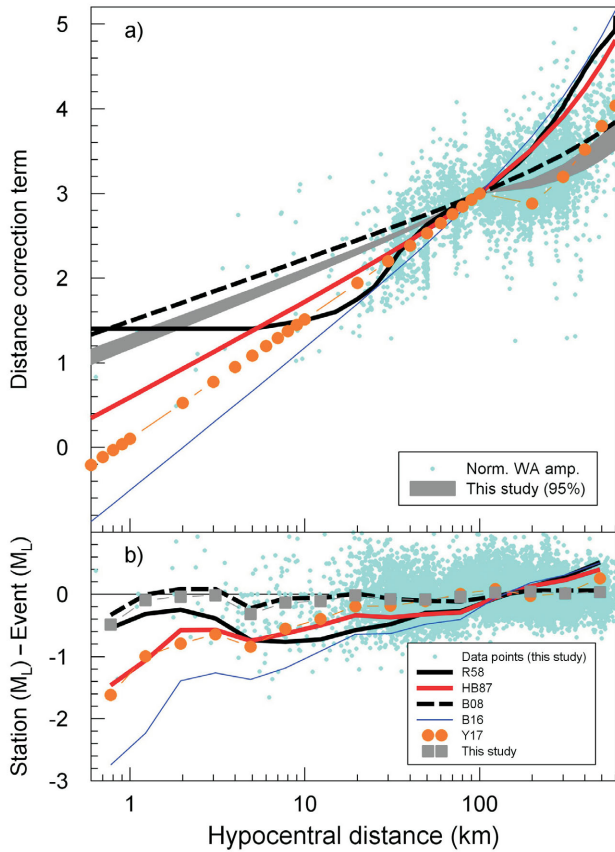


**Figure 3.** a) Distance correction term  $[-\log(A_0)]$  versus hypocentral distance. Data is the normalized (Norm.) Wood-Anderson (WA) amplitudes (amp.) in the reference distance bin 90–110 km. Grey area shows the 95% confidence interval for  $-\log(A_0)$  obtained in this study. b) Individual data points for this study and the average of the difference between the station and event local magnitudes ( $M_L$ ) in equally log-spaced distance bins, using  $-\log(A_0)$  from Richter (1958), Hutton and Boore (1987), Brazier et al. (2008), Bona (2016), Yenier (2017) and this study, versus hypocentral distance. The  $M_L$  values were not corrected for the station term ( $S$  in equation 1). Event  $M_L$  is the median of station  $M_L$  values. Abbreviations: B08, Brazier et al. (2008); B16, Bona (2016); HB87, Hutton and Boore (1987); R58, Richter (1958); Y17, Yenier (2017).

$$h_0 = \frac{\tau}{2 \times \sqrt{\left(\frac{1}{v_0^2}\right) - \left(\frac{1}{v_1^2}\right)}} \quad (4)$$

Equation (4) gives 33 km for the thickness of the crust. The critical distance  $x_c$ , below which the head waves disappear, is obtained as (Stein and Wysession, 2003)

$$x_c = 2 \times h_0 \times \frac{v_0/v_1}{\sqrt{1 - \left(\frac{v_0^2}{v_1^2}\right)}} \quad (5)$$

In this case,  $x_c$  is 85 km. Therefore, the bilinear function of the form

$$\begin{cases} b_1 \times \log\left(\frac{R_{hypo}}{100}\right) & R_{hypo} \leq 85 \text{ km} \\ b_2 \times \log\left(\frac{R_{hypo}}{100}\right) & R_{hypo} > 85 \text{ km} \end{cases} \quad (6)$$

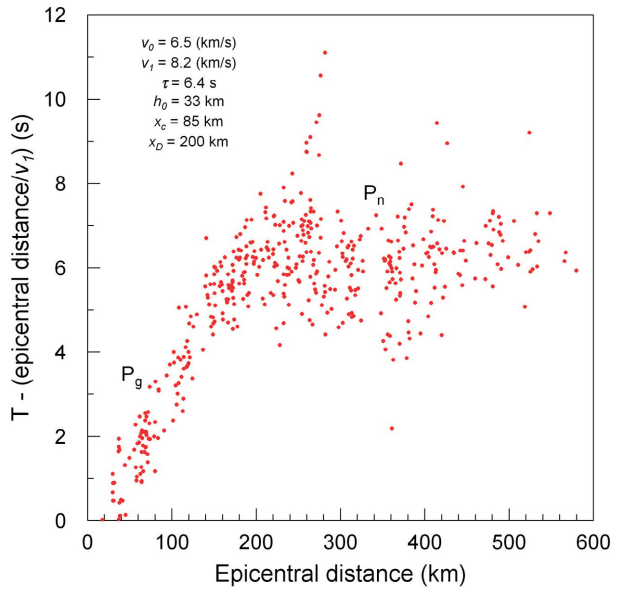


**Figure 4.** Reduced P-wave travel time versus epicentral distance. Abbreviations:  $h_0$ , crust thickness;  $P_g$ , direct P-wave;  $P_n$ , head (refracted) P-wave;  $\tau$ , intercept;  $T$ , time;  $v_0$ , velocity of direct P-wave within the crust;  $v_1$ , velocity of head P-wave within the mantle;  $x_c$ , critical distance;  $x_D$ , crossover distance.

was used to model the effect of geometrical spreading,  $n$ , where  $b_1$  and  $b_2$  are the coefficients to be determined.

### Distance Correction Term for WCSB

Using the equations (3) and (6), model parameters ( $b_1$ ,  $b_2$ ,  $k$ ,  $M_L$ ,  $S$ ) were obtained through the maximum likelihood estimation. For this study, only those events with at least five observations were used (1586 events with 12 000 WA amplitudes). Figure 5 shows  $\epsilon$  versus hypocentral distance and event  $M_L$  (median of station  $M_L$  values based on Richter [1958] distance correction term and without the  $S$  term). Although data is sparse at close distances ( $R_{hypo} < 10$  km) and larger magnitudes ( $M_L > 4$ ), there are no trends in the residuals with distance or magnitude, which means that the inversion was successful assuming the functional forms for the attenuation and geometric spreading. Therefore, in this study, the distance correction term,  $-\log(A_0)$ , for WCSB is

$$\begin{cases} 0.7974 \times \log\left(\frac{R_{hypo}}{100}\right) + 0.0016 \times (R_{hypo} - 100) + 3.0 & R_{hypo} \leq 85 \text{ km} \\ -0.1385 \times \log\left(\frac{R_{hypo}}{100}\right) + 0.0016 \times (R_{hypo} - 100) + 3.0 & R_{hypo} > 85 \text{ km} \end{cases} \quad (7)$$

Overall, the distance correction term (equation 7) appears to work well at all distances and is similar to Brazier et al. (2008; Figure 3).

Figure 6 shows event  $M_L$  (median of station  $M_L$  without the  $S$  term) computed with the distance correction term obtained in this study versus Richter (1958), Hutton and Boore (1987), Brazier et al. (2008), Bona (2016) and Yenier

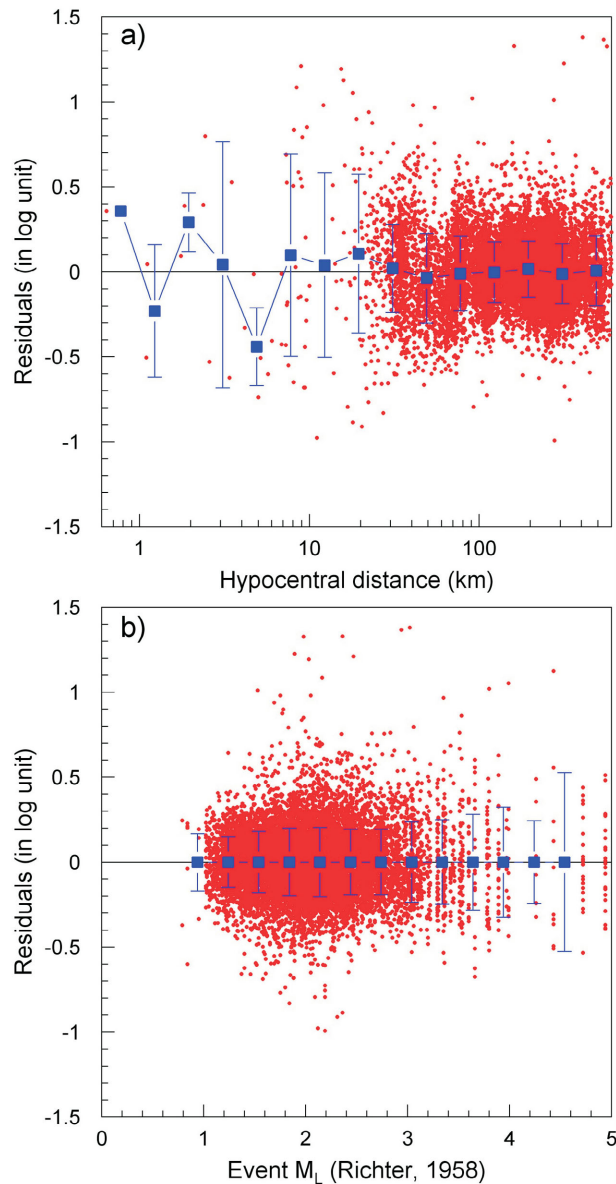


**Figure 5.** Residuals (observed minus predicted) of the inversion process versus **a)** hypocentral distance and **b)** event local magnitude ( $M_L$ ). Squares are the mean of residuals in equally log-spaced distance bins and equally linear-spaced magnitude bins and the error bars are one standard deviation. The  $M_L$  values were calculated using the vertical component of Wood-Anderson amplitudes based on the Richter (1958) distance correction term without correcting for the station term ( $S$  in equation 1). Event  $M_L$  is the median of station  $M_L$  values.

(2017). The  $AVR_M$  in Figure 6 is the average of the difference between  $M_L$  values ( $M_L$  from another study minus  $M_L$  from this study). Overall,  $M_L$  values from this study are lower than those obtained using  $-\log(A_0)$  of Richter (1958), Hutton and Boore (1987), Brazier et al. (2008) and Bona (2016) but higher than Yenier (2017).

To further analyze the difference between  $M_L$  values, the event  $M_L$  was calculated from station  $M_L$  (median of

station magnitudes without the  $S$  term) at different distance bins ( $R_{hypo} \leq 50$  km,  $50 \text{ km} < R_{hypo} \leq 100$  km,  $100 \text{ km} < R_{hypo} \leq 200$  km,  $R_{hypo} > 200$  km) using the distance correction terms obtained in this study and Yenier (2017). In Figure 7, the difference between  $M_L$  values ( $M$ ) from Yenier (2017) and this study is plotted against  $M_L$  values from this study. Also plotted are the averages of  $M$  in equally linear-spaced magnitude bins. The largest deviation between this study's  $M_L$  values and Yenier (2017) values occurs when all stations are below 50 km for which the  $M_L$  values from Yenier (2017) are lower by an average of 0.27 unit. For larger distance bins, the values are more similar. The lower  $M_L$  values from Yenier (2017) at short distances are due to the fact that Yenier (2017) assigned a higher rate for the geometrical attenuation of ground-motion amplitudes for distances  $< 100$  km (1.4 for Yenier [2017] versus 0.8 in this study).

## Conclusions

Determination of an accurate local magnitude ( $M_L$ ) for induced earthquakes requires adjustments to the region-specific distance correction term,  $-\log(A_0)$ , in Richter's (1935) magnitude equation. When the maximum magnitude of induced events is close to the threshold set by regulators to suspend injections, having an accurate  $M_L$  can have important economic consequences for operators. For this reason, a comprehensive catalogue of Wood-Anderson amplitudes from earthquakes in the Western Canada Sedimentary Basin (WCSB) was used to analyze the  $-\log(A_0)$  term previously obtained for WCSB and several other regions. By assuming a bilinear model for the attenuation of ground-motion amplitudes, a new formula of  $-\log(A_0)$  was obtained specifically for monitoring induced seismicity in WCSB using Natural Resources Canada's  $M_L$  calculation routine. This study's correction term for distance is

$$\begin{cases} 0.7974 \times \log\left(\frac{R_{hypo}}{100}\right) + 0.0016 \times (R_{hypo} - 100) + 3.0 & R_{hypo} \leq 85 \text{ km} \\ -0.1385 \times \log\left(\frac{R_{hypo}}{100}\right) + 0.0016 \times (R_{hypo} - 100) + 3.0 & R_{hypo} > 85 \text{ km} \end{cases}$$

where  $R_{hypo}$  is the hypocentral distance. This study's distance correction term results in lower  $M_L$  values by an average of 0.29, 0.27, 0.12 and 0.34 units compared to those obtained by Richter (1958; California), Hutton and Boore (1987; California), Brazier et al. (2008; Ethiopia plateau) and Bona (2016; Italy), respectively, when all distance ranges are considered. However, it gives higher  $M_L$  values than those obtained by Yenier (2017; WCSB) by an average of 0.12 unit over the distance range of 0 to 600 km. When comparing this study to Yenier's (2017) study, this difference in  $M_L$  varies with  $R_{hypo}$ : 0.27 unit for  $R_{hypo} \leq 50$  km, 0.08 unit for  $50 \text{ km} < R_{hypo} \leq 100$  km, 0.12 for  $100 \text{ km} < R_{hypo} \leq 200$  km, and 0.10 for  $R_{hypo} > 200$  km.

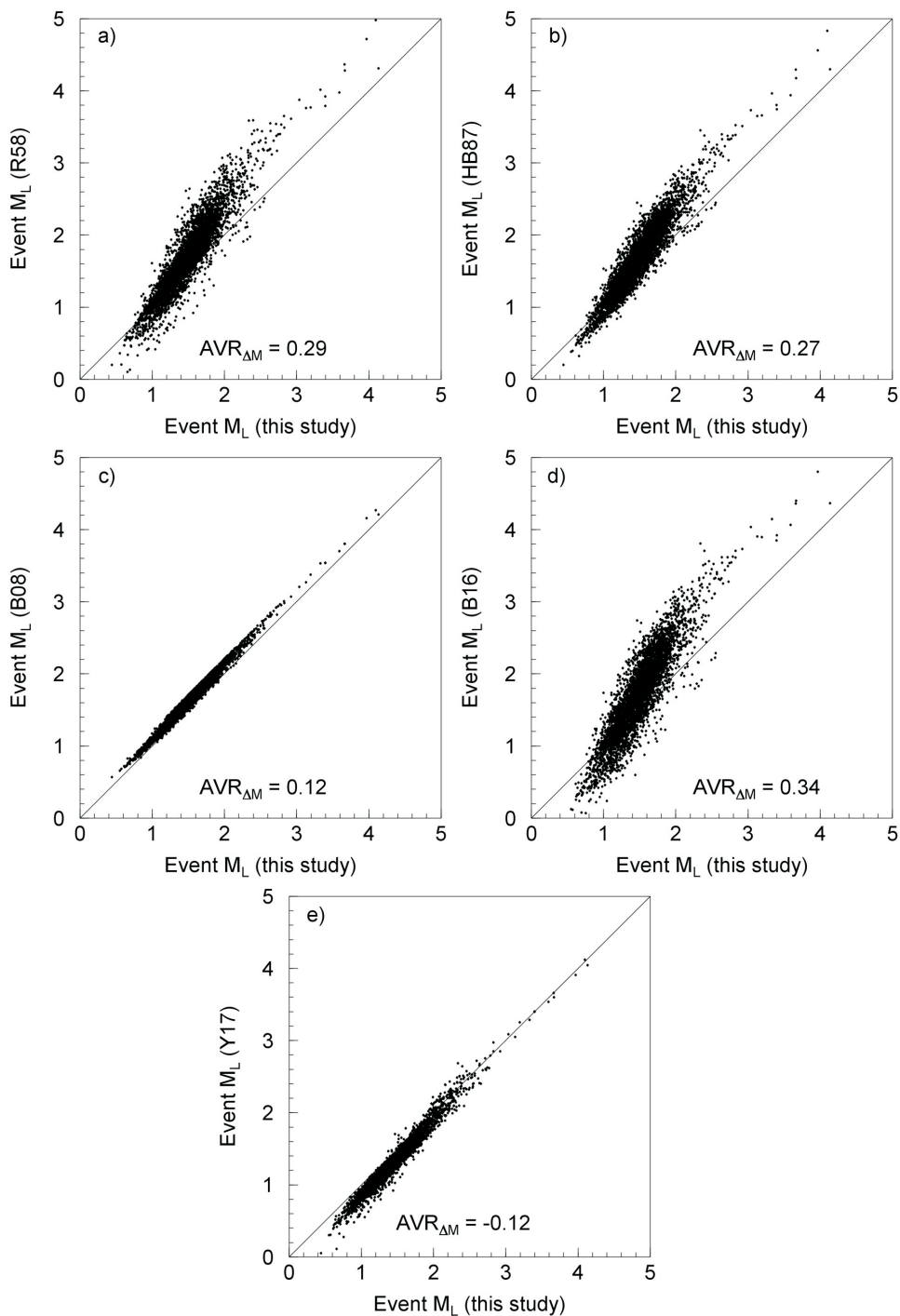


**Figure 6.** Event local magnitude ( $M_L$ ) computed from the distance correction terms obtained in this study versus those obtained by **a)** Richter (1958; R58); **b)** Hutton and Boore (1987; HB87); **c)** Brazier et al. (2008; B08); **d)** Bona (2016; B16); and **e)** Yenier (2017; Y17). The  $AVR_M$  is the average deviation of  $M_L$  values ( $M_L$  from another study minus  $M_L$  from this study). The solid lines show the 1:1 agreement of magnitude estimates. The  $M_L$  values were not corrected for the station term ( $S$  in equation 1). Event  $M_L$  is the median of station  $M_L$  values.

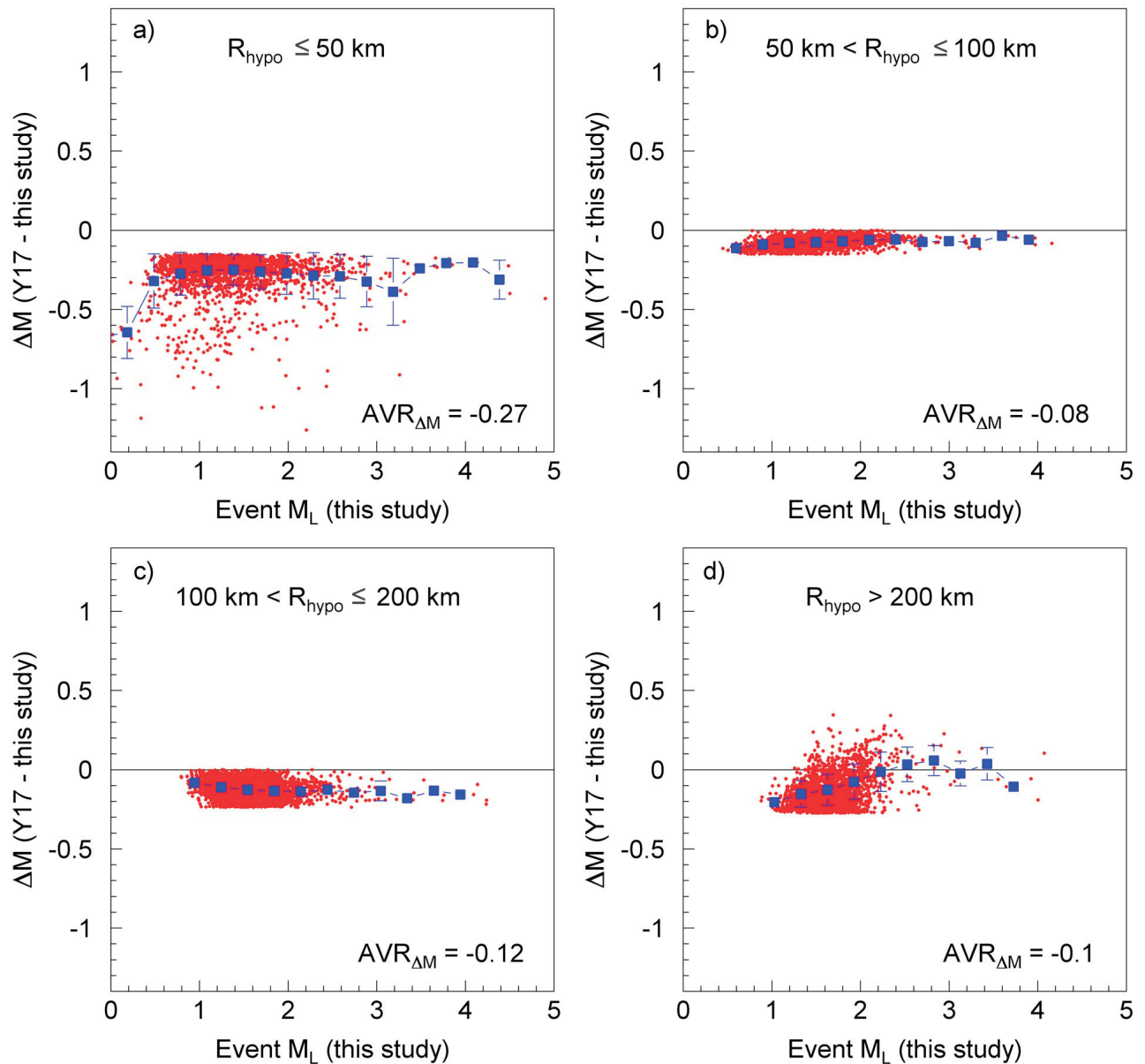


**Figure 7.** Difference ( $\Delta M$ ) between event local magnitudes ( $M_L$ ) computed from the distance correction terms obtained in this study versus those obtained by Yenier (2017; Y17) using stations in different hypocentral distance ( $R_{hypo}$ ) bins: **a)**  $R_{hypo} \leq 50$  km; **b)**  $50 \text{ km} < R_{hypo} \leq 100$  km; **c)**  $100 \text{ km} < R_{hypo} \leq 200$  km; and **d)**  $R_{hypo} > 200$  km. The  $AVR_{\Delta M}$  is the average deviation of  $M_L$  values ( $M_L$  from Yenier [2017] study minus  $M_L$  from this study). The solid lines show the 1:1 agreement of magnitude estimates. Squares are the averages of  $\Delta M$  in equally linear-spaced magnitude bins with the error bars showing one standard deviation. The  $M_L$  values were not corrected for the station term ( $S$  in equation 1). Event  $M_L$  is the median of station  $M_L$  values.

## Acknowledgments

The authors would like to thank R. Visser for providing the Wood-Anderson amplitudes and comments on the Natural Resources Canada magnitude calculation. Also thanked is E. Yenier for his explanations regarding the inversion process. This project was partially supported by BC Seismic Research Consortium (Geoscience BC, BC Oil and Gas Research and Innovation Society, Canadian Association of Petroleum Producers, BC Oil and Gas Commission, Yukon Geological Survey). The authors appreciate comments by Seismological Research Letters' Z. Peng, and three anonymous reviewers who helped improve the manuscript.

Natural Resources Canada, Lands and Minerals contribution 20180221

## References

- Anderson, J.A. and Wood, H.O. (1925): Description and theory of the torsion seismometer; *Bulletin of the Seismological Society of America*, v. 15, p. 1–72.
- Atkinson, G.M., Eaton, D., Ghofrani, H., Walker, D., Cheadle, B., Schultz, R., Scherbakov, R., Tiampo, K., Gu, Y.J., Harrington, R., Liu, Y., van der Baan, M. and Kao, H. (2016): Hydraulic fracturing and seismicity in the Western Canada Sedimentary Basin; *Seismological Research Letters*, v. 87, p. 631–647.
- Babaie Mahani, A. and Atkinson, G.M. (2012): Evaluation of functional forms for the attenuation of small-to-moderate-earthquake response spectral amplitudes in North America; *Bulletin of the Seismological Society of America*, v. 102, p. 2714–2726.
- Babaie Mahani, A., Kao, H., Walker, D., Johnson, J. and Salas, C. (2016): Performance evaluation of the regional seismograph network in northeast British Columbia, Canada, for monitoring of induced seismicity; *Seismological Research Letters*, v. 87, p. 648–660.
- Babaie Mahani, A., Schultz, R., Kao, H., Walker, D., Johnson, J. and Salas, C. (2017): Fluid injection and seismic activity in the northern Montney Play, British Columbia, Canada, with special reference to the 17 August 2015 Mw 4.6 induced earthquake; *Bulletin of the Seismological Society of America*, v. 107, p. 542–552.
- Bobbio, A., Vassallo, M. and Festa, G. (2009): A local magnitude scale for southern Italy; *Bulletin of the Seismological Society of America*, v. 99, p. 2461–2470.
- Bona, M.D. (2016): A local magnitude scale for crustal earthquakes in Italy; *Bulletin of the Seismological Society of America*, v. 106, p. 242–258.
- Boore, D.M. (1989): The Richter scale: its development and use for determining earthquake source parameters; *Tectonophysics*, v. 166, p. 1–14.
- Brazier, R.A., Miao, Q., Nyblade, A.A., Ayele, A. and Langston, C.A. (2008): Local magnitude scale for the Ethiopia plateau; *Bulletin of the Seismological Society of America*, v. 98, p. 2341–2348.
- Gutenberg, B. and Richter, C.F. (1942): Earthquake magnitude, intensity, energy, and acceleration; *Bulletin of the Seismological Society of America*, v. 32, p. 163–191.
- Hutton, L.K. and Boore, D.M. (1987): The ML scale in southern California; *Bulletin of the Seismological Society of America*, v. 77, p. 2074–2094.
- Kao, H., Eaton, D.W., Atkinson, G.M., Maxwell, S. and Babaie Mahani, A. (2016): Technical meeting on the traffic light protocols (TLP) for induced seismicity: summary and recommendations; Geological Survey of Canada, Open File 8075, 20 p.
- Menke, W. (1984): *Geophysical Data Analysis: Discrete Inverse Theory*; Academic Press, San Diego, California, 289 p.
- Ottmoller, L. and Sargeant, S. (2013): A local magnitude scale for the United Kingdom; *Bulletin of the Seismological Society of America*, v. 103, p. 2884–2893.
- Rezapour, M. and Rezaei, R. (2011): Empirical distance attenuation and the local magnitude scale for northwest Iran; *Bulletin of the Seismological Society of America*, v. 101, p. 3020–3031.
- Richter, C.F. (1935): An instrumental earthquake magnitude scale; *Bulletin of the Seismological Society of America*, v. 25, p. 1–31.
- Richter, C.F. (1958): *Elementary Seismology*; W.H. Freeman and Co., San Francisco, California, 578 p.
- Ristau, J., Harte, D. and Salichon, J. (2016): A revised local magnitude (ML) scale for New Zealand earthquakes; *Bulletin of the Seismological Society of America*, v. 106, p. 398–407.
- Ristau, J., Rogers, G.C. and Cassidy, J.F. (2003): Moment magnitude-local magnitude calibration for earthquakes off Canada's west coast; *Bulletin of the Seismological Society of America*, v. 93, p. 2296–2300.
- Savage, M.K. and Anderson, J.G. (1995): A local-magnitude scale for the western Great Basin–eastern Sierra Nevada from synthetic Wood-Anderson seismograms; *Bulletin of the Seismological Society of America*, v. 85, p. 1236–1243.
- Stein, S. and Wysession, M. (2003): *An Introduction to Seismology, Earthquakes, and Earth Structure*; Blackwell Publishing, Malden, Massachusetts, 512 p.
- Uhrhammer, R.A. and Collins, E.R. (1990): Synthesis of Wood-Anderson seismograms from broadband digital records; *Bulletin of the Seismological Society of America*, v. 80, p. 702–716.
- Uhrhammer, R.A., Hellweg, M., Hutton, K., Lombard, P., Walters, A.W., Hauksson, E. and Oppenheimer, D. (2011): California integrated seismic network (CISN) local magnitude determination in California and vicinity; *Bulletin of the Seismological Society of America*, v. 101, p. 2685–2693.
- Visser, R., Smith, B., Kao, H., Babaie Mahani, A., Hutchinson, J. and McKay, J.E. (2017): A comprehensive earthquake catalogue for northeastern British Columbia and western Alberta, 2014–2016; Geological Survey of Canada, Open File 8335, 28 p.
- Yenier, E. (2017): A local magnitude relation for earthquakes in the Western Canada Sedimentary Basin; *Bulletin of the Seismological Society of America*, v. 107, p. 1421–1431.

# Ground-Motion Data from Seismicity Induced in the Southern Montney Formation, Northeastern British Columbia

**A.M.M. Bustin**, The University of British Columbia, Vancouver, BC, [abustin@eos.ubc.ca](mailto:abustin@eos.ubc.ca)

**E.O. Munson**, The University of British Columbia, Vancouver, BC

**D.J. Jones**, The University of British Columbia, Vancouver, BC

**G.R.L. Chalmers**, The University of British Columbia, Vancouver, BC

---

Bustin, A.M.M., Munson, E.O., Jones, D.J. and Chalmers, G.R.L. (2019): Ground-motion data from seismicity induced in the southern Montney Formation, northeastern British Columbia; *in* Geoscience BC Summary of Activities 2018: Energy and Water, Geoscience BC, Report 2019-2, p. 55–62.

## Introduction

The limited availability of data to researchers is arguably the greatest challenge to advancement of the understanding of induced seismicity in Western Canada and hence to the development of proactive mitigation schemes and frameworks for hazard assessment. To address the data gap, a 15-station array is being developed to densely monitor hydraulic-fracturing operations in the Montney Formation. The pre-existing accelerographs, which are now providing real-time data to an online interactive platform, were deployed to monitor two disposal wells and four hydraulic-fracturing operations in the past year. Although no events have yet been detected after 1.5 years by the station installed to monitor a disposal in a seismically inactive area, 12 events were recorded on the four-station array installed to monitor a disposal in an active area. Single stations were deployed within 3 km of the four completions, three of which were in seismically active areas. No events were detected on the smallest of the three operations, while four and six events were recorded during the two larger operations. In total, 25 events were recorded during the deployments, with site-corrected, peak ground accelerations (PGAs) ranging from 0.027%g to 0.23%g. The real-time ground-motion parameters are calculated for the geometric mean of the horizontal components, which are then corrected to a reference site using correction factors calculated during post-processing. For events located by the NRCan network or the local operator-deployed array, the corrected PGAs were plotted versus hypocentral distances. A good fit between the data and the prediction models was demonstrated by Babaie Mahani and Kao (2017). The dataset was also used to confirm the completeness threshold.

In order to detect smaller events and to facilitate locating events and calculating magnitudes in real time, one of the

stations was upgraded to include a three-component (3C), 4.5 Hz geophone. This paired station was recently deployed to a seismically active area, where it is co-located with a long-term station and two temporary stations. The four accelerometers were installed at different depths (30, 60, 90 and 120 cm) in order to test the impact of burial depth on the response spectra. Additional ongoing work includes the addition of algorithms to the online portal for real-time calculation of hypocentres and magnitudes. Following testing of the paired station, geophones will be added to the other stations and the entire array will be deployed to densely monitor hydraulic-fracturing operations on three to five multilateral wellpads. The datasets will then be integrated into three-dimensional (3-D) hydro-geomechanical models to address the study's objectives, summarized by Bustin and Longobardi (2017).

## Station Design

The design for this low-cost, mobile, easy-to-install station was modified from the early earthquake detectors developed by the Earthquake Engineering Research Facility (EERF) at The University of British Columbia and installed in BC schools for the Earthquake Early Warning System (Azpiri, 2016). The units are powered by a solar panel with an absorbent glass mat (AGM) deep-cycle battery. For long-term and distant stations, two solar panels and three batteries were used for backup. Advanced RISC (reduced instruction set computer) machine (ARM) processors running Linux, which are stored within protective (weather- and animal-proof) cases, run the system, while the data are stored on ultra-high-capacity USB drives. The protective case also encloses a global positioning system (GPS) for timing and station location. Telemetry is currently provided by cellphone modems with antennas and, in some cases, machine-to-machine (M2M) cellphone boosters to improve the signal. Satellite M2M systems are currently being investigated to provide telemetry in more remote locations. The solar panels are mounted on an aluminum frame that was designed in house, which has recently been upgraded

---

*This publication is also available, free of charge, as colour digital files in Adobe Acrobat® PDF format from the Geoscience BC website: <http://www.geosciencebc.com/s/SummaryofActivities.asp>.*

to include a raised, covered shelf to enclose the protective case and batteries off the ground.

The commercial, 3C, microelectromechanical systems (MEMS) accelerometers are enclosed in sealed tubes, 50–80 cm in length and 7.5 cm in diameter, that are buried beneath surficial alluvium with a shovel to depths of 30–120 cm. To improve the detection, location and magnitude calculation of events, the stations are being augmented with commercial, 3C, 4.5 Hz geophones. The geophones are shallowly buried in conical, 15 cm long enclosures. The first of these paired stations was recently deployed for testing.

The raw data are collected and stored at 250 Hz for the accelerometers and 500 Hz for the geophones. When a ground motion is recorded above a set threshold, an alert is emailed and the data are transferred to the online, interactive platform (dashboard). The platform can then be used to plot the accelerations and calculate the ground-motion parameters for the event. The raw data are first run through a 0.1 Hz, high-pass, 4<sup>th</sup> order, Butterworth filter. The maximum amplitude for the peak ground acceleration (PGA) is then determined for the vertical component and the geometric mean of the horizontal components. The filtered acceleration data are integrated to velocities, which are then further integrated to displacements. The peak ground velocity (PGV) and peak ground displacement (PGD) are then determined for the vertical component and the geometric mean of the horizontal components. Additionally, the spectral intensity (SI), which provides a measure of the damage potential to structures by events, is calculated according to Rosenberger (unpublished report, 2010). The study defines SI as the maximum velocity of two, 20% dampened, single-degree-of-freedom systems with resonant frequencies of 1.5 s and 2.5 s. An example of an event recorded by one of the stations, displayed on the dashboard, is shown in Figure 1. Additional algorithms are currently being developed for real-time calculation of magnitudes, hypocentres and shake maps.

A simple amplitude threshold is being used for event detection. More sophisticated autodetection techniques were investigated (for a summary, see Li et al., 2018); however, the heavy contamination of the recordings at all stations from large-amplitude animal and anthropogenic noise makes auto-discrimination of seismic events difficult. In particular, seismic events recorded on single stations are difficult to discriminate from noise when the amplitudes are close to the digital noise (0.2 cm/s<sup>2</sup> for geometric mean of the horizontal components and 0.4 cm/s<sup>2</sup> for the vertical component). During dense deployments, a stacked local similarity function will be used for real-time discrimination of seismic events to ensure detection of smaller events.

## Dataset

During the past year, the accelerographs were deployed to monitor two disposal wells, one in an active area of induced seismicity, and four hydraulic-fracturing completions, three of which were in an active area of induced seismicity. While a four-station array was deployed to monitor the disposal in the active area, single-station deployments were used to monitor the other operations. In addition to sites obtained through operator agreements, stations are also currently deployed at research sites and on a private ranch.

Although no events have yet been detected after 1.5 years by the station installed to monitor the disposal in a seismically inactive area, 12 events were recorded by the four-station array during its 6 months of operation. One event was recorded on three stations and three events were recorded on two stations. The event recorded by three stations in the array was the largest magnitude event reported by Natural Resources Canada (NRCAN) from the Canadian National Seismograph Network (CNSN) stations during the deployment. The three events detected on two stations and five events detected by single stations were not reported by NRCAN, while three other events detected by single stations were reported by NRCAN. Two events reported by NRCAN were missed by the four-station array (discussed further in the ‘Magnitude of Completeness’ section). All events recorded by both the study’s array and the NRCAN network have magnitudes between 2 and 3, and hypocentral distances between 10 and 14 km.

No events were detected during the first hydraulic-fracturing operation monitored this year, which was the smallest of the three operations in the seismically active area. The station was deployed for two months following the completions, in which time eight events with  $M_w > 1.5$  were recorded on the local, operator-deployed (local) array in the area. The two largest events were recorded by the study’s station, the largest of which was also reported by NRCAN. During pre-completion monitoring, the two events were also detected by the station that was deployed for the second operation. Five out of the six  $M_w > 1.5$  events and one event with  $M_w < 1.5$  recorded by the local array during the second completion were detected by the study’s station. One of the five events with  $M_w > 1.5$  recorded on the local array during the third operation was not detectable above the digital noise.

In total, 25 events were recorded during the deployments, with pre-site-corrected PGAs (for geometric mean of horizontal components) ranging from 0.035%g to 0.29%g. Examples of typical 3-axis acceleration data for events recorded by the study’s stations are shown in Figure 2.

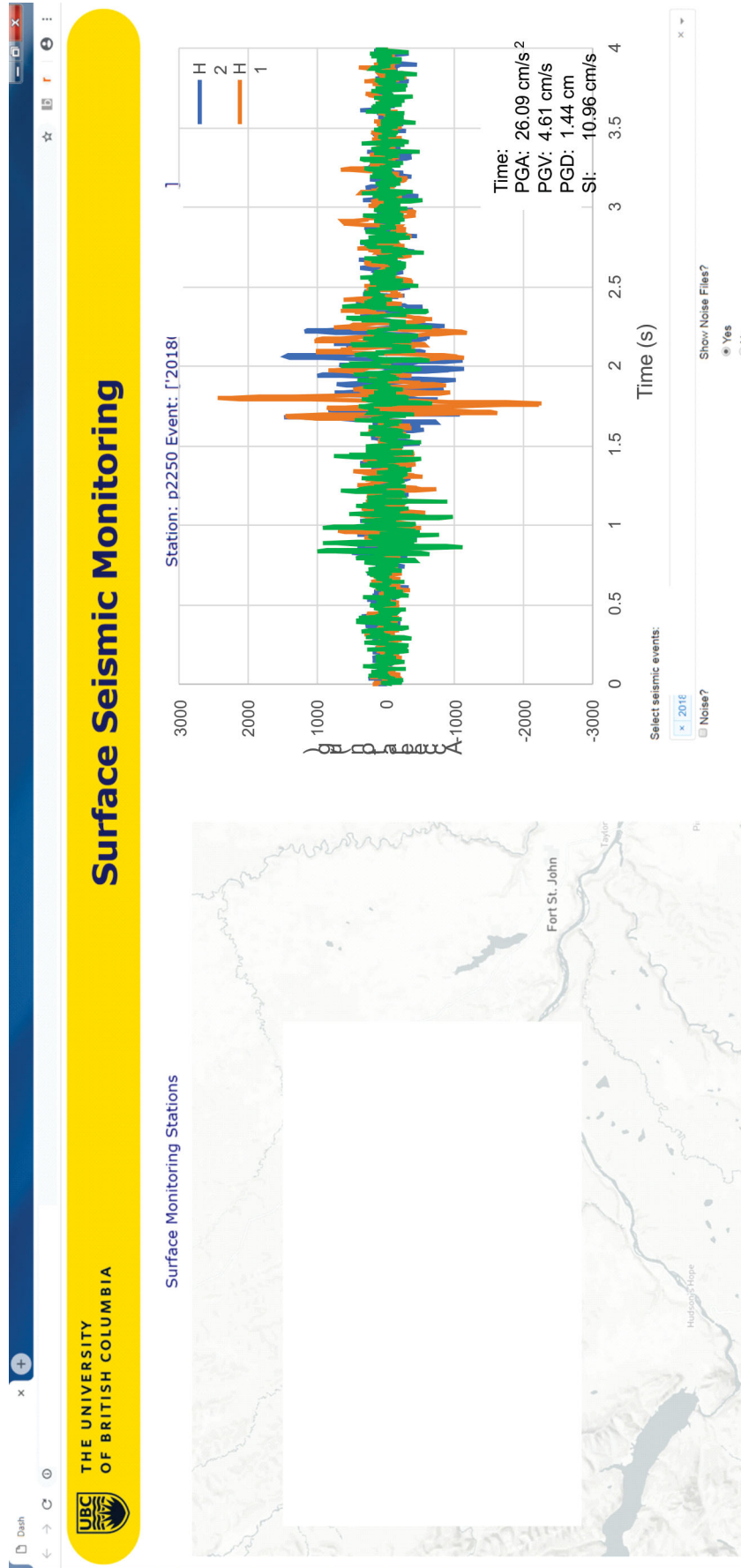


**Figure 1.** Example of typical 3-axis acceleration data recorded for a seismic event by one of the study's stations, as displayed on the online, interactive dashboard. Event time and station location have been removed for confidentiality.

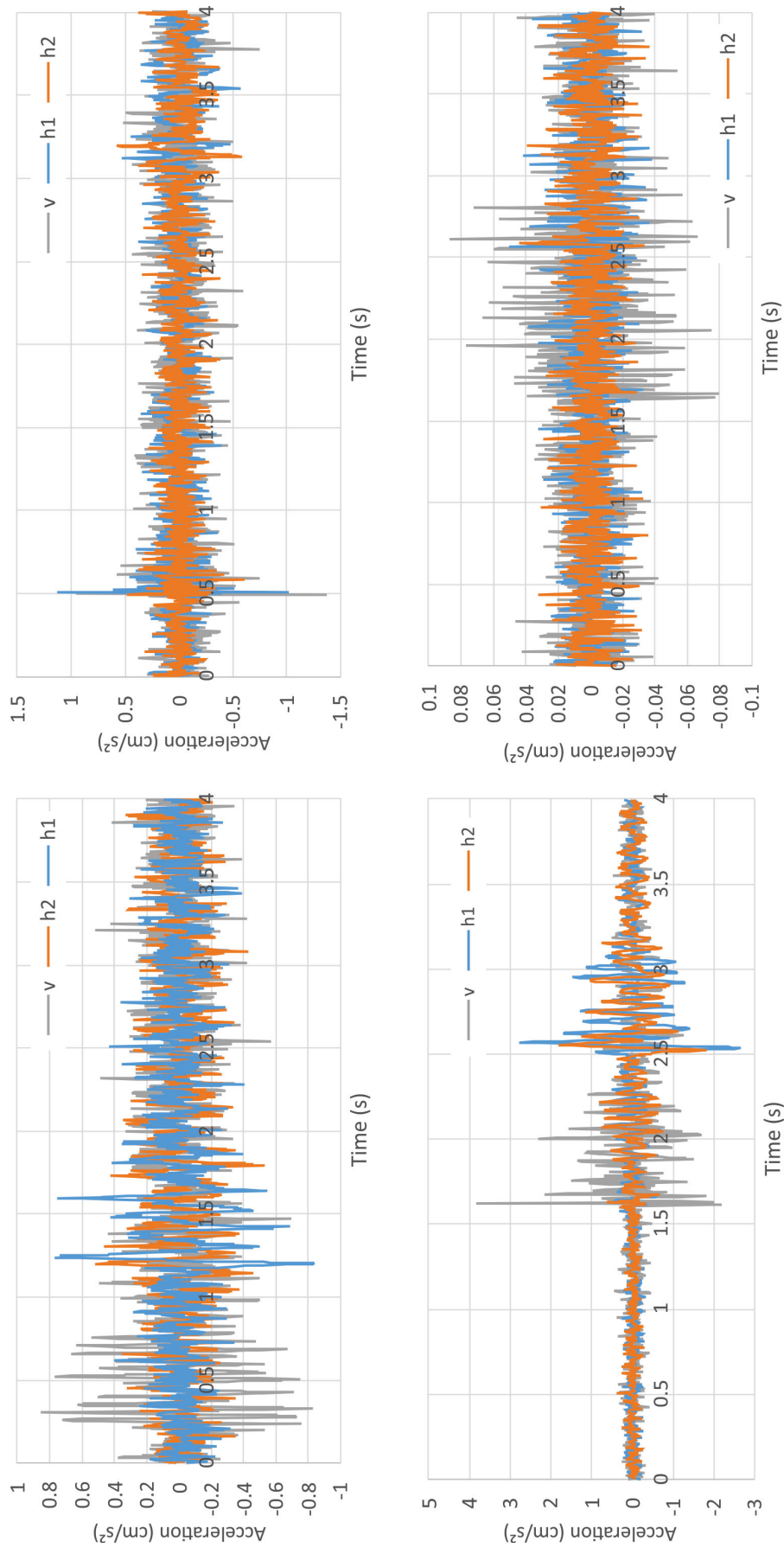


**Figure 2.** Examples of 3-axis acceleration data recorded for seismic events by the study's stations.

## Site Corrections

The measured PGAs were corrected for each event to a reference site-class with a time-averaged shear-wave velocity over the top 30 m ( $V_{s30}$ ) of 760 m/s using the amplification factors from Seyhan and Stewart (2014). In the first step, the response spectral acceleration (PSA) was calculated at frequencies of 0.1–100 Hz for the geometric mean of the horizontal components and the vertical component. The spectral ratio of the horizontal to vertical components (H/V) was then calculated for each event, following which the H/V ratios were log-averaged for each station. The H/V spectral ratios calculated for the study’s stations are shown in Figure 3. The fundamental frequency ( $f_{peak}$ ) was then defined as the frequency at the peak H/V amplitude. Using the correlation of Hassani and Atkinson (2016),  $V_{s30}$  values were estimated from  $f_{peak}$  for each station with recorded events. The class for each site could then be determined from  $V_{s30}$  based on the classification of the National Earthquake Hazards Reduction Program (NEHRP), which could then be used to determine the PGA correction factor ( $F_{PGA}$ ). The  $V_{s30}$ ,  $f_{peak}$ , site class and  $F_{PGA}$  for the study’s stations are shown in Table 1. Following correction, the PGAs for the 25 recorded events range from 0.027%g to 0.23%g. The corrected PGAs, as well as the event magnitude and hypocentral distance when available, are shown in Table 2.

## Attenuation

The site-corrected PGAs versus hypocentral distances for seismic events recorded by the study’s stations were overlain on the data and predictive models presented for the Montney Formation by Babaie Mahani and Kao (2017).

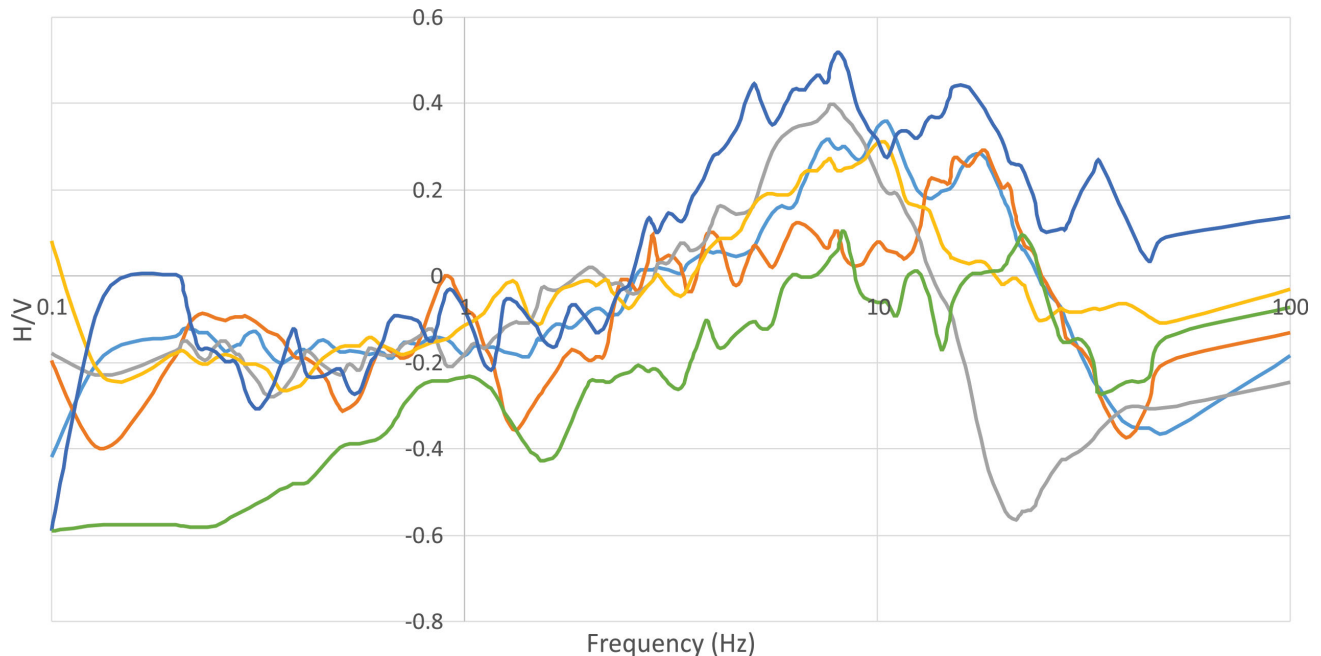


**Figure 3.** Log-averaged spectral ratio of horizontal to vertical components (H/V) versus frequency for each of the study’s stations with recorded seismic events.

The results, which are plotted in Figure 4, show that the datasets are consistent; however, the predictive model for area (a) slightly underestimates the study’s data.

## Magnitude of Completeness

To investigate the magnitude of completeness for the sensors, the magnitude was plotted versus hypocentral distance in Figure 5 for events that were detected by one or more of the study’s stations (blue) and events that were not detected (red). The results indicate that  $M > 1.5$  events are consistently detected within 5 km and  $M > 2$  events within 10 km of one of the stations. It is not possible to comment on the detection threshold for events with  $M < 1.5$  because many smaller events are currently being missed by the simple amplitude threshold and single-station deployments. Three events stand out on Figure 5: one  $M \approx 1.5$  event with hypocentral distance of  $< 1$  km and two  $M \approx 2$  events at distances of  $\sim 5$  km. A denser array would have been required to discriminate the cause of the lower-than-expected ground motions recorded for these events. A possible explanation is that the source radiated asymmetrically with a minimum axis in the direction of the study’s stations.

**Table 1.** Values of  $V_{s30}$ ,  $f_{peak}$ , site class and  $F_{PGA}$  for the study’s stations with recorded seismic events.

Station	$f_{peak}$ (Hz)	$V_{s30}$ (m/s)	Class	$F_{PGA}$
1	8	587.42	C	1.3
2	10	676.08	C	1.3
3	8.33	602.57	C	1.3
4	10.5	697.19	C	1.3
5	18.2	985.93	B	0.9
6	7.7	573.44	C	1.3

**Table 2.** Site-corrected PGA for each seismic event recorded by the study's stations, as well as event magnitude and hypocentral distance when available.

Event	PGA <sub>h</sub> (cm/s <sup>2</sup> )	Distance (km)	M
1	0.48	5.9	1.8
2	0.27	5	1.64
3	0.55	2.2	1.77
4	0.68	1.2	1.74
5	2.22	9.1	2.88
	0.31	17.5	
6	0.27	13.3	2.5
7	0.27	12.6	2.3
8	0.35	12.2	2.5
9	1.54	11	2.7
	0.55	10.4	
	0.76	10.4	
10	0.3	4.6	1.74
11	0.52	5.9	1.54
12	0.31	4.6	1.62
13	0.46	5.1	1.88
14	0.33	6.4	1.72
15	0.36	5.6	1.57
16	0.54	4.9	2.23
17	0.96	4.5	
18	2.01		
	0.79		
19	0.57		
20	0.64		
21	0.97		
22	0.45		
23	0.76		
	1.44		
24	0.28		
	0.93		
25	1.07		

### Depth of Burial

To investigate any possible effects that depth of burial of the study's sensors might have on recorded ground motions, four sensors were installed very recently at different depths (30, 60, 90 and 120 cm) at a single site in a seismically active area. The 90 cm station is the new paired station, while the 60 cm station is a long-term station already located at the site. The sensors are a maximum of 5 m apart, with the 30 and 90 cm sensors and the 60 and 120 cm sensors being within 1 m of each other. While waiting for an event, a test was performed in which a steel I-beam was struck several times with a sledgehammer at a distance of ~15 m from the stations. Due to the short distance between the tests and the stations, the difference in amplitudes (presented in Table 3 for a typical test) results from the varying source-receiver distance and not the depth of burial.

### Summary

The study's accelerographs, which are now providing real-time data to an online interactive dashboard, were deployed

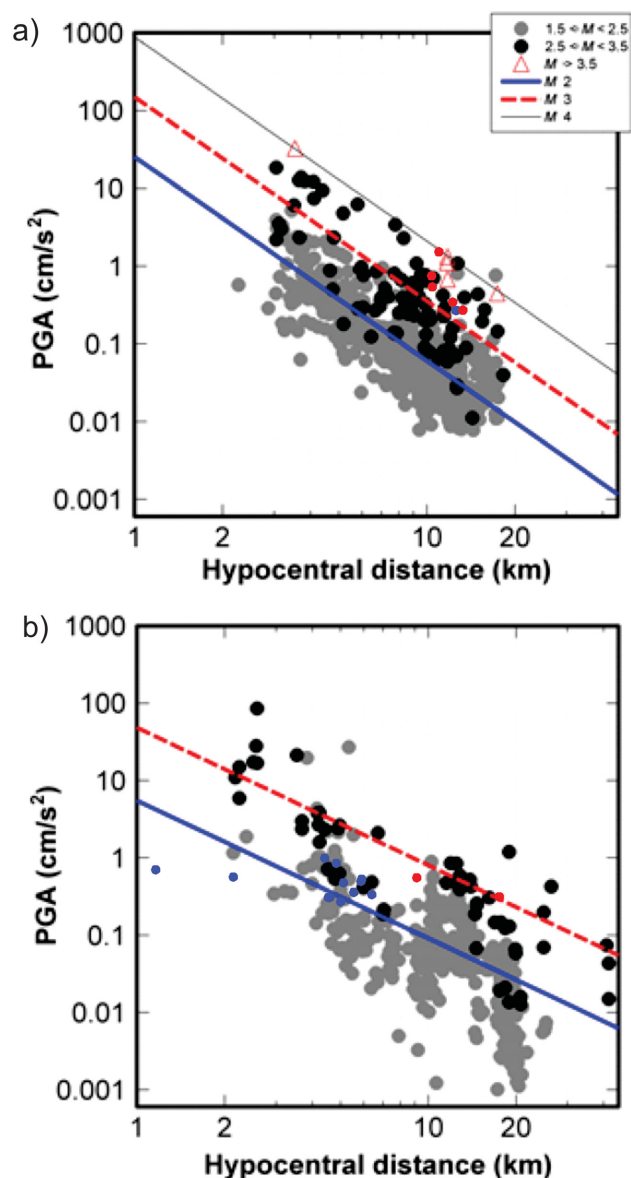


**Figure 4.** Site-corrected PGA versus hypocentral distance for seismic events recorded by the study's array, with events of  $2.5 < M < 3.5$  plotted as red dots (a) and those of  $1.5 < M < 2.5$  plotted as blue dots (b) on figures from Babaie Mahani and Kao (2017).

to monitor two disposal wells and four hydraulic-fracturing operations in the past year. Twenty-five events were recorded during the deployments, with site-corrected PGAs for the geometric mean of the horizontal components ranging from 0.027%g to 0.23%g. These values are consistent with the data and prediction models previously presented for the Montney Formation. The study's first paired station with both a 3C accelerometer and a 3C geophone was recently deployed for testing, and algorithms are being developed for use with the dashboard to locate events and calculate magnitudes in real time. Additional ongoing work includes a study testing the impact of sensor burial depth on recorded ground motions.

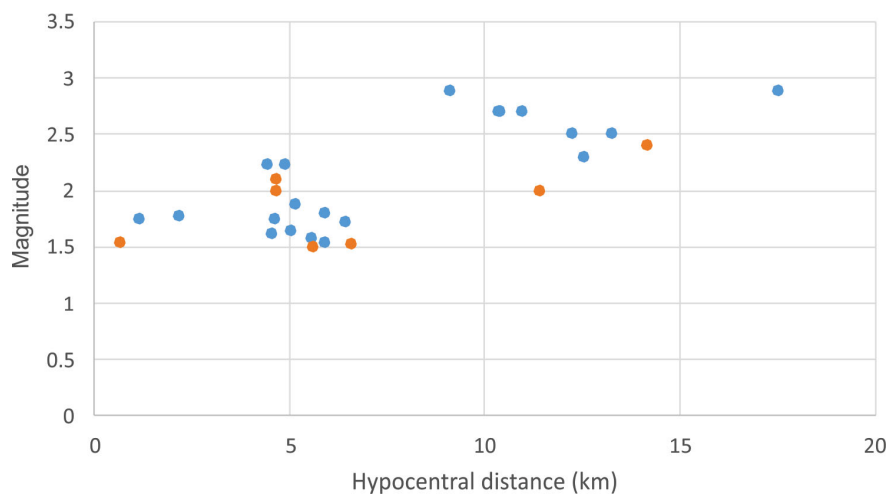


**Figure 5.** Magnitude versus hypocentral distance for events that were detected by one or more of the study's stations (blue) and events that were not detected (red).

**Table 3.** Comparison of PGA (PGA<sub>h</sub>, geometric mean of horizontal components; PGV, vertical component) from a typical I-beam test for the four stations co-located with different depths of burial.

Depth (cm)	PGA <sub>h</sub> (cm/s <sup>2</sup> )	PGV (cm/s <sup>2</sup> )
30	18.05	22.84
60	32.21	42.51
90	27.48	41.83
120	10.24	17.23

## Acknowledgments

The authors thank Geoscience BC for their support and funding for this study. Thanks also go to K. Johansen and C. Ventura for their help with the design and construction of the sensors, and R.M. Bustin for his review of this manuscript.

## References

Azpiri, J. (2016): Early-warning system successfully detects B.C. earthquake; Global News, URL <<http://globalnews.ca/news/2429129/early-warning-system-successfully-detects-b-c-earthquake/>> [December 2018].

Babaie Mahani, A. and Kao, H. (2017). Ground motion from M1.5 to 3.8 induced earthquakes at hypocentral distance <45 km in the Montney play of northeast British Columbia, Canada; *Seismological Research Letters*, v. 89, no. 1, p. 22–34, URL <<https://doi.org/10.1785/0220170119>> [November 2018].

Bustin, A.M.M. and Longobardi, M. (2017). Collecting ground-motion data for the mitigation and prevention of seismicity induced by hydraulic fracturing in the Montney Formation, northeastern British Columbia; *in* Geoscience BC Summary of Activities 2017: Energy, Geoscience BC, Report 2018-4, p. 23–28, URL <[http://cdn.geosciencebc.com/pdf/SummaryofActivities2017/Energy/SoA\\_2017\\_E\\_Bustin.pdf](http://cdn.geosciencebc.com/pdf/SummaryofActivities2017/Energy/SoA_2017_E_Bustin.pdf)> [November 2018].

Hassani, B. and Atkinson G.M. (2016). Applicability of the site fundamental frequency as a VS30 proxy for central and eastern North America; *Bulletin of Seismological Society of America*, v. 106, no. 2, p. 653–664, URL <<https://doi.org/10.1785/0120150259>> [November 2018].

Li, Z., Peng, Z., Hollis, D., Zhu, L. and McClellan, J. (2018). High-resolution seismic event detection using local similarity for large-N arrays; *Scientific Reports*, v. 8, article 1646, URL <<https://doi.org/10.1038/s41598-018-19728-w>> [November 2018].

Seyhan, E. and Stewart, J.P. (2014). Semi-empirical nonlinear site amplification from NGA-West2 data and simulations; *Earthquake Spectra*, v. 30, no. 3, p. 1241–1256, URL <<https://doi.org/10.1193/063013EQS181M>> [November 2018].



# Source Properties of Earthquakes around Hydraulic-Fracturing Sites near Dawson Creek, Northeastern British Columbia

J. Onwuemeka, McGill University, Montréal, QC, john.onwuemeka@mail.mcgill.ca

R.M. Harrington, Ruhr University, Bochum, Germany

Y. Liu, McGill University, Montréal, QC

H. Kao, Natural Resources Canada, Geological Survey of Canada–Pacific, Sidney, BC

Onwuemeka, J., Harrington, R.M., Liu, Y. and Kao, H. (2019): Source properties of earthquakes around hydraulic-fracturing sites near Dawson Creek, northeastern British Columbia; in Geoscience BC Summary of Activities 2018: Energy and Water, Geoscience BC, Report 2019-2, p. 63–66.

## Introduction

Tectonic earthquakes occur due to failure of critically stressed faults. The source of stress perturbation could be natural or anthropogenic. Anthropogenic sources of stress perturbation include solid-matrix stress transfer and pore-pressure enhancement that could result from enhanced hydrocarbon recovery and wastewater injection. In the last few decades, several studies have shown a clear correlation between reservoir stimulation and seismicity (e.g., Schultz et al., 2015; Atkinson et al., 2016). The fluid-injection operations increase fault loading rate to levels above tectonic loading rate. This mechanism reduces recurrence intervals and produces earthquakes with moment magnitude up to  $M_w$  5+ (e.g., 2016  $M_w$  5.8 Pawnee, Oklahoma earthquake; United States Geological Survey, 2016). The recent increase in seismicity related to anthropogenic activities in northeastern British Columbia (BC) and western Alberta (e.g., Atkinson et al., 2016) necessitates a better understanding of the fault-rupture processes for adequate seismic-risk assessment. The source properties, such as stress drop and fault-plane solution of earthquakes, provide insight into crustal-stress conditions and delineate ‘blind’ faults and possible amplitude of induced ground motion.

This project involves monitoring seismicity near hydraulic-fracturing sites in northeastern BC through a data-acquisition campaign employing nine temporary broadband and two permanent Canadian National Seismograph Network (CNSN) stations (Figure 1). The continuous waveform data are scanned to detect earthquakes, including events that are below the detection threshold of the current permanent seismic stations of CNSN around the study area. Fault-plane solution and stress drop of the events are determined from further analysis of the data to delineate seismotectonic structures and infer crustal stresses and their orientation(s), relative fault maturity and ground-motion potential.

*This publication is also available, free of charge, as colour digital files in Adobe Acrobat® PDF format from the Geoscience BC website: <http://www.geosciencebc.com/s/SummaryofActivities.asp>.*

## Methods

### Fault-Plane Solution

Fault-plane solutions are determined by fitting a suite of synthetic waveforms, precalculated for ~35 000 possible moment-tensor solutions using a 1-D velocity model, to observed data. To infer the moment-tensor solutions, a bootstrap-based full moment-tensor probabilistic-inversion scheme (Grond), with capability to infer moment-tensor solution of small earthquakes recorded by a sparse seismic network, is used to determine fault-plane solutions (Dahm et al., 2018). Synthetic waveforms, precalculated using Qseis code (Wang, 1999), are fit to recorded waveforms to determine the best fault-plane solution.

### Stress Drop

Stress drop (i.e., the difference between initial and final stress on a fault following an earthquake) is calculated by analyzing observed data in the frequency domain. An earthquake waveform is a convolution of source term, instrument term and path term (i.e., velocity structure between source and instrument locations). To isolate the source term, the instrument and path terms must first be removed. The spectral ratio of co-located events with magnitude difference  $\geq 1$  is computed to determine their relative source term; proximity of event pairs are quantified by their cross-correlation values. The spectral-ratio approach is used to infer parameters such as corner frequency (a measure of the source duration) and seismic moment (a measure of energy), hence stress drop. The spectral ratios are fit to determine corner frequency of the larger event, as well as the smaller event if resolvable, and their relative seismic moment using the expression

$$\Omega(f) = \frac{\Omega_0^m}{\Omega_0^e} \left[ \frac{\left(1 + \left(f/f_c^e\right)^{2n}\right)}{\left(1 + \left(f/f_c^m\right)^{2n}\right)} \right]^{1/2}$$

where the  $m$  and  $e$  superscripts refer to the main event and empirical Green’s Function (eGF) event, respectively, and

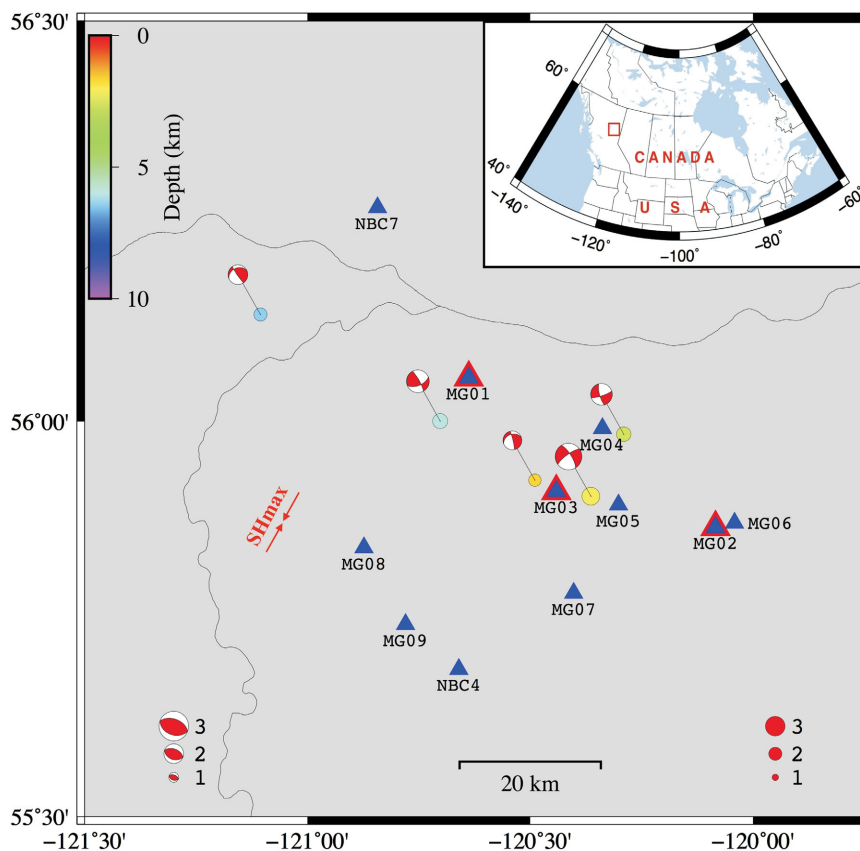


**Figure 1.** Study area in northeastern British Columbia. Coloured circles are scaled by local magnitude and represent events reported in the Natural Resources Canada catalog. ‘Beachballs’ represent the fault-plane solution of each event. Blue triangles indicate nine temporary broadband stations (MG01 to MG09) and two permanent CNSN stations (NBC4 and NBC7). Triangles with red border indicate co-located broadband and strong-motion stations. Red arrows indicate approximate orientation of regional maximum compressional stress inferred from P-axes trend.

$\Omega_0$  is the long-period spectra amplitude,  $f$  is frequency,  $f_c$  is corner frequency,  $n$  is the spectra falloff rate and  $\gamma$  is a factor that controls the shape of the corner (Boatwright, 1978; Hartzell, 1978).

## Results and Next Steps

Preliminary fault-plane solutions highlight failure on faults oriented roughly northwest-southeast from northeast-southwest regional maximum horizontal compression (Figure 1), possibly exerted by the subduction of the Pacific Plate beneath the North American Plate.

The next steps involve refinement of the velocity model using a tomography technique. The refined velocity model would further constrain the moment-tensor solutions. The python script for the spectral-ratio analysis is almost completed and testing will begin in the coming months. This project will be completed by mid-2019 as part of the lead author’s graduate research and published in the lead author’s thesis.

## Acknowledgments

This project is funded by a Natural Sciences and Engineering Research Council of Canada Strategic Fund to R.M. Harrington and Y. Liu, with support from the Geological Survey of Canada and British Columbia Oil and Gas Commission. J. Onwuemeka thanks the reviewer, J. Kubanek, for constructive comments that helped improve this paper, and also acknowledges support through the Geoscience BC Graduate Scholarship.

## References

- Atkinson, G.M., Eaton, D.W., Ghofrani, H., Walker, D., Cheadle, B., Schultz, R., Shcherbakov, R., Tiampo, K., Gu, J., Harrington, R.M. and Liu, Y. (2016): Hydraulic fracturing and seismicity in the Western Canada Sedimentary Basin; *Seismological Research Letters*, v. 87, no. 3, p. 631–647.
- Boatwright, J. (1978): Detailed spectral analysis of two small New York State earthquakes; *Bulletin of the Seismological Society of America*, v. 68, no. 4, p. 1117–1131.
- Dahm, T., Heimann, S., Funke, S., Wendt, S., Rappsilber, I., Bindi, D., Plenefisch, T. and Cotton, F. (2018): Seismicity in the block mountains between Halle and Leipzig, central Ger-

- many: centroid moment tensors, ground motion simulation, and felt intensities of two  $M \sim 3$  earthquakes in 2015 and 2017; *Journal of Seismology*, v. 22, no. 4, p. 985–1003, URL <<https://link.springer.com/article/10.1007/s10950-018-9746-9>> [November 2018].
- Hartzell, S.H. (1978): Earthquake aftershocks as Green's functions; *Geophysical Research Letters*, v. 5, no. 1, p. 1–4.
- Schultz, R., Stern, V., Novakovic, M., Atkinson, G. and Gu, Y.J. (2015): Hydraulic fracturing and the Crooked Lake Sequences: insights gleaned from regional seismic networks; *Geophysical Research Letters*, v. 42, no. 8, p. 2750–2758.
- United States Geological Survey (2016): M 5.8 – 14 km NW of Pawnee, Oklahoma; United States Geological Survey, Earthquake Hazards Program, <<https://earthquake.usgs.gov/earthquakes/eventpage/us10006jxs/executive>> [November 2018].
- Wang, R. (1999): A simple orthonormalization method for stable and efficient computation of Green's functions; *Bulletin of the Seismological Society of America*, v. 89, no. 3, p. 733–741.



## GHGMap: Detection of Fugitive Methane Leaks from Natural Gas Pipelines, British Columbia and Alberta

M.J. Whiticar, University of Victoria and Geochemical Analytic Services Corporation, Victoria, BC  
whiticar@uvic.ca

L.E. Christensen, NASA Jet Propulsion Laboratory, California Institute of Technology, Pasadena, US

C.J. Salas, Geoscience BC, Vancouver, BC

P. Reece, InDro Robotics Corp., Salt Spring Island, BC

---

Whiticar, M.J., Christensen, L.E., Salas, C.J. and Reece, P. (2019): GHGMap: detection of fugitive methane leaks from natural gas pipelines, British Columbia and Alberta; *in* Geoscience BC Summary of Activities 2018: Energy and Water, Geoscience BC, Report 2019-2, p. 67–76.

### Introduction

GHGMap is a research and development project focusing on developing and testing new instrumentation and approaches to measure atmospheric greenhouse gases (GHG). The new consortium of Geoscience BC, Geochemical Analytic Services Corporation, NASA/Jet Propulsion Laboratory (JPL) and InDro Robotics Corp. has developed the capability to provide detailed, unmanned, aerial, regional and site surveys of GHG.

The consortium has developed a system that uses the combined technologies of a state-of-the-art open-path laser spectrometer (OPLS), developed by NASA/JPL (Christensen, 2014), deployed on a specialized small unmanned aerial vehicle (UAV; Figure 1; Whiticar et al., 2018). This OPLS/UAV platform can measure trace levels of GHG in the atmosphere, including methane, ethane and carbon dioxide. This system is ideal for the detection, quantification and source differentiation of GHG emissions and budgets because of the extreme detection sensitivity of the OPLS (parts per billion); the high measurement frequency (10 Hz) of the sensor; the small size, weight and low power consumption of the sensor; and the precise operation and navigation of the UAV.

This novel monitoring capability permits verifiable identification, control and quantitation of emissions (e.g., well and/or pipeline integrity, landfills, feedlots, etc.) and monitoring of mitigation operations. The initial program focuses on major GHG emitters in western Canada (i.e., British Columbia, Alberta, Saskatchewan; Whiticar et al., 2018), but is expanding to private sector enterprise both nationally and internationally.

A critical exclusive feature of the OPLS/UAV platform is that it can fly close to (<1 m) and hover over identified anomalies, with real-time flight-path and navigation capabilities (Figure 2). In concert with the methane (CH<sub>4</sub>) measurements, simultaneous wind direction and speed measurements can also be made by sonic anemometry.

The data collected is stored on the OPLS and sent in real-time to the receiver station for the drone control (Whiticar et al., 2018). The high precision navigation on the drone allows repeatable positioning of the UAV within 50 cm and extremely reduced flying altitude (~1–10 m) in contrast to helicopter or fixed-wing aircraft surveys (>150 m). These high precision, close proximity measurements by the OPLS/UAV platform combined with the low flight velocities (1–3 m/s) permit increased and precise detection capabilities (Figure 2). These are unparalleled by other methods, such as handheld monitors, land-vehicle-mounted mobile sensors, manned aircraft or satellites.

The OPLS/UAV platform is now mature and has been deployed over a wide range of methane emitters (Whiticar et



**Figure 1.** GHGMap's open-path laser spectrometer (OPLS) on a small unmanned aerial vehicle (UAV).

---

*This publication is also available, free of charge, as colour digital files in Adobe Acrobat® PDF format from the Geoscience BC website: <http://www.geosciencebc.com/s/SummaryofActivities.asp>.*

al., 2018). In 2016 and 2017, initial OPLS/UAV test surveys were successfully conducted over several natural gas distribution and pumping facilities, gas well sites, a landfill and a sewage treatment plant. A summary of the basic technology and these results has been published in Whitar et al. (2018). This paper discusses a further application of the OPLS/UAV platform, namely the ability to detect leaks from surficial and buried natural gas pipelines.

### Pipeline Survey Demonstration Locations

With the generous support of AltaGas Utilities Inc. (AltaGas), the GHGMap team was invited to demonstrate the OPLS/UAV technology along their high pressure natural gas pipeline in Alberta (Figure 3). The tests were conducted in November 2017 with temperatures at approximately  $-5^{\circ}\text{C}$ . The first test involved a small, short,



**Figure 2.** GHGMap's open-path laser spectrometer/unmanned aerial vehicle (OPLS/UAV) platform surveying at a gas distribution plant, Victoria region, British Columbia.

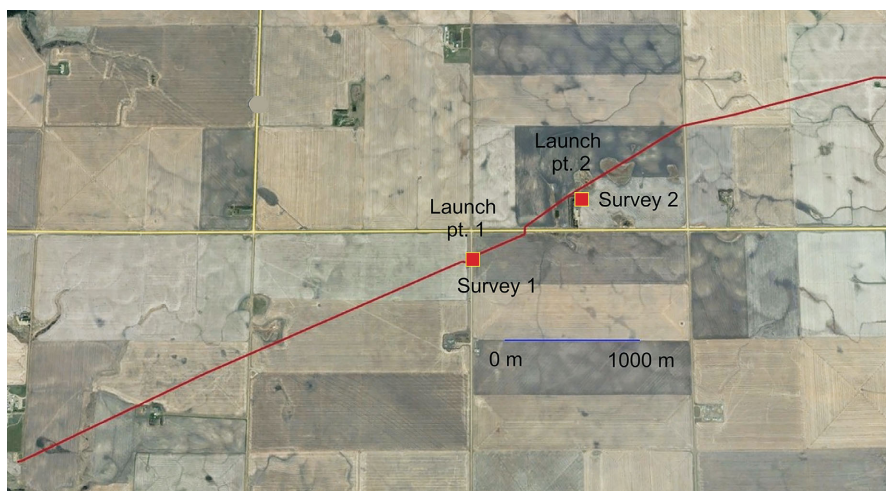


**Figure 3.** Survey map of AltaGas Utilities Inc. pipeline testing area, Alberta. The red line shows the location of the buried, high-pressure gas pipeline. The red squares show the two launch points of the open-path laser spectrometer/unmanned aerial vehicle (OPLS/UAV) platform for the test surveys. Abbreviation: pt, point.

controlled release of natural gas on the AltaGas property. AltaGas then chose two segments of their buried high pressure natural gas pipeline for further testing (Figure 4). At a point along each of the two segments, there was a controlled natural gas release point established by AltaGas. The GHGMap team did not know the locations of these two releases beforehand. The natural gas is predominantly  $\text{CH}_4$  ( $>95\%$ ), so the test was well-suited to the OPLS  $\text{CH}_4$  sensor. The launch points and approximated survey path are indicated in Figure 4. Although the OPLS/UAV platform could fly for greater than 2 km ( $\sim 15$  min) in these cold temperatures, the flights were set to approximately 10 min or  $\sim 1$  km total flight distance (out and back). In warmer temperatures (approx.  $>5^{\circ}\text{C}$ ), the flight time increases to  $\sim 45$  min.

### Pre-Survey Calibration Release Test

As an initial, pre-survey check, AltaGas set-up a small, controlled release of natural gas on their Alberta property. This limited, surface release test was to calibrate the UAV navigation and verify that the OPLS could detect  $\text{CH}_4$  prior to the fieldwork. This successful test is illustrated in Figure 5, which is a time series plot of the UAV altitude (red line) and the OPLS  $\text{CH}_4$  concentration (black line). For the first half of this test (38 090–38 190 s), the drone was stationary, as indicated by the altimetry, and approximately 50 m from the point of the small  $\text{CH}_4$  release. During this time the  $\text{CH}_4$  concentrations measured by the OPLS were generally low. However, there were some minor kicks of elevated  $\text{CH}_4$  concentrations during this time period, suggesting the presence of a gas leak in the vicinity. The detection of these  $\text{CH}_4$  concentrations that were higher than background levels likely depended on the wind direction and strength. At approximately 38 190 s (Figure 5), the UAV rose to  $\sim 150$ – $350$  cm above the ground as it traversed

across the AltaGas property. As the UAV passed the controlled emission point on the two transects (approx. 38 230 and 38 300 s, Figure 5), the  $\text{CH}_4$  spiked to values up to 15 ppm, which is approximately 10 times the tropospheric  $\text{CH}_4$  background levels. This controlled natural gas release demonstrated that the OPLS/UAV system could readily detect and localize a small surficial gas leak.

### Natural Gas Pipeline Release Surveys

Four individual flights were made by the OPLS/UAV platform at the two AltaGas buried pipeline locations and a total of 23 445 discrete

methane (CH<sub>4</sub>) measurements were taken (Table 1). The weather was approximately -4°C, with clear conditions and firm winds predominantly from the west (0–4.7 m/s, mean = 1.57 m/s; Figure 6). A detailed map of the actual flight paths flown by the OPLS/UAV at each of the locations 01 and 02 is shown in Figure 7. Two flight segments were made at each of the locations.

The minimum CH<sub>4</sub> value measured was 1.58 ppm and the highest was 25.8 ppm, which is more than 16 times higher than normal tropospheric CH<sub>4</sub> background levels (Table 1). The mean CH<sub>4</sub> concentration was 2.61 ppm with a standard deviation of 0.95 ppm. As anticipated, the vast majority of the CH<sub>4</sub> measurements revealed concentrations that were at, or close to, the expected background tropospheric CH<sub>4</sub> level of ~1.8 ppm. This is illustrated in Figure 8a and b with the histograms of measured CH<sub>4</sub> concentrations (1.5–4 ppm and 4–30 ppm). Table 1 also reveals a strong skewness and kurtosis to the CH<sub>4</sub> distributions at the two locations. The strong skewness is also evident in the unidirectional tails of CH<sub>4</sub> concentration in the histograms. Similarly, the probability plot (Figure 8c) clearly shows the single-ended tailing of methane to higher concentrations.

The importance of elucidating the CH<sub>4</sub> distributions is to determine thresholds for the classification and delineation of background and anomalous CH<sub>4</sub> values. Using this information, the following categories for CH<sub>4</sub> concentration were defined:

- 1) background, 1.6 to <2.5 ppm CH<sub>4</sub> (blue colour);
- 2) elevated, 2.5 to <4.0 ppm CH<sub>4</sub> (green colour);
- 3) anomalous, 4.0 to <10.0 ppm CH<sub>4</sub> (orange colour);
- 4) highly anomalous, ≥10.0 ppm CH<sub>4</sub> (red colour).

### Pipeline Release Location 01 (Flights 01, 02)

The location 01 surveys were conducted over an open harvested grain field. The ground was frozen and had a light snow cover (Figures 9, 10). As illustrated in Figure 6, the

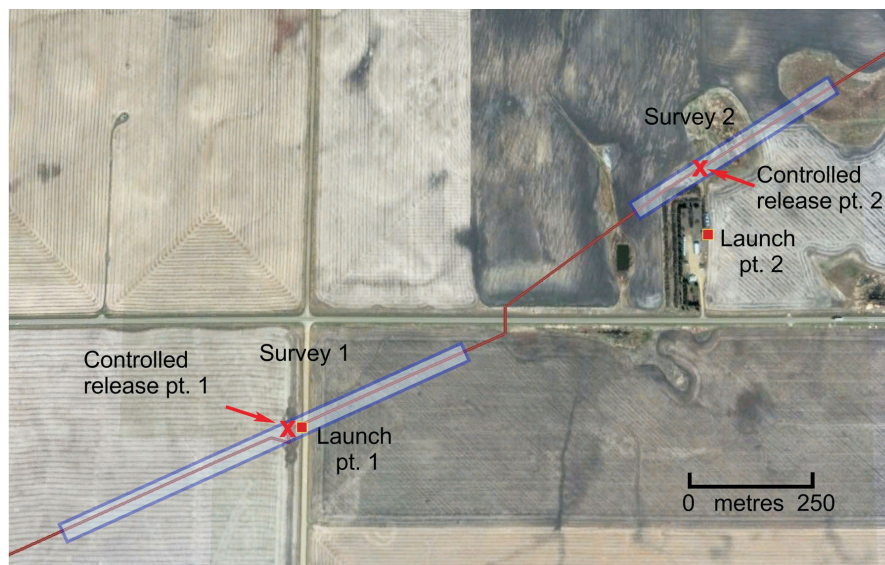


**Figure 4.** Detailed locations of two AltaGas Utilities Inc. (AltaGas) pipeline test leak detection surveys, Alberta. The red line shows the location of the buried, high-pressure gas pipeline. The red squares show the two launch points of the open-path laser spectrometer/unmanned aerial vehicle (OPLS/UAV) platform for the test surveys. The two controlled natural gas release points set by AltaGas are marked by X. Abbreviation: pt, point.

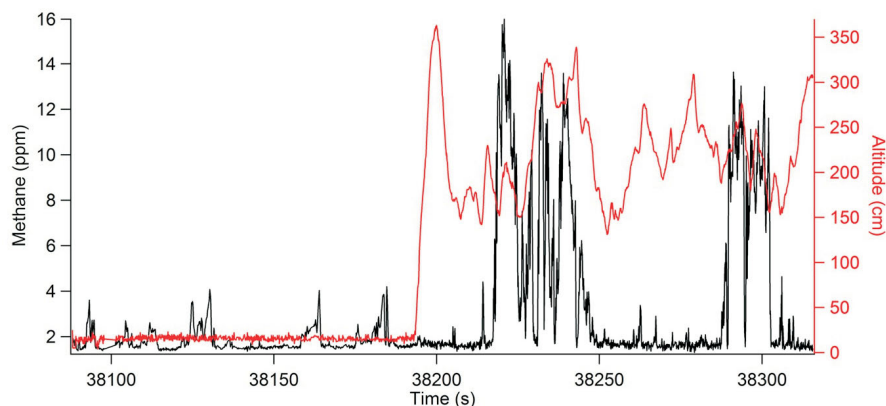


**Figure 5.** Small, controlled natural gas release at AltaGas Utilities Inc., Alberta. The red line is the altitude of the unmanned aerial vehicle (UAV). The black line is the methane concentration detected in real-time by the open-path laser spectrometer (OPLS).

**Table 1.** Statistics of methane concentration measurements for locations 01, 02 and all four flights combined, at AltaGas Utilities Inc., Alberta.

Parameter	Location 01	Location 02	Combined
Minimum (ppm)	1.58	1.58	1.58
Maximum (ppm)	25.8	25.4	25.8
Number of measurement points	11 479	11 970	23 445
Mean (ppm)	2.64	2.59	2.61
Median (ppm)	2.54	2.43	2.48
Standard deviation (ppm)	0.913	0.976	0.95
Variance	0.833	0.952	0.89
Standard error	0.0085	0.00892	0.0062
Skewness	10.79	10.42	10.61
Kurtosis	168	166	168

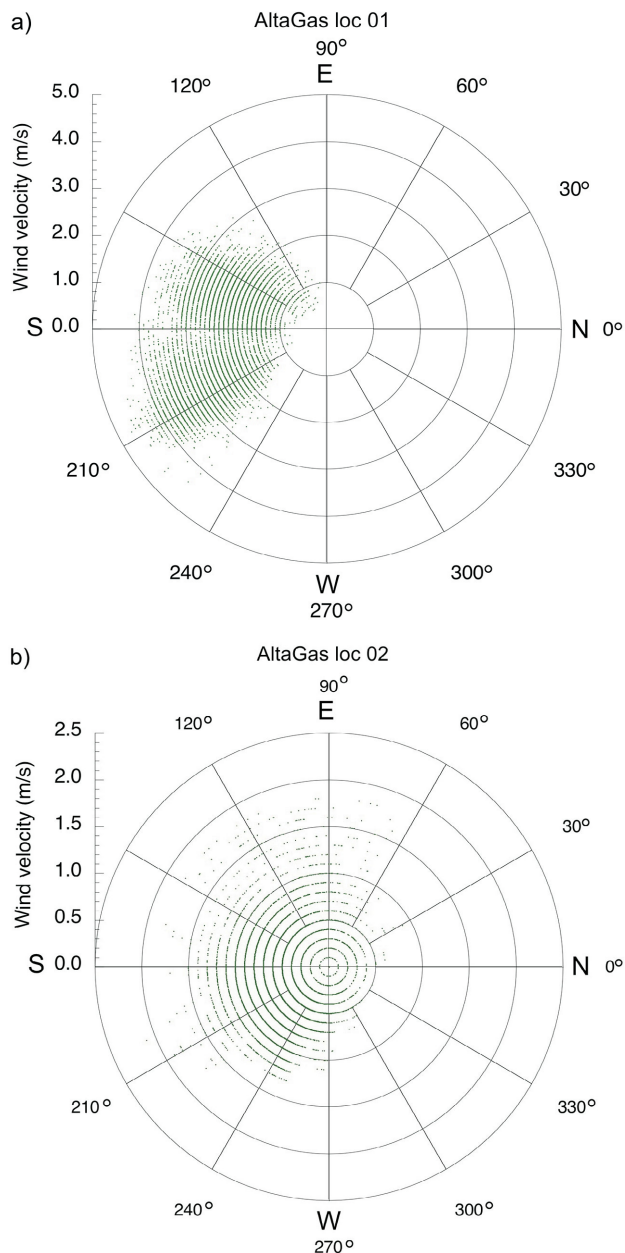
wind during flights 01 and 02 was firm and steady from the west and southwest at up to 5 m/s (18 km/h). The highest gusts were approaching the operational limits of a light UAV.

The 11 479 discrete CH<sub>4</sub> measurements by OPLS at location 01 generally had low concentrations, i.e., <4.0 ppm CH<sub>4</sub>, with a mean value of 2.64 ppm CH<sub>4</sub> and a standard deviation of 0.913 ppm (Table 1). Figure 11 shows that the two flights (01 and 02), for the most part, revealed background levels of CH<sub>4</sub>. However, at the location of the controlled natural gas release, significantly elevated levels of

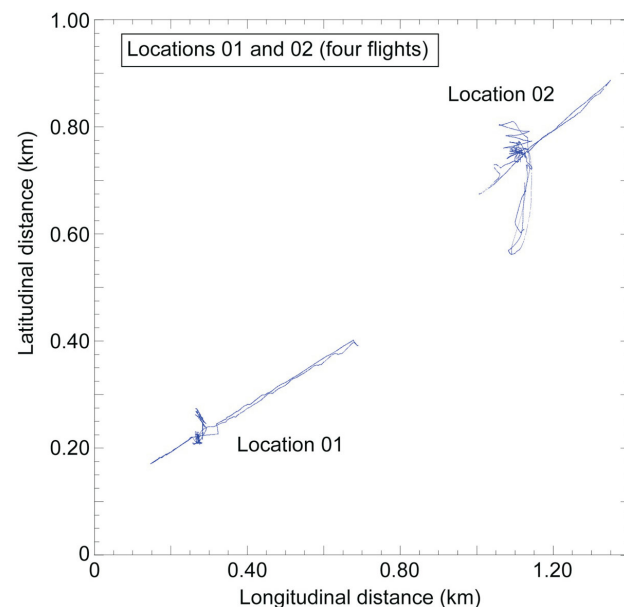
CH<sub>4</sub> were detected, up to 26 ppm. The moderately high values directly to the north of the release point reflect the strong winds (Figure 6) that rapidly dispersed the CH<sub>4</sub> plume.

Figure 12 shows an aerial view of the OPLS/UAV platform survey tracks (black line) for location 01, flight 02, proximal to and directly at the controlled release point. The CH<sub>4</sub> concentrations during the survey are represented by the coloured points in the figure, with cooler colours representing higher concentrations. The figure also shows the anemometry wind vectors to the anomalous CH<sub>4</sub> concentration (i.e., above CH<sub>4</sub> background levels) points in flight 02. These vectors show the wind directions and speeds at the time of the CH<sub>4</sub> measurement. The real-time measurement combination of the wind direction and strength with the CH<sub>4</sub> concentration permits a back-trajectory calculation of the natural gas plume anomaly to the source.

Time series plots of the CH<sub>4</sub> concentrations and the flight altitude of the OPLS/UAV platform for location 01, flight 02, are shown in Figure 13. The strongly delineated points of higher CH<sub>4</sub> concentrations clearly demonstrate the ability of the OPLS/UAV platform to make precise and spatially focused measurements in real time. The figure also illustrates a critical advantage of the drone-based measurement strategy. By flying the OPLS/UAV platform at different altitudes, not only can the horizontal distribution and footprint of CH<sub>4</sub> plumes be surveyed, but also the vertical distribution. Figure 13 indicates that the anomalous CH<sub>4</sub> concentrations measured at close to ground level (~1–2 m) are not observed at higher altitudes, up to 20 m. This indicates that the anomalous CH<sub>4</sub> plume is essentially



**Figure 6.** Windroses of wind directions and velocities at **a)** location (loc) 01 and **b)** location 02, at AltaGas Utilities Inc. (AltaGas), Alberta. The data refer to the direction the wind blows from, i.e., predominantly from the west.



**Figure 7.** Detailed flight location paths of four pipeline test leak detection flights at locations 01 and 02, at AltaGas Utilities Inc., Alberta.

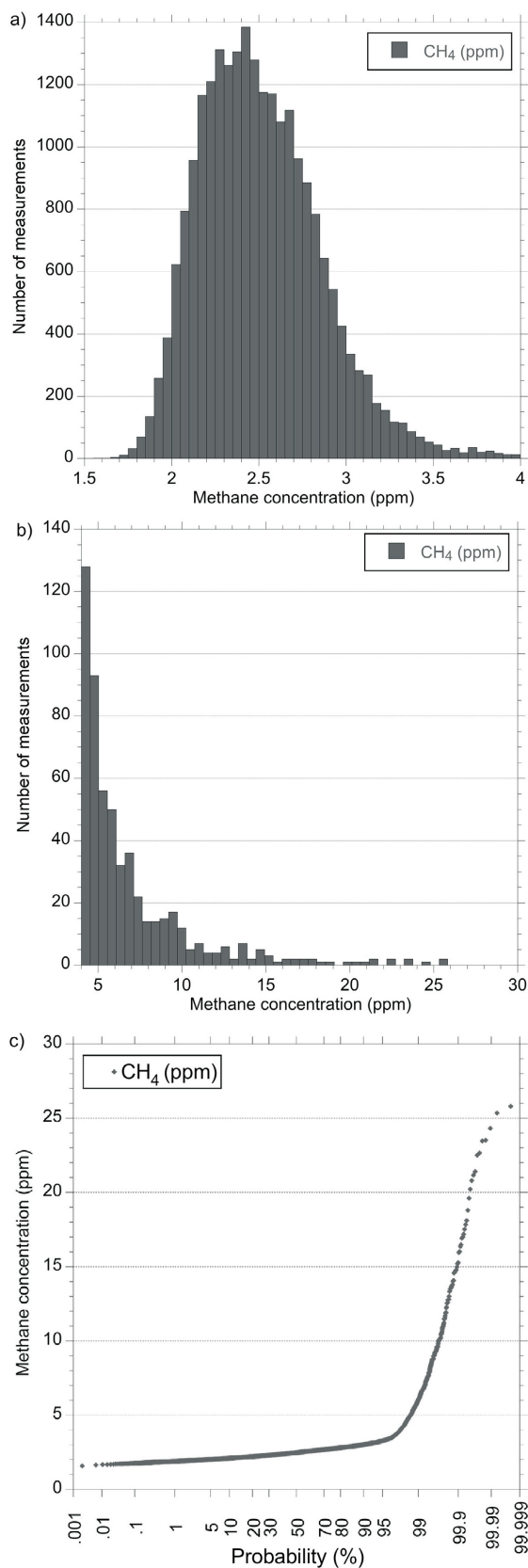


**Figure 8.** Measured methane (CH<sub>4</sub>) concentrations at locations 01 and 02 (combined), at AltaGas Utilities Inc., Alberta: **a)** histogram of 1.5–4 ppm range, **b)** histogram of 4–30 ppm range and **c)** probability plot .



**Figure 9.** Photograph of survey field containing the buried, high-pressure natural gas pipeline at location 01, at AltaGas Utilities Inc., Alberta.



**Figure 10.** Photograph of open-path laser spectrometer/unmanned aerial vehicle (OPLS/UAV) platform at location 01 survey site, at AltaGas Utilities Inc., Alberta.

restricted to ground level and dissipates very rapidly at higher elevations.

This altitude dependence of the CH<sub>4</sub> concentration anomaly is clearly observed in Figure 14. Most of the elevated CH<sub>4</sub> values are at ground level. The small number of hits at 5 and 8 m were measured downstream of the plume release point.

#### Pipeline Release Location 02 (Flights 03, 04)

Analogous to location 01, the location 02 test survey consisted of two flights (03 and 04) over frozen fields with a light snow cover (Figure 15). The winds during flights 03 and 04 were <2.5 m/s (<10 km/h), which is substantially lower than at location 01 (Figure 6). The dominant wind direction was still from the west, but there was considerably more directional variability than at location 01.

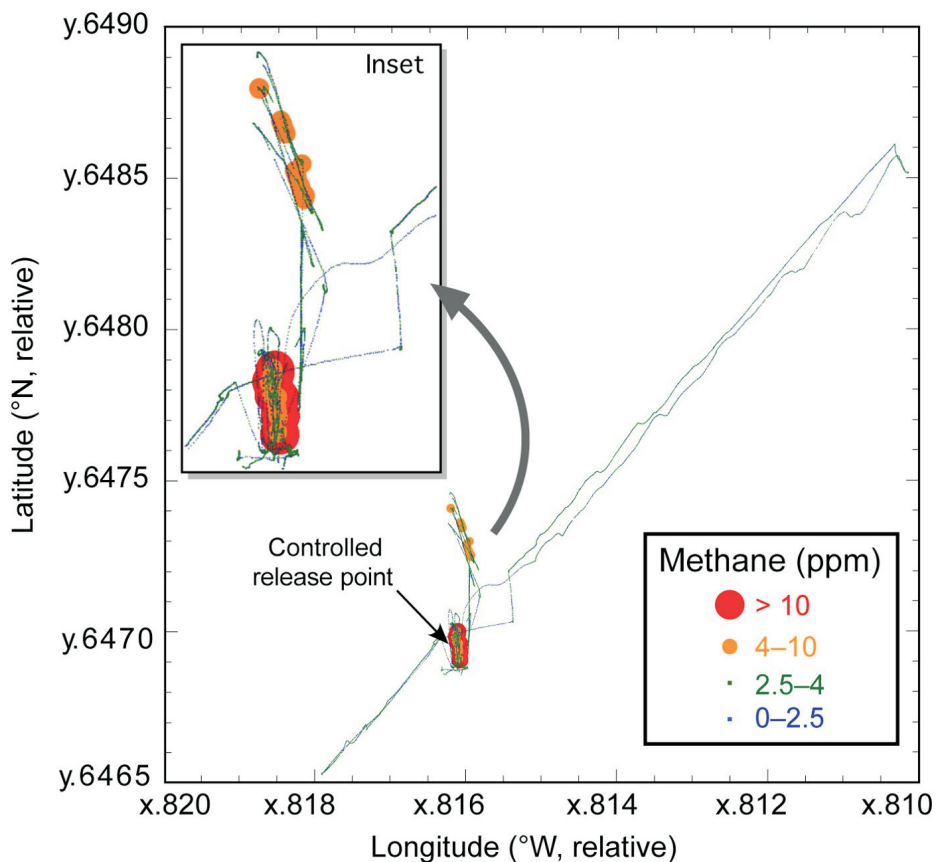


**Figure 11.** Overview of methane concentrations for location 01, flights 01 and 02, at AltaGas Utilities Inc., Alberta. The warmer (orange/red) colours indicate anomalously higher methane concentrations (significantly above background levels for methane).

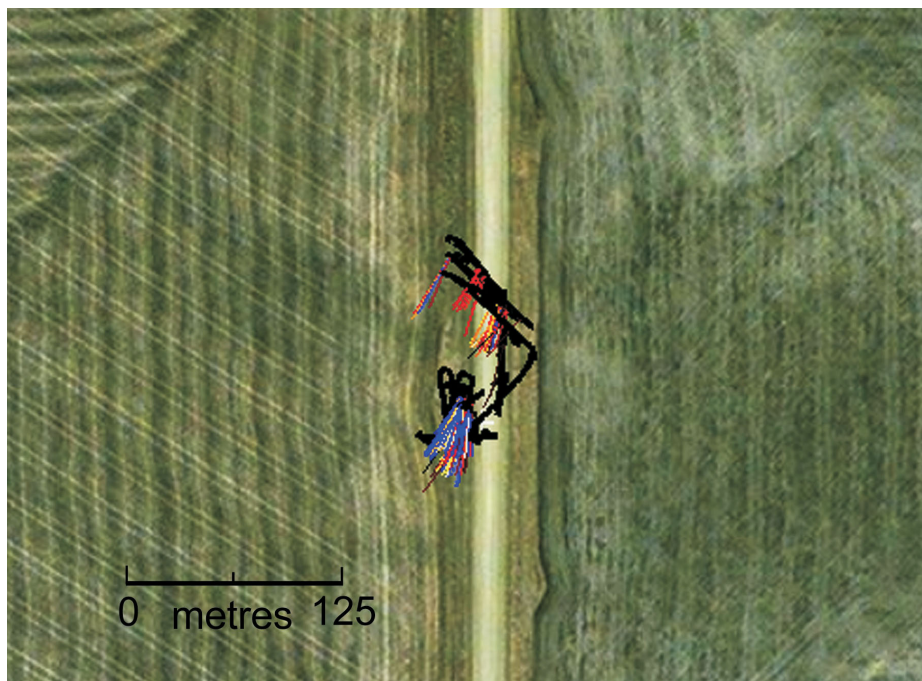


**Figure 12.** Overview of methane concentrations and wind vectors for location 01, flight 02, at AltaGas Utilities Inc., Alberta. The cooler colours indicate anomalously higher methane concentrations (above background levels for methane). The black line is the open-path laser spectrometer/unmanned aerial vehicle (OPLS/UAV) platform survey track.

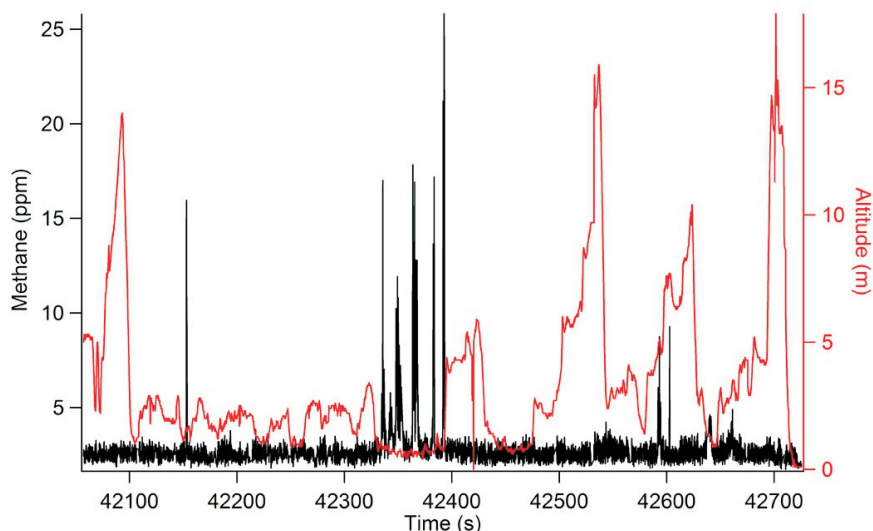


**Figure 13.** Time series plot of methane concentrations (black line) and open-path laser spectrometer/unmanned aerial vehicle (OPLS/UAV) platform altitude (red line) for location 01, flight 02, at AltaGas Utilities Inc., Alberta.

There were 11 970 discrete CH<sub>4</sub> measurements taken during the two flights at location 02 (flights 03, 04). Both flights generally returned low background CH<sub>4</sub> concentrations, <4.0 ppm (Table 1), similar to that measured at location 01. The mean CH<sub>4</sub> value was 2.59 ppm with a standard deviation of 0.976 ppm (Table 1). The mapping of the CH<sub>4</sub> concentrations to the flight track is shown in Figure 16. The two flights 03 and 04 results were dominated by background values for CH<sub>4</sub>. However, at the place of the con-

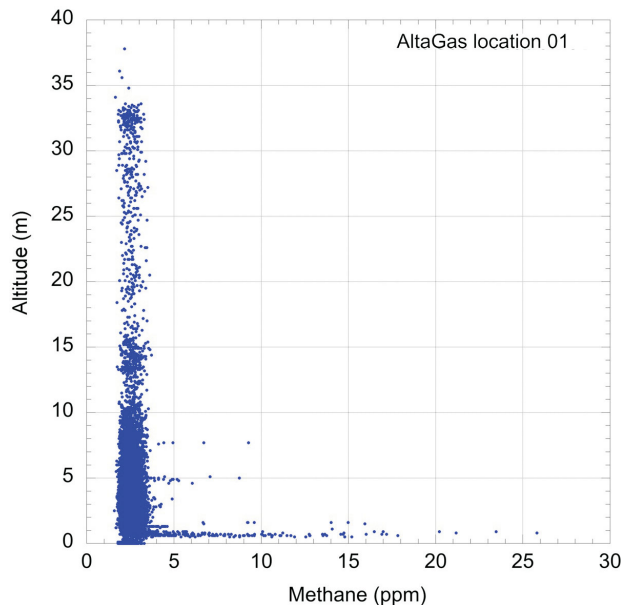


**Figure 14.** Relationship of methane concentration to the altitude (determined by light detection and ranging [LiDAR] measurements) of the open-path laser spectrometer/unmanned aerial vehicle (OPLS/UAV) platform at the time of measurement, location 01, at AltaGas Utilities Inc. (AltaGas), Alberta.

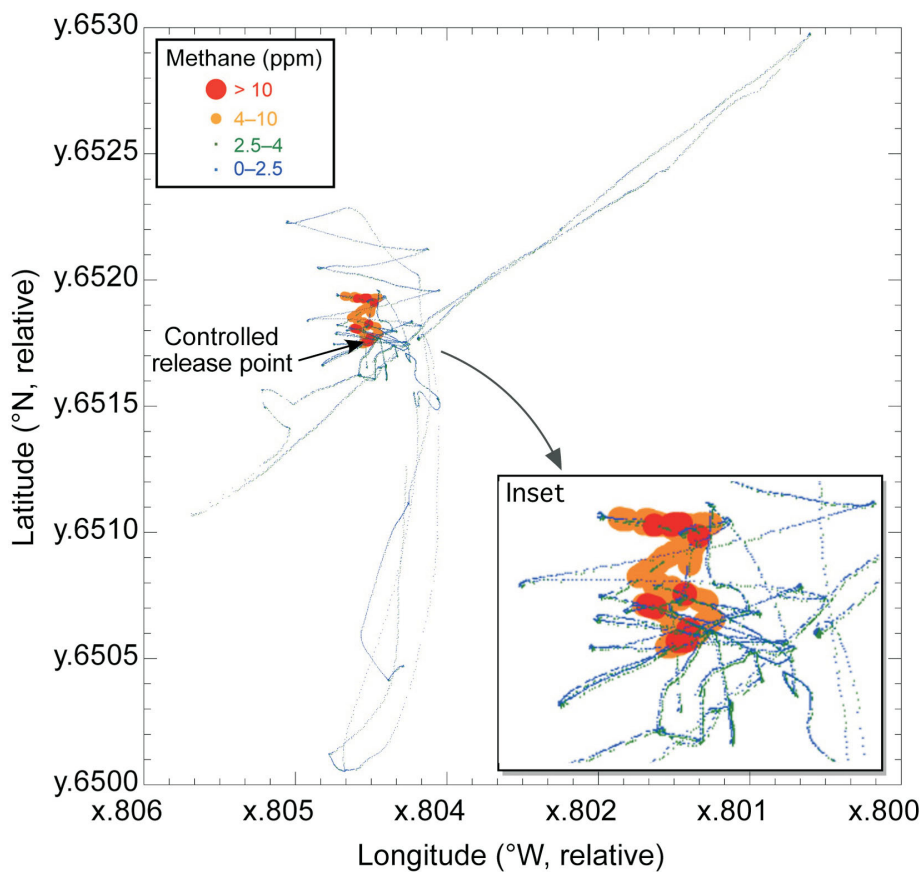
trolled natural gas release, significantly elevated levels of CH<sub>4</sub> were detected, up to 25 ppm, again similar to location 01. The dispersion of the CH<sub>4</sub> plume at location 02 was less pronounced than at location 01.

Figure 17 shows the aerial view of location 02 with the OPLS/UAV platform survey tracks for flight 04, with the CH<sub>4</sub> concentrations overlain at each point. The figure shows the location of the elevated CH<sub>4</sub> concentrations at the controlled release point. The anomalous CH<sub>4</sub> concentrations are flagged by colour, with cooler colours (blue) indicating higher CH<sub>4</sub> concentrations.

Time series plots of the CH<sub>4</sub> concentrations and the flight altitude of the OPLS/UAV platform for location 02, flight 04, are shown in Figure 18. The times when the CH<sub>4</sub> concentrations were substantially higher than the CH<sub>4</sub> background levels can easily be observed. As at location 01, the OPLS/UAV platform can clearly and quickly pinpoint the areas of higher emissions and hence leaks. The higher CH<sub>4</sub> concentration measurements are restricted to lower flight altitudes (<5 m). Vertical profiling, seen in Figure 18, revealed that elevated CH<sub>4</sub> was only observed at close to ground level. This finding of anomalous CH<sub>4</sub> only at or below 5 m is also substantiated by the plot of CH<sub>4</sub> concentration with altitude (Figure 19).



**Figure 15.** Photograph of survey field containing the buried, high-pressure natural gas pipeline at location 02 (flights 03 and 04), at AltaGas Utilities Inc., Alberta.



**Figure 16.** Overview of methane concentrations for location 02, flights 03 and 04, at AltaGas Utilities Inc., Alberta. The warmer (orange/red) colours indicate anomalously higher methane concentrations (significantly above background levels for methane).

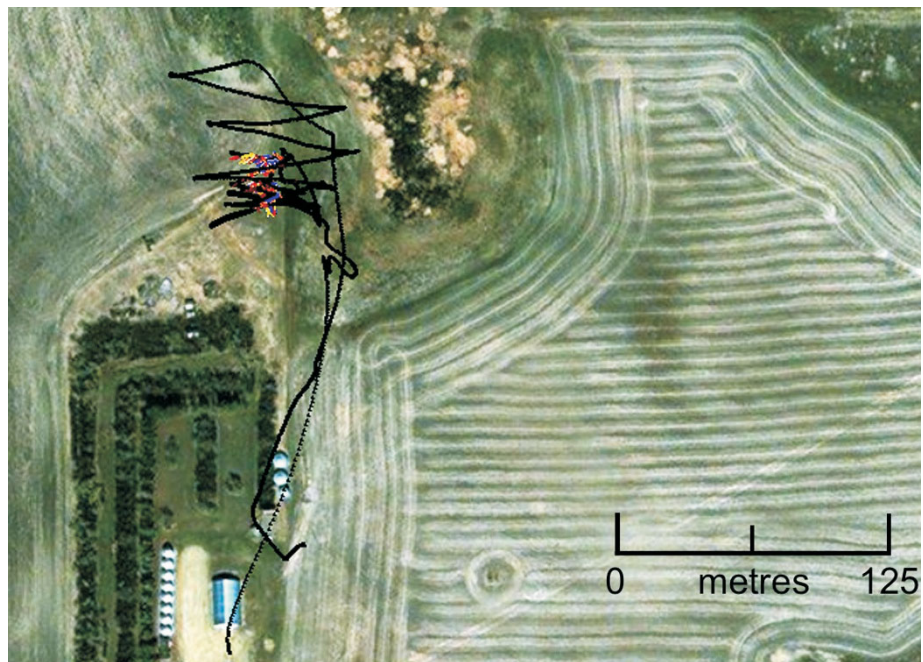


**Figure 17.** Overview of methane concentrations for location 02, flight 04, at AltaGas Utilities Inc., Alberta. The cooler colours indicate anomalously higher methane concentrations (above background levels for methane). The black line is the open-path laser spectrometer/unmanned aerial vehicle (OPLS/UAV) platform survey track.

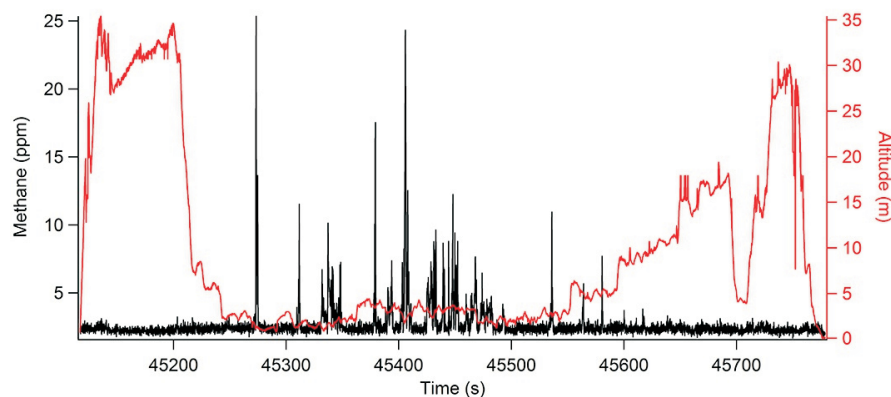


**Figure 18.** Time series plot of methane concentrations (black line) and open-path laser spectrometer/unmanned aerial vehicle (OPLS/UAV) platform altitude (red line) for location 02, flight 04, at AltaGas Utilities Inc., Alberta.

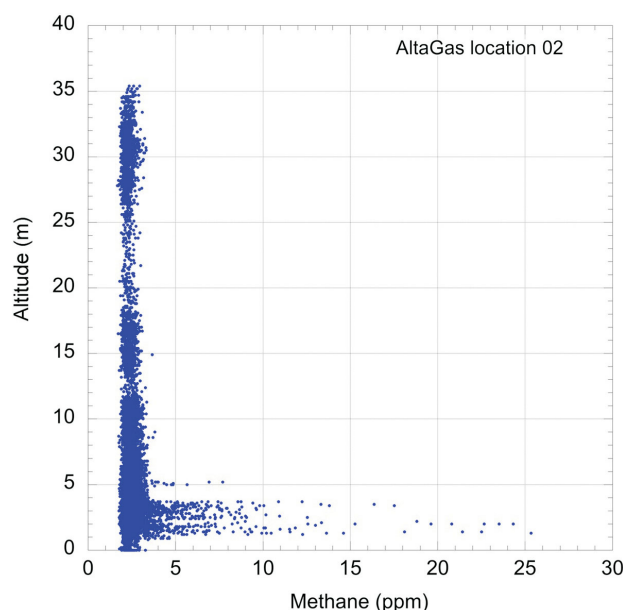


**Figure 19.** Relationship of methane concentration to the altitude (determined by light detection and ranging [LiDAR] measurements) of the open-path laser spectrometer/unmanned aerial vehicle (OPLS/UAV) platform at the time of measurement, location 02, at AltaGas Utilities Inc. (AltaGas), Alberta.

## Summary and Conclusions

The GHGMap team was able to conduct a total of five flights at three locations during a single afternoon of testing. A total of 23 445 discrete CH<sub>4</sub> measurements were made at two locations by the novel OPLS, combined with the small UAV platform over the course of the testing. This enormous number of data points coupled with the parts per billion (ppb) sensitivity of the OPLS allows for a high degree of confidence in identifying and reporting anomalous CH<sub>4</sub> concentration levels, which are higher than the atmospheric background levels.

Elevated CH<sub>4</sub> concentrations of up to 26 ppm (location 01, flight 02) were detected by the OPLS/UAV platform at the above-ground release and at both of the buried pipeline locations. Due to the highly constrained vertical dispersion of the CH<sub>4</sub> plumes, due to the windy conditions, it is unlikely that vehicles operating at higher altitudes (e.g., fixed-wing, helicopter, etc.) would have been successful in detecting the plume under the weather conditions on that day.

This effective measurement method offers high personnel safety as a small UAV surveys the site as opposed to people with monitors. This method also reduces the potential exposure of people to gas leaks as well as hazards associated with activities such as climbing, walking, etc.

Despite the very positive results, it is felt that the OPLS operated at suboptimum levels (noise and detection limits) during the surveys. In comparison with previous calibrations and tests at gas plants and wells, the instrument was somewhat less sensitive. The team identified that the issue is largely due to the cold environmental conditions. As a result, the team changed the OPLS hardware after the survey to allow it to operate as expected at subfreezing temperatures. Changes are also being made to better and permanently integrate the OPLS with the UAV (power, communication, navigation). As a consequence, it is expected that the system will perform better in the future.

Based on these demonstration results, there is confidence in this new technology and the logistics for deployment. It is anticipated that further testing on pipelines and controlled releases will move ahead quickly. It is also expected that it will be possible to initiate service operations that provide efficient and effective OPLS/UAV platform surveys to clients in the oil and gas industry with fugitive greenhouse gas emission measurement and monitoring needs.

## Acknowledgments

The GHGMap team would like to thank AltaGas Utilities Inc. (AltaGas) for their time, effort, expense and enthusiastic support of the open-path laser spectrometer/unmanned aerial vehicle (OPLS/UAV) platform tests at their pipeline. In particular, R. Wintersgill at AltaGas is thanked for his engagement with this emerging technology and for his review of this document.

Funding for GHGMap is generously provided by grants from Geoscience BC and Western Economic Diversification Canada.

### References

Christensen, L.E. (2014): Miniature tunable laser spectrometer for detection of a trace gas; United States Patent and Trademark

Office, patent number 9,671,332, URL <<https://www.uspto.gov>> [November 2017].

Whiticar, M.J., Christensen, L.E., Salas, C.J. and Reece, P. (2018): GHGMap: novel approach for aerial measurements of greenhouse gas emissions, British Columbia; *in* Geoscience BC Summary of Activities 2017: Energy, Geoscience BC, Report 2018-4, p. 1–10.

# Molecular Composition and Isotope Mapping of Natural Gas in the British Columbia Natural Gas Atlas

C. Evans, School of Earth and Ocean Sciences, University of Victoria, Victoria, BC, c2evans@uvic.ca

---

Evans, C. (2019): Molecular composition and isotope mapping of natural gas in the British Columbia Natural Gas Atlas; *in* Geoscience BC Summary of Activities 2018, Geoscience BC, Report 2019-1, p. 77–84.

## Introduction

Natural gas is a combustible fossil fuel of marketable value composed mainly of methane (CH<sub>4</sub>). It is also a source for chemical derivatives such as feedstock to the plastics industry (Hunt, 1996). Natural gas emissions are a large component of the natural and artificial greenhouse gas budget (Whiticar, 1990, 1993; Khalil, 2000; Archer, 2009, 2010). The production of natural gas is a focus for economic development in the province of British Columbia (BC), including the development of liquefied natural gas exports (BC Ministry of Energy, Mines and Petroleum Resources, 2012a–c; BC Government, 2018; BC Ministry of Environment and Climate Change Strategy, 2018). In the last ten years, there has been a shift of commercial natural gas production in northeastern British Columbia (NEBC) to unconventional natural gas reservoirs (Hayes, 2018). These unconventional reservoirs can be hosted by a variety of stratigraphic formations and often require advanced completion technologies to yield economic volumes.

The British Columbia Natural Gas Atlas (BC-NGA) was initiated as a three-year project to collect samples and data on molecular composition (MC) and stable isotope ratio (ISO) geochemistry of natural gas (Evans and Whiticar, 2017) from wells in NEBC (Evans and Hayes, 2018, Figure 1). New analyses of the samples was undertaken by the Biogeochemistry Facility at the School of Earth and Ocean Sciences (BF-SEOS), University of Victoria, under contract with Geoscience BC.

The primary objective of the project is the collection, interpretation and dissemination of data through a publicly accessible website. The resulting information would be synthesized into a series of maps and well profiles of MC and ISO data collected from gas tests, including mud gas collected during drilling. Many of the samples were collected as part of the regulatory requirements of the BC Oil and Gas Commission (2015, 2016).

---

*This publication is also available, free of charge, as colour digital files in Adobe Acrobat® PDF format from the Geoscience BC website: <http://www.geosciencebc.com/s/SummaryofActivities.asp>.*

## Background

A geological framework for NEBC, published as the Conventional Natural Gas Play Atlas (BC Ministry of Energy, Mines and Petroleum Resources, 2006a–c), formed the foundation upon which the geochemistry data from this project were correlated (Evans and Hayes, 2018), but it did not include any geochemistry data. The BC Oil and Gas Commission requires geochemistry data from natural gas wells in BC to be publicly available; there are hundreds of reports available via download from the BC Oil and Gas Commission's website. A consolidated Geoscience BC database is planned to facilitate the dissemination of data from this project.

The study area is in NEBC and is part of the Western Canada Sedimentary Basin (Mossop and Shetsen, 1994). The sedimentary rocks form a thick stratigraphic package spanning thousands of metres of thickness and hundreds of millions of years. Within this stratigraphic column are hydrocarbon reservoirs that have been developed as a source for oil and gas production (BC Ministry of Energy, Mines and Petroleum Resources, 2006a–c). New unconventional hydrocarbon targets have been identified: the Horn River sub-basin (BC Ministry of Energy, Mines and Petroleum Resources, 2011), the Montney play (BC Oil and Gas Commission, 2012; BC Ministry of Energy, Mines and Petroleum Resources, 2013a), the Cordova Embayment (BC Ministry of Forests, Lands, Natural Resource Operations and Rural Development, 2015) and the Liard sub-basin (Ferri et al., 2017).

Natural gas is predominantly methane (CH<sub>4</sub>, labelled C1) with smaller amounts of ethane (C<sub>2</sub>H<sub>6</sub>, labelled C2), propane (C<sub>3</sub>H<sub>8</sub>, labelled C3), butane (C<sub>4</sub>H<sub>10</sub>, labelled nC4), isobutane (C<sub>4</sub>H<sub>10</sub>, branching and labelled iC4) and often sour gas (hydrogen sulphide or H<sub>2</sub>S). All sedimentary strata in NEBC contains organic material of some form and concentration, which has been the source for much of the natural gas. These gases are, by definition, biogenic, because they are sourced from organic material irrespective of microbial activity or thermogenic processes. Biogenic natural gas can be divided into two subcategories: microbial natural gas, which is gas sourced from organic activities, and thermogenic natural gas, which is gas produced by buried organic material altered by both pressure and temperature.

Interpreting isotopic data of hydrocarbon compounds as the ratio of the stable isotopes of  $^{13}\text{C}/^{12}\text{C}$  and  $^2\text{H}/^1\text{H}$  provides an indication of petroleum source and migration (Tissot and Welte, 1984; Rashid, 1985; Hunt, 1996). These data are visually presented in the form of Bernard and CD diagrams (e.g., Evans and Whiticar, 2016), crossplots ( $\delta^{13}\text{C}1$  versus  $\delta^{13}\text{C}2$ ;  $\delta^{13}\text{C}2$  versus  $\delta^{13}\text{C}3$ ; after Whiticar, 1999), plus Lorant and Prinzhofer diagrams (Prinzhofer and Battani, 2003).

The use of basic software is intentional. Using off-the-shelf software on a laptop was intended to demonstrate that not only the data are accessible for everyday users, the interpretation also does not require sophisticated hardware or software.

### Data Sources

Gas samples from the petroleum industry gas wells were collected by an operating company and sent to the BF-SEOS for MC plus ISO analysis. The results were reported to the operating company with the understanding that a report would be submitted by them to the BC Oil and Gas Commission. Parallel analyses were completed by other labs with results sent to the BC Oil and Gas Commission and held under the confidentiality period for the wells. During 31 months, just less than 200 gas samples from mud-gas on three wells and production gas from 20 wells were submitted to BF-SEOS. Table 1 lists the samples submitted and the sample count.

### Data Analysis and Results

The first step in the analysis was to confirm that the samples were representative of the reservoir fluids and not affected by more recent microbial or thermal exposure. Anomalous trends were determined and flagged as possible problem locations, but none of these map points or well profiles had isotopic data associated with them. Mud-gas samples were assumed to be a representative indication of the reservoir isotopes (Tilley and Muehlenbachs, 2006, 2013), despite

inherently being contaminated by the atmosphere while drilling. Data previous to this study (Tilley and Muehlenbachs, 2013; Norville, 2014) have not been submitted to the BC Oil and Gas Commission.

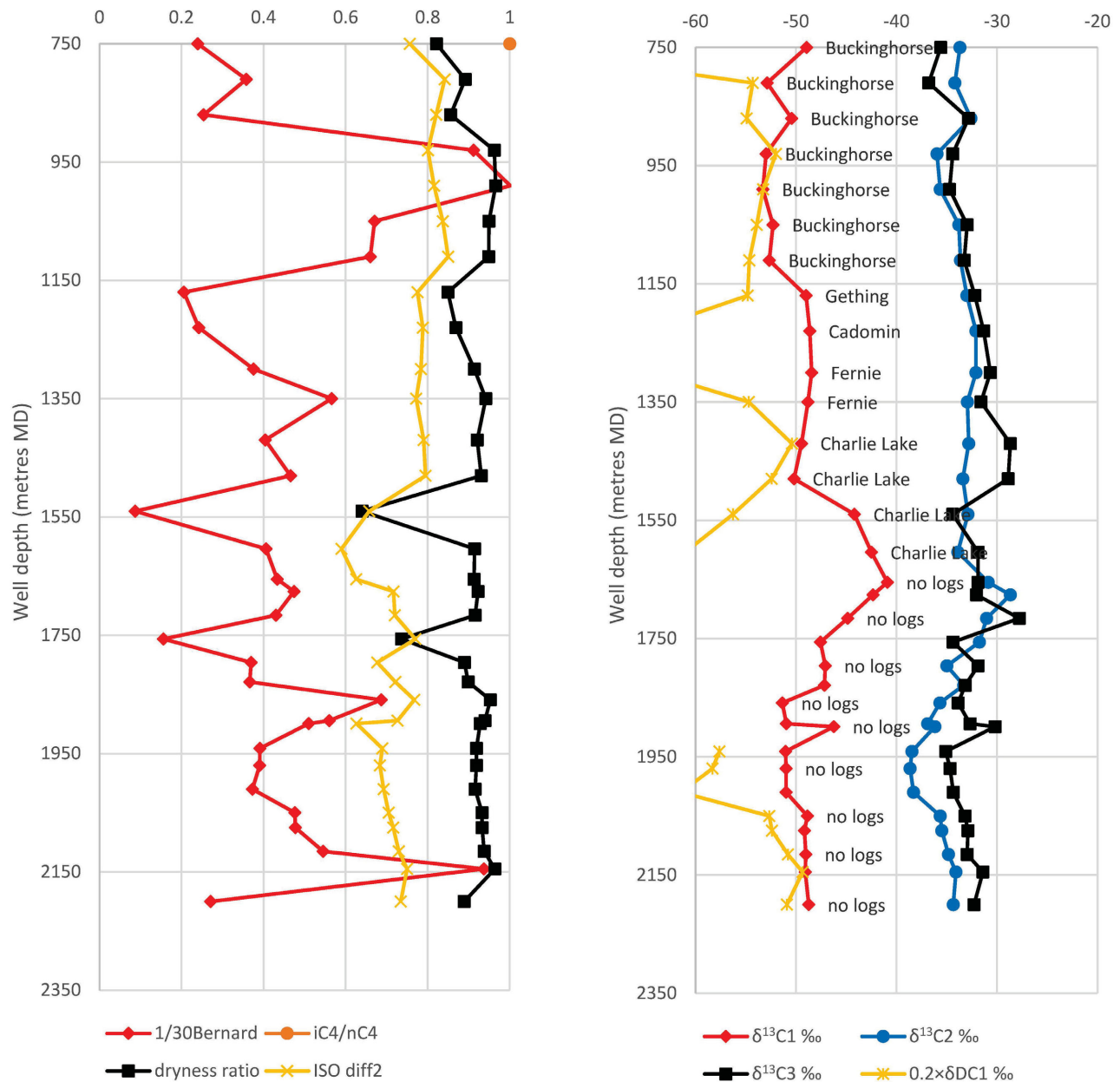
Data collected and analyzed are geographically widely variable due to the specific focus of exploration and development activities undertaken by oil and gas companies. As such, widespread contouring of data presents specific problems due to data clustering and gaps. As a result, it was decided to avoid data contouring and instead use only representative ‘coloured pins’ to post raw data on the maps. These maps are available on the Geoscience BC website (<http://www.geosciencebc.com/s/2015-013.asp>). Detailed gas composition profiles will be presented in the author’s thesis (Evans, 2018). Figure 1 shows a detailed gas composition profile for well with well authorization (WA) number 32990 (YOHO HZ INGA 11-24-087-24, unique well identifier [UWI] 00/11-24-087-24W6/0).

Figure 2 is a crossplot (after Whiticar, 1994; after Tilley and Muehlenbachs, 2013) for the example well profile (WA#32990) by the BF-SEOS. Many of the deeper samples shift ‘downward’ on the graph to isotopically  $^{13}\text{C}$  depleted methane.

The isotopic shift of  $\delta^{13}\text{C}1$  (methane) in hydrocarbon-bearing horizons has been observed in other samples as well. Figure 3a and b are crossplots of all horizontal wells in the Montney play. There is a distinct shift in the apparent  $\delta^{13}\text{C}1$  baseline away from the anticipated response of the kerogen in Figure 3a ( $\delta^{13}\text{C}1$  versus  $\delta^{13}\text{C}2$ ), whereas the  $\delta^{13}\text{C}2$  and  $\delta^{13}\text{C}3$  appear to be within normal distribution of the kerogen in Figure 3b ( $\delta^{13}\text{C}2$  versus  $\delta^{13}\text{C}3$ ; after Whiticar, 1994). The new data from BF-SEOS and the Montney play data plot off trend of the data from similar diagrams (Tilley and Muehlenbachs, 2013). If this is an indication of a consistent kerogen shift, the previously used Bernard and CD diagrams for NEBC (e.g., Norville, 2014) should be adjusted. Further analysis using nitrogen and helium data (e.g., Whiticar, 1994) should be undertaken.

**Table 1.** List of gas samples submitted to the Biogeochemistry Facility at the School of Earth and Ocean Sciences (BF-SEOS), University of Victoria, with new analyses completed for stable isotope ratio data. Abbreviation: SCVF, surface casing vent flow.

Operator	Number of production gas wells	Number of mud-gas wells	Number of samples	Well authorization number listed	Date received at the lab
Yoho Resources Inc.		1	32	32990 single	October 4, 2017
Suncor Energy Inc.	2		2	Two wells (samples from SCVF)	November 8, 2016
Crew Energy Inc.	2		3	30876 and 31960	October 28, 2016
Shell Canada	2		4	29926, 29921	July 19, 2016
Crew Energy Inc.	14		29	Multiple wells	June 7, 2016
Saguaro Energy Ltd.		1	61	30308 single	April 29, 2016
Chevron Corporation		1	55	29747 single	April 22, 2016



**Figure 1.** Well profile of molecular composition (MC) ratios and stable isotope (ISO) ratios in Upper Cretaceous to Triassic strata from vertical well WA#32990 (YOHO HZ INGA 11-24-087-24, unique well identifier [UWI] 00/11-24-087-24W6/0). There are no geophysical well logs taken for deeper horizons, but total depth was just below the Montney play. Abbreviations: Buckingham, Buckingham Formation; C1, methane; C2, ethane; C3, propane; iC4, isobutane; nC4, butane; Cadomin, Cadomin Formation; Charlie Lake, Charlie Lake Formation; D, deuterium; diff2, isotope difference ratio; Fernie, Fernie Formation; Gething, Gething Formation; MD, measured distance along well bore; WA, well authorization.

If analysis of postmigration methane generation by Wood and Sanei (2016, cited in Evans and Hayes [2017]) is consistent with results from this study, another interpretation technique using the Lorant and Prinzhofer diagrams (Prinzhofer and Battani, 2003) is required to explain this variation. The Prinzhofer diagram (Figure 4a) is only based on molecular composition as a crossplot of ratios ( $C2/C3$  versus  $C2/iC4$ ), but it illustrates a trend toward thermogenic processes. The Lorant diagram (Figure 4b) is an ex-

pression of an isotopic difference ( $\delta^{13}C2 - \delta^{13}C3$ ) compared to a molecular composition ratio ( $C2/C3$ ) and infers that ‘secondary cracking of oil and gas’ is the dominant process. The trend to having migrated oil undergoing secondary cracking to methane may explain the shift downward to lighter kerogens that was originally seen in the BF-SEOS results for well WA#32990 (Figure 5a, b). A further extrapolation to secondary cracking of gas may be assumed from the last data point (Figure 5b).

Further evaluation is required for data on the stable isotopes of carbon, and possibly hydrogen if available, from the kerogens and pyrobitumens of NEBC.

### Future Work

Geoscience BC has extended the BC-NGA project as a result of anticipated increased industry activity planned for new wells and sampling of production gas. Additional samples are expected in the next few months and recent analysis

is already requiring integration. Further work is planned for increased analysis of individual segments of the well profiles, analysis for kerogen isotopes and new reporting on enhanced findings.

### Conclusions

Much of the details of the three-year study are contained in the author's thesis, which was a requirement of BC-NGA. Maps of each play will be one of the primary products, but

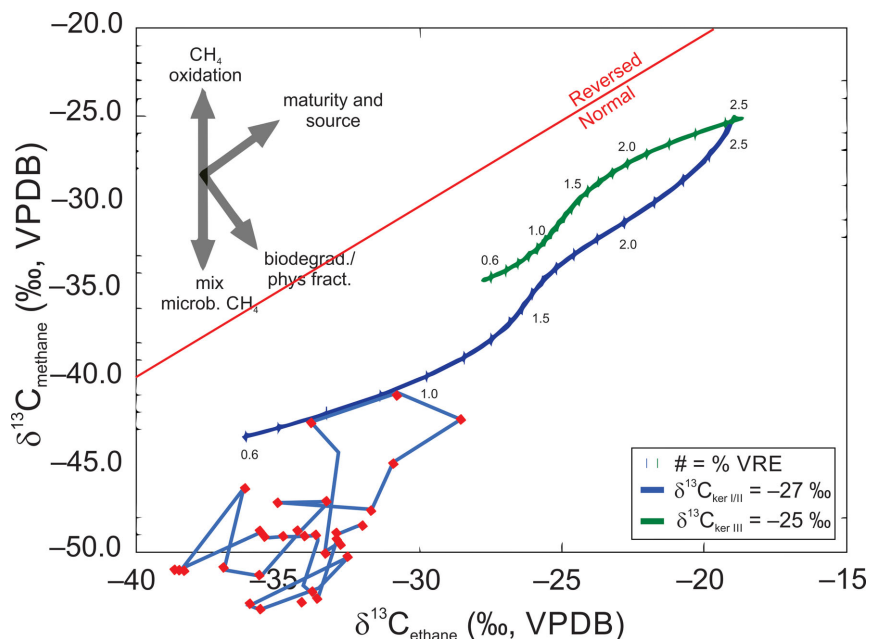


**Figure 2.** Crossplot of  $\delta^{13}C_1$  versus  $\delta^{13}C_2$  for well WA#32990 (YOHO HZ INGA 11-24-087-24, unique well identifier [UWI] 00/11-24-087-24W6/0), after Berner and Faber (1996). Abbreviations: biodegrad., biodegradable; ker, kerogen; microb., microbial; phys. fract., physical fraction; VPDB, Vienna Pee Dee Belemnite; VRE, vitrinite reflectance equivalent; WA, well authorization.

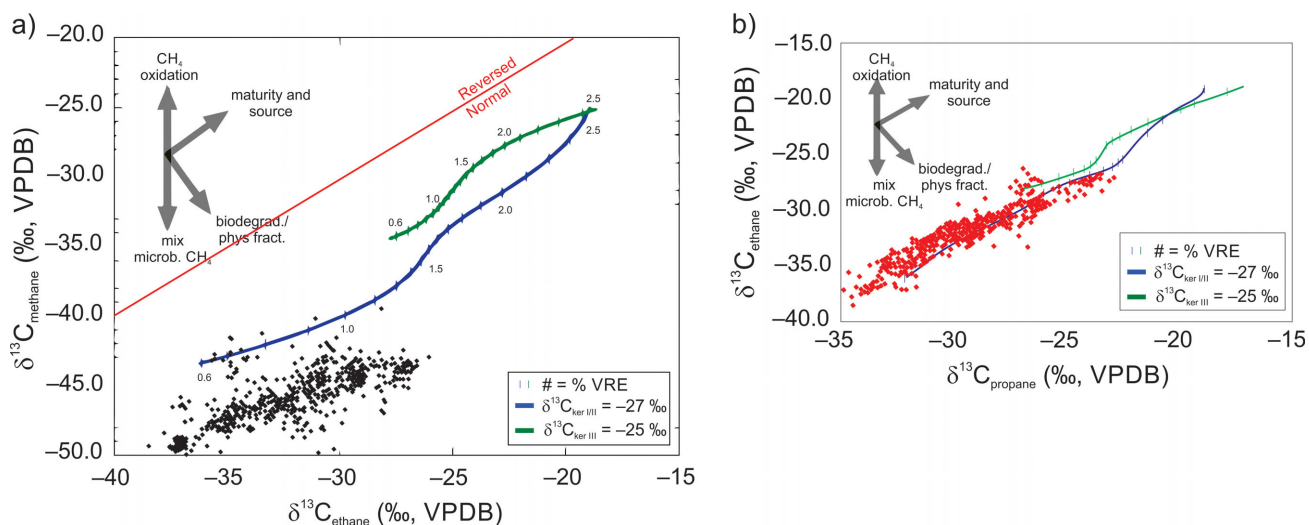


**Figure 3.** Crossplots of a)  $\delta^{13}C_1$  versus  $\delta^{13}C_2$  and b)  $\delta^{13}C_2$  versus  $\delta^{13}C_3$  for all horizontal wells in the Montney play, after Berner and Faber (1996). Abbreviations: biodegrad., biodegradable; C1, methane; C2, ethane; C3, propane; ker, kerogen; microb., microbial; phys. fract., physical fraction; VPDB, Vienna Pee Dee Belemnite; VRE, vitrinite reflectance equivalent.

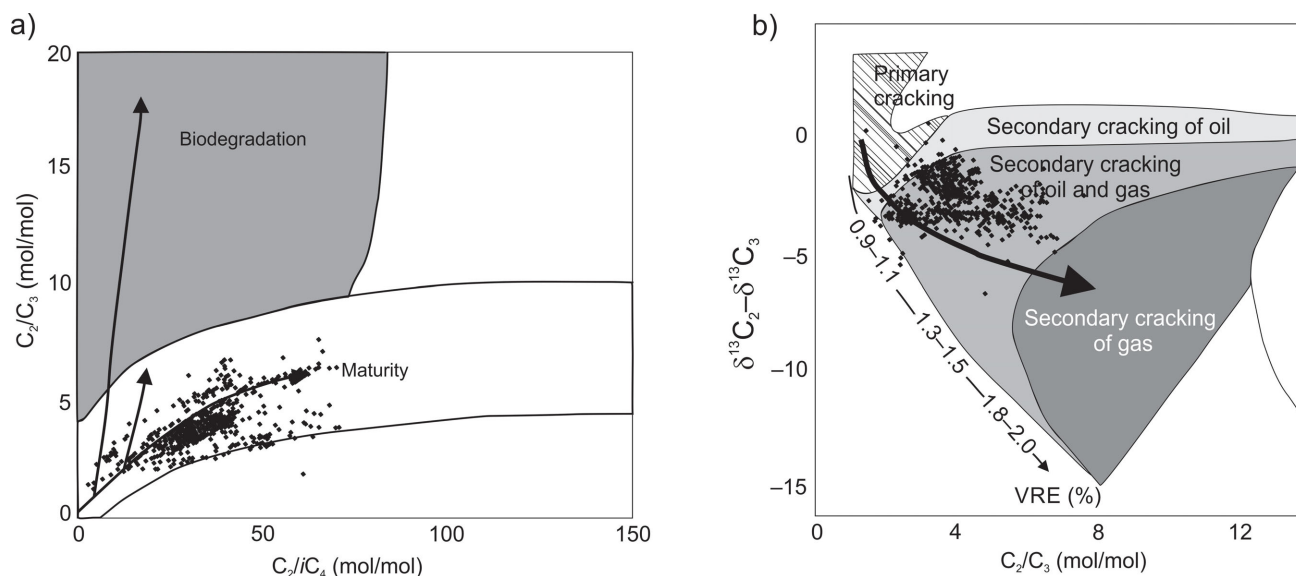


**Figure 4.** a) Prinzhofe C<sub>2</sub>/C<sub>3</sub> versus C<sub>2</sub>/iC<sub>4</sub> and b) Lorant δ<sup>13</sup>C<sub>2</sub>–δ<sup>13</sup>C<sub>3</sub> versus C<sub>2</sub>/C<sub>3</sub> diagrams for the Montney play horizontal profiles. Almost all Montney play gas is secondary cracking of oil and gas, but there are three separate paths of cracking that occur along some of the profiles. This requires further study as most data is from horizontal wells. Abbreviations: C<sub>2</sub>, ethane; C<sub>3</sub>, propane; iC<sub>4</sub>, isobutane; VRE, vitrinite reflectance equivalent.

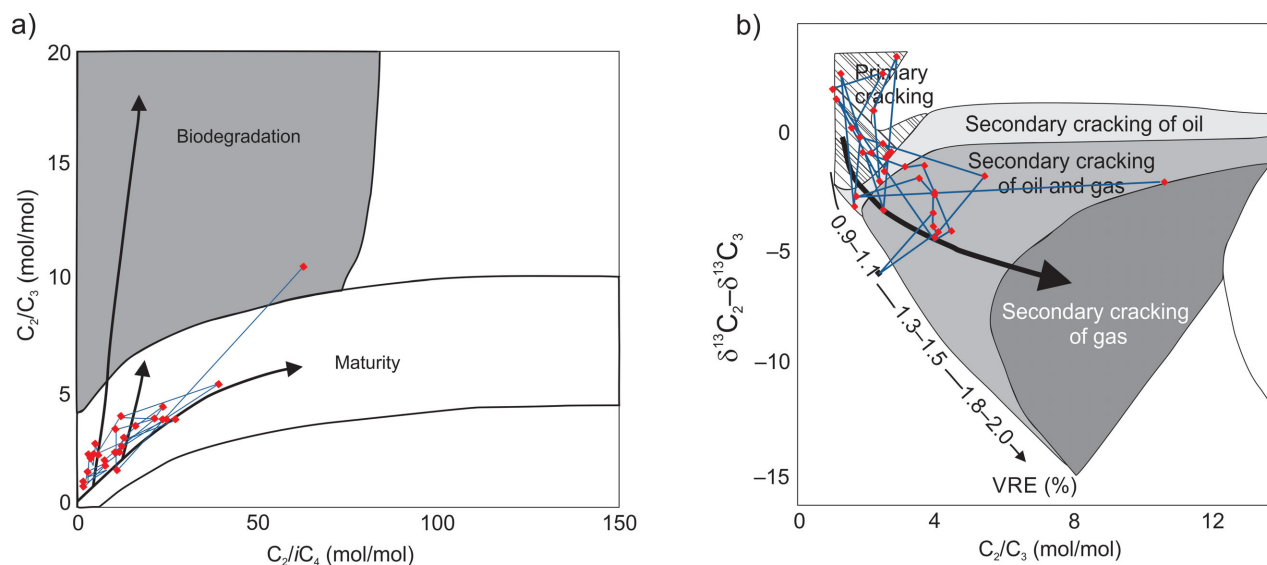


**Figure 5.** a) Prinzhofe C<sub>2</sub>/C<sub>3</sub> versus C<sub>2</sub>/iC<sub>4</sub> and b) Lorant δ<sup>13</sup>C<sub>2</sub>–δ<sup>13</sup>C<sub>3</sub> versus C<sub>2</sub>/C<sub>3</sub> diagrams for the unique vertical profile for well WA#32990 (YOHO HZ INGA 11-24-087-24, unique well identifier [UWI] 00/11-24-087-24W6/0). Abbreviations: C<sub>2</sub>, ethane; C<sub>3</sub>, propane; iC<sub>4</sub>, isobutane; VRE, vitrinite reflectance equivalent; WA, well authorization.

there are also combinations of ISO profiles that are possible from the well data. The BC Oil and Gas Commission instituted a regulatory requirement (BC Oil and Gas Commission, 2015) for mud-gas profiles and these are usually anticipated to be a vertical profile through the stratigraphy. Another profile orientation based on horizontal (HZ) profiles along multilateral HZ legs of unconventional gas wells may provide further insights into the geochemistry of the unconventional reservoirs.

Interpretation is required to identify the source and migration of many gases present in NEBC. Interpretative tools used in this study consisted of crossplots of molecular composition and isotopic data with some isotopic crossplots, such as δ<sup>13</sup>C<sub>1</sub> versus δ<sup>13</sup>C<sub>2</sub> crossplots, are more informative than others. The isotopic data trends presented here are not comparable to other published interpretations such as Bernard or CD plots, which should not be used in NEBC.

## Acknowledgments

The author thanks Geoscience BC and the BC Oil and Gas Research and Innovation Society (OGRIS) for the opportunity to undertake this project. Support for the BC-NGA project has been sustained by the BC Oil and Gas Commission; the staff has been very helpful in supplying data, explaining data analysis and providing updates to the source database. Discussions with staff at Geoscience BC have influenced the direction of studies and Geoscience BC is releasing map products. Further support has been provided by the members of the Geoscience BC Project Advisory Committee. Also, the active operators have been very open with discussions and have provided support for the interim results. Acknowledgments are also due to G. Niebergall at Yoho Resources Inc. for the release of the data from well WA#32990. The author thanks M. Dawson for his review of this paper.

## References

- Archer, D. (2009): *The Long Thaw: How Humans are Changing the Next 100,000 Years of Earth's Climate*; Princeton University Press, Princeton, New Jersey, 200 p.
- Archer, D. (2010): *The Global Carbon Cycle*, Princeton Primers in Climate; Princeton University Press, Princeton, New Jersey, 216 p.
- BC Government (2018): New framework for natural gas development puts focus on economic and climate targets; British Columbia Government news 2018PREM0012-000480, March 22, 2018, BC Office of the Premier, URL <<https://news.gov.bc.ca/16681>> [November 2018].
- BC Ministry of Energy, Mines and Petroleum Resources (2006a): Conventional natural gas play atlas, part 1; BC Ministry of Energy, Mines and Petroleum Resources, Oil and Gas Division, Resource Development and Geoscience Branch, Petroleum Geology Publication 2006-01, p. 1–46, URL <[http://www2.gov.bc.ca/assets/gov/farming-natural-resources-and-industry/natural-gas-oil/petroleum-geoscience/oil-gas-reports/og\\_report\\_2006-1\\_nebc\\_atlas\\_part1.pdf](http://www2.gov.bc.ca/assets/gov/farming-natural-resources-and-industry/natural-gas-oil/petroleum-geoscience/oil-gas-reports/og_report_2006-1_nebc_atlas_part1.pdf)> [November 2018].
- BC Ministry of Energy, Mines and Petroleum Resources (2006b): Conventional natural gas play atlas, part 2; BC Ministry of Energy, Mines and Petroleum Resources, Oil and Gas Division, Resource Development and Geoscience Branch, Petroleum Geology Publication 2006-01, p. 47–97, URL <[http://www2.gov.bc.ca/assets/gov/farming-natural-resources-and-industry/natural-gas-oil/petroleum-geoscience/oil-gas-reports/og\\_report\\_2006-1\\_nebc\\_atlas\\_2\\_part2.pdf](http://www2.gov.bc.ca/assets/gov/farming-natural-resources-and-industry/natural-gas-oil/petroleum-geoscience/oil-gas-reports/og_report_2006-1_nebc_atlas_2_part2.pdf)> [November 2018].
- BC Ministry of Energy, Mines and Petroleum Resources (2006c): Conventional natural gas play atlas, part 3; BC Ministry of Energy, Mines and Petroleum Resources, Oil and Gas Division, Resource Development and Geoscience Branch, Petroleum Geology Publication 2006-01, p. 98–151, URL <[http://www2.gov.bc.ca/assets/gov/farming-natural-resources-and-industry/natural-gas-oil/petroleum-geoscience/oil-gas-reports/og\\_report\\_2006-1\\_nebc\\_atlas\\_part3.pdf](http://www2.gov.bc.ca/assets/gov/farming-natural-resources-and-industry/natural-gas-oil/petroleum-geoscience/oil-gas-reports/og_report_2006-1_nebc_atlas_part3.pdf)> [November 2018].
- BC Ministry of Energy, Mines and Petroleum Resources (2011): Ultimate potential for unconventional natural gas in northeastern British Columbia's Horn River Basin; BC Ministry of Energy, Mines and Petroleum Resources, Oil and Gas Report 2011-1, 39 p., URL <[https://www2.gov.bc.ca/assets/gov/farming-natural-resources-and-industry/natural-gas-oil/petroleum-geoscience/oil-gas-reports/og\\_report2011-1.pdf](https://www2.gov.bc.ca/assets/gov/farming-natural-resources-and-industry/natural-gas-oil/petroleum-geoscience/oil-gas-reports/og_report2011-1.pdf)> [November 2018].
- BC Ministry of Energy, Mines and Petroleum Resources (2012a): British Columbia's natural gas strategy: fuelling B.C.'s economy for the next decade and beyond; BC Ministry of Energy, Mines and Petroleum Resources, 21 p., URL <[http://www.gov.bc.ca/ener/natural\\_gas\\_strategy.html](http://www.gov.bc.ca/ener/natural_gas_strategy.html)> [November 2018].
- BC Ministry of Energy, Mines and Petroleum Resources (2012b): LNG: liquefied natural gas: a strategy for B.C.'s newest industry; BC Ministry of Energy, Mines and Petroleum Resources, 9 p., URL <[http://www.gov.bc.ca/ener/popt/download/liquefied\\_natural\\_gas\\_strategy.pdf](http://www.gov.bc.ca/ener/popt/download/liquefied_natural_gas_strategy.pdf)> [November 2018].
- BC Ministry of Energy, Mines and Petroleum Resources (2012c): LNG 101: a guide to British Columbia's liquefied natural gas sector; BC Ministry of Energy, Mines and Petroleum Resources, 12 p., URL <<http://www.gov.bc.ca/mngd/doc/LNG101.pdf>> [November 2018].
- BC Ministry of Energy, Mines and Petroleum Resources (2013a): The ultimate potential for unconventional petroleum from the Montney Formation of British Columbia and Alberta; BC Ministry of Energy, Mines and Petroleum Resources, Oil and Gas Report 2013-3, 17 p., URL <[https://www2.gov.bc.ca/assets/gov/farming-natural-resources-and-industry/natural-gas-oil/petroleum-geoscience/oil-gas-reports/og\\_report\\_2013-1\\_montney\\_assessment.pdf](https://www2.gov.bc.ca/assets/gov/farming-natural-resources-and-industry/natural-gas-oil/petroleum-geoscience/oil-gas-reports/og_report_2013-1_montney_assessment.pdf)> [November 2018].
- BC Ministry of Environment and Climate Change Strategy (2018): Towards a clean growth future for B.C.; BC Ministry of Environment and Climate Change Strategy, 7 p., URL <<https://engage.gov.bc.ca/app/uploads/sites/391/2018/07/MoE-IntentionsPaper-Introduction.pdf>> [November 2018].
- BC Ministry of Forests, Lands, Natural Resource Operations and Rural Development (2015): Unconventional natural gas assessment for the Cordova Embayment in northeastern British Columbia; BC Ministry of Forests, Lands, Natural Resource Operations and Rural Development Oil and Gas Report 2015-01, 7 p., URL <[https://www2.gov.bc.ca/assets/gov/farming-natural-resources-and-industry/natural-gas-oil/petroleum-geoscience/oil-gas-reports/og\\_report\\_2015-1.pdf](https://www2.gov.bc.ca/assets/gov/farming-natural-resources-and-industry/natural-gas-oil/petroleum-geoscience/oil-gas-reports/og_report_2015-1.pdf)> [November 2018].
- BC Oil and Gas Commission (2012): Montney Formation Play Atlas NEBC; BC Oil and Gas Commission, 35 p., URL <<https://www.bcogc.ca/montney-formation-play-atlas-nebc>> [November 2018].
- BC Oil and Gas Commission (2015): Isotopic analysis and submission guideline; BC Oil and Gas Commission, 2 p., URL <<https://www.bcogc.ca/isotopic-analysis-and-submission-guideline>> [November 2018].
- BC Oil and Gas Commission (2016): INDB 2016-07 submission of isotopic gas analyses; BC Oil and Gas Commission, 1 p., URL <<https://www.bcogc.ca/indb-2016-07-submission-isotopic-gas-analyses>> [November 2018].
- Berner, U. and Faber, E. (1996): Empirical carbon isotope/maturity relationships for gases from algal kerogens and terrigenous organic matter, based on dry, open-system pyrolysis; *Organic Geochemistry*, v. 24, p. 947–955, URL <[https://doi.org/10.1016/S0146-6380\(96\)00090-3](https://doi.org/10.1016/S0146-6380(96)00090-3)> [November 2018].
- Evans, C. (2018): Molecular composition and isotope mapping of natural gas in the British Columbia Natural Gas Atlas; M.Sc. thesis, University of Victoria.
- Evans, C. and Hayes, B.J. (2018): British Columbia Natural Gas Atlas update 2017: recorelation changes the picture; *in*

- Geoscience BC Summary of Activities 2017, Geoscience BC, Report 2018-1, p. 11–14, URL <[http://cdn.geosciencebc.com/pdf/SummaryofActivities2017/Energy/SoA2017\\_E\\_Evans.pdf](http://cdn.geosciencebc.com/pdf/SummaryofActivities2017/Energy/SoA2017_E_Evans.pdf)> [November 2018].
- Evans, C. and Whiticar, M.J. (2016): BC Natural Gas Atlas: geochemical characterization of our energy resources; Unconventional Gas Technical Forum, Victoria, British Columbia, April 4, 2016, poster presentation.
- Evans, C. and Whiticar, M.J. (2017): British Columbia Natural Gas Atlas project: 2016 project update; *in* Geoscience BC Summary of Activities 2016, Geoscience BC, Report 2017-1, p. 75–78, URL <[http://www.geosciencebc.com/i/pdf/SummaryofActivities2016/SoA2016\\_Evans.pdf](http://www.geosciencebc.com/i/pdf/SummaryofActivities2016/SoA2016_Evans.pdf)> [November 2018].
- Ferri, F., McMechan, M., Ardakani, O.H. and Sanei, H. (2017): The Garbutt Formation of Liard Basin, British Columbia: a potential liquids-rich play; *Bulletin of Canadian Petroleum Geology*, v. 65, no. 2, p. 279–306, URL <<https://doi.org/10.2113/gscpgbull.65.2.279>> [November 2018].
- Hayes, M. (2018): BC natural gas production: an overview 2017; 11th Unconventional Gas Technical Forum, Victoria, British Columbia, April 24, 2018, presentation.
- Hunt, J.M. (1996): *Petroleum Geochemistry and Geology* (2<sup>nd</sup> edition), W.H. Freeman and Company, New York, New York, 743 p.
- Khalil, M.A.K. (2000): Atmospheric methane: an introduction; *in* *Atmospheric Methane: Its Role in the Global Environment*, M.A.K. Khalil (ed.), Springer, Berlin, Germany, p. 1–8, URL <[https://doi.org/10.1007/978-3-662-04145-1\\_1](https://doi.org/10.1007/978-3-662-04145-1_1)> [November 2018].
- Mossop, G.D. and Shetsen, I., compilers (1994): *Geological atlas of the Western Canada Sedimentary Basin*; Canadian Society of Petroleum Geologists, Calgary, Alberta and Alberta Research Council, Edmonton, Alberta, 510 p.
- Norville, G. (2014): Isotope geochemistry of natural gas from the Horn River Basin: understanding gas origin, storage and transport in an unconventional shale play; Ph.D. thesis, University of Alberta, 231 p., URL <[https://era.library.ualberta.ca/items/e3c79a1f-5d5b-48da-8764-0ea5ab32c5d0/view/8a257210-4f00-4d66-b76a-47ebd8c77d00/Norville\\_Giselle\\_A\\_201406\\_PhD.pdf](https://era.library.ualberta.ca/items/e3c79a1f-5d5b-48da-8764-0ea5ab32c5d0/view/8a257210-4f00-4d66-b76a-47ebd8c77d00/Norville_Giselle_A_201406_PhD.pdf)> [November 2018].
- Prinzhofer, A. and Battani, A. (2003): Gas isotopes tracing: an important tool for hydrocarbons exploration; *Oil & Gas Science and Technology – Revue*, v. 58, no. 2, p. 299–311, URL <<https://doi.org/10.2516/ogst.2003018>> [November 2018].
- Rashid, M.A. (1985): *Geochemistry of Marine Humic Compounds*; Springer-Verlag New York, New York, 300 p.
- Tilley, B. and Muehlenbachs, K. (2006): Gas maturity and alteration systematics across the Western Canada Sedimentary Basin from four mud gas isotope depth profiles; *Organic Geochemistry*, v. 37, no. 12, p. 1857–1868, URL <<https://doi.org/10.1016/j.orggeochem.2006.08.010>> [November 2018].
- Tilley, B. and Muehlenbachs, K. (2013): Isotope reversals and universal stages and trends of gas maturation in sealed, self-contained petroleum systems; *Chemical Geology*, v. 339, p. 194–204, URL <<https://doi.org/10.1016/j.chemgeo.2012.08.002>> [November 2018].
- Tissot, B.P. and Welte, D.H. (1984): *Petroleum Formation and Occurrence*, 2<sup>nd</sup> edition; Springer-Verlag, Berlin, Germany, 721 p.
- Whiticar, M.J. (1990): A geochemical perspective of natural-gas and atmospheric methane; *Organic Geochemistry*, v. 16, no. 1–3, p. 531–547, URL <[https://doi.org/10.1016/0146-6380\(90\)90068-B](https://doi.org/10.1016/0146-6380(90)90068-B)> [November 2018].
- Whiticar, M.J. (1993): Stable isotopes and global budgets; *in* *Atmospheric Methane: Sources, Sinks, and Role in Global Change*, M.A.K. Khalil (ed.), NATO ASI Series (Series I: Global Environmental Change), v. 13, p. 138–167, Springer, Berlin, Germany, URL <[https://doi.org/10.1007/978-3-642-84605-2\\_8](https://doi.org/10.1007/978-3-642-84605-2_8)> [November 2018].
- Whiticar, M.J. (1994): Correlation of natural gases with their sources; *in* *The Petroleum System – From Source to Trap*, L.B. Magoon and W.G. Dow (ed.), AAPG Memoir 60, p. 261–283, URL <<http://archives.datapages.com/data/specpubs/methodo2/data/a077/a077/0001/0250/0261.htm>> [November 2018].
- Whiticar, M.J. (1999): Carbon and hydrogen isotope systematics of bacterial formation and oxidation of methane; *Chemical Geology*, v. 161, no. 1–3, p. 291–314, URL <[https://doi.org/10.1016/S0009-2541\(99\)00092-3](https://doi.org/10.1016/S0009-2541(99)00092-3)> [November 2018].
- Wood, J.M. and Sanei, H. (2016): Secondary migration and leakage of methane from a major tight-gas system; *Nature Communications*, v. 7, art. 13614, URL <<http://doi.org/10.1038/ncomms13614>> [November 2018].



## Comprehensive Volcanic-Hazard Map for Mount Meager Volcano, Southwestern British Columbia (Part of NTS 092J)

**R.K. Warwick**, Department of Earth Sciences, Simon Fraser University, Burnaby, BC, [rachel\\_warwick@sfu.ca](mailto:rachel_warwick@sfu.ca)

**G. Williams-Jones**, Department of Earth Sciences, Simon Fraser University, Burnaby, BC

**J. Witter**, Department of Earth Sciences, Simon Fraser University, Burnaby, BC and Innovate Geothermal Ltd., Vancouver, BC

**M.C. Kelman**, Natural Resources Canada, Geological Survey of Canada–Pacific, Vancouver, BC

---

Warwick, R.K., Williams-Jones, G., Witter, J. and Kelman M.C. (2019): Comprehensive volcanic-hazard map for Mount Meager volcano, southwestern British Columbia (part of NTS 092J); *in* Geoscience BC Summary of Activities 2018: Energy and Water, Geoscience BC, Report 2019-2, p. 85–94.

### Introduction

The Mount Meager Volcanic Complex, located in southwestern British Columbia (BC), has a 2 million year history of intermittent explosive volcanism (Read, 1990). It is currently in a state of quiescence, the last eruption having occurred 2360 calendar years BP from the Bridge River vent on the flank of Plinth Peak. It currently has an active hydrothermal system manifested by two fumaroles and multiple hot springs. The fumaroles were detected in 2016, breaching the surface of Job Glacier on the western flank of Plinth Peak (Venugopal et al., 2017; Roberti et al., 2018), indicating that the volcanic system is not extinct. A hazard and risk assessment was completed by Friele et al. (2008) and Friele (2012) to address the landslide risk at Mount Meager. Currently, there is no volcanic-hazard assessment outlining the multifaceted hazards to expect from the next phase of volcanic activity at this complex. This project, therefore, focuses on the volcanic hazards that are inherent to Mount Meager, exempting landslide hazards not directly related to eruptive activity.

Volcanic-hazard assessments are a principal resource that communities, policy makers and scientists use in an effort to understand the spatial and temporal scales of associated hazards (Calder et al., 2015). They are a useful tool for informing building codes and the development of community- and emergency-response plans that need to take into account mitigation strategies in the context of risk management.

Volcanic-hazard assessments are often based on the volcano's eruptive history, thus requiring accurate information about the hazard types, magnitudes and frequencies of eruption episodes (Stasiuk et al., 2003). For this project,

however, a base level of knowledge for these characteristics is limited. The geological footprint of the last explosive eruption from Mount Meager has been well documented and mapped, and inferences have been made from the deposits from older volcanic activity throughout the complex (Read, 1990; Hickson et al., 1999). However, data from only one past eruption is insufficient to develop a volcanic-hazard assessment based purely on the geology of the system.

The aim of this project is to develop a numerical-modelling-based volcanic-hazard assessment informed by the documented deposits of the last eruption at Mount Meager, and analogous volcanic systems that have well-documented eruptions. While all volcanoes are unique, reasonable inferences can be applied to Mount Meager based on the studies of similar volcanic settings. For the most part, this will be a deterministic hazard assessment, meaning that hazards and scenarios will be categorized in accordance with the 'most likely' events to occur in a future eruption. Ideally, the approach would follow a probabilistic framework, given that a probability of occurrence does exist for multiple scenarios and hazard types (Rouwet et al., 2017). However, this requires in-depth knowledge of the volcano's history and a baseline understanding of its volcanic activity (Newhall and Hoblitt, 2002), which does not exist at Mount Meager. This project will provide insight into what can be accomplished and delivered in a volcanic-hazard assessment despite limited data on a volcano's geological history.

The completed volcanic-hazard assessment for Mount Meager will be of use to agencies and managers at regional, provincial and federal levels. This includes Squamish-Lillooet regional district managers, the Lil'wat Nation community, Emergency Management BC, and the Canadian Hazard Information Service (CHIS) and Public Safety Geoscience Program of Natural Resources Canada (NRCan). The hazard assessment will include estimated timescales of

---

*This publication is also available, free of charge, as colour digital files in Adobe Acrobat® PDF format from the Geoscience BC website: <http://www.geosciencebc.com/s/SummaryofActivities.asp>.*

inundation and impact from the various likely hazards. This will inform emergency response plans, providing an advanced interpretation of the risks associated with this system. This preliminary assessment can be used to prioritize mitigation strategies and inform a monitoring program.

This paper presents the numerical modelling that has been undertaken to simulate the volcanic-debris-flow hazard, and tephra dispersal and deposition hazards stemming from an eruption of Mount Meager. Parameters incorporated into the models are based on three reasonable scenarios of eruption style, ranging from small-scale to large-scale eruption. Volcanic-debris flows and tephra have the potential to inflict the most damage across the largest area of all hazards expected from an eruption at Mount Meager. This paper describes the numerical models being used for the task and discusses the outcomes as they pertain to the impacts from any future eruption of this volcano.

### Background

The Mount Meager Volcanic Complex, part of the Coast Mountains in British Columbia, is 150 km northwest of Vancouver. It is adjacent to the confluence of Meager Creek

and the upper Lillooet River which flow along the base of the complex (Figure 1). The upper Lillooet River extends to Pemberton, the closest community, which is located 65 km to the southeast. The summit of Mount Meager, partially glacier clad, reaches 2645 m asl. It has been subjected to dynamic processes, such as dissection by glacier advance and retreat, during the Pleistocene Epoch (Clague and Ward, 2011), as well as extensive hydrothermal alteration (Venugopal et al., 2017).

The complex is part of the Garibaldi volcanic belt, connected to the Cascade magmatic arc that extends into Washington State (Green et al., 1988; Read, 1990). Volcanism along this arc is related to subduction of the Juan de Fuca Plate beneath the North American Plate (Green et al., 1988). Unlike the American volcano counterparts, Mount Meager does not exhibit the recognizable conical peak associated with other stratovolcanoes. It has been suggested that tectonism in this section of southwestern BC has been driving rapid uplift for the last 10 m.y. (Farley et al., 2001). The high rate of uplift, coupled with dissection by glacier cover, has been balanced by high rates of erosion and con-

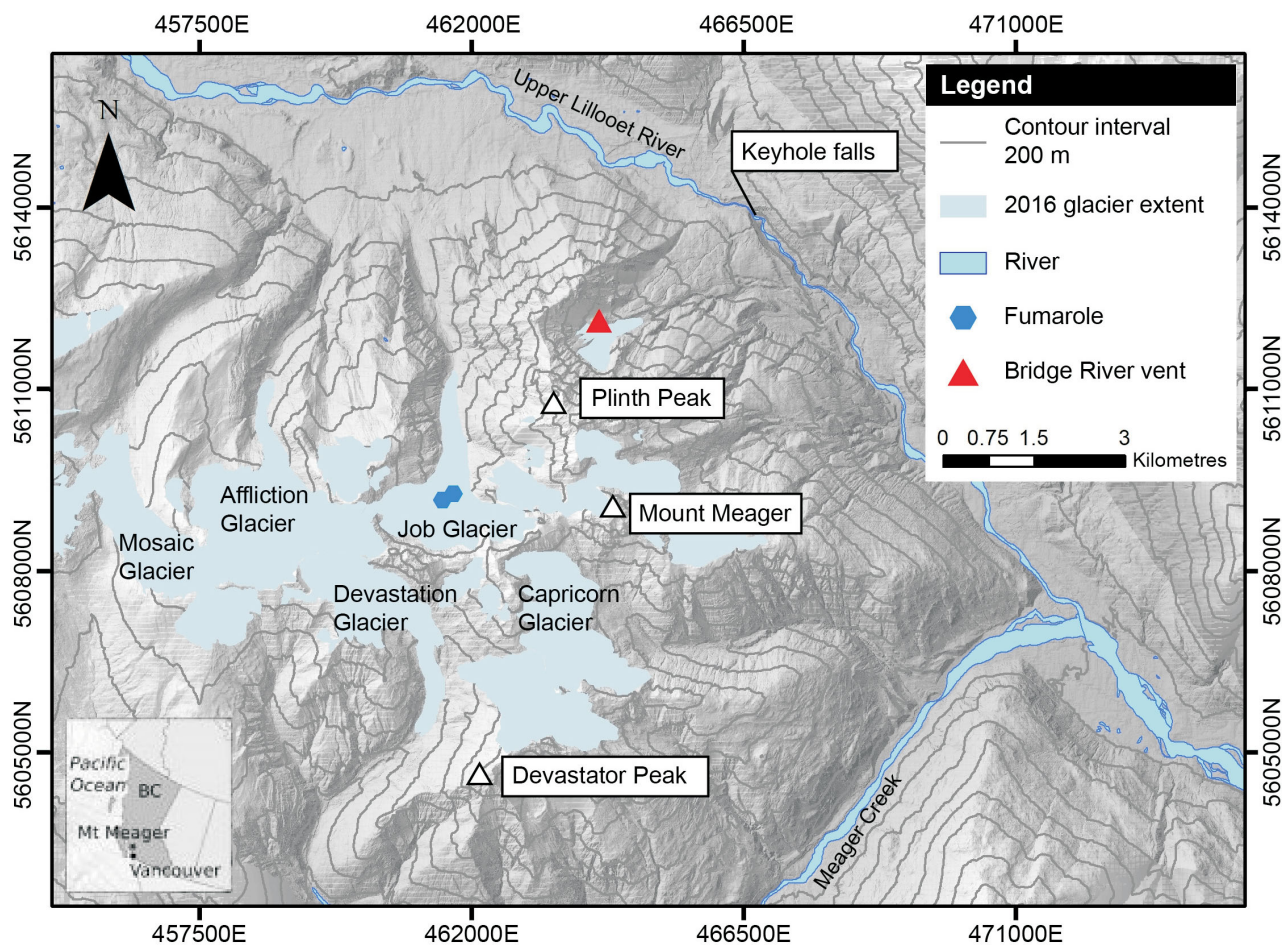


**Figure 1.** Overview of the Mount Meager Volcanic Complex, showing 2016 glacier cover and locations of the Bridge River vent and known fumaroles. Modified from Roberti et al. (2017). All co-ordinates are in UTM Zone 10, NAD 83.

tinuous mass-wasting events, resulting in a highly dissected morphology.

Despite being a large volcanic system, Mount Meager is far more recognized for its history of frequent, large-scale mass-wasting events. In 2010, the largest landslide in Canadian history ( $\sim 53 \times 10^6 \text{ m}^3$ ) was generated on the flanks of Capricorn Mountain, flowing into a portion of the upper Lillooet River, with a maximum path length of 12.7 km (Roberti et al., 2017).

## Geological History

The 2 million year eruptive history of Mount Meager has constructed several peaks, resulting in the complex that stands today (Read, 1990; Farley et al., 2001). Mapping by Read (1990) and supported by Hickson et al. (1999) shows that volcanism at this complex can be split into three periods: early- and late-stage rhyodacite, and a middle stage of andesitic activity. The eruptive suite includes pyroclastic deposits, overlapping andesite and rhyodacite flows, and dacite domes, as well as peripheral basaltic flows (Read, 1990; Hickson et al., 1999). The volcanic deposits, which, on average, form the upper 600 m (topographic) of the complex, overlie Mesozoic plutonic and metamorphic basement rocks (Read, 1990; Roberti, 2018).

Extensive work by Simpson et al. (2006), Friele et al. (2008) and Friele (2012) has documented the long record of landslides and established a hazard assessment based on the large-scale and frequent landslides prevalent throughout the complex. Work has continued to document recent mass-wasting events and identify unstable slopes throughout the massif (Hetherington, 2014; Roberti et al., 2017, 2018). Only one of the documented debris-flow events has been directly associated with the last eruption (Simpson et al., 2006). A question remains regarding what relationship might exist between a deep-seated mass-wasting event and the depressurization of the underlying volcanic system, possibly triggering an eruption.

## Summary of Past Volcanic Hazards

A number of hazards associated with the last eruption of Mount Meager have been discerned from the mapped deposits of this event. These deposits exhibit eruption characteristics that suggest an initial phase of sub-Plinian activity that transitioned to a Vulcanian eruptive episode. Welded block and ash-flow deposits form the banks of the upper Lillooet River directly below the 2360 BP eruptive vent. This deposit is the remnant of an impermeable dam that blocked the upper Lillooet River, creating a temporary lake with a volume of  $0.25\text{--}1.0 \times 10^9 \text{ m}^3$  that eventually failed catastrophically (Stasiuk et al., 1996; Hickson et al., 1999; Andrews et al., 2014). The failure produced an outburst flood that is associated with a volcanic debris-flow deposit identified 42–47 km downstream beneath present-day

Pemberton (Simpson et al., 2006; Friele et al., 2008). A short lava flow stemming from the Bridge River vent is also associated with this period of volcanic activity (Hickson et al., 1999). Thin layers of tephra attributed to this particular eruption have been identified in Alberta, 530 km from the Bridge River vent (Nasmith et al., 1967; Mathewes and Westgate, 1980; Leonard, 1995; Jensen and Beaudoin, 2016).

## Likely and Expected Volcanic Hazards

The likely and expected hazards resulting from an explosive eruption at Mount Meager can be organized based on the area of land they may impact and their potential to reach populated areas. Firstly, the propagation of an ash cloud and subsequent tephra fall are likely to affect the largest area due to their ejection into the atmosphere and transport by wind. Volcanic debris-flows are also expected to occur, given the large volume of ice (a potential supply of water) overlying the heated system; this particular hazard is both primary and secondary in nature, in that it can be triggered by an eruption or occur at a different time. All of these can impact areas up to 100 km from the source volcano (Pierson et al., 2014). Next, pyroclastic flows may occur, given the likely development of an eruption column that would eventually collapse once the energy of the eruption subsided. Field evidence suggests that a dome collapse likely triggered the welded block and ash-flow deposits blanketing the river valley below the Bridge River vent (Michol et al., 2008). Finally, a lava flow is also likely to occur within the timeframe of an eruption; however, given the dominant geological characteristics of the system, the lava flow would be highly viscous, travelling only a short distance and affecting only the topography of the volcano flank. It should be noted that basaltic lavas have also been documented around the periphery of the complex (Hickson et al., 1999), which suggests potential for less viscous and farther reaching lava flows, thus increasing the inundation footprint; however, this is not the dominant rock type of the complex.

## Methods

Numerical modelling was undertaken to examine potential inundation zones and timescales of propagation of the hazards that are explored in this paper. The choice of numerical-modelling programs used for each type of hazard was based on ease of use, open access and applicability to the specific hazard being investigated. These are important characteristics to consider for volcanic-hazard numerical models due to the reality that actual volcanic eruptions can be crisis events where the development of hazard maps and assessments needs to be rapid. Identifying the numerical models that are suggested as the best-practice programs for the Canadian context will provide the best support in the event of a volcanic-eruption crisis.

The input parameters chosen for each numerical-model simulation were divided into three conceivable scenarios. To represent a large-scale scenario, the 1980 eruption of Mount St. Helens, an ice-clad volcanic system in Washington State, was chosen. This case study was chosen due to its well-documented, large-magnitude eruption (Wolfe and Pierson, 1995) and its occurrence in the Cascade magmatic arc, which is closely associated with the Garibaldi volcanic belt that includes Mount Meager. The mid-range scenario is based on the eruption of Nevado del Ruiz in 1985, which resulted in the propagation of a volcanic-debris flow originating from snow and ice melt that resulted from an eruption onto the volcano's glacier (Herd et al., 1986; Voight, 1990). Finally, the small-scale eruption was based on a 2015 eruptive event at Cotopaxi volcano in Ecuador, which resulted in an eruption of ash and a small volume of volcanic-debris flows (Global Volcanism Program, 2016). This latter case study was chosen because Cotopaxi is a well-monitored and documented volcano with similar geological characteristics to Mount Meager (e.g., rhyolitic and andesitic eruption compositions; Hall and Mothes, 2008). Table 1 shows the scenarios and the corresponding numerical-model input parameters used in Ash3d and LAHARZ, two numerical models described below.

### Modelling Tephra Hazards

The United States Geological Survey (USGS) program Ash3d was used for tephra deposition and dispersion. This program is actively used by several volcano-monitoring agencies, such as Instituto Geofísico (IGEPN) in Ecuador and the USGS in their response to volcanic eruption crises around the world. It is an atmospheric model for tephra transport, deposition and dispersion run on a web interface (Schwaiger et al., 2012; Mastin et al., 2013). The atmosphere is divided into a 3-D grid and flow of mass is calculated through each grid cell. Considering the wind field taken from a weather-forecast model, ash particles fall in the model depending on their settling velocity in air (Schwaiger et al., 2012). A limitation of this program is that vent location is not user-defined but rather a predetermined general location of the volcano itself defined by the USGS.

At the moment, this is not a concern for Mount Meager, as there have been no studies to determine future vent locations. Furthermore, tephra dispersion and deposition are more dependent on wind direction at the time of eruption, which ASH3d does consider. See Table 1 for the input parameters used in the development of the scenario-based simulations.

### Modelling Volcanic-Debris Flows

Two numerical-model programs have been used to investigate the volcanic-debris flow hazard at Mount Meager: the USGS-developed LAHARZ and VolcFlow.

LAHARZ is a readily available program run within a Geographic Information System (GIS) that is widely used by many volcanologists (Muñoz-Salinas et al., 2009). It is a semi-empirically-based program designed to estimate potential zones of inundation based on specified debris-flow volumes (Schilling, 2014).

VolcFlow is a depth-averaged approach intended to model geophysical flows and has the ability to manipulate rheological-flow parameters (Kelfoun et al., 2009; Kelfoun and Vargas, 2016). In practice, VolcFlow requires a steeper learning curve than LAHARZ, based on the user interface. However, VolcFlow allows the user more opportunity to place constraints on flow parameters, thus providing more opportunity to simulate realistic flows. Table 2 displays the input parameters that were used for the simulation of two volcanic-debris flows in VolcFlow. Table 1 includes the volume chosen for the simulation of volcanic-debris flows in LAHARZ, which is the only physical input parameter required by that program.

In this paper, only volcanic-debris flows originating from Job Glacier have been presented. This point of origin was chosen to start this research due to the presence of active fumarolic activity within the complex. Other points of origin around the complex will be investigated at a later date using the same scenario parameters described in Tables 1 and 2.

**Table 1.** Three eruption scenarios and the corresponding parameter values used in numerical models. Abbreviation: VEI, Volcano Explosivity Index.

Scenario	Tephra characteristics	Volcanic-debris-flow characteristics
Cotopaxi volcano, Ecuador, 2015 eruption, VEI 1-2	Plume height: 27 km asl Erupted volume: 0.0390 km <sup>3</sup> Eruption duration: 45 minutes	Volume: 1–3 × 10 <sup>6</sup> m <sup>3</sup> Runout length: 15–18 km
Nevado del Ruiz, Columbia, 1985 eruption, VEI 3	Plume height: 5 km asl Erupted volume: 0.0001 km <sup>3</sup> Eruption duration: 1 hour	Volume: 5 × 10 <sup>7</sup> m <sup>3</sup> Runout length: 60–100 km
Mount St. Helens, U.S.A., 1980 eruption, VEI 5	Plume height: 24 km asl Erupted volume: 1.4 km <sup>3</sup> Eruption duration: 9 hours	Volume: 5 × 10 <sup>8</sup> m <sup>3</sup> Runout length: 80–100 km

**Table 2.** VolcFlow input parameters.

Input parameters	Value
VEI 1–2 volume	$5 \times 10^6 \text{ m}^3$
VEI 5 volume	$5 \times 10^8 \text{ m}^3$
Viscosity	25 Pa·s
Density	1500 kg/m <sup>3</sup>
Yield strength	1500 kPa
Internal and basal-friction angle	0

## Results

### Tephra Dispersion and Deposition with Ash3d

Simulations using Ash3d were run on a nearly daily basis from June 2 to August 17, 2018 for the three scenarios. Both the Nevado del Ruiz and the Mount St. Helens scenarios were simulated to track tephra for 24 hours after the start of an eruption. This was also followed by the Cotopaxi case partway through the investigation. However, the Cotopaxi-based scenario was initially set to track tephra for only 6 hours after a simulated eruption. Within this time frame Ash3d reported no cities being affected by tephra deposition for the majority of the simulation runs. From August 2 onward, additional runs were set up to simulate the distribution of tephra 24 hours after the eruption in order to obtain observable results. The following results are based on only 46 runs during the June 2 to August 17 time period.

A majority of the simulations showed tephra being dispersed and deposited to the east and northeast of Mount Meager. For the Mount St. Helens scenario, Kamloops and Williams Lake are most often in the path of tephra dispersion, relative to any other city in BC, in 40 of 46 runs. Port Hardy, northwest of Mount Meager, is simulated to receive tephra in 32 of 46 runs. Vancouver, south of Mount Meager, received tephra in 22 of 46 simulated runs. Similar outcomes occur with the Nevado del Ruiz scenario. However, a difference is that Port Hardy is the city in the path of tephra dispersion most frequently, in 45 of 46 runs.

Regarding the Cotopaxi-based scenario for observations over 24 hours, only one or two cities are shown to be impacted by tephra. Based on 8 runs over a 24-hour period, the communities impacted by tephra dispersion are Kamloops (3/8), Kelowna (2/8), Merritt (2/8), Duncan (1/8) and Williams Lake (2/8).

Isopleth maps were generated using data extracted from tephra deposition generated in Ash3d (Figure 2). Different outcomes are displayed using the Mount St. Helens and Nevado del Ruiz scenarios. The map displaying the Cotopaxi scenario is based on the most likely occurrence 6 hours after a simulated eruption.

### Volcanic-Debris Flow with LAHARZ

All three scenarios result in a volcanic-debris flow reaching the upper Lillooet River, which runs along the eastern base of Mount Meager. The simulated runout length differs for all three scenarios. Given a failure volume of  $1 \times 10^6 \text{ m}^3$  for the smallest eruption scenario, a runout length of 9 km is simulated. A volume of  $5 \times 10^7 \text{ m}^3$  equates to a runout length of 34 km and the largest failure volume of  $5 \times 10^8 \text{ m}^3$  generates a debris-flow runout of 65 km, which reaches the town of Pemberton. All three debris-flow simulations show that the failure follows the confines of the river channel (Figure 3).

### Volcanic-Debris Flow with VolcFlow

Two scenarios using the VolcFlow program are presented here. The first involves a debris-flow–failure volume of  $5 \times 10^7 \text{ m}^3$ , representing a scenario between the small- and mid-scale eruption scenarios. The runout length for that failure is 6 km. The simulation representing a large-scale eruption with a failure volume of  $5 \times 10^8 \text{ m}^3$  results in a runout length of 13 km. Both simulations show that even a small-volume failure would reach the upper Lillooet River. The VolcFlow program simulates the mass of both failures dispersing across the floodplain that exists at the bottom of the watershed holding the Job Glacier, rather than strictly following the gradient of topography propagating to lowest elevation points. The large-scale eruption scenario shows the failure stopping at Keyhole falls, which is a location of significant elevation drop. The VolcFlow program may be unable to solve for significant changes in elevation inherent in the pixels of the Digital Elevation Model used for the simulation. Further research will be required to determine whether the simulated failure would travel farther without the significant elevation drop. Figure 4 displays the outcomes obtained using the VolcFlow program. In both cases, the program calculates the propagation of failure across 20 minutes (1200 seconds).

## Discussion and Conclusions

The results of these simulations offer an example of the benefits of using numerical-modelling tools in the absence of in-depth geological information in a volcanic-hazard environment. The three numerical models displaying two types of volcanic hazards likely for Mount Meager exemplify the varying spatial scale of impact possible from an eruption.

Tephra dispersion is a regional scale hazard that has the potential to impact communities beyond the borders of British Columbia. Volcanic-debris flows are a proximal/local hazard capable of impacting industrial activities at the base of Mount Meager, given a small-scale eruption, and additionally impacting the community of Pemberton, given the large-scale scenario.

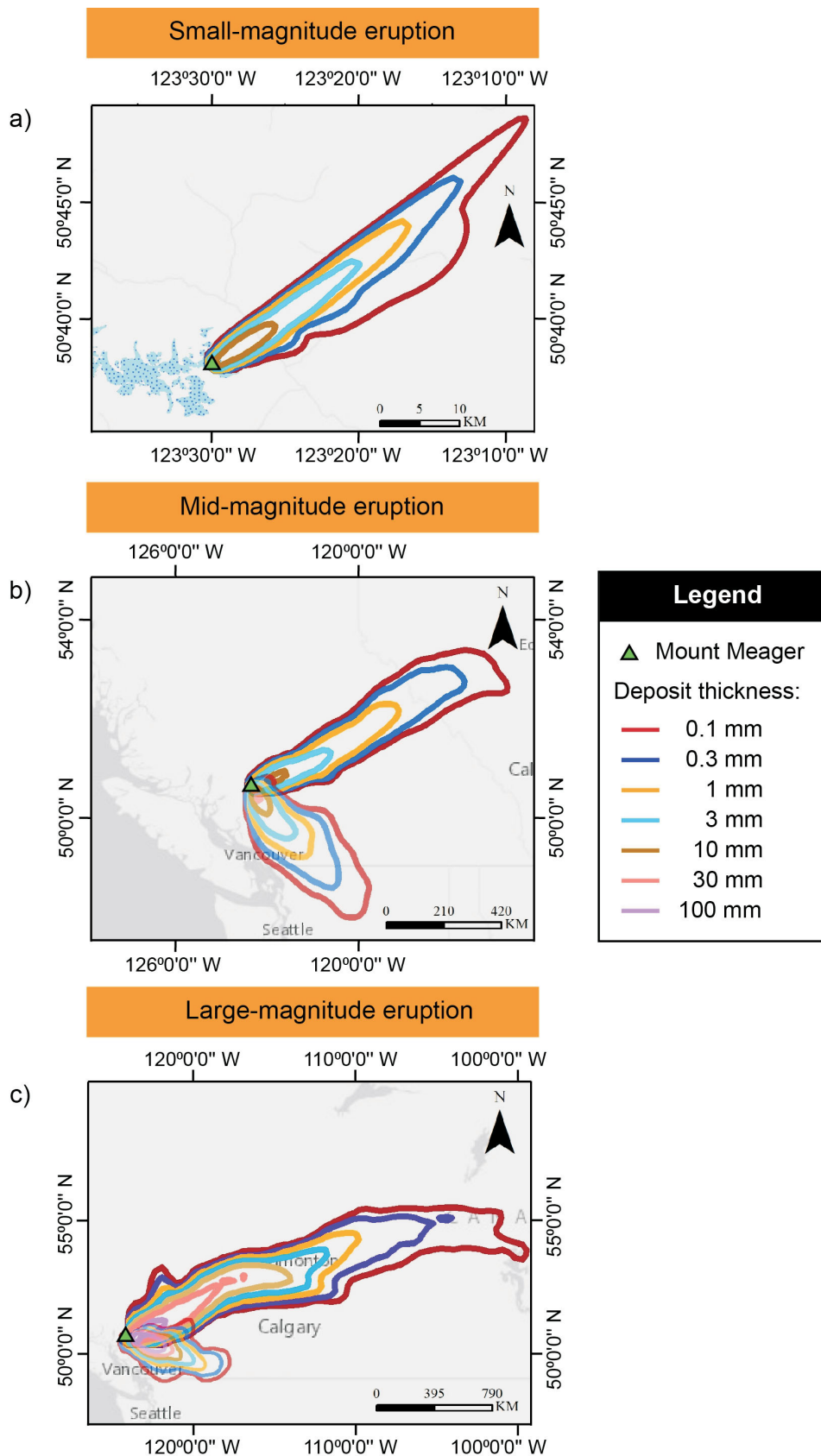


**Figure 2.** Surface distribution of tephra, showing variations in direction of deposition based on different possible wind patterns: **a)** Cotopaxi eruption characteristics 6 hours after eruption, **(b)** Nevado del Ruiz eruption characteristics 24 hours after eruption, and **(c)** Mount St. Helens eruption characteristics 24 hours after eruption.

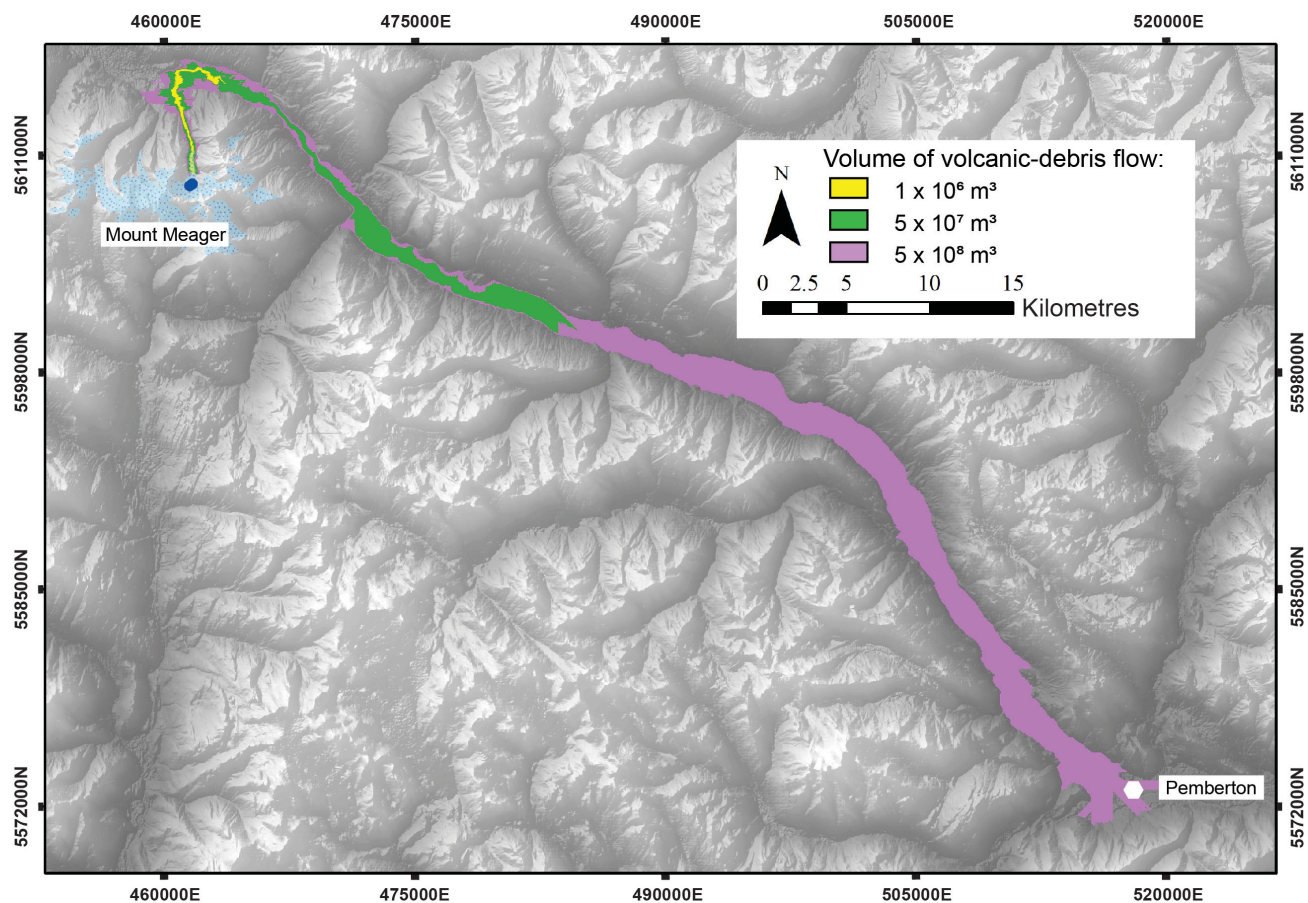


**Figure 3.** Surface expression of the inundation zones from simulated volcanic-debris flows as modelled by LAHARZ. Co-ordinates are in UTM Zone 10, NAD 83.

Results show that an eruption above Volcano Explosivity Index 2 (the smallest scale eruption scenario) is likely to impact multiple cities in southern British Columbia and beyond. The exact trajectory of tephra dispersion is dependent on wind patterns. Although westerly wind patterns are the dominant prevailing winds across BC, any direction of wind pattern is possible. A large mass of erupted material that is able to reach several kilometres into the atmosphere equates to more distant tephra dispersion.

The results of simulating volcanic-debris flows with the LAHARZ program versus the VolcFlow code are different. Using the same failure volume for the worst-case eruption scenario, the LAHARZ program models a runout length 52 km greater than those from VolcFlow. However, LAHARZ is limited by the simplistic functions. The rheological characteristics of the flow cannot be manipulated and the program only propagates the failure mass down gradient. VolcFlow is flawed by its inherent inability to solve for significant changes in the elevation profile of the environment. At Mount Meager, this is a significant problem given the existence of Keyhole falls in the path of likely failure propagation. However, results showing that the failure mass of a large-scale eruption reaches Keyhole falls are of

significance nonetheless, suggesting that failure material may possibly propagate farther or at least form a dam, given the constricting nature of the valley at that point along the river. The dam would be inherently unstable and could pose a secondary hazard of outburst flooding, similar to the events of the last eruption 2360 years BP (although that dam was created from the welded block and ash-flow deposit rather than from debris-flow material). It is important to note that the development of a dam created from the material of the volcanic-debris flow was not actually intended or simulated with VolcFlow; it is merely a hypothesis for the outcome of a buildup of material being confined at the location of Keyhole falls.

This paper outlines the preliminary investigations of two likely hazards generated from an eruption at Mount Meager. It is a scenario-based approach to simulate the propagation of these hazards and is limited in scope to just three scales of eruption: small, medium and large. This paper should not, therefore, be used as a forecast or prediction of the events that will occur during the next eruption at Mount Meager. Rather, it serves to display the preliminary results of three conceivable outcomes of future volcanic activity.

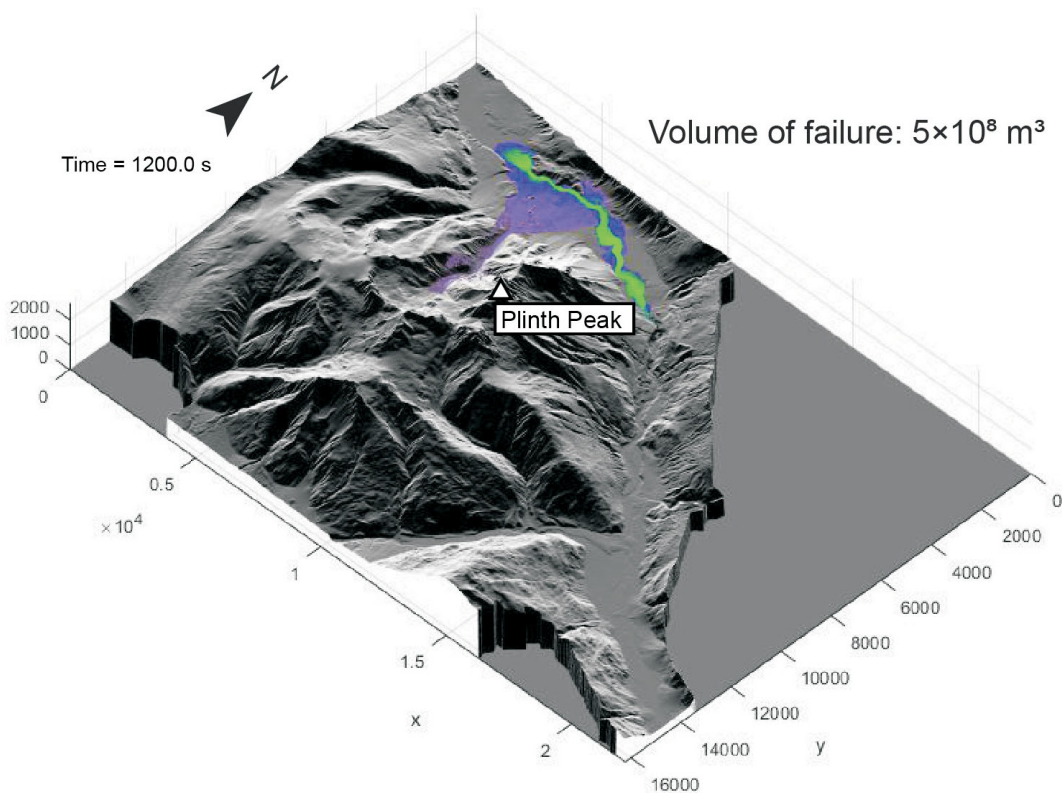
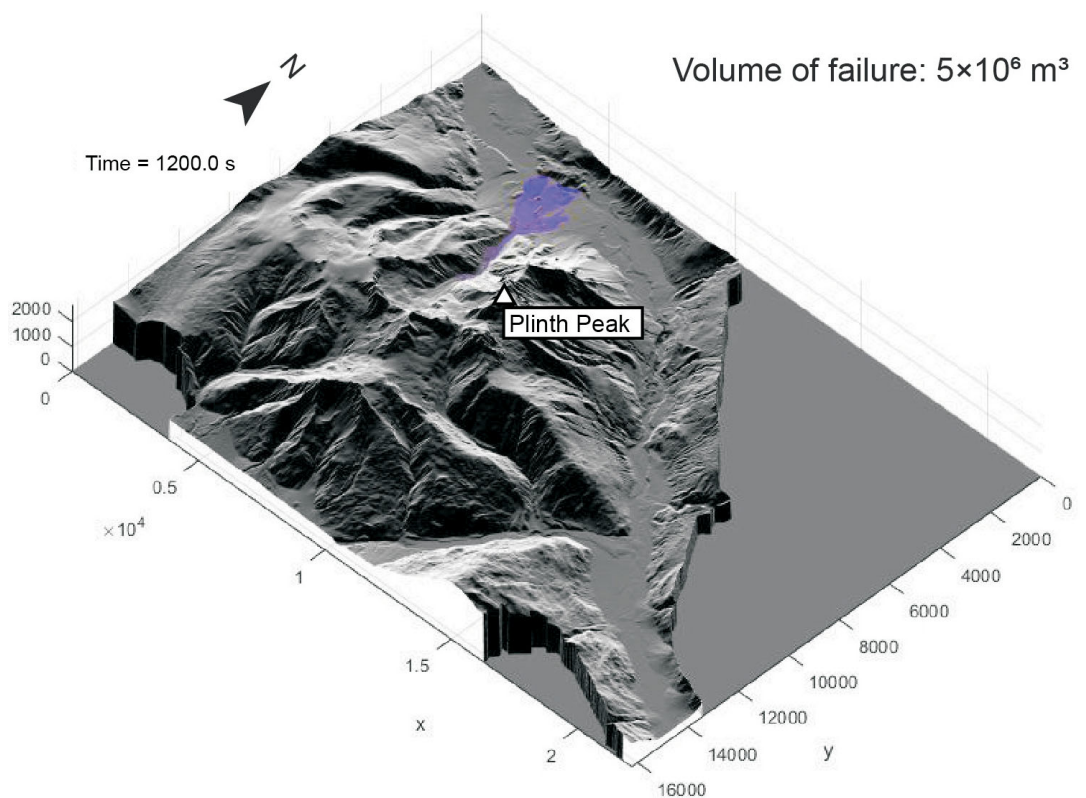


**Figure 4.** Surface expression of the inundation zones from simulated volcanic-debris flows as modelled by VolcFlow, assuming initial volume of failure of a)  $5 \times 10^7 \text{ m}^3$ , and b)  $5 \times 10^8 \text{ m}^3$ . Axes show distance in metres.

## Future Work

This paper presents the findings of numerically modelling the tephra hazards and volcanic-debris flow hazards from Mount Meager. Future work will expand on the possible hazards stemming from an eruption to include lava flows and pyroclastic flows, both of which are considered proximal hazards. Numerical models for volcanic-debris flows, lava flows and pyroclastic flows will be applied to multiple locations around the complex, which is necessary given the uncertainty in vent location during any future eruption. This paper does not comment on the time frames of inundation expected from the volcanic-debris flow hazard, but this will be addressed with further research. Ultimately, the results of numerical-model simulations for each type of hazard will be combined and included in a comprehensive volcanic-hazard map and assessment for Mount Meager.

## Acknowledgments

The authors acknowledge the financial support from Geoscience BC, the Natural Sciences and Engineering Research Council of Canada (NSERC) through a Discovery Grant, and the Jack Kleinman Memorial Fund. Thanks also go to A. Calahorrano-Di Patre for providing a review of this manuscript.

## References

- Andrews, G.M., Russell, J.K. and Stewart, M.L. (2014): The history and dynamics of a welded pyroclastic dam and its failure; *Bulletin of Volcanology*, v. 76, no. 4, p. 811–826, URL <<https://doi.org/10.1007/s00445-014-0811-0>> [November 2018].
- Calder, E.S., Wagner K. and Ogburn, S.E. (2015): Volcanic hazard maps; *in* Global Volcanic Hazards and Risk, S.C. Loughlin, R.S.J. Sparks, S.K. Brown, S.F. Jenkins and C. Vye-Brown (ed.), Cambridge University Press, Cambridge, United Kingdom.
- Clague, J.J. and Ward, B. (2011): Pleistocene glaciation of British Columbia; Chapter 44 *in* Quaternary Glaciations – Extent and Chronology: A Closer Look, L. Ehlersk, P.L. Gibbard and P.D. Hughes (ed.), Developments in Quaternary Science, Elsevier, Amsterdam, Netherlands, v. 15, p. 563–573, URL <<https://doi.org/10.1016/B978-0-444-53447-7.00044-1>> [November 2018].
- Farley, K.A., Rusmore, M.E. and Bogue, S.W. (2001): Post-10 Ma uplift and exhumation of the northern Coast Mountains, British Columbia; *Geology*, v. 29, no. 2, p. 99–102.
- Friele, P. (2012): Volcanic landslide risk management, Lillooet River valley, BC: start of North and South FSRs to Meager Confluence, Meager Creek and Upper Lillooet River; report to BC Ministry of Forests, Lands and Natural Resource Operations, Cordilleran Geoscience, Squamish District.
- Friele, P., Jakob, M. and Clague, J. (2008): Hazard and risk from large landslides from Mount Meager volcano, British Columbia, Canada; *Georisk: Assessment and Management of Risk for Engineered Systems and Geohazards*, v. 2, no. 1, p. 48–64, URL <<https://doi.org/10.1080/17499510801958711>> [November 2018].
- Global Volcanism Program (2016): Report on Cotopaxi (Ecuador); *Bulletin of the Global Volcanism Network*, E. Venzke (ed.), Smithsonian Institution, v. 41, no. 4.
- Green, N.L., Armstrong, R.L., Harakal J.E., Souther J.G. and Read P.B. (1988): Eruptive history and K-Ar geochronology of the late Cenozoic Garibaldi volcanic belt, southwestern British Columbia; *Geological Society of America Bulletin*, v. 100, p. 563–579.
- Hall, M., and Mothes, P. (2008): The rhyolitic-andesitic eruptive history of Cotopaxi volcano, Ecuador; *Bulletin of Volcanology*, v. 70, no. 6, p. 675–702, URL <<https://doi.org/10.1007/s00445-007-0161-2>> [November 2018].
- Herd, D.G. and Comité de Estudios Vulcanológicos (1986): The 1985 Ruiz volcano disaster; *EOS, Transactions of the American Geophysical Union*, v. 67, p. 457–460.
- Hetherington, R.M. (2014): Slope stability analysis of Mount Meager, south-western British Columbia, Canada; M.Sc. thesis, Michigan Technological University, Houghton, Michigan, 68 p.
- Hickson, C.J., Russell, J.K. and Stasiuk, M.V. (1999): Volcanology of the 2350 B.P. eruption of Mount Meager volcanic complex, British Columbia, Canada: implications for hazards from eruptions in topographically complex terrain; *Bulletin of Volcanology*, v. 60, p. 489–507, URL <<https://doi.org/10.1007/s004450050247>> [November 2018].
- Jensen, B.L., and Beaudoin, A.B. (2016): Geochemical characterization of tephra deposits at archeological and paleoenvironmental sites across south-central Alberta and Saskatchewan; *Archeological Survey of Alberta, Occasional Paper 36*, p. 154–160.
- Kelfoun, K. and Vargas S.V. (2016): VolcFlow capabilities and potential development for the simulation of lava flows; *Geological Society of London, Special Publications*, v. 426, p. 337–343, URL <<https://doi.org/10.1144/SP426.8>> [November 2018].
- Kelfoun, K., Samaniego, P., Palacios, P. and Barba, D. (2009): Testing the suitability of frictional behaviour for pyroclastic flow simulation by comparison with a well constrained eruption at Tungurahua volcano (Ecuador); *Bulletin of Volcanology*, v. 71, no. 9, p. 1057–1075, URL <<https://doi.org/10.1007/s00445-009-0286-6>> [November 2018].
- Leonard, E.M. (1995): A varve-based calibration of the Bridge River tephra fall; *Canadian Journal of Earth Sciences*, v. 32, p. 2098–2102.
- Mastin, L.G., Randall, M.J., Schwaiger, H.F. and Denlinger, R.P. (2013): User’s guide and reference to Ash3d – a three-dimensional model for eulerian atmospheric tephra transport and deposition; United States Geological Survey, Open-File 2013–1122, URL <<https://pubs.usgs.gov/of/2013/1122/>> [November 2018].
- Mathewes, R.W. and Westgate J.A. (1980): Bridge River tephra: revised distribution and significance for detecting old carbon errors in radiocarbon dates of limnic sediments in southern British Columbia; *Canadian Journal of Earth Sciences*, v. 17, p. 1454–1461.
- Michol, K.A., Russell, J.K. and Andrews, G.M. (2008): Welded block and ash flow deposits from Mount Meager, British Columbia, Canada; *Journal of Volcanology and Geothermal Research*, v. 169, p. 121–144, URL <<https://doi.org/10.1016/j.jvolgeores.2007.08.010>> [November 2018].
- Muñoz-Salinas, E., Castillo-Rodríguez, M., Manca, V., Manca, M. and Palacios, D. (2009): Lahar flow simulations using

- LAHARZ program: application for the Popocatepetl volcano, Mexico; *Journal of Volcanology and Geothermal Research*, v. 182, no. 1–2, p. 13–22, URL <<https://doi.org/10.1016/j.jvolgeores.2009.01.030>> [November 2018].
- Nasmith, H., Mathews, W.H. and Rouse, G.E. (1967): Bridge River ash and some recent ash beds in British Columbia; *Canadian Journal of Earth Sciences*, v. 4, p. 163–170.
- Newhall, C.G. and Hoblitt (2002): Constructing event trees for volcanic crises; *Bulletin of Volcanology*, v. 64, no. 1, p. 3–20, URL <<https://doi.org/10.1007/s004450100173>> [November 2018].
- Pierson, C.P., Wood, N.J. and Driedger, C.L. (2014): Reducing risk from lahar hazards: concepts, case studies, and roles for scientists; *Journal of Applied Volcanology*, v. 3, no. 16, URL <<https://doi.org/10.1186/s13617-014-0016-4>> [November 2018].
- Read, P.B. (1990): Mount Meager Complex, Garibaldi Belt, southwestern British Columbia; *Geoscience Canada*, v. 17, p. 167–170, URL <<https://journals.lib.unb.ca/index.php/GC/article/view/3672>> [November 2018].
- Roberti, G. (2018): Introduction in Mount Meager, a glaciated volcano in a changing cryosphere: hazard and risk challenges; Ph.D. thesis, Simon Fraser University, Burnaby, British Columbia, Chapter 1, p. 1–17.
- Roberti, G., Ward, B., van Wyk de Vries, B., Falorni, G., Menounos, B., Friele, P., Williams-Jones, G., Clague, J.J., Perotti, G., Giardino, M., Baldeon, G. and Freschi, S. (2018): Landslides and glacier retreat at Mt. Meager volcano: hazard and risk challenges; *Canadian Geotechnical Society, Proceedings of Geohazards 7 Conference*, June 3–7, 2018, Canmore, Alberta.
- Roberti, G., Ward, B., Van Wyk De Vries, B., Friele, P.A., Perotti, L., Clague, J.J. and Giardino, M. (2017): Precursory slope distress prior to the 2010 Mount Meager landslide, British Columbia; *Landslides*, v. 15, no. 4, p. 637–647, URL <<https://doi.org/10.1007/s10346-017-0901-0>> [November 2018].
- Rouwet, D., Constantinescu, R. and Sandri, L. (2017): Deterministic versus probabilistic volcano monitoring: not “or” but “and”; Chapter 4 in *Advances in Volcanology*, URL <[https://doi.org/10.1007/11157\\_2017\\_8](https://doi.org/10.1007/11157_2017_8)> [November 2018].
- Schilling, S.P. (2014): Laharz-py: GIS tools for automated mapping of lahar inundation hazard zones; United States Geological Survey, Open-File 2014-1073.
- Schwaiger, H.F., Denlinger, R.P. and Mastin L.G. (2012): Ash3d: a finite-volume, conservative numerical model for ash transport and tephra deposition; *Journal of Geophysical Research*, v. 117, no. 4, p. 1–20, URL <<https://doi.org/10.1029/2011JB008968>> [November 2018].
- Simpson, K.A., Stasiuk, M., Shimamura K., Clague J.J. and Friele P. (2006): Evidence for catastrophic volcanic debris flows in Pemberton Valley, British Columbia; *Canadian Journal of Earth Sciences*, v. 43, p. 679–689, URL <<https://doi.org/10.1139/e06-026>> [November 2018].
- Stasiuk, M.V., Hickson, C.J. and Mulder, T. (2003): The vulnerability of Canada to volcanic hazards; *Natural Hazards*, v. 28, no. 2–3, p. 563–589, URL <<https://doi.org/10.1023/A:1022954829974>> [November 2018].
- Stasiuk, M.V., Russell, J.K. and Hickson, C.J. (1996): Distribution, nature and origins of the 2400 BP eruption products of Mount Meager, British Columbia: linkages between magma chemistry and eruption behaviour; *Geological Survey of Canada, Bulletin 486*, 33 p.
- Venugopal, S., Moune, S., William-Jones, G., Wilson, A. and Russell, K. (2017): Gas emissions and magma source of the Mount Meager Volcanic Complex, Garibaldi volcanic belt, BC; IAVCEI Scientific Assembly Abstracts, August 14–18, 2017, Submission 244, Portland, Oregon.
- Voight, B. (1990): The 1985 Nevado del Ruiz volcano catastrophe: anatomy and retrospection; *Journal of Volcanology and Geothermal Research*, v. 44, p. 349–386.
- Wolfe, E.W. and Pierson, T.C. (1995): Volcanic-hazard zonation for Mount St. Helens, Washington, 1995; United States Geological Survey, Open-File Report 95-497.

## **Implementation and Operation of a Multidisciplinary Field Investigation Involving a Subsurface Controlled Natural Gas Release, Northeastern British Columbia**

**A.G. Cahill**, The University of British Columbia, Vancouver, BC, [acahill@eoas.ubc.ca](mailto:acahill@eoas.ubc.ca)

**B. Ladd**, The University of British Columbia, Vancouver, BC

**J. Chao**, The University of British Columbia, Vancouver, BC

**J. Soares**, The University of British Columbia, Vancouver, BC

**T. Cary**, University of Calgary, Calgary, AB

**N. Finke**, The University of British Columbia, Vancouver, BC

**C. Manning**, The University of British Columbia, Vancouver, BC

**C. Chopra**, The University of British Columbia, Vancouver, BC

**I. Hawthorne**, The University of British Columbia, Vancouver, BC

**O.N. Forde**, The University of British Columbia, Vancouver, BC

**K.U. Mayer**, The University of British Columbia, Vancouver, BC

**A. Black**, The University of British Columbia, Vancouver, BC

**S. Crowe**, The University of British Columbia, Vancouver, BC

**B. Mayer**, University of Calgary, Calgary, AB

**R. Lauer**, University of Calgary, Calgary, AB

**C. van Geloven**, British Columbia Ministry of Forests, Lands, Natural Resource Operations and Rural Development, Prince George, BC

**L. Welch**, British Columbia Oil and Gas Commission, Kelowna, BC

**R.D. Beckie**, The University of British Columbia, Vancouver, BC

---

Cahill, A.G., Ladd, B., Chao, J., Soares, J., Cary, T., Finke, N., Manning, C., Chopra, C., Hawthorne, I., Forde, O.N., Mayer, K.U., Black, A., Crowe, S., Mayer, B., Lauer, R., van Geloven, C., Welch, L. and Beckie, R.D. (2019): Implementation and operation of a multidisciplinary field investigation involving a subsurface controlled natural gas release, northeastern British Columbia; *in* Geoscience BC Summary of Activities 2018: Energy and Water, Geoscience BC, Report 2019-2, p. 95–104.

### **Introduction**

Fugitive gas, comprising primarily methane, can be unintentionally released from upstream oil and gas development either at surface from leaky infrastructure or in the subsurface through wellbore integrity failure. For the latter, compromised cement seals around well casings can permit flow of natural gas into the subsurface, tending toward ground surface and potentially into the atmosphere. Concerns associated with fugitive gas release at surface and in the subsurface include contributions to greenhouse gas emissions, subsurface migration leading to accumulation in nearby infrastructure and explosive risk, and impacts to

groundwater quality. Current knowledge of fugitive gas is incomplete, including how to best detect and monitor it over time, particularly its migration and fate in the subsurface at the individual event scale. Consequently, an experimental field observatory has been established to evaluate surface and subsurface fugitive gas leakage in an area hosting historic and ongoing hydrocarbon resource development within the Montney resource play of the Western Canada Sedimentary Basin, northeastern British Columbia (BC). At the field laboratory, natural gas was intentionally released at various low rates (<10 m<sup>3</sup> per day), durations and configurations. Resulting migration patterns and impacts are being evaluated through examination of the geology, hydrogeology, hydrogeochemistry, isotope geochemistry, hydrogeophysics, vadose zone and soil gas processes, microbiology and atmospheric conditions.

---

*This publication is also available, free of charge, as colour digital files in Adobe Acrobat® PDF format from the Geoscience BC website: <http://www.geosciencebc.com/s/SummaryofActivities.asp>.*

The ongoing progress through 2018 is outlined here, including a summary of the unsaturated zone experiment, final preparation and enabling works for the saturated zone injection experiment, completion and installation of the saturated zone injection system, execution of the saturated zone injection experiment, multidisciplinary monitoring activities and some initial example results.

## Background

Fugitive methane ( $\text{CH}_4$ ) from energy wells causes concern as it poses three potential risks to human health and/or the environment. Firstly, fugitive  $\text{CH}_4$  poses an explosion hazard if released into a confined space (lower explosive limit 5% in air [LeBreton, 2009]). Secondly,  $\text{CH}_4$  is a potent greenhouse gas (a factor of 25 times greater in a 100-year period than carbon dioxide [ $\text{CO}_2$ ]; Intergovernmental Panel on Climate Change, 2014). Considering emissions of  $\text{CH}_4$  from energy-resource development (particularly shale gas operations) have been identified as potentially significant (Caulton et al., 2014), fugitive  $\text{CH}_4$  therefore has potential to contribute significantly to climate change (Shindell et al., 2009). Thirdly, fugitive  $\text{CH}_4$  can impact groundwater resources by migrating in the aqueous phase and forming an explosion risk following extraction, and also following microbial attenuation (based on availability of electron acceptors, according to the redox sequence; Christensen et al., 2000; Le Mer and Roger, 2001) where it may generate undesirable byproducts (e.g.,  $\text{H}_2\text{S}$ ,  $\text{Fe}^{2+}$ ,  $\text{Mn}^{2+}$ ) or potentially induce the release of trace metals (Bennett and Dudas, 2003; Van Stempvoort et al., 2005, 2007; Amos et al., 2012; Ng et al., 2015). Although much research has recently been undertaken with respect to fugitive  $\text{CH}_4$ , it has for the most part taken the form of retrospective environmental forensic studies to assess if detectable impacts to groundwater have occurred. Unfortunately, little research has comprehensively assessed migration, impacts and fate

of fugitive  $\text{CH}_4$  in a holistic manner or at the single event scale. Exceptionally, a recent multidisciplinary study (Cahill et al., 2017), upon which the current study builds, monitored groundwater, soil gas and surface efflux at high spatiotemporal resolution during release of a small volume of natural gas into a shallow (i.e., ~9 m depth) unconfined aquifer system. Results from this study showed that although a significant proportion of injected gas reached the surface and emitted to atmosphere (with some oxidation observed in the unsaturated zone), a large portion remained in the saturated zone where it created a dispersed and laterally extensive volume of impacted groundwater (Cahill et al., 2017). Although this study provided important and detailed insights regarding fugitive  $\text{CH}_4$ , it forms only a single site specific study and its overall applicability and relevance to regions of resource development (e.g., Western Canada Sedimentary Basin) is limited. Consequently, many knowledge gaps remain and more studies such as this are needed in a range of geological settings where petroleum resource development takes place in order to improve an understanding of fugitive  $\text{CH}_4$ .

In March 2017, Geoscience BC entered into a contribution agreement with The University of British Columbia's Energy and Environment Research Initiative (UBC EERI; co-directed by R. Beckie and A. Cahill), located at the Department of Earth, Ocean and Atmospheric Sciences, in order to better understand fugitive gas impacts, particularly in a BC context. Cahill et al. (2018) described the initiation of this project including the significant leveraging of base funding provided by Geoscience BC to bring more disciplines into the research program. Subsequently, it described activities undertaken in order to select and attain two separate field locations near Hudson's Hope in northeastern BC: 1) a saturated (i.e., a confined aquifer) zone site and 2) an unsaturated zone (vadose zone) site (Figure 1). This paper includes a description of the follow-on work

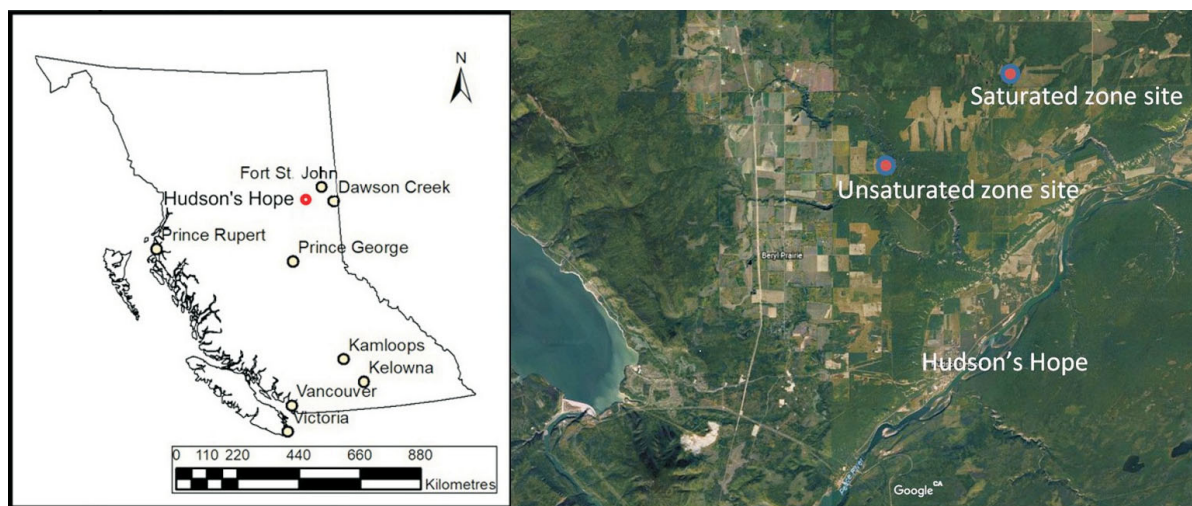


Figure 1. Location of unsaturated and saturated zone sites, Hudson's Hope area, northeastern British Columbia.

from this successful first year. Activities at both sites are described but there is a focus on the saturated zone site, including final set-up for the injection experiment, execution of the injection and ongoing monitoring activities with some examples of experimental results.

## Summary of Activities and Progress

### Unsaturated Zone Injection Experiment

Following attainment and set-up at the unsaturated zone site (as described in Cahill et al., 2018), 29 m<sup>3</sup> of compressed natural gas were injected at 12 m depth over five days with monitoring of gas migration and fate conducted for a further 28 days at the end of 2017. After 28 days (i.e., as of early November 2017), monitoring was unexpectedly ceased prematurely by a severe snowstorm and damage to equipment by cattle following an escape. No further sampling was undertaken during the winter and spring period (2018) and one final round of soil gas samples were collected at the site in August 2018.

The unsaturated zone injection experiment has proved highly successful and generated data of great significance in the context of gas migration and fugitive gas. Currently EERI is in the process of publishing several peer-reviewed journal articles related to this experiment:

- 1) barometric-pumping controls fugitive gas emissions from a vadose zone natural gas release by O.N. Forde, A.G. Cahill, R.D. Beckie and K.U. Mayer (submitted to Nature Geoscience), and
- 2) quantification of attenuation capacity and fate of fugitive gas leakage into unsaturated soils by O.N. Forde, A.G. Cahill, I. Hawthorne, A. Black, R.D. Beckie and K.U. Mayer (to be submitted to Science of the Total Environment or a similar journal).

Figure 2 shows methane and ethane percent composition for the final soil gas samples taken in August 2018, nearly one year after the injection of gas. Results show gas still present where elevated ethane is correlated to elevated methane. The presence of ethane above detection is conclu-

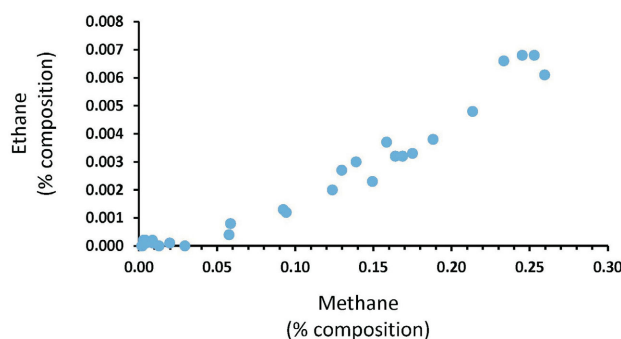


**Figure 2.** Methane versus ethane percent composition in soil gas samples taken in August 2018, showing persistence of low levels of natural gas one year following injection of compressed natural gas at the unsaturated zone site, northeastern British Columbia.

sive evidence for persistence of the injected gas (as ethane is not naturally present in this shallow soil system). All other results are being reviewed and assessed with full conclusions on the migration, impacts and fate of injected gas to follow in short order.

In order to insure integrity of overall findings from this study and to avoid compromising publication of results in top journals (which stipulate results must not have been previously published elsewhere) no further results from this experiment will be presented in this Summary of Activities paper. However, published journal articles will be provided to Geoscience BC and intermediate results will be made available via the Geoscience BC website in due course.

### Saturated Zone Injection Experiment

#### Preparation and Execution

In 2017, significant effort was made to characterize the geology, hydrogeology and groundwater quality of the saturated zone site (as described in Cahill et al., 2018). Following on from this, in 2018, the site was further characterized, various multidisciplinary monitoring networks were established/installed, injection infrastructure constructed (including a synthetic Montney gas designed by the experiment team) and the injection experiment was conducted. In summary, 100 m<sup>3</sup> of a synthetic Montney gas (Table 1) was injected at 26 m vertical depth into the aquifer at a rate of 1.5 m<sup>3</sup>/day, commencing on June 12, 2018, and continuing for 72 days. Figures 3 and 4 show the injection system and an aerial image of the experimental site with all infrastructure in place. The following sections describe the activities of each discipline-specific team. It should be noted that this experiment is still ongoing and results are still being collected and interpreted. Consequently, only example results are shown and no full results, conclusions or key findings are presented here.

#### Discipline-Specific Activities

##### Hydrogeology

In the first half of 2018, additional hydrogeological-focused intrusive investigations were performed to prepare for the injection experiment. In January 2018, nine cone penetration test (CPT) holes were pushed to depths ranging from 12.2 to 23 m below ground level (bgl) directly around the injection zone. These tests allowed greater character-

**Table 1.** Proportional composition of a typical Montney gas and The University of British Columbia's Energy and Environment Research Initiative (EERI) synthetic Montney gas formulated for the saturated zone injection experiment. Abbreviations: C1, methane; C2, ethane; C3, propane; C4, butane; >C4, all hydrocarbons with a chain length greater than 4.

Gas	C1	C2	C3	>C4	CO <sub>2</sub>	N <sub>2</sub>	He
Typical Montney gas	0.85	0.08	0.03	0.02	0.001	0.002	0.0001
EERI synthetic Montney gas	0.85	0.08	0.05	0	0.01	0.005	0.005

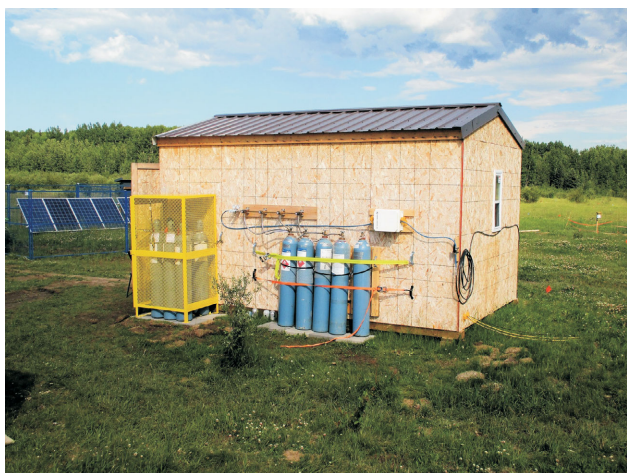


**Figure 3.** Completed injection system at the saturated zone site, northeastern British Columbia.



**Figure 4.** Aerial drone image of saturated zone experimental site with solar array, injection control laboratory and various multidisciplinary monitoring systems around the injection point, northeastern British Columbia.

ization of stratigraphy and heterogeneity and showed the confined upper diamict layer to be relatively continuous (i.e., 12 m thick) with the underlying confined aquifer (composed of interbedded sand, silt, gravel) being highly heterogeneous with limited lateral continuity of permeable zones. The detailed stratigraphy provided by CPT results allowed identification of horizons of potentially higher permeability in which to install sampling screens. Consequently, 13 multilevel monitoring wells (MW), with monitoring ports at various depths (e.g., 12, 16, 18, 20 m bgl),

and six single-screened larger diameter (12.5 cm) monitoring wells were drilled and installed around the injection zone in March and April 2018. In summary, prior to injection a total of six single-screened (PW) and 13 multilevel MW with 35 water-flowing monitoring ports were installed (Figure 5). Subsequently, background groundwater samples were collected prior to the injection through various sample points and several sampling campaigns showed a weakly basic (pH ranging from 7.1 to ~7.48) Ca-Mg-HCO<sub>3</sub>

water type with relatively moderate total dissolved solids (620–735 mg/L) and very low dissolved natural CH<sub>4</sub> (~0.01–0.1 mg/L) of biogenic origin.

Physical (i.e., temperature, specific conductance, pH, oxidation-reduction potential) and aqueous chemistry (cation, anion, dissolved gas composition) were subsequently monitored through all groundwater sampling infrastructure every one to two weeks before, during and after injection. Monitoring will be ongoing through 2019.

### Geophysics

The geophysics team visited the site approximately every two weeks from the time of injection until the end of September. During these visits, refraction seismic surveys and electrical resistivity tomography (ERT) surveys were carried out. These surveys were designed for time-lapse analysis. Hence, the location of each survey

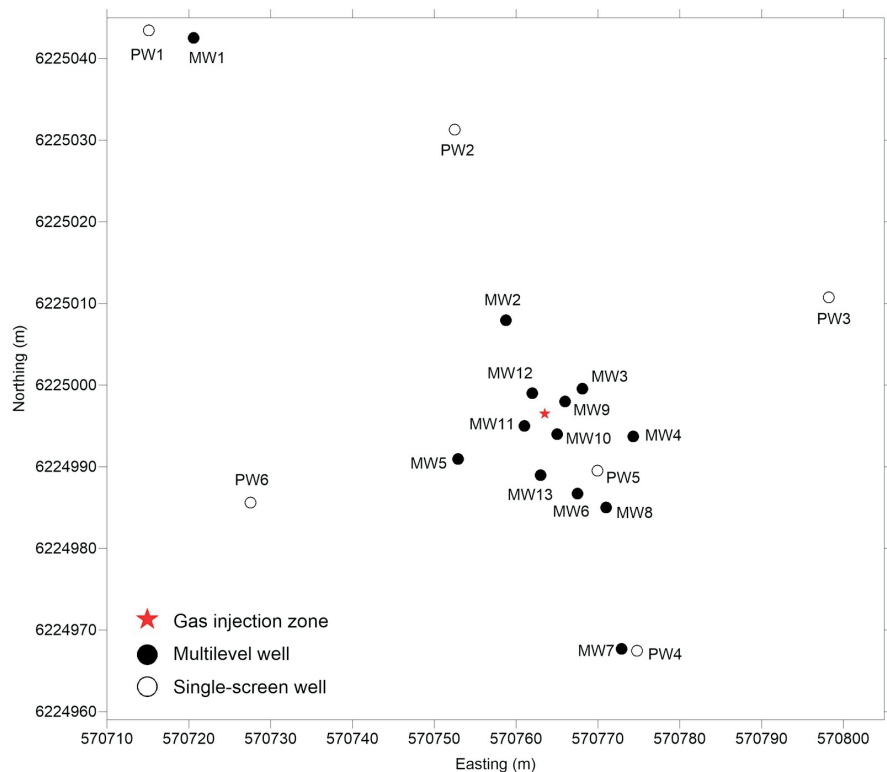


**Figure 5.** The layout of the 13 multilevel monitoring wells (filled-in circles), six single-screened monitoring wells (open circles) and gas injection zone (red star), northeastern British Columbia.



**Figure 6.** Vertical seismic profile set-up, saturated zone site, northeastern British Columbia.

was the same for each visit. To accomplish this, permanent electrodes were installed in the ground in early June. During the May drilling campaign, fibre optic cables were installed in four wells. These cables were used to measure temperature variations in the subsurface during injection, known as distributed temperature sensing (DTS). Vertical seismic profile (VSP) data were collected pre-injection (June 5) and post-injection (September 25) to create a time-lapse dataset (Figure 6). In total there are seven ERT and refraction seismic datasets. Analysis of the data is ongoing.

### Microbiology

Background sampling for microbiological analyses commenced in October 2017 (Table 2). At that time only the six PW wells had been installed. Those wells were sampled to recover microbial biomass through chemical flocculation. Samples were also collected for cell counting and single cell genomic analyses, as well as for  $\Sigma\text{H}_2\text{S}$  determination. The samples collected for  $\Sigma\text{H}_2\text{S}$  will also be used for determining the S-isotopic composition of relevant S-pools. During well installation consolidated materials were recovered for microbial community analyses.

Further sampling was conducted June 6–13, 2018, immediately prior to gas injection. All wells were sampled at this time for  $\Sigma\text{H}_2\text{S}$ , microbial community analyses, cell counting and single cell genomics. Process rate measurements (methane oxidation, methanogenesis, sulphate reduction) were conducted on wells MW2, MW7 and MW10 in early August. This subset was justified given that MW2 was upstream of the injection well, serving as a pseudocontrol, MW7 and MW10 were downstream at varying distances and thus likely to capture a time-resolved response to injection. Following injection, the majority of the sampling was focused on MW wells in the immediate vicinity of the injection well. Samples were collected roughly every two weeks, however, low temperatures precluded sampling in

**Table 2.** Samples taken for microbial community analyses and process rate measurements at the saturated zone site, northeastern British Columbia. Abbreviations: 10X, first borehole drilled; CC, cell counts; MD, microbial diversity; MG, methanogenesis; MOX, aerobic methane oxidation; MW, multilevel monitoring well; PW, single-screened monitoring well; SAG, single cell amplified genomes; SRR, sulphate reduction rates.

Date	Wells	Samples
Oct. 19, 2017	PW1–6, 10X	$\text{H}_2\text{S}$ , CC, SAG, MD
May 1–5, 2018	MW1, 3, 6	Soil
Jun. 6–13, 2018	PW1–6, MW1–13	$\text{H}_2\text{S}$ , CC, SAG, MD, MOX, MG, SRR
Jun. 27–29, 2018	MW1, 9, 11	CC, SAG, MD
Jul. 12–13, 2018	MW1, 9–12	CC, SAG, MD
Jul. 27–30, 2018	MW1–3, 9–12	CC, SAG, MD
~Aug. 5, 2018	MW2, 7, 10	MOX, MG, SRR
Aug. 15, 2018	MW1–3, 9–12	CC, SAG, MD
Aug. 27, 2018	MW1–3, 9–12	CC, SAG, MD
Sep. 18, 2018	MW1–3, 9–12	CC, SAG, MD

late September. Going forward, the sampling strategy will capture wells where  $\text{CH}_4$  is detected in addition to the two innermost rings of wells around the injection well, so as not to miss wells receiving migrating gas. Microbial sample analyses and interpretation is ongoing.

### Soil Gas and Surface Efflux

To monitor soil gas concentrations and surface effluxes, 12 dynamic long-term chambers (8100-104, LI-COR, Inc.) were deployed and 21 soil gas sampling ports were installed around the field site, primarily along two transects radiating from the injection zone. The 12 long-term dynamic chambers each periodically measure  $\text{CO}_2$  and  $\text{CH}_4$  effluxes at the designated locations, providing high-resolution time series data. The 21 soil gas sampling locations were manually augured with sampling ports at 0.45 and 1.15 m below ground surface, allowing for the collection of soil gas samples for compositional and isotope analyses. Additionally, 103 survey collars were placed in the ground and an additional set of analyzers allowed for survey flux measurements of  $\text{CH}_4$  and  $\text{CO}_2$  to be obtained across the site, providing detailed spatially distributed data at selected times. Figure 7 shows installed infrastructure at the site. Survey flux measurements and soil gas samples for isotopic and compositional analysis were collected every 2–4 weeks starting on May 28, 2018, and ending on October 1, 2018, due to weather restrictions. An example of  $\text{CO}_2$  efflux from the site as measured from long-term chambers is shown in Figure 8.

### Eddy Covariance and Micrometeorology

The eddy-covariance (EC) system was installed at the saturated zone site on May 14, 2018, and was powered up on June 1 (Figure 9). It was located at 56.1649°N, 121.860°W. Various climate sensors were added in the following few weeks, and the entire system, with all the necessary components has been fully operational since June 28, 2018. The



**Figure 7.** Long-term chambers (rectangular-based instruments), survey collars (green circles) and soil gas sampling wells (white standpipes) at saturated zone site, northeastern British Columbia.

EC system comprises a 3-D sonic anemometer (CSAT3B, Campbell Scientific, Inc. [CSI]), which measures wind direction and speed in three dimensions and also provides the sonic air temperature (Figures 10, 11). The gas analyzers being used are the LI-COR, Inc. LI-7700 for CH<sub>4</sub>, which is

an open-path system, and a LI-COR, Inc. LI-7200 for CO<sub>2</sub> and water vapour, which is an enclosed infrared gas analyzer. There is also a flow module (7200-101) with the LI-7200, which is responsible for maintaining a precise and controllable flow of air. An LI-7550 analyzer interface unit (AIU) was also set-up, which integrates data from the sonic anemometer, and LI-7200 and LI-7700 analyzers. A self-contained climate system was also set-up and has been fully operational since June 28, 2018. This consists of a net radiometer (CNR4, Kipp & Zonen B.V.), a 2-D anemometer (WindSonic, Gill Instruments Limited), and CSI sensors (manufactured by Vaisala Corporation) for barometric pressure (CS106), temperature and relative humidity (HMP155A). Three sensors (GS3, Decagon Devices, Inc.) were also installed to measure soil moisture content, soil electrical conductivity and soil temperature over the 0 to 5 cm depth. Two soil heat flux plates (HFP01-L, HFP01SC-L, Hukseflux Thermal Sensors B.V.) were installed at a depth of 5 cm, the latter being self-calibrating. There is also a tipping bucket rain gauge (TE525WS, Texas Electronics, Inc.), which is designed to be used with a precipitation adapter in case of snow.

A datalogger (CR1000, Campbell Scientific, Inc.) at the site collects all the climate data from the various components, and compiles it giving the averages, maximum and minimum values of these traces for each half hour. These data together with the computed EC fluxes (by a SmartFlux 2 System, LI-COR, Inc.) are transmitted to the UBC Biometeorology Soil and Physics Group lab daily at 6 a.m. via a modem (RV50, Sierra Wireless S.A.). The high-frequency data are collected onto a USB data stick present at the site, which is sent back and forth between the site and UBC on a biweekly basis. This arrangement allows for the continual reprocessing of the high-frequency data, the use



**Figure 8.** Example of carbon dioxide fluxes as measured from the long-term dynamic chambers, saturated zone site, northeastern British Columbia. It shows natural fluctuation before and shortly after injection (June 12) commenced.

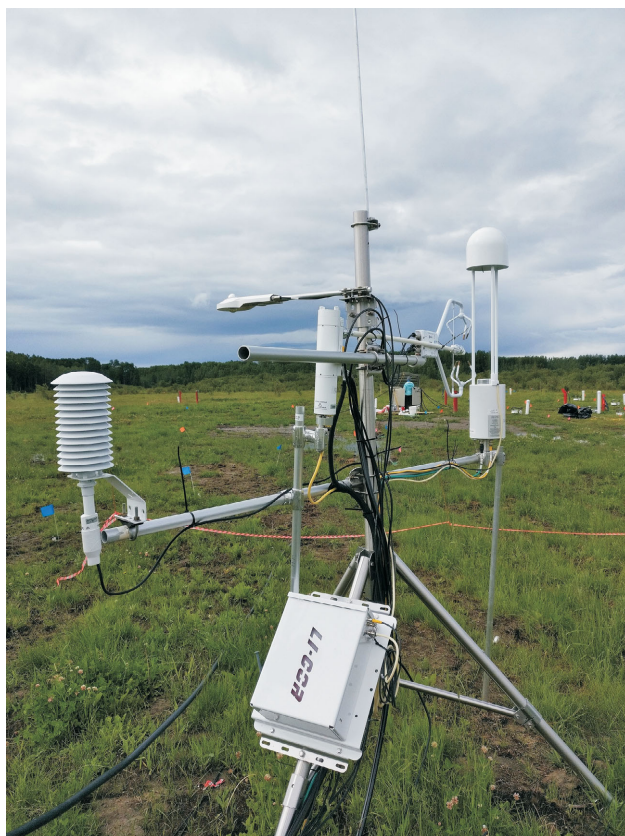


**Figure 9.** Eddy-covariance flux tower at the saturated zone site, northeastern British Columbia.



**Figure 10.** The instruments shown are the 1) sonic anemometer (CSAT3B, Campbell Scientific, Inc.), 2) open-path methane analyzer (LI-7700, LI-COR, Inc.), and 3) air sampling tube connected to the enclosed infrared gas analyzer for carbon dioxide and water vapour (LI-7200, LI-COR, Inc.).

of different computational methods and the application of corrections to flux calculations.

Routine tests were carried out to ensure accurate functioning of the components. Regular filtering of the data is done to account for the effects of wind direction and turbulence.

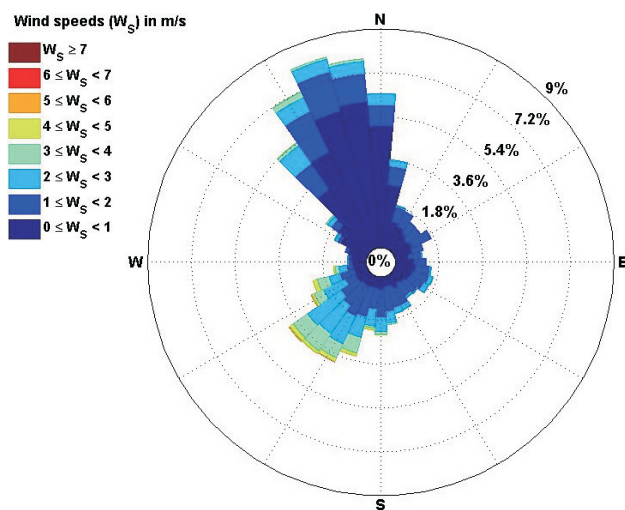


**Figure 11.** Windrose generated from eddy-covariance system measurements recorded at the saturated zone site, northeastern British Columbia. The majority of the winds are from the northwest, along with a portion of the high-speed winds from the southwest. Wind speeds at the site were usually between 1.5 and 3 m/s.

For the LI-7700 gas analyzer to adjust to the onset of winter, its temperature settings were changed, as recommended by LI-COR staff, from warm to cool mode on September 20. This was done because the sensor would not be able to perform a line-lock as lasers drift during cool temperatures. Following this, analyses to assess energy balance closure were carried out, because good closure indicates correct functioning of the EC system, and hence reliable flux measurements.

The complete EC system has collected continuous high-resolution data (including concentrations of CH<sub>4</sub> and CO<sub>2</sub> as well as complementary detailed micrometeorology measurements), which will allow the detection, quantification and assessment of any experimental injected gas that reaches the atmosphere. Measurements are ongoing and planned to continue until summer 2019. Processing of results is also ongoing.

### Public and First Nations Engagement

The UBC EERI team has taken care to create opportunities for engagement by First Nation communities and other interested stakeholders. In late 2017, two information letters were sent to neighbouring First Nations communities to in-



**Figure 12.** The University of British Columbia's Energy and Environment Research Initiative's Field Demonstration Day, July 25, 2018.

form them of the upcoming controlled natural gas release experiment to be performed in the summer of 2018, as well as to ask for input and provide details on a line of communication for questions, concerns or comments. These were sent in October and December of 2017. On March 13, 2018, the UBC EERI team attended the Northeast Water Strategy meeting in Fort St. John. They described their projects, including the controlled natural gas release experiment, to various stakeholders. Once the experiment was underway, a Field Demonstration Day was held on July 25 for funders, government officials, industry and community leaders. Unfortunately, no First Nations members attended. Starting with a tour of the resource development in the Montney region, proximal to the sites, and a quick geology and hydrogeology lesson, the 32 attendees ended the day with a tour and 'show-and-tell' of the saturated zone site and the various monitoring methodologies in use. The day was a great success and generated discussion and insights, formed new relationships and increased buy-in from the various stakeholders (Figure 12).

## Ongoing Work

Research is ongoing at two separate but closely located sites at which controlled gas release experiments have been performed. Data from the unsaturated zone gas injection experiment is being processed and publications are being formulated to report key findings and conclusions to the wider scientific community. This experiment has generated an extensive and important dataset from which many insights with respect to fugitive gas leakage into unsaturated soils is set to be gained. The saturated zone experiment is ongoing. Monitoring to track and assess migration, impacts and fate of injected gas will continue in a multidisciplinary manner into 2019. Reporting of results in peer-reviewed publications will begin in due course.

## Summary of Progress

The following forms a summary of the progress made to date with respect to The University of British Columbia's Energy and Environment Research Initiative's controlled natural gas release experiment:

- the unsaturated zone experiment was completed and manuscripts are being formulated for submissions to top-tier journals (one article in submission with *Nature Geoscience*);
- preparations for injection and set-up of the extensive multidisciplinary monitoring networks to track migration, impacts and fate of fugitive gas at the saturated zone site were successfully performed;
- 100 m<sup>3</sup> of a synthetic Montney gas analogue was successfully injected at 26 m vertical depth into the saturated zone site aquifer at a rate of 1.5 m<sup>3</sup>/day, commencing on June 12, 2018, and continuing for 72 days;
- large multidisciplinary datasets are being developed to show in high spatiotemporal resolution the impacts of the injected gas migration and its fate in the environment following its release into the saturated zone; and
- reporting of main findings and conclusions from the saturated zone experiment in peer-reviewed literature will follow in short order.

## Acknowledgments

Peer reviewed by L. Smith. This work was funded by Geoscience BC and the Natural Resources Canada's Energy Innovation Program.

## References

- Amos, R.T., Bekins, B.A., Cozzarelli, I.M., Voytek, M.A., Kirshstein, J.D., Jones, E.J. and Blowes, D.W. (2012): Evidence for iron-mediated anaerobic methane oxidation in a crude oil-contaminated aquifer; *Geobiology*, v. 10, issue 6, p. 506–517, URL <<https://doi.org/10.1111/j.1472-4669.2012.00341.x>> [November 2018].
- Bennett, B. and Dudas, M.J. (2003): Release of arsenic and molybdenum by reductive dissolution of iron oxides in a soil with enriched levels of native arsenic; *Journal of Environmental Engineering and Science*, v. 2, issue 4, p. 265–272, URL <<https://doi.org/10.1139/s03-028>> [November 2018].
- Cahill, A.G., Chao, J., Ford, O., Ladd, B., Prystupa, E., Mayer, K.U., Tannant, D., Black, A., Crowe, S., Hallam, S., Mayer, B., van Geloven, C., Welch, L., Levson, V. and Beckie, R.D. (2018): Establishment of field stations for the multidisciplinary study of controlled natural gas releases, north-eastern British Columbia; *in* Geoscience BC Summary of Activities 2017: Energy, Geoscience BC, Report 2018-4, p. 65–76.
- Cahill, A.G., Steelman, C.M., Forde, O., Kuloyo, O., Ruff, S.E., Mayer, B., Mayer, K.U., Strous, M., Ryan, M.C., Cherry, J.A. and Parker, B.L. (2017): Mobility and persistence of methane in groundwater in a controlled-release field experiment; *Nature Geoscience*, v. 10, issue 4, p. 289–294, URL <<https://doi.org/10.1038/ngeo2919>> [November 2018].

- Caulton, D.R., Shepson, P.B., Santoro, R.L., Sparks, J.P., Howarth, R.W., Ingraffea, A.R., Cambaliza, Sweeney, C., Karion, A., Davis, K.J., Stirm, B.H., Montzka, S.A. and Miller, B.R. (2014): Toward a better understanding and quantification of methane emissions from shale gas development; *Proceedings of the National Academy of Sciences of the United States of America*, v. 111, no. 17, p. 6237–6242, URL <<https://doi.org/10.1073/pnas.1316546111>> [November 2018].
- Christensen, T.H., Bjerg, P.L., Banwart, S.A., Jakobsen, R., Heron, G. and Albrechtsen, H. (2000): Characterization of redox conditions in groundwater contaminant plumes; *Journal of Contaminant Hydrology*, v. 45, issue 3–4, p. 165–241, URL <[https://doi.org/10.1016/S0169-7722\(00\)00109-1](https://doi.org/10.1016/S0169-7722(00)00109-1)> [November 2018].
- Intergovernmental Panel on Climate Change (2014): *Climate change 2013: the physical science basis – contribution of Working Group I to the fifth assessment report of the Intergovernmental Panel on Climate Change*; T.F. Stocker, D. Qin, G.-K. Plattner, M. Tignor, S.K. Allen, J. Boschung, A. Nauels, Y. Xia, V. Bex and P.M. Midgley (ed.), Cambridge University Press, Cambridge, United Kingdom and New York, New York, 1535 p., URL <<https://doi.org/10.1017/CBO9781107415324>> [November 2018].
- LeBreton, E. (2009): Confined space; Transport Canada, URL <<https://www.tc.gc.ca/eng/canutec/articles-confined-456.htm>> [December 2017].
- Le Mer, J. and Roger, P. (2001): Production, oxidation, emission and consumption of methane by soils: a review; *European Journal of Soil Biology*, v. 37, issue 1, p. 25–50.
- Ng, G.H.C., Bekins, B.A., Cozzarelli, I.M., Baedeker, M.J., Bennett, P.C., Amos, R.T. and Herkelrath, W.N. (2015): Reactive transport modeling of geochemical controls on secondary water quality impacts at a crude oil spill site near Bemidji, MN; *Water Resources Research*, v. 51, issue 6, p. 4156–4183, URL <<https://doi.org/10.1002/2015WR016964>> [November 2018].
- Shindell, D.T., Faluvegi, G., Koch, D.M., Schmidt, G.A., Unger, N. and Bauer, S.E. (2009): Improved attribution of climate forcing to emissions; *Science*, v. 326, issue 5953, p. 716–718, URL <<https://doi.org/10.1126/science.1174760>> [November 2018].
- Van Stempvoort, D., Maathuis, H., Jaworski, E., Mayer, B. and Rich, K. (2005): Oxidation of fugitive methane in groundwater linked to bacterial sulfate reduction; *Groundwater*, v. 43, issue 2, p. 187–199.
- Van Stempvoort, D.R., Armstrong, J. and Mayer, B. (2007): Microbial reduction of sulfate injected to gas condensate plumes in cold groundwater; *Journal of Contaminant Hydrology*, v. 92, issue 3–4, p. 184–207, URL <<https://doi.org/10.1016/j.jconhyd.2007.01.006>> [November 2018].



# Characterizing Dissolved Methane in Groundwater in the Peace Region, Northeastern British Columbia, Using a Regional, Dedicated, Groundwater Monitoring Well Network

**A.G. Cahill, The University of British Columbia, Vancouver, BC, [acahill@eoas.ubc.ca](mailto:acahill@eoas.ubc.ca)**

**R.D. Beckie, The University of British Columbia, Vancouver, BC**

**M. Goetz, The University of British Columbia, Vancouver, BC**

**A. Allen, Simon Fraser University, Burnaby, BC**

**B. Ladd, The University of British Columbia, Vancouver, BC**

**L. Welch, British Columbia Oil and Gas Commission, Kelowna, BC**

**D. Kirste, Simon Fraser University, Burnaby, BC**

**B. Mayer, University of Calgary, Calgary, AB**

**C. van Geloven, British Columbia Ministry of Forests, Lands, Natural Resource Operations and Rural Development, Prince George, BC**

---

Cahill, A.G., Beckie, R.D., Goetz, M., Allen, A., Ladd, B., Welch, L., Kirste, D., Mayer, B. and van Geloven, C. (2019): Characterizing dissolved methane in groundwater in the Peace region, northeastern British Columbia, using a regional, dedicated, groundwater monitoring well network; *in* Geoscience BC Summary of Activities 2018: Energy and Water, Geoscience BC, Report 2019-2, p. 105–122.

## Introduction

Methane in groundwater in areas of oil and gas development is a complex issue and the subject of much controversy. Although methane is naturally ubiquitous in groundwater, there have been isolated documented instances of unintentional release into the subsurface from oil and gas development activities, leading to anthropogenic impacts on groundwater. Previous research to investigate the prevalence of anthropogenic sources of methane in groundwater has proved inconclusive due to two key limitations: 1) scientifically designed and purpose-built monitoring wells have not been used to collect data; and 2) natural ‘background’ dissolved methane concentrations have not been adequately characterized from which anthropogenic impacts, or lack thereof, can be assessed. Consequently, much conjecture has ensued with deterioration of public confidence and backlash against increasing development. Through this project, this issue will be addressed in the Peace region of northeastern British Columbia (BC) through review of existing data and installation of 30 purpose-built and scientifically designed groundwater monitoring wells, to generate a comprehensive scientifically defensible groundwater dataset. Through this project, groundwater dissolved methane and geochemistry conditions within the Peace region of northeastern BC will be

comprehensively and conclusively characterized, along with details of subsurface geological and aquifer conditions. The results will be used to inform appropriate groundwater monitoring strategies in light of continued oil and gas development for the region. As a legacy, the project will provide a scientifically designed and extensive regional groundwater monitoring network available for future scientific research and ongoing monitoring of groundwater quality in the Peace region.

The progress made in the first year of this project is described herein. This includes refinement and finalization of the scientific plan, identification of potential areas at which to assess baseline conditions, a desk study to review existing groundwater data, scoping and drilling of the first monitoring wells (including geological characterization and sampling), and various public engagement activities.

## Background

Methane may be present in groundwater in areas of oil and gas resource development due to both natural and anthropogenic factors. Dissolved methane is known to be naturally ubiquitous (e.g., commonly up to 5 mg/L) in groundwater systems (Darling and Gooddy, 2006), present within an ambient or background range. Such background methane can be microbial and/or thermogenic (Brantley et al., 2014), and concentrations are primarily controlled by methane source and prevailing redox conditions of a given groundwater system (Humez et al., 2016a, b). Other natural factors have also been suggested to affect both groundwa-

---

*This publication is also available, free of charge, as colour digital files in Adobe Acrobat® PDF format from the Geoscience BC website: <http://www.geosciencebc.com/s/SummaryofActivities.asp>.*

ter methane concentrations and the presence of shallow gas-phase methane in areas of hydrocarbon resource development, and occurrences in excess of the typical background range have been documented. For example, soil gas survey methods to identify surface methane seeps and their origins have been employed as a method to explore for gas resources (e.g., von der Dick et al., 2002; von der Dick and Bosman, 2011), suggesting geological and resource-related factors affect the distribution of subsurface methane in sedimentary basins. Dissolved methane in domestic water wells has been associated with specific geological features such as coal beds in West Virginia (Harkness et al., 2017), natural fault systems in east Texas (Nicot et al., 2017) and undeveloped shale bed gas resources in Ontario (Hamilton et al., 2015). Finally, topography has also been identified as a potential factor influencing natural distribution of dissolved methane concentrations in northeastern Pennsylvania (Molofsky et al., 2013).

In regions of oil and gas development, anthropogenically derived occurrences of elevated subsurface methane have also been documented as occurrences of ‘gas migration’. Gas migration, with respect to upstream oil and gas resource development (as defined in *Drilling and Production Regulation, Section 41* [Province of British Columbia, 2017]), refers to the development of pathways within a cemented wellbore permitting the buoyant flow of natural gas (primarily composed of methane) vertically upward toward or directly into the shallow subsurface via inadequately sealed wellbores (i.e., leaky wells; e.g., Dusseault and Jackson, 2014; Ingraffea et al., 2014). Available data indicate observed and documented cases of gas migration originate from approximately 0.73% of oil and gas wells in Alberta (Bachu, 2017). Gas migration, as “the flow of gas outside the surface casing of a well” (BC Oil and Gas Commission, 2017), may be identified by the observation of bubbles in standing water around a wellhead (Briskin, 2015; BC Oil and Gas Commission, 2017) or may manifest as an unobserved subsurface occurrence. A concern with observed or unobserved gas migration is the potential for elevated levels of dissolved methane in surrounding groundwater. It has been shown that if gas migration is occurring in the subsurface, an extensive and dispersed plume of dissolved hydrocarbons in groundwater can be generated (Cahill et al., 2017).

Consequently, anthropogenically derived methane sources and their management are topics of interest to academics, regulators, industry and the general public (Kelly et al., 1985; Van Stempvoort et al., 2005; Darling and Goody, 2006; Canadian Association of Petroleum Producers, 2012; Vidic et al., 2013; Council of Canadian Academies, 2014; Vengosh et al., 2014; BC Oil and Gas Commission, 2017). Although methane itself is nontoxic, colourless and odorless, and there are no federal or provincial regulatory standards for drinking water or for the protection of aquatic

life, several key questions regarding the consequences of fugitive methane in groundwater remain. For example, it has been shown that anthropogenic methane may change groundwater chemistry when microbially metabolized, potentially reducing groundwater quality (Cahill et al., 2017), and there is continuing research to understand these processes (Cahill et al., 2019). Additionally, elevated dissolved concentrations of methane in groundwater, above the solubility limit, can indicate a potential fire or explosion hazard due to exsolution and accumulation of gas phase methane in confined spaces or infrastructure. In response to this concern, which has been historically associated with coal mining, dissolved methane in water at concentrations >10 mg/L has been specified as a warning level to indicate potential for accumulation of free gas (Eltschlager et al., 2001). And finally, due to buoyancy forces, subsurface anthropogenic methane may find a path to the ground surface and emit to the atmosphere, contributing to greenhouse gas emissions.

Regulations and engineering standards for well drilling, cementing, testing and maintenance (e.g., BC Oil and Gas Commission, 2017; Province of British Columbia, 2017) are in place to minimize the potential for the development of gas migration, leading to the reduction of both the likelihood of occurrence and the degree or extent of associated dissolved methane in groundwater, should pathways develop. However, key scientific questions and controversy remain regarding the origins of groundwater methane across regions of oil and gas development, as well as the prevalence of unobserved gas migration and its effects on groundwater. For example, a strong and pervasive association of elevated levels of dissolved methane in groundwater with energy well locations have been suggested by some researchers utilizing available groundwater data from domestic wells (e.g., Osborn et al. [2011a] and Jackson et al. [2013] for northeastern Pennsylvania; Sherwood et al. [2016] for Colorado). A subsequent study for the same northeastern Pennsylvania area using an enhanced domestic well dataset, however, found no statistical association between elevated levels of dissolved methane and energy wells (Siegel et al., 2015).

Controversy related to the above noted research is due, in part, to two key factors:

- 1) lack of a scientifically designed groundwater monitoring network and reliance on data from domestic wells; and
- 2) lack of characterization of background levels of groundwater methane to provide a basis to distinguish anthropogenic impacts.

With respect to key factor (1), the limitations of using data from domestic wells to investigate environmental impacts in areas of oil and gas development are well known (e.g., Gorody, 2012; Jackson and Heagle, 2016), and include lo-

cation biases; confidentiality issues limiting documentation of results; lack of well and system maintenance; uncontrolled sample collection points (e.g., posttreatment from faucets or taps); unknown potential contamination sources; uncertainty in well information (geology and well construction); and well ownership and property access constraints. Thus, although domestic wells can provide for inexpensive and large datasets, such wells are not located and designed with scientific integrity in mind, and reliance on data solely from domestic wells limits the conclusions that can be made. With respect to key factor (2), as described herein, dissolved methane may be naturally ubiquitous at low levels or naturally elevated due to geological, topographic and/or other factors. Consequently, adequate characterization of natural background levels of dissolved methane is required to support the identification of anthropogenic impacts.

No regional-scale studies to date have fully addressed the two key factors noted above, leading to continued scientific debate regarding groundwater methane origins in areas of oil and gas development (Jackson et al., 2011; Osborn et al., 2011b; Saba and Orzechowski, 2011). To address this controversy, ongoing research must be supported with a scientifically designed groundwater monitoring well network, which includes both purpose-built monitoring wells and appropriately selected domestic wells, and must include characterization of natural background methane concentrations. Such an approach will provide the benefits of a large sample population and regional coverage (i.e., through selected domestic wells) with a means to verify and augment domestic well data (i.e., with purpose-built monitoring wells). From such an endeavour, a robust, scientifically defensible groundwater dataset can be compiled upon which science-based regulatory policy can be developed and appropriate and effective long-term groundwater monitoring strategies determined. To date no such research initiative has been initiated in Canada or elsewhere.

Such a study is being undertaken in the Peace region of northeastern BC by The University of British Columbia (UBC) in collaboration with Simon Fraser University, University of Calgary, BC Oil and Gas Commission (BCOGC) and BC Ministry of Forests, Lands, Natural Resource Operations and Rural Development. It will involve the design and installation of a scientific groundwater monitoring well network for the region. It will be placed in and amongst ongoing resource development and more than 150 domestic water wells from which baseline samples have recently been taken. Approximately 30 purpose-built groundwater monitoring wells will be installed to verify and augment the existing groundwater data, leading to establishment of a reliable and detailed scientific groundwater database. The monitoring well network and data collection methodology will be designed to establish background conditions for dissolved methane across the region, and to assess any

potential association of elevated methane in groundwater proximal to oil and gas wells.

This paper describes progress made in year one of the three-year project. As per the proposal, progress planned for year one (i.e., 2018) is as follows:

- phase 1: experimental design finalization, site selection criteria development, desk study of currently existing data, work plan formulation and field campaign planning;
- phase 2: initial drilling and field campaign;
- phase 3: data analyses and interpretation, review of progress and methodology refinement.

## Summary of Activities and Progress

### Project Kick Off and Student Recruitment

The project officially commenced in January 2018, whereby a one-day kick-off meeting with the project principal investigator team (A.G. Cahill, R.D. Beckie, L. Welch, D. Kirste, B. Mayer) and select invited participants (from Geoscience BC and BC Ministry of the Environment and Climate Change Strategy) was held on January 30. During the kick-off meeting, multiple aspects of the project were discussed in-depth by the project team including 1) review of project proposal and concept; 2) review of existing chemistry data for the Peace region; 3) review of criteria for selecting background locations; 4) methods and approaches for drilling of background wells; 5) possible re-sampling of select existing domestic wells; and 6) identification of criteria for targeted monitoring wells proximal to oil and gas well sites. Additionally, various logistical aspects of the project were discussed including hiring of students, formation of a project technical advisory committee, budget tracking, project management and field and project safety. During the winter and spring of 2018, two students were identified and recruited to the project through which they would work toward their M.Sc. degrees. Firstly, M. Goetz received his undergraduate degree in Earth and Planetary Sciences from McGill University. He has four years of geoscience experience in the mining industry, primarily working as a site geologist/hydrogeologist at a copper porphyry-skarn mine in New Mexico. Secondly, A. Allen is a recent Simon Fraser University graduate, who completed his B.Sc. (Honours) in Earth Sciences. His thesis topic was sources and distribution of arsenic in groundwater on the Gulf Islands of BC. He has a diverse background across geosciences and geology, with particular expertise in hydrogeology, hydrogeochemistry and geographic information sciences and is experienced with laboratory experiments and analytical equipment.

## Phase 1

### Experimental Design Finalization and Site Selection Criteria Development

During phase 1, the experimental design and concept were further refined and developed. An internal report was generated as part of this process (available on request), the outcomes of which are summarized here. Site selection criteria were finalized for the first background monitoring wells (MW; approximately 8–10 planned), each of which will be either paired with an existing water well (e.g., a domestic water well, provincial observation well, industry water source well) or unpaired. Approximately six paired MW will be located in proximity (i.e., 500–1000 m) to an existing water well for which groundwater chemistry and dissolved hydrocarbon concentrations are available. All background wells should be at least 1.5 km away from an existing oil or gas well. Of the paired wells, half will be selected to be proximal to a water well with elevated levels of dissolved methane (i.e., above a determined threshold level) and half with lower levels of dissolved methane. Paired wells are employed to increase the chance of success with drilling and hitting water in what is a highly heterogeneous area. The four unpaired monitoring wells will not be associated with an existing water well and can therefore be placed in areas for which no data is currently available, thus increasing the geographic range of the MW network and allowing effective leveraging of other existing groundwater data for the region. The MW are proposed to be located in eight geographic areas within the Peace region based on draft selection criteria and design-concept outlines, which were confirmed as suitable in principle by the wider project team. These areas are shown in Figure 1 and summarized in Table 1.

#### Desk Study of Currently Existing Data

Following agreement on initial MW site locations and experimental concept design, desk studies were conducted for each area whereby existing geological and groundwater data were reviewed and compiled. Maps were subsequently generated, including buffer zones for proximity to oil and gas wells and existing water wells. These maps were used to preselect potentially suitable background monitoring well locations. An example of the results of the desk study for area 1 (Hudson's Hope–Beryl Prairie) is shown in Figures 2 and 3.

#### Work Plan Formulation and Field Campaign Planning

A flexible approach, which allowed plans to be revised and refined, maximized the chance of successfully completing a functioning monitoring well. Accordingly, five of the eight selected background areas were prioritized and a two-phased approach to the initial drilling plan was adopted. Drilling was planned to commence at areas 1 to 4 and 7 (i.e., Hudson's Hope–Beryl Prairie, Chetwynd, northwest of

Fort St. John, west and northwest of Dawson Creek and Groundbirch field) in August 2018 with the remainder to be drilled in January 2019. The prioritized sites are shown in Figure 4.

Consequently, a field reconnaissance campaign was undertaken to scope and identify exact drilling sites at each area and assess enabling works needed to allow access. Where possible, sites adjacent to a road and within BC Ministry of Transportation land were selected and relevant permissions obtained. In several cases (i.e., Groundbirch field and west and northwest of Dawson Creek), an excavator was needed to clear the borehole location (Figure 5). Precise drilling sites are summarized in Table 2.

## Phase 2

### Sonic Drilling

Sonic drilling commenced on August 21 with a field plan to collect 10 cm core to total depth and install six multilevel MW (including shallow bedrock and soil gas sample points where possible). However, due to a number of factors including personnel and material delays by the drilling contractor and drilling method limitations (the sonic rig being unable to efficiently drill through bedrock), only four MW were completed. Based upon this experience, other drilling methods are being considered for future boreholes. Four wells (EERI-1–4) were completed, with core logged and samples taken for later analyses, and are summarized in Table 3. Photographs of the well installations and core are shown in Figures 6–8. Full geological logs and monitoring well installations are shown in Figures 9–12.

### Monitoring Well Assessment and Sampling Campaigns

As it was not possible to determine accurate static water levels or take samples at each borehole location during the drilling campaign (i.e., due to the presence of drilling water), a field trip was made at the end of September. Water level information would be essential to guide selection of a sampling pump with sufficient lift and suitable flow rate. During this campaign, static water levels were assessed and other tasks performed as follows. A subfrost artesian packer was installed successfully in the artesian Groundbirch field well. Development of 7.5 cm polyvinyl chloride (PVC) wells was attempted using a 7.5 cm Grundfos Holding A/S SQE submersible pump with restrictor valve. Unfortunately, the pump (which has a flow rate of around 225 L/min) proved too powerful even with the flow restrictor applied fully (lowering flow rate to 22.5–45 L/min) whereby it dried the wells out within a few minutes, prohibiting full development and sampling. The only sample successfully obtained on this campaign was one from the 0.6 cm polyethylene tubing of EERI-4. Based on results of this campaign a new sampling pump is being purchased; one that is able to lift required head and at a variable and

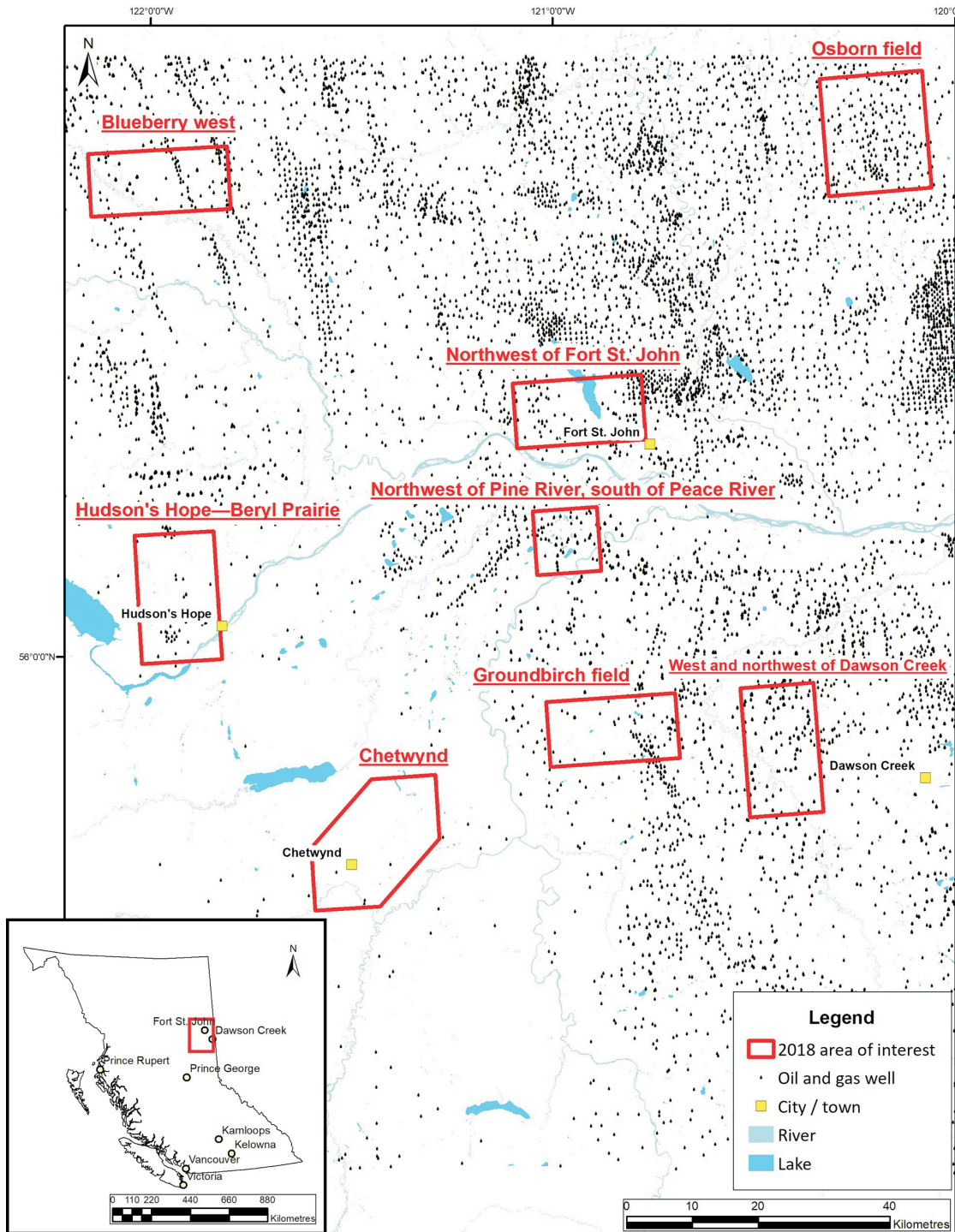


**Figure 1.** Regional map showing eight areas (red boxes) identified as potential sites for monitoring well installation, Peace region, British Columbia. Exact location of each well within each area will adhere to stated criteria and will be determined following desk study and site reconnaissance. Well data from BC Oil and Gas Commission (2018) and background data from DataBC (2018b).

**Table 1.** Areas selected for installation of background monitoring wells, Peace region, British Columbia. Note, Fort St. John Group, Cruiser Formation comprises fine clastic sedimentary rocks (mudstone, siltstone, shale); Dunvegan Formation comprises coarse clastic sedimentary rocks; Smoky Group, Kaskapau Formation comprises fine clastic sedimentary rocks (mudstone, siltstone, shale).

Area of interest	Area name	Surficial (SURF) and bedrock (BR) geology	Estimated depth to bedrock (BR) and groundwater (GW) in m
1	Hudson's Hope–Beryl Prairie	SURF: glaciofluvial fan deposits with lesser colluvial channels and alluvial terraces	35 (GW)
		BR: undifferentiated Fort St. John Group	32 (BR)
2	Chetwynd (Laser Farm and Campbell Road)  (2 MW)	SURF: extremely varied area; mainly variations of glacial till > glaciolacustrine plains > alluvial plains > glaciofluvial plains > aeolian ridges	16 (GW)
		BR: Fort St. John Group, Cruiser Formation	25 (BR)
3	Northwest of Fort St. John	SURF: mostly glacial till veneer, with lesser colluvial and glaciolacustrine deposits	25 (GW)
		BR: Dunvegan Formation	21 (BR)
4	West and northwest of Dawson Creek	SURF: glacial till plain, with similar amounts glaciolacustrine plain deposits, and minor alluvial plain deposits	8 (GW)
		BR: Smoky Group, Kaskapau Formation	16 (BR)
5	Blueberry west	SURF: glacial till, with lesser glaciolacustrine blanket deposits	NA (GW)
		BR: Dunvegan Formation or Fort St. John Group, Sully Formation	NA (BR)
			Limited data available
6	Osborn field	SURF: glacial till blanket, with lesser glaciolacustrine deposits	NA (GW)
		BR: Kotaneelee Formation	NA (BR)
			Limited data available
7	Groundbirch field	SURF: glacial streamlined till blanket, with lesser glaciolacustrine veneer deposits, and minor alluvial fan sediments	10 (GW)
		BR: Dunvegan Formation or Smoky Group, Kaskapau Formation	22 (BR)
8	Northwest of Pine River, south of Peace River	SURF: glaciolacustrine plain with lesser colluvial and alluvial terrace-plain sediments to the south	NA (GW)
		BR: Fort St. John Group	NA (BR)
			Limited data available

Abbreviations: MW, monitoring well; NA, not available.

**Table 2.** The six sites chosen for drilling in August 2018 (NAD 83, UTM Zone 10N).

Proposed drilling site area	Well	Easting	Northing
Hudson's Hope–Beryl Prairie	EERI-4	559562.81	6219144.64
Chetwynd (Laser Farm)	–	590854.62	6175341.25
Chetwynd (Campbell Road)	–	582343.78	6171309.31
Northwest of Fort St. John	EERI-3	623067.76	6239730.15
West and northwest of Dawson Creek	EERI-2	664110.19	6197643.10
Groundbirch field	EERI-1	625846.36	6191692.33

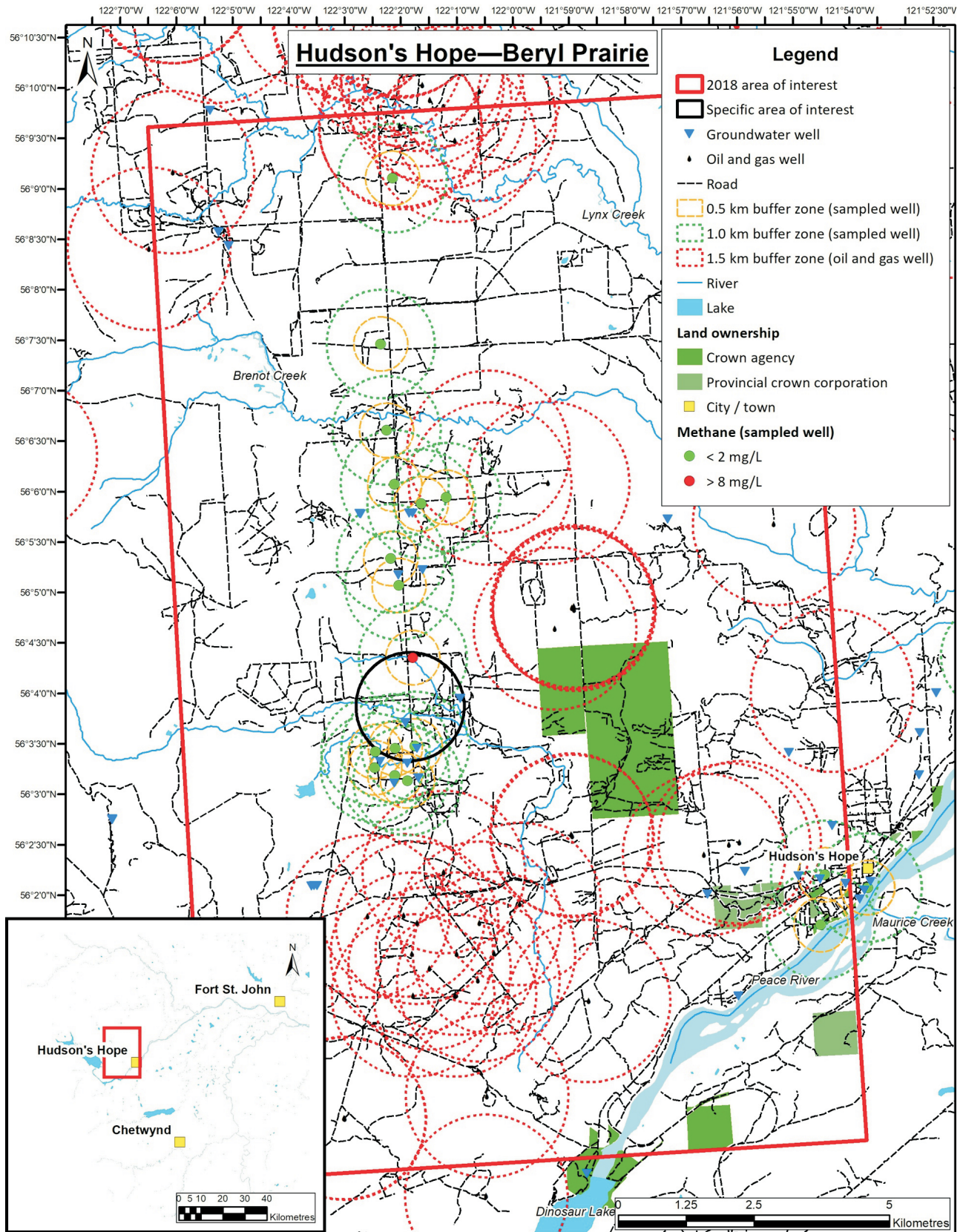


**Figure 2.** Map of area 1 (Hudson's Hope—Beryl Prairie) enclosed by red boundary, Peace region, British Columbia. Black circle indicates potential locations for paired well installation, red circles are 1.5 km buffer zones from oil and gas wells, orange and green circles indicate buffer zones (0.5 and 1.0 km, respectively) from sampled water wells. Well data from BC Oil and Gas Commission (2018) and DataBC (2018c) and background data from DataBC (2018a, b, d).

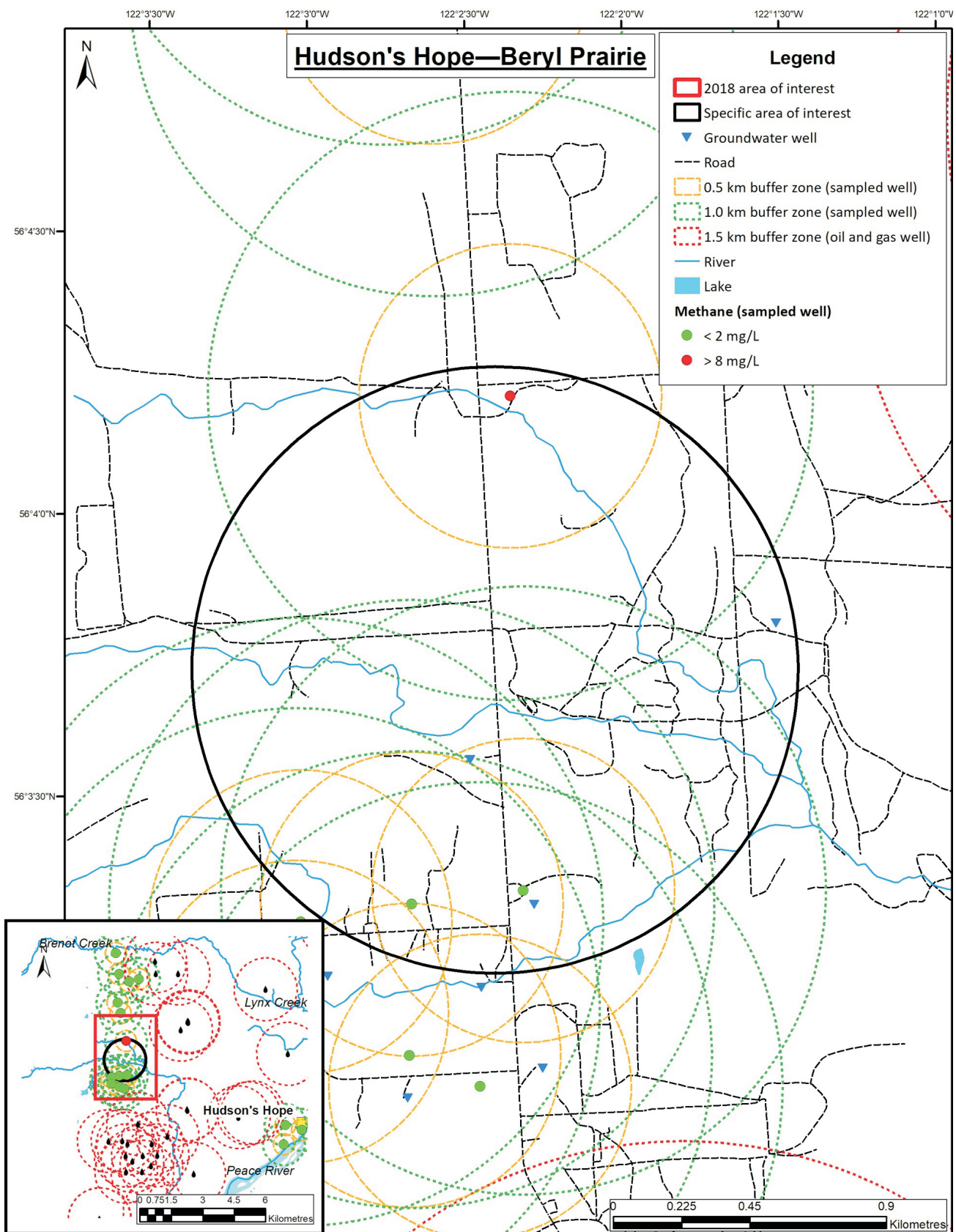


**Figure 3.** Detailed portion of area 1 (Hudson's Hope—Beryl Prairie), Peace region, British Columbia. Black circle indicates potential location for paired well installation, red circles are 1.5 km buffer zones from oil and gas wells, orange and green circles indicate buffer zones (0.5 and 1.0 km, respectively) from sampled water wells. Well data from DataBC (2018c) and background data from DataBC (2018a, b).

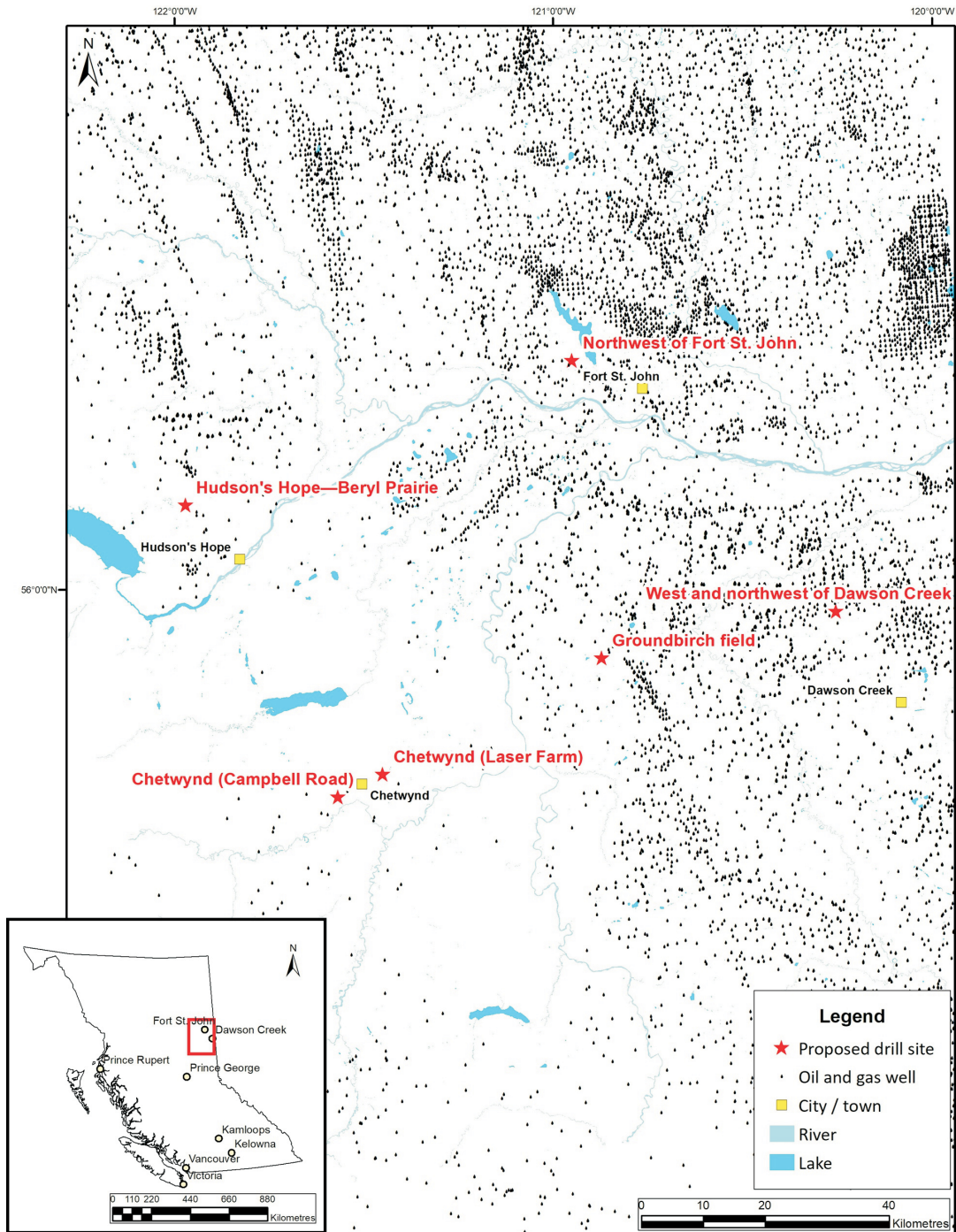


Figure 4. Map showing prioritized drilling sites, Peace region, British Columbia. Well data from BC Oil and Gas Commission (2018) and background data from DataBC (2018b).



**Figure 5.** Site preparation at Groundbirch field prior to drilling, Peace region, British Columbia.



**Figure 6.** Sonic drilling in progress at Groundbirch field, Peace region, British Columbia.



**Figure 7.** Sonic core composed of glacial clay/diamict, which dominates the upper portion of the Quaternary section throughout the Peace region, British Columbia.



**Figure 8.** Artesian well flowing (approximately 22.5–45 L/min) after completion at Groundbirch field, Peace region, British Columbia. The well was immediately and temporarily sealed with a polyvinyl chloride (PVC) end cap and subsequently permanently sealed with a subfrost artesian packer with built-in sampling valve during a follow-up fieldwork campaign.

**Table 3.** Summary of four wells completed during first drilling campaign in August 2018, Peace region, British Columbia.

Well	Area name	Total depth (m)	Generalized geology	Estimated depth to water (m agl)
EERI-1	Groundbirch field	66	43 m of diamict interlayered with silty clay, overlying 14 m of artesian (1.2 m agl of artesian pressure) sandy gravel, overlying 8 m of clay with lesser diamict	1.2
EERI-2	West and northwest of Dawson Creek	49	28 m of silty clay, overlying bedrock shale with lesser siltstone	-28.9
EERI-3	Northwest of Fort St. John	55	5 m of clay, overlying 21 m of diamict, overlying 22 m of medium sandstone, overlying 6 m of shale/siltstone	-46.51
EERI-4	Hudson's Hope–Beryl Prairie	51	10 m of clay, overlying a 11 m sequence of silt to medium sand, overlying 11 m of diamict, overlying 19 m of siltstone	-22.07

Abbreviation: agl, above ground level

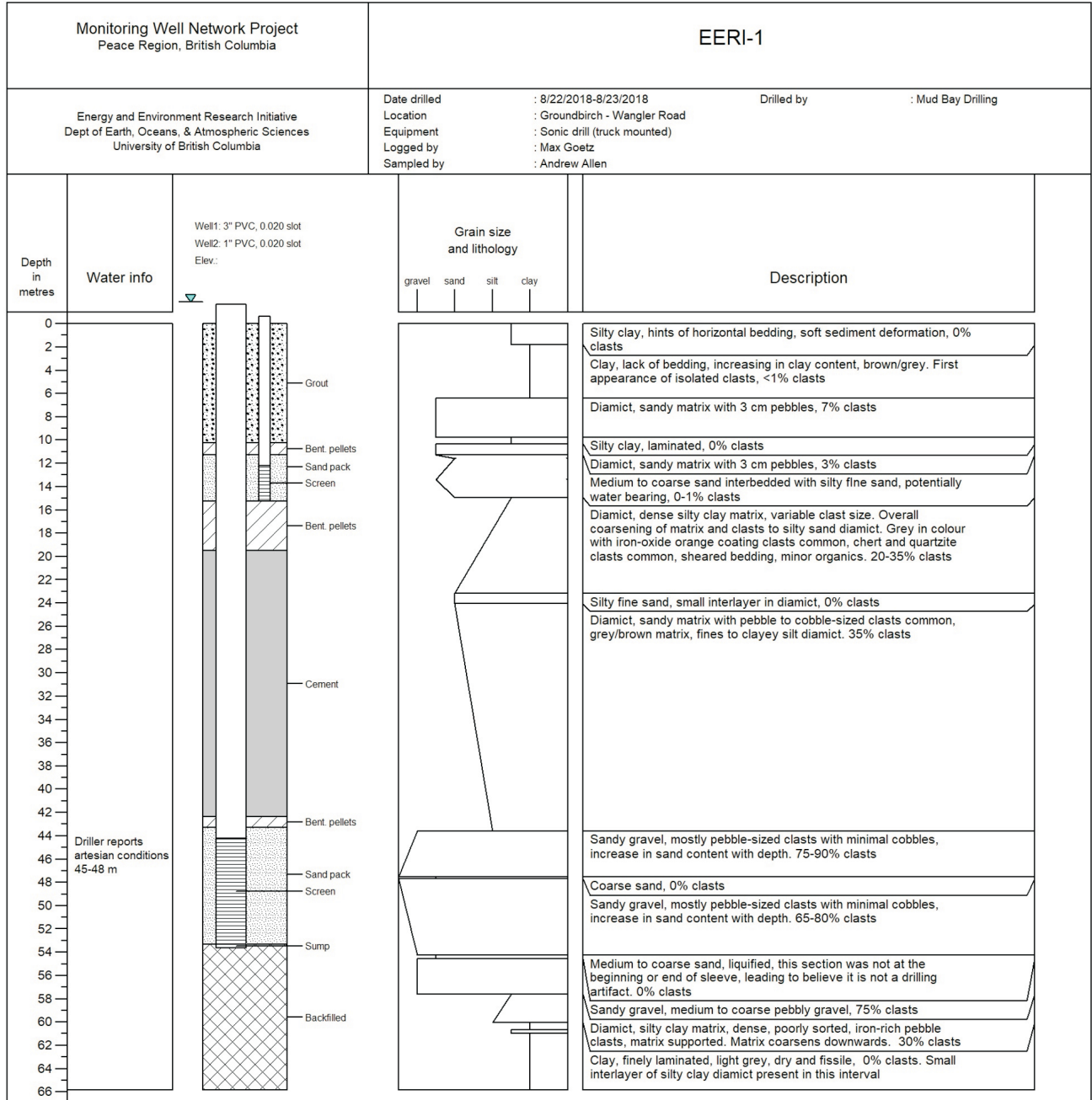


Figure 9. Well installation log for EERI-1, Groundbirch field, Peace region, British Columbia. Abbreviations: Bent., bentonite; PVC, polyvinyl chloride.

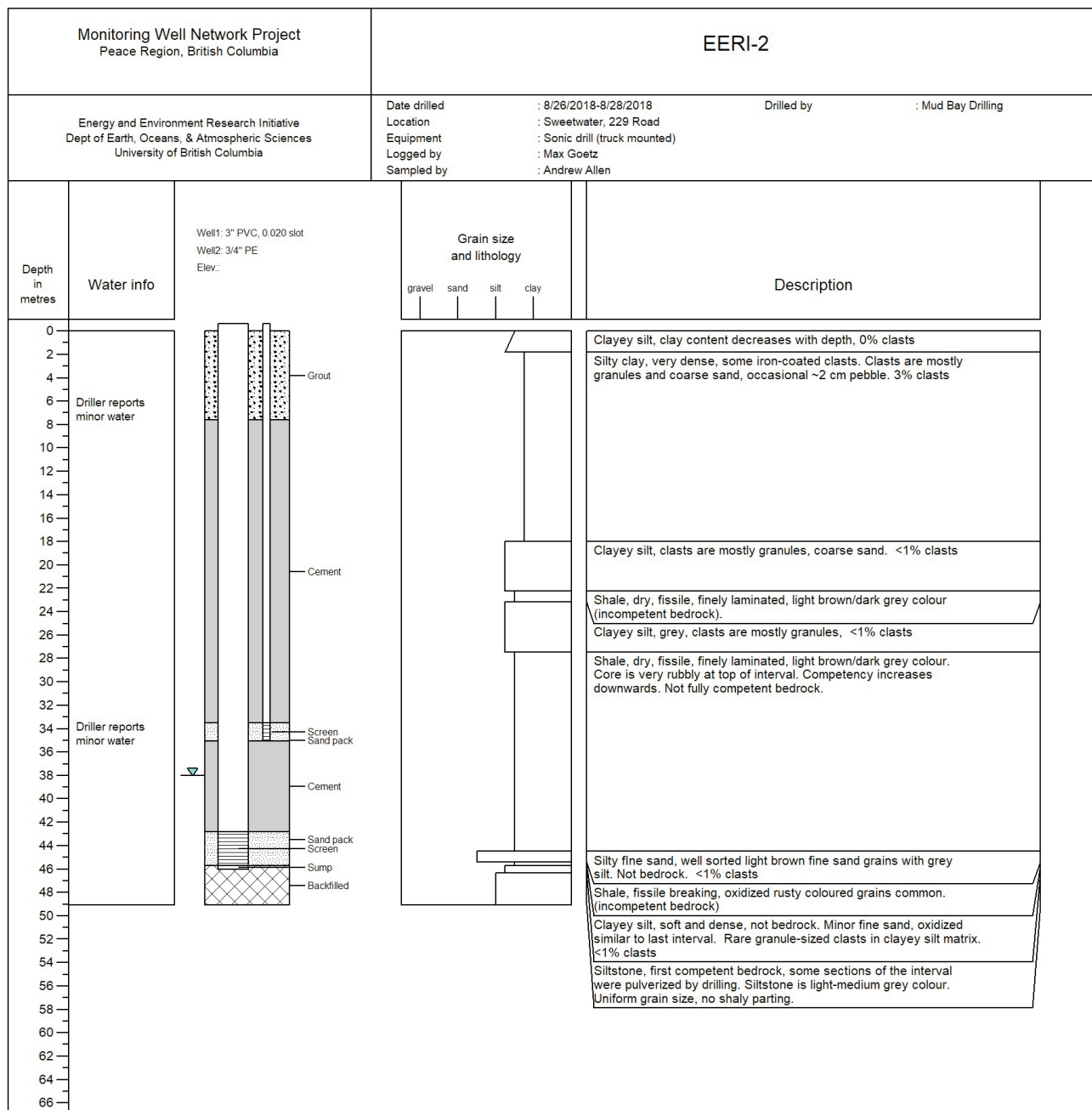


Figure 10. Well installation log for EERI-2, west and northwest of Dawson Creek, Peace region, British Columbia. Abbreviations: PE, polyethylene; PVC, polyvinyl chloride.

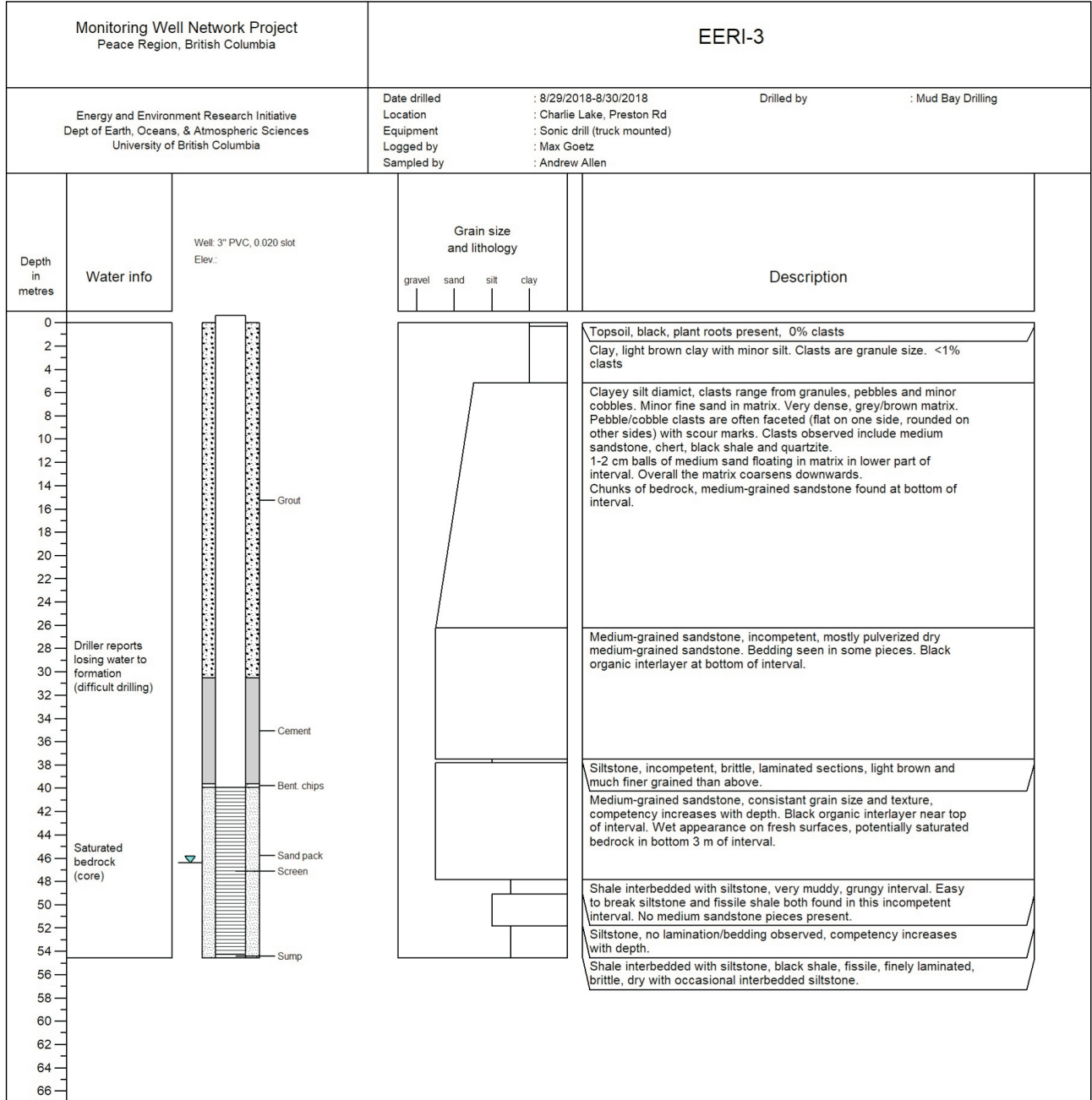
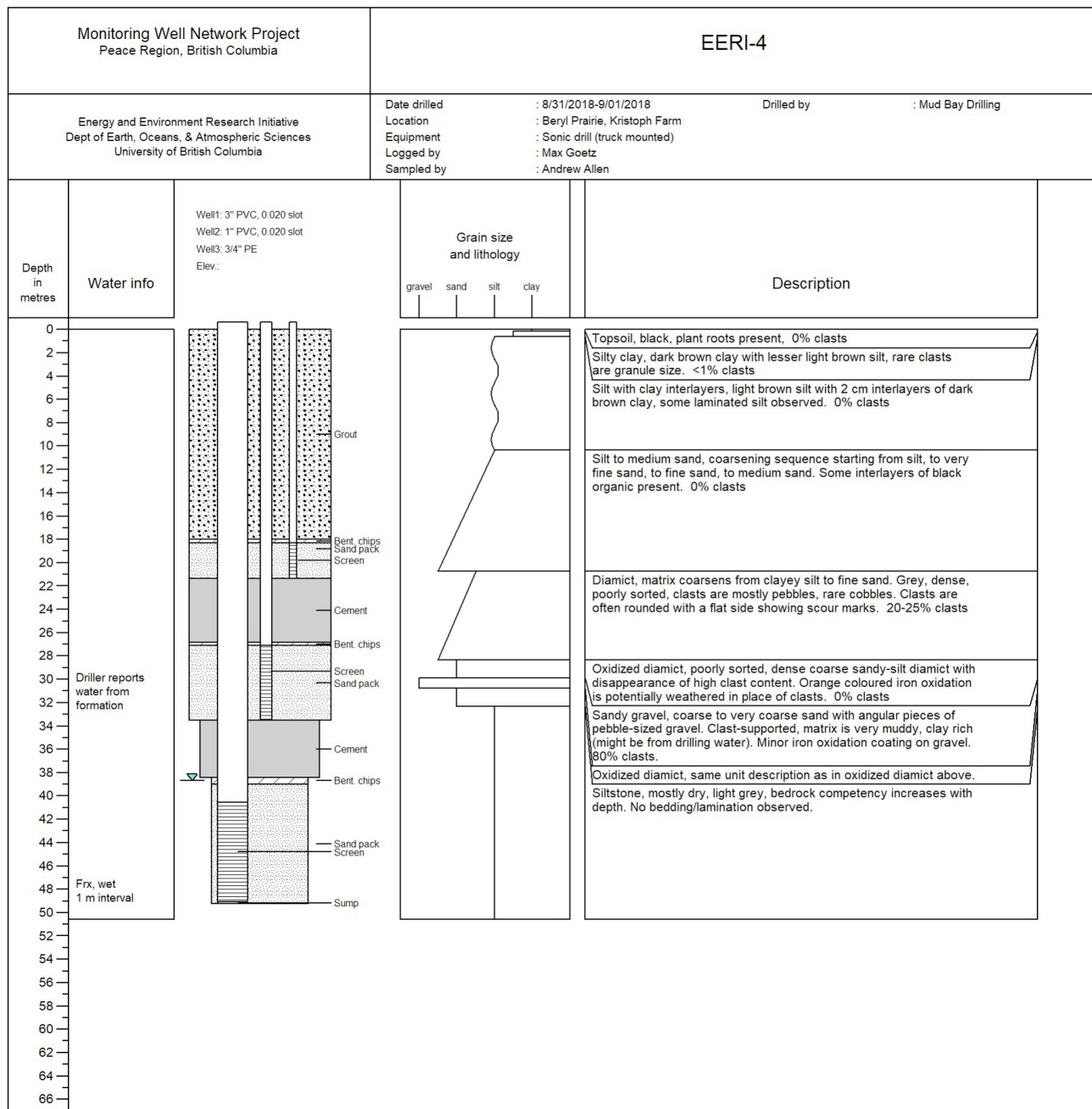


Figure 11. Well installation log for EERI-3, northwest of Fort St. John, Peace region, British Columbia. Abbreviations: Bent., bentonite; PVC, polyvinyl chloride.



**Figure 12.** Well installation log for EERI-4, Hudson's Hope–Beryl Prairie, Peace region, British Columbia. Abbreviations: Bent., bentonite; Frx, fractured; PE, polyethylene; PVC, polyvinyl chloride.

**Table 4.** Analysis type and rationale for geological sample analyses program.

Analyses type	Information gained	Relevance to project and fugitive gas and/or gas migration
X-ray diffraction, SEM-EDX and total digestion (aqua-regia)	Grain structure and mineralogy	General hydrogeochemical information and indication of aquifer matrix reactivity
Targeted/sequential extractions	Elemental content by phase/reactivity	Identify presence and quantify reactive minerals potentially involved in methane mediated redox reactions
Cation exchange capacity (CEC)	Exchangeable cation composition and total capacity	Identify elements present and quantify CEC potentially involved in water quality changes associated with methane-associated redox reactions
Permeability and grain-size distribution	Indicate permeability	Indicate permeability with respect to groundwater and potential migration of fugitive gases

Abbreviation: SEM-EDX, scanning electron microscope–energy dispersive X-ray spectrometry

low flow rate. Currently plans are underway to sample wells and perform hydraulic testing before the end of 2018.

### Phase 3

#### Geological Sample Analyses

During drilling a total of 181 samples were taken from the sonic core across the four holes. These samples are in the process of being analyzed in the laboratories at UBC and Simon Fraser University in order to determine a depth profile of various physical and chemical properties. Sample analyses and rationale are provided in Table 4. It is expected that these results will be available by the end of 2018.

#### Community and First Nations Engagement

Community engagement efforts have centred on two main strategies: newsletter dissemination and in-person community outreach events. Two newsletters were sent to eight First Nation communities along with the Treaty 8 Tribal Association and six municipal associations. The first was sent on March 2, 2018, which described the project, its goals and the plan for phases 1 and 2 of the project. The second newsletter was sent on May 23, 2018, outlining eight tentative areas to drill the first eight to ten wells, and invited feedback and input from the communities. These newsletters generated general interest and support, and resulted in a phone call from the West Moberly First Nations Chief and Council asking for further information.

On March 13, 2018, the UBC Energy and Environment Research Initiative’s (EERI) team attended the Northeast Water Strategy meeting in Fort St. John, in which the Peace region groundwater monitoring well network was described to various stakeholders. The team was approached by the Doig River First Nation Chief, resulting in a visit to the Doig River community and a meeting with the Chief and Council, as well as a trip to a leaky well on their land. This

has further informed the selection process for future drilling sites for the Peace region groundwater monitoring well network.

On June 13, 2018, a community engagement open house event was held in Fort St. John at the local Whole Wheat & Honey Cafe. Representatives from UBC, Geoscience BC and the BCOGC spoke about the different aspects and perspectives of the project, and more importantly, answered questions from the community. The event began with an Elder Welcoming from the Doig River First Nation, and over 35 people from the community attended. Overall, it was a successful event, with active participation and interest from the community. Comments and questions were recorded to be incorporated in project plans as the project progresses.

#### Summary of Progress and Ongoing Work

The following forms a summary of the progress made to date with respect to The University of British Columbia Energy and Environment Research Initiative’s Peace region groundwater monitoring well network project:

- refined and finalized the experimental plan and concept for the background monitoring wells location with a paired and unpaired approach;
- eight areas were identified for the first monitoring wells and detailed desk studies on these areas were performed;
- five of the eight areas were prioritized and a field reconnaissance trip taken to plan and prepare for drilling;
- four boreholes were drilled by sonic method with full cores attained and ~180 samples taken for physical and chemical analyses; each borehole was completed with a custom-built multilevel sampling system; significant challenges were experienced during the sonic drilling program leading to consideration of alternative methods for ongoing drilling;

- an artesian gravel was encountered at the Groundbirch field site, subsequently sealed with a custom built subfrost artesian packer and sampling system; and
- static water levels were determined and development and sampling of new wells attempted; however, the currently available equipment was not optimal and it was not possible to take groundwater samples yet.

The following key tasks are in progress or ongoing:

- a field campaign is planned to sample the groundwater in wells EERI-1–4 using a suitable and newly purchased pump before the end of 2018;
- the four remaining background monitoring wells are planned to be drilled in January 2019 (using air rotary drilling method);
- sediment analyses is being undertaken;
- downhole and surface geophysics at the initial drill sites are being planned; and
- an integrated interpretation of all results in terms of geology, hydrogeology and groundwater conditions in the Peace region is ongoing.

## Acknowledgments

Peer reviewed by L. Smith.

## References

- Bachu, S. (2017): Analysis of gas leakage occurrence along wells in Alberta, Canada, from a GHG perspective – gas migration outside well casing; *International Journal of Greenhouse Gas Control*, v. 61, p. 146–154.
- BC Oil and Gas Commission (2017): Well activity: completions, maintenance and abandonment; Chapter 9 *in* Oil and Gas Activity Operations Manual, BC Oil and Gas Commission, Sections 9.7.3, 9.7.5, 9.7.6, URL <<http://www.bcogc.ca/industry-zone/documentation/oil-and-gas-activity-operations-manual>> [December 2017].
- BC Oil and Gas Commission (2018): Well surface hole locations (permitted); BC Oil and Gas Commission, URL <[https://data-bcogc.opendata.arcgis.com/datasets/9149cb556e694617970a5774621af8be\\_0?geometry=-120.77%2C56.315%2C-120.607%2C56.331](https://data-bcogc.opendata.arcgis.com/datasets/9149cb556e694617970a5774621af8be_0?geometry=-120.77%2C56.315%2C-120.607%2C56.331)> [May 2018].
- Brantley, S., Yoxheimer, D., Arjmand, S., Grieve, P., Vidic, R., Pollak, J., Llewellyn, G., Abad, J. and Simon, C. (2014): Water resource impacts during unconventional shale gas development: the Pennsylvania experience; *International Journal of Coal Geology*, v. 126, p. 140–156.
- Briskin, J. (2015): Potential impacts of hydraulic fracturing for oil and gas on drinking water resources; *Groundwater*, v. 53, no. 1, p. 19–21.
- Cahill, A.G., Ladd, B., Chao, J., Soares, J., Cary, T., Finke, N., Manning, C., Chopra, C., Hawthorne, I., Forde, O.N., Mayer, K.U., Black, A., Crowe, S., Mayer, B., Lauer, R., van Geloven, C., Welch, L. and Beckie, R.D. (2019): Implementation and operation of a multidisciplinary field investigation involving a subsurface controlled natural gas release, northeastern British Columbia; *in* Geoscience BC Summary of Activities 2018: Energy and Water, Geoscience BC, Report 2019-2, p. 95–104.
- Cahill, A.G., Steelman, C.M., Forde, O., Kuloyo, O., Ruff, S.E., Mayer, B., Mayer, K.U., Strous, M., Ryan, M.C., Cherry, J.A. and Parker, B.L. (2017): Mobility and persistence of methane in groundwater in a controlled-release field experiment; *Nature Geoscience*, v. 10, issue 4, p. 289–294, URL <<https://doi.org/10.1038/ngeo2919>> [November 2018].
- Canadian Association of Petroleum Producers (2012): CAPP hydraulic fracturing operating practice: baseline groundwater testing; Canadian Association of Petroleum Producers, 4 p., URL <<http://www.capp.ca/publications-and-statistics/publications/218135>> [November 2018].
- Council of Canadian Academies (2014): Environmental impacts of shale gas extraction in Canada: the expert panel on harnessing science and technology to understand the environmental impacts of shale gas extraction; Council of Canadian Academies, Ottawa, Ontario, 262 p.
- Darling, W.G. and Goody, D.C. (2006): The hydrogeochemistry of methane: evidence from English groundwaters; *Chemical Geology*, v. 229, issue 4, p. 293–312.
- DataBC (2018a): Digital road atlas (DRA) – master partially-attributed roads; Province of British Columbia website, URL <<https://catalogue.data.gov.bc.ca/dataset/digital-road-atlas-dra-master-partially-attributed-roads>> [May 2018].
- DataBC (2018b): Freshwater atlas rivers; Province of British Columbia website, URL <<https://catalogue.data.gov.bc.ca/dataset/freshwater-atlas-rivers>> [May 2018].
- DataBC (2018c): Ground water wells; Province of British Columbia website, URL <<https://catalogue.data.gov.bc.ca/dataset/e4731a85-ffca-4112-8caf-cb0a96905778>> [May 2018].
- DataBC (2018d): TANTALIS – surveyed parcels; Province of British Columbia website, URL <<https://catalogue.data.gov.bc.ca/dataset/tantalisis-surveyed-parcels>> [May 2018].
- Dusseault, M. and Jackson, R. (2014): Seepage pathway assessment for natural gas to shallow groundwater during well stimulation, in production, and after abandonment; *Environmental Geosciences*, v. 21, no. 3, p. 107–126.
- Eltischlager, K., Hawkins, J., Ehler, W. and Baldassare, F. (2001): Technical measures for the investigation and mitigation of fugitive methane hazards in areas of coal mining; Office of Surface Mining Reclamation and Enforcement, Pittsburgh, Pennsylvania, 130 p.
- Gorody, A. (2012): Factors affecting the variability of stray gas concentration and composition in groundwater; *Environmental Geosciences*, v. 18, no. 1, p. 17–31.
- Hamilton, S., Grasby, S., McIntosh, J. and Osborn, S. (2015): The effect of long-term regional pumping on hydrochemistry and dissolved gas content in an undeveloped shale-gas-bearing aquifer in southwest Ontario, Canada; *Hydrogeology Journal*, v. 23, p. 719–739.
- Harkness, J., Darragh, T., Warner, N., Whyte, C., Moore, M., Millot, R., Kloppmann, W., Jackson, R. and Vengosh, A. (2017): The geochemistry of naturally occurring methane and saline groundwater in an area of unconventional shale gas development; *Geochemica et Cosmochimica Acta*, v. 208, p. 302–334.
- Humez, P., Mayer, B., Ing, J., Nightingale, M., Becker, V., Kingston, A., Akbilgic, O. and Taylor, S. (2016a): Occurrence and origin of methane in groundwater in Alberta (Canada): gas geochemical and isotopic approaches; *Science of the Total Environment*, v. 541, p. 1253–1268.

- Humez, P., Mayer, B., Nightingale, M., Ing, J., Becker, V., Jones, D. and Lam, V. (2016b): An 8-year record of gas geochemistry and isotopic composition of methane during baseline sampling at a groundwater observation well in Alberta (Canada); *Hydrogeology Journal*, v. 24, issue 1, p. 109–122.
- Ingraffea, A.R., Wells, M.T., Santoro, R.L. and Shonkoff, S.B.C. (2014): Assessment and risk analysis of casing and cement impairment in oil and gas wells in Pennsylvania, 2000–2012; *Proceedings of the National Academy of Sciences*, v. 111, no. 30, p. 10955–10960.
- Jackson, R. and Heagle, D. (2016): Sampling domestic/farm wells for baseline groundwater quality and fugitive gas; *Hydrogeology Journal*, v. 24, issue 2, p. 269–272, URL <<https://doi.org/10.1007/s10040-016-1369-z>> [November 2018].
- Jackson, R., Gorody, A., Mayer, B., Roy, J., Ryan, M. and Van Stempvoort, D. (2013): Groundwater protection and unconventional gas extraction: the critical need for field-based hydrogeological research; *Groundwater*, v. 51, no. 4, p. 488–510.
- Jackson, R.B., Osborn, S.G., Vengosh, A. and Warner, N.R. (2011): Reply to Davies: hydraulic fracturing remains a possible mechanism for observed methane contamination of drinking water; *Proceedings of the National Academy of Sciences*, v. 108, no. 43, p. E872.
- Kelly, W.R., Matisoff, G. and Fisher, J.B. (1985): The effects of a gas-well blow-out on groundwater chemistry; *Environmental Geology and Water Sciences*, v. 7, issue 4, p. 205–213.
- Molofsky, L.J., Connor, J.A., Wylie, A.S., Wagner T. and Farhat, S.K. (2013): Evaluation of methane sources in groundwater in northeastern Pennsylvania; *Groundwater*, v. 51, issue 3, p. 333–349.
- Nicot, J., Larson, T., Darvari, R., Mickler, P., Sloten, M., Ardrige, J., Uhlman, K. and Costley, R. (2017): Controls on methane occurrences in shallow aquifers overlying the Haynesville Shale Gas Field, Texas; *Groundwater*, v. 55, issue 4, p. 443–454, URL <<https://doi.org/10.1111/gwat.12500>> [November 2018].
- Osborn, S.G., Vengosh, A., Warner, N.R. and Jackson, R.B. (2011a): Methane contamination of drinking water accompanying gas-well drilling and hydraulic fracturing; *Proceedings of the National Academy of Sciences*, v. 108, no. 20, p. 8172–8176.
- Osborn, S.G., Vengosh, A., Warner, N.R. and Jackson, R.B. (2011b): Reply to Saba and Orzechowski and Schon: methane contamination of drinking water accompanying gas-well drilling and hydraulic fracturing; *Proceedings of the National Academy of Sciences*, v. 108, no. 37, p. E665–E666.
- Province of British Columbia (2017): Oil and Gas Activities Act, Drilling and Production Regulation; British Columbia Regulation 282/2010 (Oil and Gas Commission), URL <[http://www.bclaws.ca/civix/document/id/crbc/crbc/282\\_2010](http://www.bclaws.ca/civix/document/id/crbc/crbc/282_2010)> [November 2018].
- Saba, T. and Orzechowski, M. (2011): Lack of data to support a relationship between methane contamination of drinking water wells and hydraulic fracturing; *Proceedings of the National Academy of Sciences*, v. 108, no. 37, p. E663.
- Sherwood, O.A., Rogers, J.D., Lackey, G., Burke, T.L., Osborn, S.G. and Ryan, J.N. (2016): Groundwater methane in relation to oil and gas development and shallow coal seams in the Denver-Julesburg Basin of Colorado; *Proceedings of the National Academy of Sciences*, v. 113, no. 30, p. 8391–8396.
- Siegel, D.I., Azzolina, N.A., Smith, B.J., Perry, A.E. and Bothun, R.L. (2015): Methane concentrations in water wells unrelated to proximity to existing oil and gas wells in northeastern Pennsylvania; *Environmental Science and Technology*, v. 49, issue 7, p. 4106–4112.
- Van Stempvoort, D., Maathuis, H., Jaworski, E., Mayer, B. and Rich, K. (2005): Oxidation of fugitive methane in groundwater linked to bacterial sulfate reduction; *Groundwater*, v. 43, issue 2, p. 187–199.
- Vengosh, A., Jackson, R.B., Warner, N., Darrah, T.H. and Kondash, A. (2014): A critical review of the risks to water resources from unconventional shale gas development and hydraulic fracturing in the United States; *Environmental Science and Technology*, v. 48, issue 15, p. 8334–8348.
- Vidic, R.D., Brantley, S.L., Vandenbossche, J.M., Yoxtheimer, D. and Abad, J.D. (2013): Impact of shale gas development on regional water quality; *Science*, v. 340, issue 6134.
- von der Dick, H.H. and Bosman, D.A. (2011): Surface seep gas signals in relation to reservoir pressure: surface gas expression built-up and decay over fields; *Recovery – 2011 Canadian Society of Petroleum Geologists, Canadian Society of Exploration Geophysicists, Canadian Well Logging Society Convention*, Calgary, Alberta, May 9–11, 2011, abstract, 2 p.
- von der Dick, H.H., Barrett, K.R. and Bosman, D.A. (2002): Numerically reconstructed methane-seep signal in soil gases over Devonian gas pools and prospects (northeast British Columbia): surface microseeps and postsurvey discovery; *in* *Surface Exploration Case Histories: Applications of Geochemistry, Magnetism, and Remote Sensing*, D. Schumacher and L.A. Leschack (ed.), American Association of Petroleum Geologists Studies in Geology no. 48 and Society of Exploration Geophysicists Geophysical References Series no. 11, p. 193–207.



# Thaw-Induced Land-Cover Change in the Southern Margin of Discontinuous Permafrost, Northeastern British Columbia and Southwestern Northwest Territories

**K.M. Haynes, Cold Regions Research Centre, Wilfrid Laurier University, Waterloo, ON, khaynes@wlu.ca**

**O.A. Carpino, Cold Regions Research Centre, Wilfrid Laurier University, Waterloo, ON**

**R.F. Connon, Cold Regions Research Centre, Wilfrid Laurier University, Waterloo, ON**

**É. Devoie, Department of Civil and Environmental Engineering, University of Waterloo, Waterloo, ON**

**W.L. Quinton, Cold Regions Research Centre, Wilfrid Laurier University, Waterloo, ON**

---

Haynes, K.M., Carpino, O.A., Connon, R.F., Devoie, É. and Quinton, W.L. (2019): Thaw-induced land-cover change in the southern margin of discontinuous permafrost, northeastern British Columbia and southwestern Northwest Territories; *in* Geoscience BC Summary of Activities 2018: Energy and Water, Geoscience BC, Report 2019-2, p. 123–132.

## Introduction

The landscape of the sporadic to discontinuous permafrost zone in the southern Taiga Plains ecoregion is undergoing rapid change as a result of accelerating rates of permafrost loss with a warming climate (Baltzer et al., 2014; Lara et al., 2016). Both vertical permafrost thaw with energy transfer from the ground surface and lateral permafrost degradation with advective transfer of energy from adjacent permafrost-free wetlands results in significant losses of permafrost terrain in this region (Rowland et al., 2010; Quinton et al., 2011). With the loss of underlying permafrost bodies, elevated forested peat plateaus subside and become inundated as they transition to treeless wetland features on the landscape (Quinton et al., 2011). Peat plateaus function as runoff generators due to their elevated topographic position and their limited water storage capacity (Wright et al., 2009). Permafrost barriers impede significant subsurface flow and collapse scar bogs, which form on the permafrost terrain, are hydrologically isolated from the basin drainage network and function as water storage features. As permafrost ‘dams’ are lost due to thaw and ground subsidence, formerly isolated bogs become connected to the drainage network through the process of ‘bog capture’ (Connon et al., 2014) facilitating more direct and efficient drainage of the landscape. Thaw-induced landscape changes in the sporadic to discontinuous permafrost zone catalyze significant rerouting of water through the landscape, which may have long-term impacts on water availability in northern communities.

Discharge from discontinuous permafrost basins throughout the Northwest Territories (NWT) has increased significantly over long-term (more than 30 years) records, with

considerable increases in flow occurring in the southern NWT (St. Jacques and Sauchyn, 2009). This increase in basin runoff has not been accompanied by an increase in precipitation over this period. The magnitude of such increases cannot solely be accounted for by the water derived from thawing permafrost and therefore is likely due to the expansion in runoff contributing area as previously isolated wetlands are ‘captured’ by the drainage network, activating both surface and subsurface hydrological flowpaths (Connon et al., 2014). The sustainability of the observed increase in basin runoff throughout the sporadic and discontinuous permafrost region is unclear. However, a maximum threshold in the amount of water contributed to runoff will likely be met as all bogs become incrementally connected to the drainage network as permafrost barriers are lost (Haynes et al., 2018). With continued permafrost loss, increased fragmentation and shrinking of peat plateaus are anticipated to occur (Baltzer et al., 2014). As the landscape transition catalyzed by permafrost thaw results in significant loss of forest cover, the progression of such large-scale changes can be monitored with remotely sensed imagery of land cover and coupled with standard climate and environmental variables to provide insight into the controls and conditions associated with the progressive stages of increasing wetland extent at the expense of forest cover (Carpino et al., 2018). A latitudinal gradient in the extent of permafrost loss and the associated pattern of land-cover type spanning the southern Taiga Plains ecoregion can be utilized as a reasonable space-for-time proxy to understand the trajectory of thaw-induced land-cover transition.

The overall objective of this project is to understand the trajectory of sporadic to discontinuous permafrost environments, with continued climatic warming, by examining the landscape changes at 10 subarctic boreal sites along a latitudinal transect spanning from the southern NWT to northeastern British Columbia (BC). This transect was established by the Consortium for Permafrost Ecosystems in

---

*This publication is also available, free of charge, as colour digital files in Adobe Acrobat® PDF format from the Geoscience BC website: <http://www.geosciencebc.com/s/SummaryofActivities.asp>.*

Transition (CPET) to understand the implications of climate- and industry-induced changes to the landscape on the availability of water resources in the region. An in-depth study of the impacts of permafrost-thaw-induced landscape change on the hydrology of the most northerly site along the transect, the Scotty Creek basin, NWT, is examined to understand the role of wetlands in either storing or conveying water as elevated permafrost plateaus become inundated and are lost over time.

## Methods

The north-south CPET transect spans a distance of approximately 200 km at the southern margin of thawing discontinuous to sporadic permafrost, from the southern NWT to northeastern BC (Figure 1). The landscape along this transect is dominated by peatlands with fragmented forested peat plateaus underlain by permafrost interspersed with permafrost-free wetlands including channel fens and bogs. The area underlain by permafrost has decreased significantly along this transect accompanied by an increase in surface water on the landscape, as permafrost terrain transitions to wetland cover with permafrost thaw (Robinson and Moore, 2000; Quinton et al., 2011; Baltzer et al., 2014). Along this transect 10 areas of interest (AOI) characterized by plateau-wetland complexes were selected to examine the rate and pattern of forest cover transition to wetland using remotely sensed imagery over a period of approximately 40 years (Figure 1). These 10 AOI range in latitude from 59.96 to 61.30°N (Figure 1). The trends in forested permafrost plateau loss across these AOI were related to climatic and environmental variables including annual and

seasonal temperature and precipitation as well as latitude and degree of plateau fragmentation (perimeter-to-area ratio) for each AOI.

A 15-year examination of water level trends on both peat plateaus and wetland features was conducted in the headwaters of the Scotty Creek basin, NWT (61.30°N, 121.30°W), the most northerly location on the CPET transect. The purpose of this case study was to examine over time the water storage trends of the dominant landscape features characteristic of the plateau-wetland complexes in the discontinuous to sporadic permafrost region. The headwaters area, located in the southern portion of the basin, is entirely composed of peatland land-cover types, including permafrost plateaus, bogs and fens. Water levels were monitored from 2003 to 2017 on a degrading peat plateau, a channel fen, as well as bogs both isolated from and connected to the drainage network. Given the hypothesis that the process of bog capture significantly contributes to basin drainage (Connon et al., 2014), the magnitude of enhanced runoff observed from the Scotty Creek basin since discharge measurements began in 1996 was compared to the overall loss of water storage from wetlands as they became connected to the drainage network over a similar 15-year timeframe. The magnitude of permanent and transient contributions to basin runoff including precipitation-induced changes in runoff from direct precipitation on the channel fen, and the nonprecipitation-induced sources of primary runoff from the plateau flanks, and moisture derived from thawing permafrost were estimated and similarly compared to the observed excess runoff from the basin. The partitioning of runoff contributions in the Scotty

AOI	Unofficial name	Location
A	Scotty Creek, NWT	61.30°N, 121.30°W
B	Deep Lake, NWT	61.19°N, 120.45°W
C	Trout lake, NWT	60.74°N, 121.05°W
D	Trout River tributary, NWT	60.65°N, 120.64°W
E	Paradise river, NWT	60.55°N, 120.81°W
F	Tetcho Lake, NWT	60.42°N, 120.84°W
G	Trainor lake, NWT	60.41°N, 120.41°W
H	Island river, NWT	60.10°N, 120.56°W
I	Hossitl Creek, BC	59.96°N, 120.84°W
J	Calendar Creek, BC	59.97°N, 120.34°W

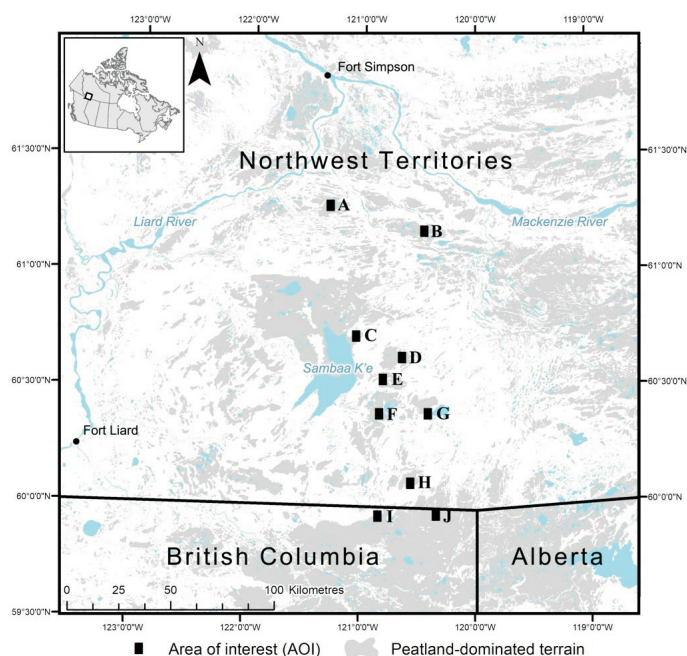


**Figure 1.** Locations of 10 areas of interest (A–J), northeastern British Columbia and southwestern Northwest Territories. Adapted from Carpino et al. (2018).

Creek basin facilitated the proposal of a new conceptual model detailing the role and timing of wetland water storage as bogs become increasingly connected to the drainage network with permafrost thaw.

## Results

### Latitudinal Land Cover Transition

All 10 AOI, which span the north-south latitudinal transect, experienced net forest loss over the 40-year period of study, from 1970 to 2010 (Figures 2, 3). This net loss of forest decreased along the latitudinal gradient, with a maximum value of 11.6% at the northerly Scotty Creek, NWT, AOI (61.30°N), and a minimum value of 6.9% at the southerly Hossitl Creek, BC, AOI (59.96°N; Figure 2). At the seven most northerly AOI, the magnitude of net forest loss closely resembled the trend in total forest loss, as rates of forest gain in these locations were negligible (ranging from 0.2 to 1%). In contrast, the two southernmost AOI experienced considerable gross forest gain, on the order of 6 to 10%, over the 40-year period (Figure 2).

### Predictors of Landscape Transition

With the examination of correlative relationships between landscape change (using the metrics of net forest loss, forest loss and forest gain at each AOI) and climatic and environmental variables along the transect, several factors emerged as significant indicators of landscape transition. Mean annual air temperature was positively correlated with both forest loss and forest gain over the study period ( $r = 0.647$ ,  $r = 0.794$ , respectively; see Table 1). Seasonal influences of temperature were also observed, with a significant negative correlation between average winter temperature and net forest loss ( $r = -0.782$ ; Table 1) and a positive correlation between average winter temperature and forest gain ( $r = 0.745$ ;

Table 1) between 1970 and 2010. However, average summer temperature did not exhibit a significant correlation with any of the landscape change metrics (Table 1). On an annual timeframe, average annual precipitation was significantly negatively correlated with net forest loss ( $r = -0.636$ ) and positively correlated with forest gain ( $r = 0.661$ ; Table 1). These trends between precipitation and landscape transition are driven by summer precipitation, with a negative correlation between average summer precipitation and net forest loss ( $r = -0.636$ ) and a positive correlation with forest gain ( $r = 0.709$ ; Table 1). No significant correlations were observed between average winter precipitation and the metrics of landscape change.

Changes in climatic variables over the 40-year study period from 1970 to 2010, likely resulting from a changing climate, significantly affected net forest loss. Changes in both summer and winter temperatures were positively correlated with net forest loss ( $r = 0.690$ ,  $r = 0.691$ , respectively; see Table 1). Winter precipitation changes over this 40-year period were negatively correlated with net forest loss ( $r = -0.762$ ; Table 1) and positively correlated with forest gain ( $r = 0.726$ ; Table 1). However, changes to summer precipitation from 1970 to 2010 did not significantly influence landscape change.

### Case Study of Landscape Change: Examining AOI A, Scotty Creek, NWT

#### Trends in Wetland Water Storage

Over the 15-year period from 2003 to 2017, the water levels in bogs, with varying degrees of connection to the drainage network, declined (Table 2; Figure 4). The magnitude of water drained from connected bogs over this period ranged from 44 to 219 mm (Table 2; Figure 4). The average loss of water previously stored in isolated bogs that are now con-

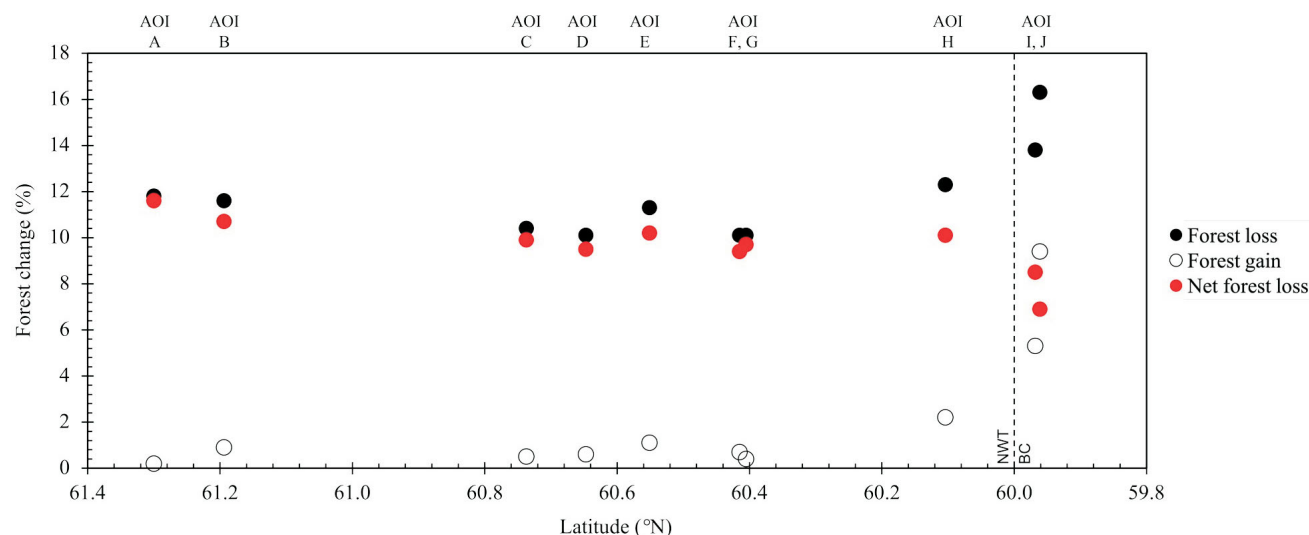
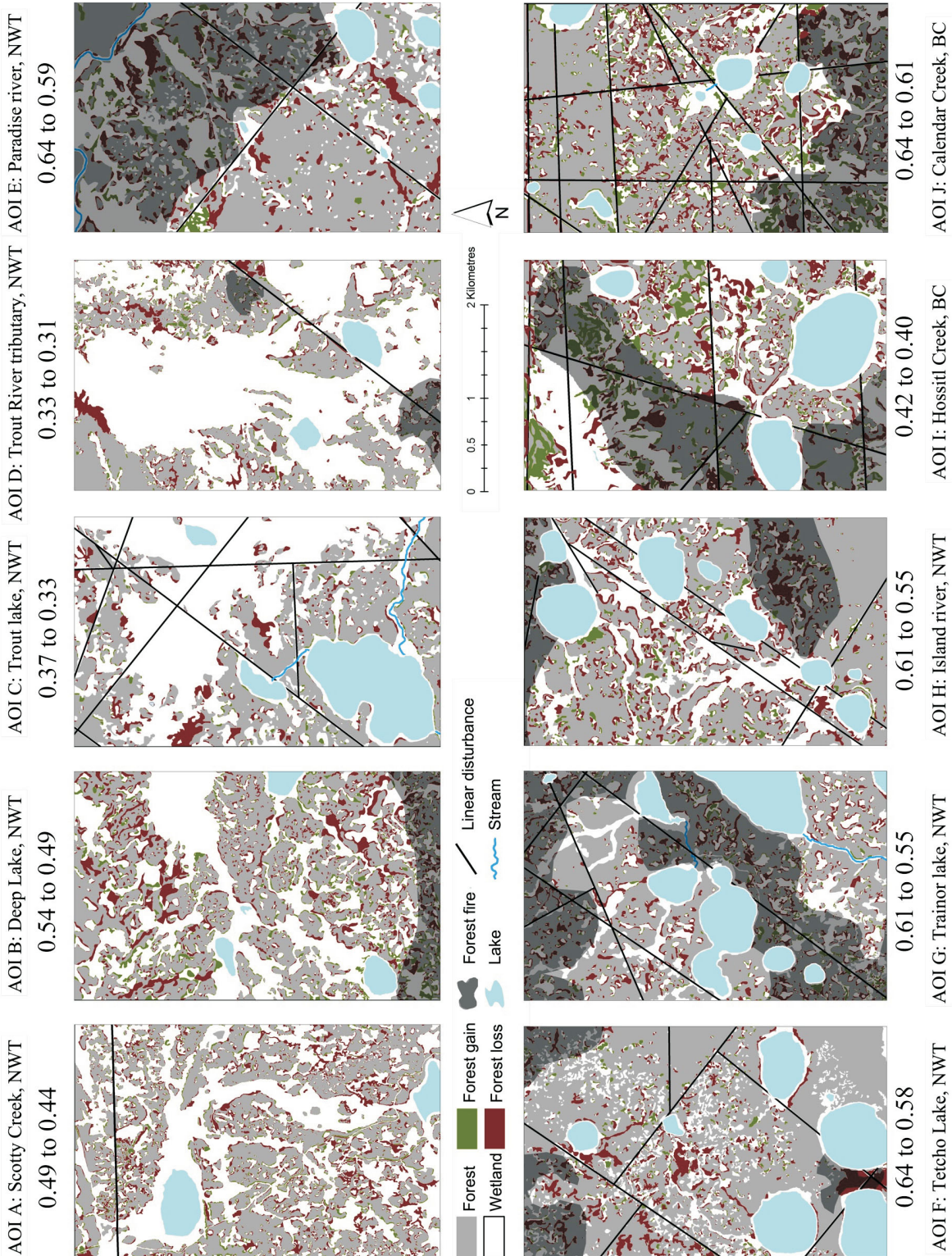


**Figure 2.** Relationships between net forest loss, forest loss and forest gain with latitude over the 1970 to 2010 study period for the 10 areas of interest (AOI), British Columbia (BC) and Northwest Territories (NWT). Adapted from Carpino et al. (2018).

**Proportion of forest from 1970 to 2010:**



**Proportion of forest from 1970 to 2010:**

**Figure 3.** The proportion of land classified as forested, and predictably underlain by permafrost, in 1970 and 2010, for a representative 10 km<sup>2</sup> subset of each of the areas of interest (AOI). Areas of forest loss and gain are presented alongside areas burned by forest fires during this 40-year period and areas of linear disturbance. Adapted from Carpino et al. (2018).

**Table 1.** Nonparametric correlation associations between net forest loss, forest loss and forest gain with climatic variables including average temperatures ( $T_{avg}$ ; 1970–2010), and average annual precipitation ( $P_{avg}$ ) as well as seasonal factors over the study period (1970–2010) including average winter and summer temperatures, average winter and summer precipitation, change in winter and summer temperature ( $\Delta T$ ; 1970–2010) and change in winter and summer precipitation ( $\Delta P$ ; 1970–2010). Significant ( $p < 0.05$ ) correlations have been highlighted by bold text. Adapted from Carpino et al. (2018).

	$T_{avg}$ (1970–2010)	$P_{avg}$ (1970–2010)	$T_{avg}$ winter (1970–2010)	$T_{avg}$ summer (1970–2010)	$P_{avg}$ winter (1970–2010)	$P_{avg}$ summer (1970–2010)	$\Delta T$ winter (1970–2010)	$\Delta T$ summer (1970–2010)	$\Delta P$ winter (1970–2010)	$\Delta P$ summer (1970–2010)
Net loss	-0.491	<b>-0.636</b>	<b>-0.782</b>	0.273	-0.612	<b>-0.636</b>	<b>0.691</b>	<b>0.690</b>	<b>-0.762</b>	0.333
Loss	<b>0.647</b>	0.313	0.387	0.387	0.362	0.436	-0.313	-0.171	0.401	-0.483
Gain	<b>0.794</b>	<b>0.661</b>	<b>0.745</b>	-0.018	0.612	<b>0.709</b>	-0.587	-0.527	<b>0.726</b>	-0.602

**Table 2.** Change in mean water level (mm) from 2003 through to 2017 calculated from best-fit trend for each of the eight long-term monitoring wells within the 0.25 km<sup>2</sup> area of study within the area of interest at Scotty Creek (see Figure 4). The p-values of significant regression trends are in bold. Adapted from Haynes et al. (2018). Abbreviation: CI, confidence interval.

	Site	Change in mean water level over record (mm)	Regression p-value
<b>Peat plateau</b>	Plateau interior	-205	0.06
	Plateau edge	-511	<b>&lt; 0.001</b>
<b>Fen</b>	Fen	-38	0.50
<b>Isolated bogs</b>	I-bog 1	+38	0.60
<b>Connected bogs</b>	C-bog 1 (fully connected)	-219	<b>&lt; 0.0001</b>
	C-bog 2 (fully connected)	-44	0.22
	C-bog 3 (partially connected)	-110	0.06
	C-bog 4 (partially connected)	-164	<b>0.03</b>
<b>All connected bogs - areal-weighted mean (n = 4 bogs) ±95% CI</b>	Areal-weighted mean:	-109 ± 15	
	With porosity of 0.85:	-93 ± 13	
	<b>Watershed scale:</b>	<b>-46 ± 6</b>	

connected bogs, as a result of permafrost thaw, was determined assuming an average peat porosity of 0.85 (Quinton and Hayashi, 2004) and estimating approximately 50% bog coverage across the entire Scotty Creek basin, given that this value represents the approximate areal coverage of wetland in the headwaters portion of the basin. The mean depth of water storage lost from the connected bogs from 2003 to 2017 was 46 ± 6 mm.

In contrast, the water level in the channel fen, which conveys water to the basin outlet, did not significantly change over the 15-year period of study (Figure 4c). Similarly, in a bog isolated from the drainage network, the water level did not significantly change with time. On an actively thawing permafrost peat plateau, the elevation of the perched water table declined significantly, with a decrease of 205 mm occurring at the interior of the plateau from 2003 to 2017 (Figure 4d). Near the edge of the plateau a considerable decline of 511 mm was observed over this period (Figure 4d). The plateau edge well was approximately 20 m from the edge of the plateau at the time of installation, but is now situated only 4 m from the receding plateau edge. The perched water level in the active layer is significantly lowering as the permafrost thaws and the plateau width shrinks. As the plateau degrades and subsides, the water level elevation at the pla-

teau edge approaches that of the adjacent bog and fen as the plateau transitions to wetland.

### Partitioning Sources of Excess Runoff

Runoff from the Scotty Creek basin has been steadily increasing since measurements began in 1996. Between 1998 and 2012 excess runoff on the order of approximately 1000 mm was observed beyond that expected based on trends in precipitation and runoff ratios prior to 1996 in neighbouring watersheds, including the Jean Marie watershed (Figure 5). Of this extra cumulative runoff approximately 52% was the result of greater effective precipitation received by the expanding channel fen areas, which is available to be partitioned to runoff. As peat plateaus became increasingly fragmented with permafrost thaw, resulting in greater perimeter-to-area ratios (Baltzer et al., 2014), runoff from the banks of the degrading plateaus (termed ‘primary runoff’; Connon et al., 2014) contributed approximately 27% of the excess observed runoff from 1998 to 2012. Using aerial imagery analysis to determine the rate of permafrost thaw based on landform conversion and an estimate of total ice volume in the basin, the amount of runoff derived directly from the thawing of permafrost accounts for 11% of the extra cumulative runoff. Collectively, these permafrost-thaw-induced changes account for 90% of the excess runoff over the 15-year period of 1998 to 2012. The residual of approximately 109 mm that cannot be accounted for by these precipitation- and nonprecipitation-induced landscape changes is of similar magnitude to the average depth of wetland drainage water from the connected bogs monitored over a similar 15-year period from 2003 to 2017.

### Discussion

Permafrost degradation and thaw results in a significant loss of forest cover as peat plateau landforms subside and become inundated by adjacent wetlands (Wright et al., 2009; Baltzer et al., 2014). This transitioning of the land-

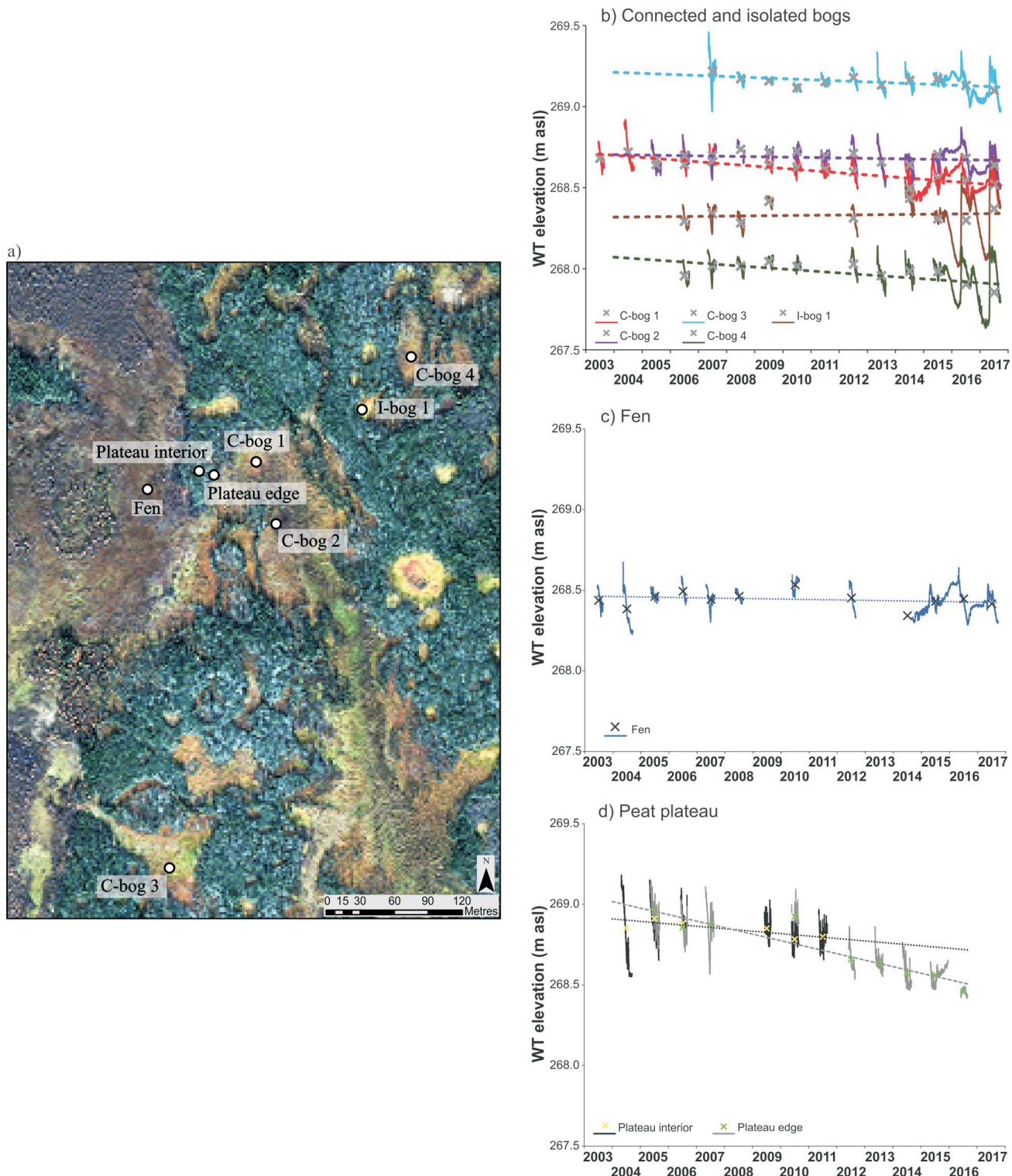


**Figure 4.** a) A 2010 WorldView-2 image (©DigitalGlobe, Inc. all rights reserved) of the 0.25 km<sup>2</sup> area of study within the Scotty Creek area of interest. White dots represent the locations of wells in each of the monitored connected bogs (C-bog), isolated bog (I-bog), as well as channel fen and peat plateau sites. Water table (WT) elevations (in m asl) from 2003 to 2017 for the b) representative connected and isolated bogs, c) channel fen, and d) peat plateau. In b), c) and d), solid lines are the 30 min water level records, 'x' symbols represent mean annual water level position in each site, and dotted lines represent linear best-fit trends in water level over the period of record. Adapted from Haynes et al. (2018).

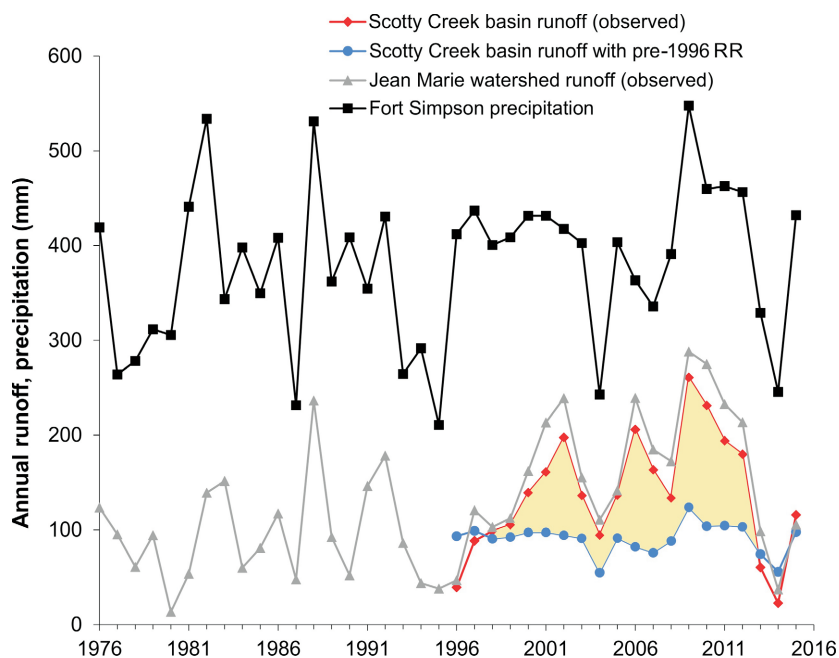


**Figure 5.** Total annual runoff (mm) measured at the Scotty Creek basin outlet (red line) and total annual precipitation (including both rain and snow; mm) measured at Fort Simpson (black line) from 1976 to 2015. Yellow area denotes extra observed runoff beyond that expected based on the mean of runoff ratios (RR) prior to 1996 and current precipitation patterns at Scotty Creek basin (blue line). Runoff from the neighbouring Jean Marie watershed (grey line), which functions similarly to the Scotty Creek basin, from 1976 to 2015 is plotted to illustrate the observed shift in increased runoff post-1998 to 2012. All runoff amounts totalled over the water year (October 1 to September 30). Adapted from Haynes et al. (2018).

scape to wetland area at the expense of forest cover was observed at all 10 AOI in this study area, which spans the discontinuous to sporadic permafrost regions of northwestern Canada. One main control on permafrost loss, as reflected by decreasing forest cover, is increasing average air temperature resulting in accelerated rates of forest cover loss. Subsidence and inundation of degrading permafrost plateaus (Quinton et al., 2009) and peat overmaturation (Zoltai, 1993; Beilman and Robinson, 2003) are the dominant mechanisms accounting for the dramatic landscape changes observed in these environments as permafrost bodies warm and thaw. The former mechanism occurs at all AOI along the CPET transect, whereas the formation of fissures in desiccating and heavy surface peat deposits as they become disconnected from the underlying water table, an indicator of peat overmaturation, is also observed at the southernmost AOI. However, the significant positive relationship between mean annual air temperature and forest gain along the CPET transect suggests that warming temperatures may also play an important, although contrasting, role in these transitioning regions depending upon the degree of landscape change. The promotion of forest regrowth with increased air temperatures has been attributed directly to enhanced forest productivity (Baltzer et al., 2014). An indirect influence of increasing air temperatures facilitating afforestation likely involves the alteration of

the magnitude and routing of hydrological flows across the landscape providing suitable conditions for tree regrowth.

The long-term trends in water levels in representative land-cover types across the Scotty Creek site illustrate the change to the amount of water stored, drained and routed across the transitioning landscape. Significant drainage of previously isolated bog features occurs as they become connected to the drainage network (Figure 4). These connected wetlands lose significant amounts of water to runoff, which was previously impounded by permafrost barriers and stored in the basin. Warming air temperatures result in the thaw and degradation of these permafrost barriers allowing for more efficient and direct routing of water to the drainage network and ultimately exporting it as runoff from the basin. Therefore, permafrost thaw results in drying of wetlands in this region. Enhanced wetland drainage coupled with amplified evapotranspiration as a result of increasing temperatures (Warren et al., 2018) indirectly enhance forest succession and regrowth by providing an optimal environment in terms of hydrology for tree establishment.

### Trajectory of Discontinuous to Sporadic Permafrost Landscape

It is likely that the hydrological mechanism responsible for controlling afforestation is favourable moisture conditions

with landscape change. The loss of permafrost barriers has resulted in increasing runoff exiting the transitioning Scotty Creek basin (Figure 5). With accelerated permafrost loss in recent decades, elevated runoff beyond that expected given pre-1996 runoff ratios and current trends in precipitation patterns is observed (Figure 5). In addition to the contributions to elevated runoff from the expansion of area contributing to the drainage network as permafrost barriers are lost, increased primary runoff from the banks of increasingly fragmented peat plateaus and direct moisture from permafrost thaw (Connon et al., 2014), draining of wetland features as they become connected to the basin drainage network accounts for approximately 10% of excess runoff.

Given the hydrological trends observed at the Scotty Creek site, a conceptual model for the anticipated relationship between water storage on the landscape and associated runoff over time is proposed (Figure 6). As the landscape continues to change with further permafrost thaw, runoff from discontinuous and sporadic permafrost basins is anticipated to increase as wetlands become incrementally connected to the drainage network (Figure 6; Quinton et al., 2009). However, once the maximum contributing area is reached, when all bogs have developed a connection to the drainage network, a threshold of peak potential runoff will be achieved, which is higher than previously observed due to the significant expansion of the runoff contributing area. The observation of afforestation in southern latitude AOI (Figure 2) reinforces the likelihood of continued wetland drainage as connections to the drainage network broaden as permafrost thaw proceeds, leading to drier wetland soils. Under such conditions hydrological connectivity within plateau-wetland complex basins will only be achieved during periods of high moisture supply, activating secondary runoff pathways (Connon et al., 2014). In periods of limited moisture availability, the lack of active runoff pathways will restrict contributions from collapse scar bogs to basin runoff.

Changes in precipitation patterns, including decreases in snowpack depth (Hinzman et al., 2005), earlier spring melt (Intergovernmental Panel on Climate Change, 2007) and increases in the frequency of mid-winter melts resulting from warm periods and rain-on-snow events (Putkonen et al., 2009), all influence permafrost stability. The relationships between winter precipitation and forest loss and gain suggest that decreases in winter precipitation promote the transition from forest to wetland due to permafrost thaw, whereas greater snow accumulation facilitates forest regrowth with reduced saturation following snowmelt. Although tree regrowth is occurring at the southern AOI of the transect, which are at an advanced stage of permafrost degradation and loss, it does not appear to be accompanied by the re-establishment of permafrost likely due to warmer

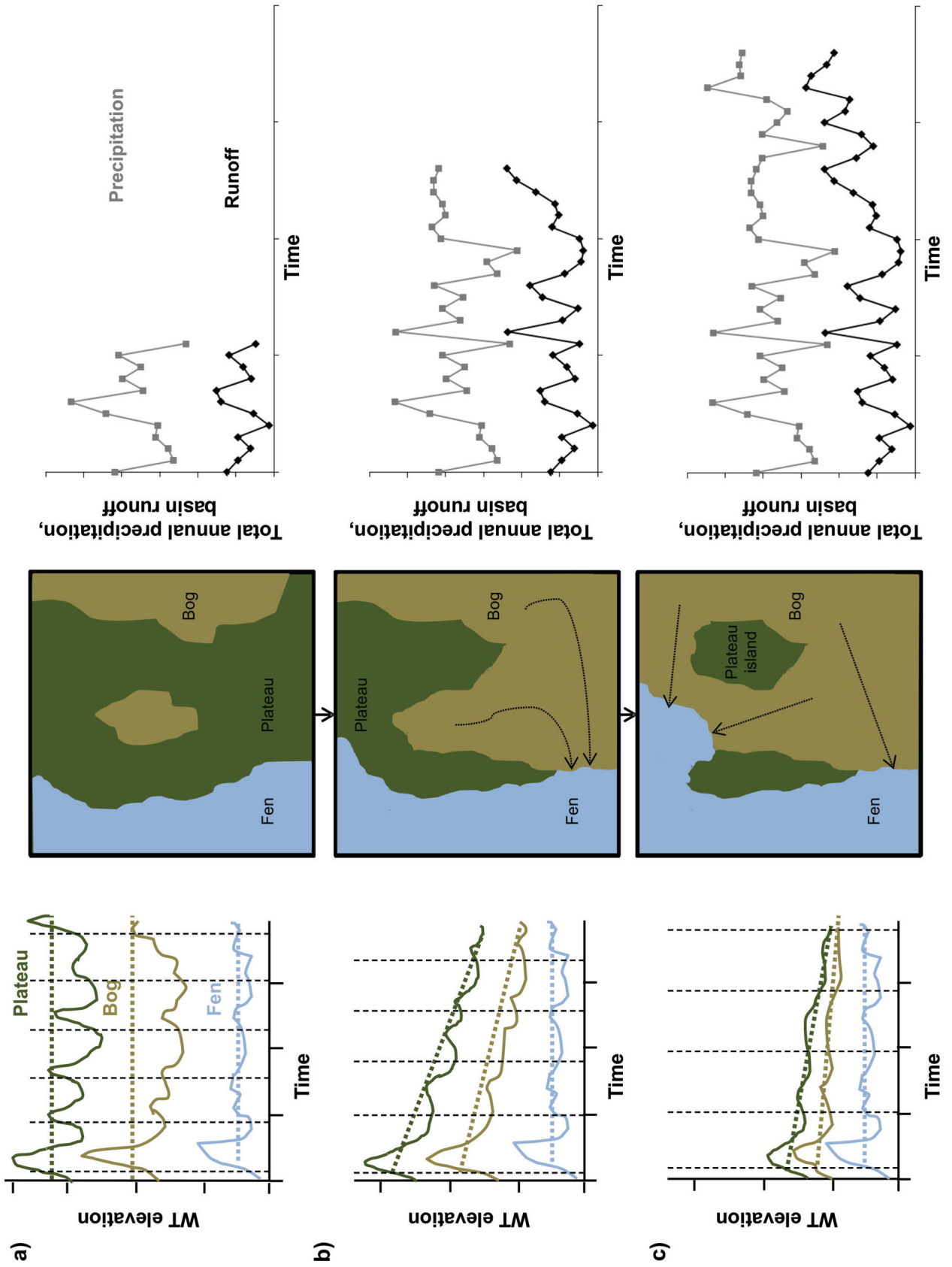
climatic conditions (Robinson and Moore, 2000; Jorgenson et al., 2010).

## Conclusions

The latitudinal gradient of the CPET transect illustrates the likely trajectory of permafrost-thaw-induced landscape change. This space-for-time substitution proxy demonstrates that net forest loss decreases with decreasing latitude, whereas forest gain is negligible other than at the most southerly locations. Therefore, considering that this transect represents the likely trajectory of permafrost-thaw-induced landscape change, it may be concluded that the landscape of forested plateaus interspersed with treeless wetlands, as observed in the Scotty Creek basin, is not likely the climax community for this region. As plateau features subside and transition to wetlands as a result of inundation, the water stored in previously isolated bogs is directed to basin runoff. Drying of wetlands through drainage enhances runoff from these environments. This significant change in hydrology facilitates the re-establishment of tree species and, in association with such climatic changes as increasing air temperatures and altered precipitation patterns, promotes afforestation in these landscapes. Further research is required to determine if conditions will be favourable for the return of permafrost beneath the newly established forest cover despite continued climate change-induced warming of air temperatures. Understanding how permafrost-thaw-induced landscape changes in the sporadic to discontinuous permafrost zone affect the hydrology of these environments is important in order to assess the availability and sustainability of freshwater resources for northern communities.



**Figure 6.** Conceptual model for the transition of the permafrost landscape, from **a**) the initial condition with wetlands isolated from drainage networks with perched, flashy water tables (WT) on permafrost terrain and interannual runoff generation in response to precipitation trends; **b**) to an intermediate condition where, as permafrost barriers are lost and perched plateau water tables subside, bogs drain as a result of the newly formed connections to channel fens, with bog and plateau water levels approaching the level of the drainage channel and runoff begins to increase without a corresponding increase in precipitation; **c**) to an advanced condition where, due to the enhanced runoff contributing area partitioning precipitation to runoff, basin runoff is elevated as compared to preconnected conditions as bog drainage across the basin approaches a diminishing return. Plateau water level responses become increasingly attenuated and follow a similar trend to adjacent wetlands. Dotted lines in the water table plots illustrate the mean water level trend for each of the bog, fen and plateau. Black vertical dashed lines in water table plots denote annual cycles, whereas points in precipitation and runoff plots represent annual totals. Black dotted arrows in the landscape images represent the direction of water flow as areas become connected to the drainage network with permafrost loss. Changes in the runoff and precipitation trends along the three transitional phases are represented by the incremental addition of data for plots a) through to c). Adapted from Haynes et al. (2018).

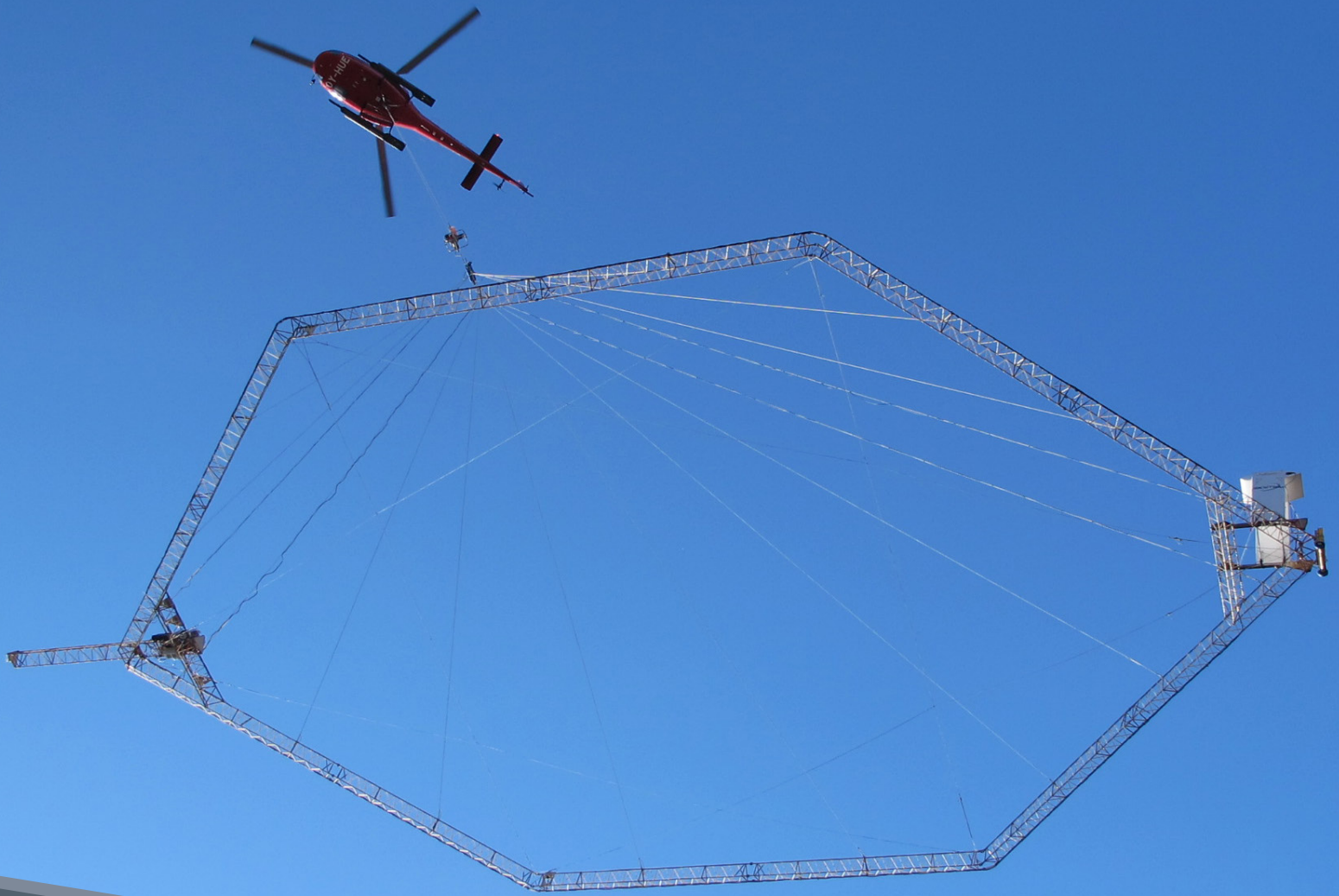


## Acknowledgments

Consortium for Permafrost Ecosystems in Transition is funded by a Natural Sciences and Engineering Research Council of Canada Collaborative Research and Development grant with partner contributions from Nexen, Petroleum Technology Alliance Canada, Geoscience BC and BC Oil and Gas Research and Innovation Society. The authors gratefully acknowledge the support of Fort Nelson First Nation, Liidlii Kue First Nation, Jean Marie River First Nation, Government of the Northwest Territories and Government of British Columbia. This paper benefited from a review by M. English, Wilfrid Laurier University.

## References

- Baltzer, J., Veness, T., Chasmer, L., Sniderhan, A. and Quinton, W. (2014): Forests on thawing permafrost: fragmentation, edge effects, and net forest loss; *Global Change Biology*, v. 20, p. 824–834.
- Beilman, D.W. and Robinson, S.D. (2003): Peatland permafrost thaw and landform type along a climatic gradient; *in* Proceedings of the Eighth International Conference on Permafrost, M. Phillips, S.M. Springman and L.U. Arenson (ed.), Zurich, Switzerland, July 21–25, 2003, A.A. Balkema, v. 1, p. 61–65.
- Carpino, O.A., Berg, A.A., Quinton, W.L. and Adams, J.R. (2018): Climate change and permafrost thaw-induced boreal forest loss in northwestern Canada; *Environmental Research Letters*, v. 13, 084018, 10 p.
- Connon, R.F., Quinton, W.L., Craig, J.R. and Hayashi, M. (2014): Changing hydrologic connectivity due to permafrost thaw in the lower Liard River valley, NWT, Canada; *Hydrological Processes*, v. 28, p. 4163–4178.
- Haynes, K.M., Connon, R.F. and Quinton, W.L. (2018): Permafrost thaw induced drying of wetlands at Scotty Creek, NWT, Canada; *Environmental Research Letters*, v. 13, 114001, 13 p.
- Hinzman, L.D., Bettez, N.D., Bolton, W.R., Chapin, F.S., Dyurgerov, M.B., Fastie, C.L., Griffith, B., Hollister, R.D., Hope, A., Huntington, H.P., Jensen, A.M., Jia, G.J., Jorgenson, T., Kane, D.L., Klein, D.R., Kofinas, G., Lynch, A.H., Lloyd, A.H., McGuire, A.D., Nelson, F.E., Oechel, W.C., Osterkamp, T.E., Racine, C.H., Romanovsky, V.E., Stone, R.S., Stow, D.A., Sturm, M., Tweedie, C.E., Vourlitis, G.L., Walker, M.D., Walker, D.A., Webber, P.J., Welker, J.M., Winker, K.S. and Yoshikawa, K. (2005): Evidence and implications of recent climate change in northern Alaska and other arctic regions; *Climatic Change*, v. 72, p. 251–298.
- Intergovernmental Panel on Climate Change (2007): Climate change 2007: synthesis report, contribution of Working Groups I, II and III to the Fourth Assessment Report of the Intergovernmental Panel on Climate Change; Intergovernmental Panel on Climate Change, Geneva, Switzerland, 104 p.
- Jorgenson, M.T., Romanovsky, V., Harden, J., Shur, Y., O'Donnell, J., Schuur, E.A.G., Kanevskiy, M. and Marchenko, S. (2010): Resilience and vulnerability of permafrost to climate change; *Canadian Journal of Forest Research*, v. 40, p. 1219–1236.
- Lara, M.J., Genet, H., McGuire, A.D., Euskirchen, E.S., Zhang, Y., Brown, D.R.N., Jorgenson, M.T., Romanovsky, V., Breen, A. and Bolton, W.R. (2016): Thermokarst rates intensify due to climate change and forest fragmentation in an Alaskan boreal forest lowland; *Global Change Biology*, v. 22, p. 816–829.
- Putkonen, J., Grenfell, T.C., Rennert, K., Bitz, C., Jacobson, P. and Russell, D. (2009): Rain on snow: little understood killer in the north; *EOS, Transactions, American Geophysical Union*, v. 90, p. 221–222.
- Quinton, W.L. and Hayashi, M. (2004): The flow and storage of water in the wetland-dominated central Mackenzie River basin: recent advances and future directions; *in* Prediction in Ungauged Basins: Approaches for Canada's Cold Regions, Canadian Water Resources Association, p. 45–66.
- Quinton, W.L., Hayashi, M. and Chasmer, L.E. (2009): Peatland hydrology of discontinuous permafrost in the Northwest Territories: overview and synthesis; *Canadian Water Resources Journal*, v. 34, p. 311–328.
- Quinton, W.L., Hayashi, M. and Chasmer, L.E. (2011): Permafrost thaw-induced land-cover change in the Canadian subarctic: implications for water resources; *Hydrological Processes (Scientific Briefing)*, v. 25, p. 152–158.
- Robinson, S.D. and Moore, T.R. (2000): The influence of permafrost and fire upon carbon accumulation in high boreal peatlands, Northwest Territories, Canada; *Arctic, Antarctic, and Alpine Research*, v. 32, p. 155–166.
- Rowland, J.C., Jones, C.E., Altmann, G., Bryan, R., Crosby, B.T., Hinzman, L.D., Kane, D.L., Lawrence, D.M., Mancino, A., Marsh, P., McNamara, J.P. and Romanovsky, V.E. (2010): Arctic landscapes in transition: responses to thawing permafrost; *EOS, Transactions, American Geophysical Union*, v. 91, p. 229–230.
- St. Jacques, J.M. and Sauchyn, D.J. (2009): Increasing winter baseflow and mean annual streamflow from possible permafrost thawing in the Northwest Territories, Canada; *Geophysical Research Letters*, v. 36, no. L01401, 6 p.
- Warren, R.K., Pappas, C., Helbig, M., Chasmer, L.E., Berg, A.A., Baltzer, J.L., Quinton, W.L. and Sonnentag, O. (2018): Minor contribution of overstorey transpiration to landscape evapotranspiration in boreal permafrost peatlands; *Ecohydrology*, v. 11, e1975, 10 p.
- Wright, N., Hayashi, M. and Quinton, W.L. (2009): Spatial and temporal variations in active layer thawing and their implication on runoff generation in peat-covered permafrost terrain; *Water Resources Research*, v. 45, p. 1–13.
- Zoltai, S.C. (1993): Cyclic development of permafrost in the peatlands of northwestern Alberta, Canada; *Arctic and Alpine Research*, v. 25, p. 240–246.



**Geoscience BC**

t: 604 662 4147

e: [info@geosciencebc.com](mailto:info@geosciencebc.com)

SUITE 1101-750 WEST PENDER ST  
VANCOUVER, BC V6C 2T7

[www.geosciencebc.com](http://www.geosciencebc.com)